NASA CR-175,842

NASA-CR-175842
19850018783

The Telecommunications and Data Acquisition Progress Report 42-81

January-March 1985

E.C. Posner
Editor

LIBRARY COPY

1985

LANGLEY RESEARCH CENTER
LIBRARY, NASA
HAMPTON, VIRGINIA

May 15, 1985

NASA
National Aeronautics and
Space Administration

Jet Propulsion Laboratory
California Institute of Technology
Pasadena, California

NF00474

The Telecommunications and Data Acquisition Progress Report 42-81

January-March 1985

E.C. Posner
Editor

May 15, 1985

NASA
National Aeronautics and
Space Administration

Jet Propulsion Laboratory
California Institute of Technology
Pasadena, California

N85-27094 #
N85-27109 #

The research described in this publication was carried out by the Jet Propulsion Laboratory, California Institute of Technology, under a contract with the National Aeronautics and Space Administration.

Reference herein to any specific commercial product, process, or service by trade name, trademark, manufacturer, or otherwise, does not constitute or imply its endorsement by the United States Government or the Jet Propulsion Laboratory, California Institute of Technology.

Preface

This quarterly publication provides archival reports on developments in programs managed by JPL's Office of Telecommunications and Data Acquisition (TDA). In space communications, radio navigation, radio science, and ground-based radio astronomy, it reports on activities of the Deep Space Network (DSN) and its associated Ground Communications Facility (GCF) in planning, in supporting research and technology, in implementation, and in operations. Also included is TDA-funded activity at JPL on data and information systems and reimbursable DSN work performed for other space agencies through NASA. The preceding work is all performed for NASA's Office of Space Tracking and Data Systems (OSTDS).

In geodynamics, the publication reports on the application of radio interferometry at microwave frequencies for geodynamic measurements. In the search for extraterrestrial intelligence (SETI), it reports on implementation and operations for searching the microwave spectrum. The latter two programs are performed for NASA's Office of Space Science and Applications (OSSA).

Finally, tasks funded under the JPL Director's Discretionary Fund and the Caltech President's Fund which involve the TDA Office are included.

This and each succeeding issue of the TDA Progress Report will present material in some, but not necessarily all, of the following categories:

OSTDS Tasks:

- DSN Advanced Systems
  - Tracking and Ground-Based Navigation
  - Communications, Spacecraft-Ground
  - Station Control and System Technology
  - Network Data Processing and Productivity
- DSN Systems Implementation
  - Capabilities for New Projects
  - Networks Consolidation Program
  - New Initiatives
  - Network Sustaining
- DSN Operations
  - Network Operations and Operations Support
  - Mission Interface and Support
  - TDA Program Management and Analysis
- GCF Implementation and Operations
- Data and Information Systems

OSSA Tasks:

- Search for Extraterrestrial Intelligence
- Geodynamics
  - Geodetic Instrument Development
  - Geodynamic Science

Discretionary Funded Tasks

Contents

OSTDS TASKS
DSN Advanced Systems
TRACKING AND GROUND-BASED NAVIGATION

Relating the Planetary Ephemerides and the Radio Reference Frame 1
A. E. Niell, X X Newhall, R. A. Preston, G. L. Berge, D. O. Muhleman, D. J. Rudy, J. K. Campbell, P. B. Esposito, and E. M. Standish
NASA Code 310-10-60-50-00

COMMUNICATIONS, SPACECRAFT-GROUND

Photo Detection With Cooled Avalanche Photodiodes: Theory and Preliminary Experimental Results 9
D. L. Robinson and D. A. Hays
NASA Code 310-20-67-55-00

STATION CONTROL AND SYSTEM TECHNOLOGY

Techniques for Computing the DFT Using the Residue Fermat Number Systems and VLSI 18
T. K. Truong, J. J. Chang, I. S. Hsu, D. Y. Pei, and I. S. Reed
NASA Code 310-30-70-84-08

Bit Error Rate of Coherent *M*-ary PSK 31
P. J. Lee
NASA Code 310-30-71-83-02

Synchronizing Heavily Encoded Data in Bad Weather 38
L. Swanson
NASA Code 310-30-71-84-04

A Software Simulation Study of a Sequential Decoder Using the Fano Algorithm 40
F. Pollara
NASA Code 310-30-71-83-04

Symbol Stream Combining in a Convolutionally Coded System 47
R. J. McEliece, F. Pollara, and L. Swanson
NASA Code 310-30-71-83-04

NETWORK DATA PROCESSING AND PRODUCTIVITY

An Integrated UNIX-Based CAD System for the Design and Testing of Custom VLSI Chips 51
L. J. Deutsch
NASA Code 310-40-72-15-00

DSN Systems Implementation
CAPABILITIES FOR NEW PROJECTS

High-Speed Digital Baseband Mixer 63
F. P. Chan, M. P. Quirk, and R. F. Jurgens
NASA Code 314-30-59-31-01

Digital Filters for Digital Phase-Locked Loops 81
M. Simon and A. Mileant
NASA Code 314-30-53-20-02

Errata 93

Maintenance of Time and Frequency in the DSN Using the Global Positioning System 94
P. A. Clements, A. Kirk, and S. E. Borutzki
NASA Code 314-30-56-56-19

NETWORK SUSTAINING

Network Information Management Subsystem 109
C. C. Chatburn
NASA Code 314-30-41-17-03

A Description of the 64-Meter Antenna Elevation Drive Gears and Their Strange Wear 116
H. McGinness
NASA Code 314-30-56-04-05

Repair of the DSS-14 Pedestal Concrete 136
D. McClure
NASA Code 314-40-48-00-10

DSN Operations

TDA PROGRAM MANAGEMENT AND ANALYSIS

Determining Availability Characteristics of DSN Data Systems Using Discrepancy Report Data 149
A. M. Ruskin and C. T. Quach
NASA Code 314-40-31-30-08

Relating the Planetary Ephemerides and the Radio Reference Frame

A.E. Niell,[1] X X Newhall, and R.A. Preston
Tracking Systems and Applications Section

G.L. Berge, D.O. Muhleman, and D.J. Rudy
California Institute of Technology

J.K. Campbell, P.B. Esposito, and E.M. Standish
Navigation Systems Section

The positions of Venus, Mars, and Jupiter have been obtained in the VLBI radio reference frame by measuring the position of a satellite (natural or artificial) of each planet relative to an extragalactic source in the radio catalogue. From the results for Mars and Venus we conclude that the offset in right ascension of the radio frame from the dynamical equinox defined in DE200 is 0".00 ±0".04. The observations for Jupiter imply a correction to its position from DE200 of -0".18 ±0".04 in right ascension and -0".06 ±0".05 in declination on 1983 April 29. The right ascension of Jupiter relative to the inner planets has been measured independently using Doppler tracking data near Jupiter encounter from Pioneers 10 and 11 and from Voyagers 1 and 2 by tying the tracking station positions, through previous spacecraft missions, to the DE200 ephemerides of the inner planets. This technique yielded a correction to Jupiter's right ascension of -0".22 ±0".05, in good agreement with the results from the direct radio measurements.

I. Introduction

There are two practical celestial reference systems, one based on stars through optical observations, the other on extragalactic objects through radio observations. For optical observations the current fundamental catalog FK4 (Ref. 1) contains positions of approximately 1500 stars which were obtained by optical meridian transit measurements and are on the B1950.0 system. This catalog will be superseded by FK5 which will contain some 4500 stars having positions on the J2000 system. The reference frame for radio sources is based on Very Long Baseline Interferometry (VLBI) observations and is on the J2000 system.

For use as a fundamental reference frame the system formed by the radio observations has two advantages: i) since the extragalactic objects are at such great distances, any velocity that they might have transverse to the line of sight is negligible, and they thus provide an effectively inertial frame of reference; and ii) the accuracy of the positions is 10 to 100 times better than for the optical system.

[1]Now at Haystack Observatory, Massachusetts Institute of Technology

A second *inertial* frame exists in the form of the ephemerides of the inner planets (Mercury through Mars) and the Moon. These ephemerides have been derived from accurate measurements of the planetary and lunar distances by radar or laser ranging to their surfaces and by ranging to spacecraft, especially the Viking Lander. (They provide an inertial system because the ranging measurements are sensitive to the motion relative to an inertial frame and not just to the motion relative to background objects.) The orbit of the earth is included in this ephemeris; thus a natural product is the calculation of the dynamical equinox, which defines the origin of right ascension. Although the accuracy of positions calculated from the ephemeris is better than for the optical system, the planetary system is not as useful because of the small number of objects visible and because the objects themselves are large in angular extent.

Since the two inertial frames are independent, it is important to establish their relative orientation. In declination the two should agree because each determines absolute values. However, in right ascension radio interferometry determines only relative values, and the origin must be found by reference to the planetary ephemeris.

An important reason for determining the relationship between these two frames arises from navigation of deep space probes (Ref. 2). Although the target of the navigation is a planet whose position is known in the planetary frame (for Mercury through Mars) or the stellar frame (for the outer planets), the spacecraft can be more precisely navigated by the measurement of differential displacements from radio sources. Thus, the problem is to determine the positions of the planets in the frame of the extragalactic radio sources.

In this report we summarize our current understanding of the relationship between the radio reference frame and the ephemerides of the planets out to Jupiter. Observations will be described which a) relate the origin of right ascension of the radio frame to the dynamical equinox; b) give the position of Jupiter in the radio frame; and c) improve the ephemeris of Jupiter relative to the inner planets.

II. Reference Frame Accuracies

A. Optical Star Catalogues

The optical reference system consists of the stars of the FK4 fundamental catalogue (Ref. 1) plus a greater number of stars whose positions have been measured relative to the primary stars, the AGK3RN. The uncertainties in position of these objects include not only the original position error but also the contribution from uncertainties in proper motion extrapolated to the epoch of interest. The combination of these errors is at least 0.″1. In addition there are systematic variations about the sky of up to 0.″2. Upon completion of the FK5 the uncertainties will be reduced, though not significantly below 0.″1. (See Ref. 3 for a more complete summary.)

B. Planetary Ephemerides

The relative positions of the *inner* planets (Mercury, Venus, and Mars) in a geocentric coordinate system have uncertainties of only a few hundredths arc second in the latest ephemerides DE118 (B1950.0) or DE200 (which is DE118 rotated to the equator and equinox of J2000) (Ref. 4). They are derived from distance measurements obtained by radar ranging to the surfaces of the planets and by ranging to spacecraft both during flybys and while orbiting the planets. The origin of right ascension for the ephemerides is the dynamical equinox, for which the uncertainty is given as ~0.″01.

The positions of the *outer* planets have been calculated from optical meridian transit observations, and their accuracies are limited both by the observational errors and by the systematic errors of the stellar reference system. As a result the uncertainties relative to the inner planets increase from ~0.″2 for Jupiter to ~1″ for Pluto (Ref. 5).

C. VLBI Radio Reference Frame

The positions of ~130 extragalactic radio sources as determined by VLBI have accuracies of better than 0.″005 in absolute declination and in relative right ascension of epoch J2000 (Refs. 6-8). These sources span the declination range -45 degrees to +84 degrees.

Since the VLBI observations are only weakly sensitive to the ecliptic, through orbital aberration, the origin of right ascension is poorly determined. In order to fix the origin for the radio frame the right ascension of one source, the quasar 3C273B, has been assigned the value obtained by Hazard *et al.* (Ref. 9). Their position was derived as an average of: i) optical measurements relative to stars, whose positions were on the FK4 system, and ii) occultations of the radio emission of 3C273B by the Moon. The two methods agreed, yielding an uncertainty in their average of 0.01 seconds of right ascension (= 0.″15 = 750 nanoradians). The accuracy of measurements of the optical position of 3C273B relative to reference stars suffers the same approximately 0.″1 limitation as measurements of the outer planet positions, due to the systematic errors which vary with right ascension and declination. The lunar occultations have a lower limit on their uncertainty of 0.″1 set by the lack of knowledge of the shape of the limb of the Moon. Thus, neither of these techniques offers the possibility of significant improvement in relating the origins of the two reference frames.

III. Observations

The value of radio interferometry, and of Very Long Baseline Interferometry in particular, is the capability of measuring the positions of compact sources of radio emission with great precision. However, the planets are large in angular size when compared to the compact components of the extragalactic radio sources and to the measurement accuracy which is possible. Thus, for interferometers with small fringe spacings, the planets would be resolved, while for larger fringe spacings the positional accuracy is degraded.

Alternatively, the position of a smaller object bound to the planet, such as a satellite or space probe, may be measured in the radio frame. The problem then consists of two parts: obtaining the position of the satellite or probe relative to the radio sources, and obtaining its trajectory or orbit about the planet.

This technique has been applied in two ways: i) an orbiter of each of Mars and Venus has been used for VLBI connection of these two planets to the Radio Reference Frame (see Section IV); ii) for Jupiter the Very Large Array (VLA) has been used to observe the Galilean satellites relative to extragalactic radio sources (see Section V). The VLA is appropriate because it provides both the sensitivity which is necessary to detect the thermal emission of the satellites and the spatial resolution which is matched to the angular sizes of the satellites. (The VLA is described by Napier *et al.* [Ref. 10].)

IV. Frame-Tie by Inner-Planet Orbiters (XXN, RAP, PBE)

The positions of the Viking Mars Orbiter and the Pioneer Venus Orbiter (PVO) relative to extragalactic radio sources were measured in several experiments from 1980 to 1983 using differential VLBI phase measurements. Data from eight passes of the Viking spacecraft and three of PVO were successfully analyzed (see Ref. 11 for more details).

The results are shown in Fig. 1 in which the apparent positions of the radio sources in the planet frame are given. The average right ascension offset is 0″.00 ±0″.04 (0 ±200 nrad) and the average declination offset is 0″.01 ±0″.05 (40 ±250 nrad). The uncertainty is obtained from the rms scatter of the eleven data points.

It is clear that the scatter of the data points is larger than would be expected from the individual experiment results. The reason for this is not understood. Among the primary sources of error are the planetary ephemerides, the positions of the radio sources for the Viking measurements, and the determination, from Doppler tracking data taken on the same orbit, of the orientation on the sky of the line of nodes of the spacecraft orbit. Estimates of these errors are included in the uncertainties assigned to each measurement. A possible source of error, not included as it was thought to be small, is the degree to which the phase connection between the individual differential VLBI observations has been successful. The correction for charged particle dispersion is only partially complete in that, although the downlink was observed at both S- and X-band, the uplink was S-band only.

Thus, although it seems fortuitous, given an *a priori* uncertainty of 0″.15 (750 nrad), the radio source and planet frames seem to agree to better than 0″.04 (200 nrad) in right ascension. In declination the results for both Mars and Venus are consistent within the *a priori* uncertainty of 0″.02 (100 nrad) (Ref. 5).

V. The Position of Jupiter in the Radio Frame (AEN, DOM, GLB, DJR)

The position of Jupiter in the radio frame has been inferred by measuring the position of its satellite Ganymede relative to two extragalactic radio sources, whose positions are accurately known by VLBI, using the VLA in the C configuration at 2-cm wavelength. The positions of Europa and Callisto were also measured, but Callisto has a larger ephemeris uncertainty than Ganymede, and the results for Europa were adversely affected by the proximity of Jupiter at the time of the observations.

The positions of the satellites were obtained by adding their positions from Lieske's Galilean satellite ephemeris E-2 (Ref. 12) to the DE200 ephemeris for Jupiter. The down-track (right ascension) uncertainties for Europa and Ganymede are about 110 km and for Callisto about 200 km, corresponding to 0″.03 and 0″.06, respectively, at the 4.5 AU distance of Jupiter at the time of observation. The cross-track (declination) uncertainties are, respectively, 80, 60, and 200 km (0″.03, 0″.02, and 0″.06) (J.H. Lieske, private communication).

The VLA observations were made at both 6-cm and 2-cm wavelength as part of a combined program to measure both the physical and the astrometric properties of the Galilean satellites. However, only the 2-cm results were used for astrometric results because the larger primary beam at 6-cm wavelength does not sufficiently attenuate the radio emission from Jupiter.

Two radio sources were used as position calibrators. They were chosen to be approximately equally spaced on either side

of the Jupiter system in order to reduce systematic errors due to elevation angle effects (e.g. tropospheric refraction) or to incorrect modeling of the Earth's orientation. The epoch J2000 positions of the two sources, NRA0530 and P1519-273, were taken from the JPL/DSN radio source catalogue designated 1983-4 (see e.g., Ref. 6) and have an absolute accuracy of ~0.″005 in declination and in relative right ascension. As discussed in the previous section the origin of right ascension is consistent with that of the inner-planet ephemeris to 0.″04.

The observables at the VLA are the amplitude and phase of the two independent circular polarizations for all interferometer pairs formed by the twenty-five operating antennas. The phases and amplitudes are calibrated by assuming that the positions and flux densities of the calibrator sources are known and then interpolating corrections for the amplitudes and phases at the time of the satellite observations. The positions of the satellites are then found by doing a least-squares fit to the amplitudes and phases (obtained during the six hours of observation each day) for the position and brightness temperature of a uniform disk the size of the satellite.

The observed displacements of the satellites from their expected positions are shown in Fig. 2. For all satellites there are two positions indicated for each day, representing the measurements in both senses of circular polarization. As can be seen the observed positions of Ganymede for the two polarizations for the two days agree within the uncertainties. The two measurements of Europa at one polarization, but on separate days, also agree with the Ganymede data. However, because of the possible corruption by Jupiter the Europa data are not used. Nor is the position of Callisto used, because of the larger uncertainty in its ephemeris and because of the disagreement of the results on the two days. This offset from Ganymede will be used to obtain an improvement to the Callisto ephemeris.

The errors which contribute to the uncertainty in these measurements are a) error due to receiver noise, atmosphere, and confusion by background sources; b) satellite ephemeris uncertainties; c) variations in physical temperature across the satellite disk; d) differential refraction for the satellite positions relative to the calibrator positions; e) bias in the positions due to the proximity of Jupiter, which is 2500 times as strong as the satellites. These errors are summarized as follows:

a) Measurement errors for two days:	0.″015
b) Ephemeris uncertainty relative to Jupiter:	0.″03 in RA 0.″04 in DEC
c), d), and e)	0.″02
RSS Total:	0.″04 in RA 0.″05 in DEC

Thus the correction to the position of the Jupiter system barycenter calculated from the DE200 ephemeris for 1983 April 29 (JD 2445453.5) as determined by the observations of Ganymede relative to the radio reference frame is

$$\Delta RA \cos DEC = -0.''18 \pm 0.''04$$
$$\Delta DEC = -0.''06 \pm 0.''05$$

VI. Jupiter Relative to the Inner Planets (JKC, EMS)

Encounters of spacecraft with the inner planets provide a relationship between those planetary ephemerides which are best known and the terrestrial coordinate system of the stations of the Deep Space Network (T.D. Moyer, private communication, 1980). Subsequent observations of spacecraft encounters with other planets, which are also sensitive to the station locations, may then be used to locate the outer planets in the frame of the inner planets. The Doppler tracking of the Mariner spacecraft to Venus, Mercury and Mars, and especially the ranging data to the Viking Orbiters, have provided relative station locations with accuracies in the equatorial plane of less than a meter, corresponding to an angular resolution of ~0.″03.

Data from the encounters with Jupiter of Pioneers 10 and 11 and Voyagers 1 and 2 (Ref 14) were included in a joint solution with all of the planetary ephemeris data, yielding a correction to the position of Jupiter relative to the inner planets as it was given in DE 118. The result is

$$\Delta RA \cos DEC = -0.''22$$
$$\Delta DEC = -0.''06$$

with uncertainties of ~0.″05.

Thus, the spacecraft data confirm the offset of Jupiter relative to the inner planets as determined by measurements relative to sources of the radio reference frame. The agreement of the two methods also provides support for the conclusion that the currently adopted value for the position of 3C273 is correct to within the measured uncertainty.

VII. Improvements

It may be possible to obtain a better tie between the radio frame and the planetary ephemerides for the inner planets

by using the VLBI determination of the relative locations of the stations of the Deep Space Network and the encounter Doppler data for the inner planets (A.E. Niell, private communication, 1984). The potential accuracy is $< 0''.02$ but may be limited by uncertainties in the ephemerides.

Continued observations of Jupiter via the Galilean satellites with the VLA should verify the results reported here and reduce the uncertainty. Observations have also been made of Titan to improve the position of Saturn in the radio frame, but the analysis is not complete (Muhleman, private communication). Uranus and Neptune are sufficiently small in angular size to permit direct observation with the VLA with a possible position uncertainty of $\sim 0''.05$ to $0''.1$.

Johnston *et al.* (Ref. 13) have reported the first measurements of the positions of minor planets with the VLA. However, even the largest asteroids are much weaker than the Galilean satellites, and the reported positional accuracy was only about $0''.1$. In the FK4 system they found the right ascension of 1 Ceres to be off by $-0''.3$ and that of 2 Pallas by $0''.7$. The *a priori* uncertainty in the optical positions was thought to be $\sim 0''.3$. Their observing program now also includes Hygeia and Vesta. All four objects are observed twice per year. With improved ephemerides for these objects they hope to establish the right ascension origin for the VLA astrometric catalogue consistent with the planetary ephemerides.

VIII. Summary

By using planetary satellites and deep space probes as sources of radio emission, it has been possible to measure the positions of the planets Venus, Mars, and Jupiter in the celestial reference frame defined by VLBI observations. While the absolute declinations and relative right ascensions of the extragalactic radio sources are accurate to better than $0''.005$, the origin of right ascension has an uncertainty of $\sim 0''.15$. The tie to Venus and Mars by VLBI observations of the orbiters of those planets reduces the uncertainty of the origin, relative to the dynamical equinox, to less than $0''.04$ in the J2000 system. The results imply that *no* change is needed to the currently assumed right ascension value for 3C273B, the compact component of 3C273, which is used to define the origin (RA(J2000)=12:29:06.6997).

The position of Jupiter in the radio reference frame has been measured with an accuracy of $0''.04$ by observing the position of Ganymede with the Very Large Array. The observed position requires corrections of $-0''.18 \pm 0''.04$ in right ascension and $-0''.06 \pm 0''.04$ in declination to the position for Jupiter calculated for 1983 April 29 from DE200.

An improvement to the ephemeris of Jupiter relative to the inner planets has been independently obtained from spacecraft encounter Doppler data, and the corrections of $-0''.22$ in right ascension and $-0''.06$ in declination, with uncertainties of $\sim 0''.05$, agree well with those derived from the direct radio observations of Jupiter and the inner planets with respect to extragalactic radio sources.

References

1. Fricke, W. and Kopff, A., "Fourth Fundamental Catalog (FK4)," 1984, Veroff. Astron. Rechen Inst., Heidelberg, No. 10.

2. Border, J. S., Donivan, F. F., Finley, S. G., Hildebrand, C. E., Moultrie, B., and Skjerve, L. J., "Determining Spacecraft Angular Position with Delta VLBI: The Voyager Demonstration," 1982 AIAA/AAS Astrodynamics Conference paper AIAA-82-1471.

3. de Vegt, C., "Interrelation of Present Optical and Radio Reference Frames," 1984, IAU Symposium No. 110: VLBI and Compact Radio Sources, R. Fanti *et al.* (eds.), Reidel, 357-360.

4. Standish, E. M., "Orientation of the JPL Ephemerides, DE200/LE200, to the Dynamical Equinox of J2000," 1982, *A.J. 114*, 297-302.

5. Standish, E. M., "On the Reference Frame of the Planetary Ephemerides," 1984, Proceedings IAU Symposium No. 109: Astrometric Techniques, Gainesville, FL (in press).

6. Fanselow, J. L., Sovers, O. J., Thomas, J. B., Purcell, G. H., Cohen, E. J., Rogstad, D. H., Skjerve, L. J., and Spitzmesser, D. J., "Radio Interferometric Determination of Source Positions Utilizing Deep Space Network Antennas – 1971 to 1980," 1984, *A.J. 89*, 987-998.

7. Ma, C., *et al.*, "J2000 Radio Source Positions from VLBI," (in preparation).

8. Niell, A. E., Fanselow, J. L., Sovers, O. J., Thomas, J. B., Liewer, K. M., Treuhaft, R. N., and Wallace, K. S., "Accurate Positions of 120 Radio Sources with Declinations above -45 degrees," 1984, Proceedings IAU Symposium No. 109, Astrometric Techniques, Gainsville, FL (in press).

9. Hazard, C., Sutton, J., Argue, A. N., Kenworthy, C. M., Morrison, L. V., and Murray, C. A., "Accurate Radio and Optical Positions of 3C273B," 1971, *Nature, 233*, 89-91.

10. Napier, P. J., Thompson, A. R., Ekers, R. D., "The Very Large Array: Design and Performance of a Modern Synthesis Telescope," 1983, *Proc. IEEE, 71*, 1295-1320.

11. Newhall, X X, Preston, R. A., and Esposito, P. B., "Relating the JPL VLBI Reference Frame and the Planetary Ephemerides," 1984, Proceedings IAU Symposium No. 109: Astrometric Techniques, Gainsville, FL (in press).

12. Lieske, J. H., "Improved Ephemerides of the Galilean Satellites," 1980, *A.J., 82*, 340-348.

13. Johnston, K. J., Seidelmann, P. K., and Wade, C. M., "Observations of 1 Ceres and 2 Pallas at Centimeter Wavelengths," 1982, *A.J., 87*, 1593-1599.

14. Campbell, J. K., and Synnott, S. P., "Gravity Field of the Jovian System From Pioneer and Voyager Tracking Data," 1985, *A.J., 90*, 364-372.

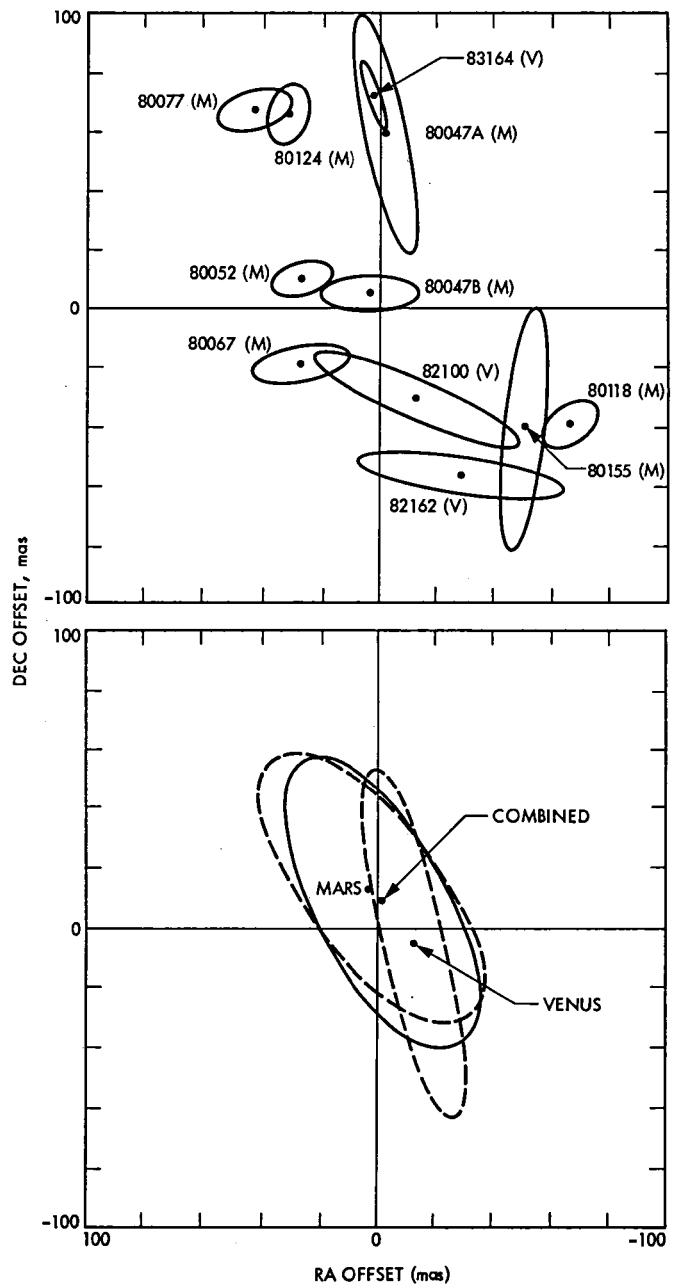

Fig. 1. Δ VLBI measurement of inner planet positions with respect to radio reference frame: (a) Offsets of radio source positions from those expected assuming planet positions from ephemeris DE200 and radio source positions from catalogue JPL 1983-4. (V): Pioneer Venus Orbiter. (M): Viking Mars Orbiter; (b) RMS scatter ellipses for each planet and for the combined data (solid ellipse).

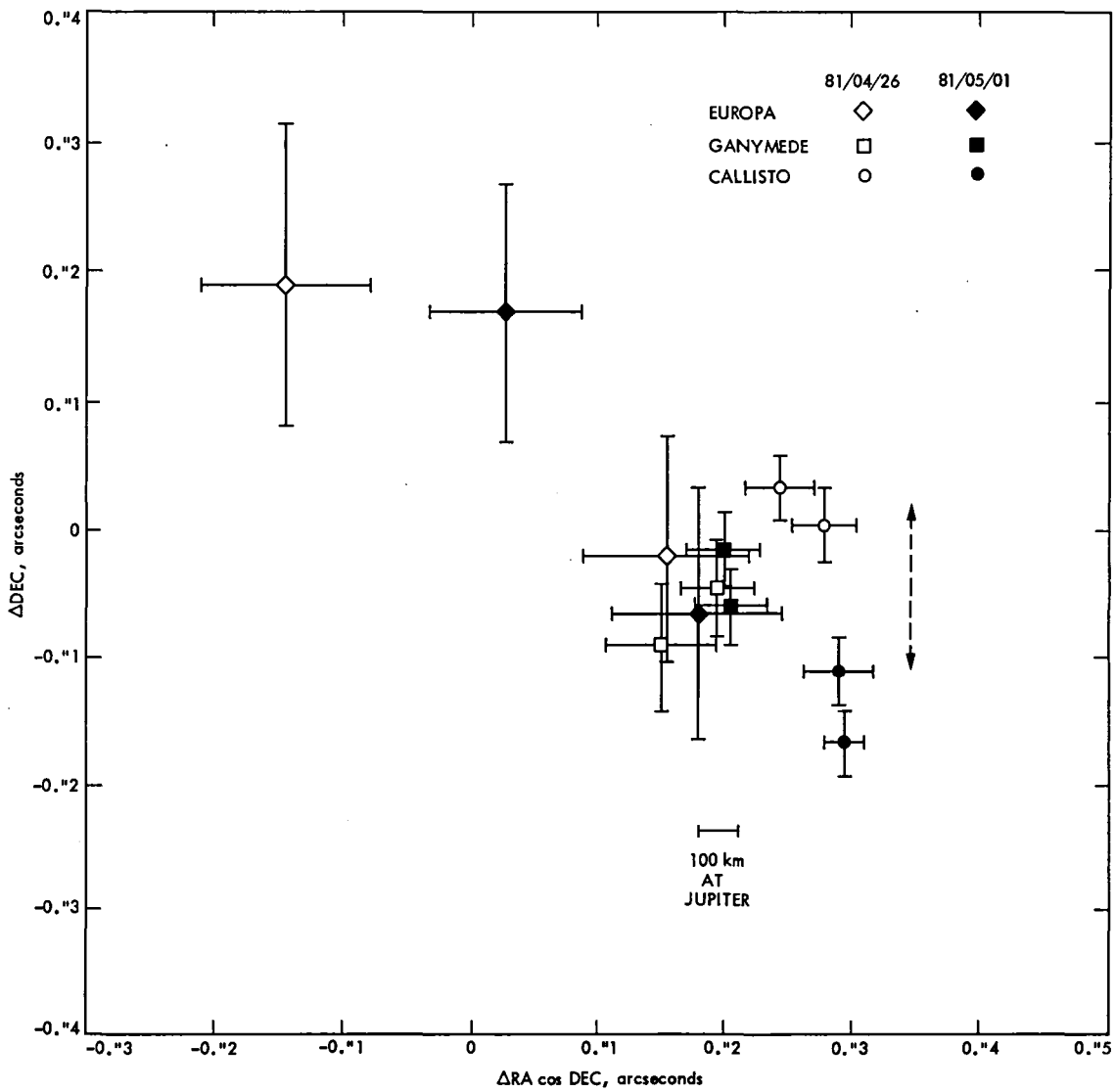

Fig. 2. Positions of the Galilean satellites in the Radio Reference Frame as determined by measurements with the VLA. The same symbol appears twice for each object on each day, since the two polarizations were treated separately. The dashed arrow indicates the declination uncertainty of Callisto relative to Ganymede.

Photon Detection With Cooled Avalanche Photodiodes: Theory and Preliminary Experimental Results

D. L. Robinson and D. A. Hays
Communications Systems Research Section

Avalanche photodiodes (APDs) can be operated in a "geiger-tube" mode so that they can respond to single electron events and thus be used as photon counting detectors. Operational characteristics and theory of APDs while used in this mode are analyzed and assessed. Preliminary experimental investigation of several commercially available APDs has commenced, and initial results for dark count statistics are presented.

I. Introduction

There are basically two facets to an optical communications system for deep space, namely transmission and reception. The transmitter consists of a laser beam transmitted through a telescope, expanding the beam diameter and reducing its divergence, while the receiver consists of a receiver telescope collecting the light and focusing it onto a detector. In order to maximize the efficiency of the overall system, one must optimize both the laser and the detector. This article deals with the latter.

There are basically two types of detection schemes, direct and heterodyne. The former, as the name implies, directly receives the transmitted optical signal. In contrast, heterodyne detection combines the received signal with a local oscillator field so that the signal may be detected even under high-background-noise conditions. Schematic representations of direct and heterodyne detection receivers are illustrated in Figure 1(a) and 1(b), respectively. In applications with little or no background noise, such as communications with spacecraft in outer planet missions, direct detection systems can outperform their heterodyne counterparts (Ref. 11). The detection scheme of the cooled APD described herein would be used under such low background conditions for single photon direct detection.

At planetary distances, the transmitted power is highly attenuated mainly due to beam divergence. Optimization of the system under such conditions necessitates the detection of light pulses containing only a few photons. In order to achieve this high degree of receiver sensitivity, we need to use photodetectors with internal gain that is sufficiently large to overcome the thermal noise of the receiver amplifier so that single photon counting is possible. In addition, the photodetector should have a very low intrinsic dark current level. Currently, photomultiplier tubes (PMT) are the only detectors capable of detecting such minimal energy levels. Internal gains in excess of 10^6 are readily available with PMTs. With a modest amount of cooling (to approximately 230 K [-40°C]) the dark current levels can be sufficiently reduced to less than 100 photoelectrons/sec. There are, however, two main drawbacks to PMTs. The first is their low quantum efficiency. The best PMTs available have only 20% quantum efficiency at $\lambda = 0.8\ \mu m$ (i.e., at that wavelength, only one photoelectron is produced on the average for each 5 photons impinging on the PMT faceplate). Secondly, since PMTs are packaged in

glass vacuum tubes and operated at higher voltages (in the kilovolt region), they are less attractive for applications requiring high reliability (i.e., space based optical communications) than solid-state photodetectors.

There is, however, a solid-state photodetector alternative to the PMT which has recently gained some attention. This solid-state alternative is the avalanche photodiode (APD) used in a geiger counter mode. Since the APD is a semiconductor device, it is potentially more reliable than a PMT. Furthermore, APDs have quantum efficiencies greater than 80% in the visible and near-infrared regions of the electromagnetic spectrum. In their common mode of operation they are biased below their avalanche breakdown voltage. However, the gain that they can thus provide (approximately 100) is not sufficient for single photon counting. Biasing the APDs at voltages beyond the avalanche breakdown where higher gains are obtainable is not possible at room temperature because of their relatively large values of dark current and excess noise (Refs. 10, 12). However, by cooling the APD to temperatures where the dark current becomes negligible it can be operated in a geiger counter mode. When the APD is used in this mode, it is biased above the avalanche breakdown, and a sustained avalanche is produced from almost every electron-hole pair generated. The effective internal gain of this process is very high (10^7 to 10^8), making single photon counting possible. This, together with the high quantum efficiency, may make cooled APDs an attractive alternative to PMTs in most applications requiring detection of low-level optical signals. There are some problems associated with APDs operating in this mode, however, and overcoming these problems is a prerequisite towards fully realizing their advantages.

Even though there has been some investigation by several groups into some of the problems encountered when the APD is used in this mode of operation (Refs. 1-8), specific characteristics unique to the application of deep space optical communication need yet to be assessed and analyzed. Some of these characteristics will be addressed in the following text.

The following section discusses the theory and operational characteristics of the APD while operated in this geiger mode. Then, in Section III the experimental set-up along with results for several commercial APDs will be discussed. Finally, Section IV summarizes and concludes the article.

II. Theory and Operational Characteristics

When an avalanche photodiode (APD) is cooled to reduce the number of thermally generated carriers, it can be biased beyond its avalanche breakdown voltage (but below its dielectric [zener] breakdown voltage) for an extended period of time. Under such conditions, the APD will perform in a geiger mode as a single photon detector. While in this mode, an electron-hole pair (either photo or thermally generated) has a high probability of initiating a breakdown. When a breakdown occurs, the voltage across the diode drops to the avalanche breakdown voltage, V_B. This voltage drop is translated into an output pulse which is large enough for detection without any further amplification. In order to clear carriers from the high field region of the diode and quench this sustained avalanche, the bias voltage across the diode must be reduced below V_B. The diode can be subsequently rebiased above V_B, thereby permitting a new carrier to initiate another avalanche. The varying bias conditions (i.e., the drop in the bias voltage below the breakdown voltage during the avalanche and subsequent re-bias above the breakdown voltage) can be implemented by either a passive or an active quenching circuit. The passive quenching circuit is simply a resistor ($\gtrsim 100\ K\Omega$) in series with the diode as shown in Fig. 2. The active quenching circuit (Ref. 7) is more complicated and involves various feedback loops as schematically shown in Fig. 3. Figure 4 illustrates the actual current-voltage curve of a cooled APD utilizing (a) a passive quenching circuit, and (b) an active quenching circuit (Ref. 7).

Specifically, referring to Figs. 4(a) and 4(b), we shall review various states of the APD while passively and actively quenched. During passive quenching, (Fig. 4[a]) the APD is reverse biased beyond the breakdown and waiting for a carrier to initiate an avalanche (1). Once a single carrier has initiated an avalanche, current flows in the APD (2). This avalanche current discharges the intrinsic capacitance of the APD resulting in a voltage drop (3) across the diode creating a detectable pulse that needs no amplification. The avalanche is then quenched (4) and recharged (1) through the load resistor above the breakdown voltage. As with the passive quenching, the active quenching (Fig. 4[b]) is biased beyond the breakdown voltage (1) waiting for a single carrier to initiate an avalanche. Once a single carrier initiates a breakdown (2) the circuit forces a fast transition by shifting the load line below the breakdown voltage (3). The circuit then forces a fast transition of recovery by shifting the load line above the breakdown voltage.

The main drawback of the passive quenching is its relatively long recovery time. Subsequent pulses may be detected during this recovery time. However, due to the transient conditions, detection efficiency is reduced, resulting in lower detection probability. Furthermore, the avalanche gain is lower since the bias is not fully reset, resulting in a lower pulse amplitude. This phenomenon was observed experimentally and will be described in the next section. By using the active

quenching circuit, this phenomenon can virtually be eliminated.

The sustained avalanche initiation probability is defined as the probability that a carrier initiates a current pulse that is limited only by the external circuit and not by the internal gain of the APD (which tends to be extremely large in this mode of operation). This APD avalanche initiation probability has been analyzed by McIntyre (Ref. 8) and Oldham, et al. (Ref. 3), above the breakdown voltage and shall be discussed next.

For an electron (hole) generated at position x within the active region of an APD, the probability, $P_e(x)$ ($P_h(x)$), that an avalanche will be initiated can be calculated from the following formulas (Ref. 8):

$$-\log\,[1 - P_h(0)] = \frac{k}{1-k}\log\,[P_h(0)f(w) + 1 - P_h(0)] \tag{1}$$

$$1 - P_h(0) = [1 - P_e(w)]^k \tag{2}$$

where the boundaries of the avalanche region are $x = 0$ and $x = w$, as illustrated in Fig. 5. The ionization coefficient ratio has been defined as $k = \alpha_h/\alpha_e$ where $\alpha_h(x)$ and $\alpha_e(x)$ are the hole and electron ionization rates respectively. The parameter $f(w)$ is defined as follows:

$$f(w) = \exp\,[(1-k)\,\delta]$$

$$\delta = \int_0^w \alpha_e(x)\,dx$$

$P_h(0)$ and $P_e(w)$ are plotted in Fig. 6 for various values of k (Ref. 8). The ideal operational conditions of the APD require high probability of detection while minimizing the over bias. (Minimal over bias is preferred to minimize dark counts.) By inspection of Fig. 6, these conditions are optimized for values of k close to unity. It is to be noted that higher asymmetric values of k are preferred for the APD when operating in its normal mode (Ref. 10). Since commercially available APDs are not optimized for the requirements of the APD while operating in the cooled geiger mode, we can expect to achieve better performance with the APDs that have been optimized for cooled detection.

The main problem, however, with the APD used in this geiger mode is the occurrence of false avalanches. When an avalanche is initiated, it is possible for some of the avalanching charge carriers to be trapped. This may be caused by defects or impurities in the crystal lattice. At a later time after the bias is reset, these trapped carriers may be released causing a secondary or false avalanche. These secondary avalanche processes may occur from several nanoseconds after the initial pulse to as long as minutes after the initial pulse (Ref. 6). The uncertainty of the time of these false events complicates the detection probability statistics. A theoretical model for the count statistics of a cooled APD has been created (Ref. 9). This model considers the APD output as a Poisson distributed primary avalanche process, plus a conditionally Poisson distributed process due to trapped-carrier induced secondary events. This model is the theoretical basis against which the experimental measurements will be compared.

III. Experimental Verification

A. Experimental Set-up

The experimental set-up is depicted in Fig. 7. The APD is cooled with a Joule Thompson Micro Miniature Refrigerator (MMR) System I. The cooler consists of an evacuated chamber with a cold finger on which the diode is mounted. Optical access to the diode is provided by a glass port. Neutral density filters can be used to control the amount of light impinging on the APD. A beam splitter diverts part of the beam to a PMT to calibrate incident detected photon intensities. An HP 5370A counter and HP 85 desktop computer are utilized for data acquisition and analysis. A storage oscilloscope (Tektronix 7834) is utilized to view individual waveforms and time intervals between successive pulses. The entire optical portion of the experiment is enclosed in a light-tight, dark enclosure.

B. Experimental Preliminary Results and Discussions

Experimental results in this report include only dark count measurements with the passive quenching circuit. The second phase of our experiment will analyze signal detection with the passive quenching circuit. Finally, the active quenching circuit will be incorporated into the experimental set-up.

Dark count noise characteristics of Si APDs have been evaluated from three manufacturers (Mitsubishi Model #PD1002, NEC Model #NDL1202, and RCA Model #C30817). Initial measurements were made without incident light in order to characterize the dark counts and gain some insight into some of the possible physical processes occurring in the device.

First, the dark count characteristic of each of the diodes as a function of temperature was characterized in order to determine the optimum operating temperature range. All experimental testing reported in the literature (Refs. 1-7) has been performed on cooled Si APDs at 77 K only. In our experimental apparatus, the temperature of the refrigerator is controllable from approximately 79 K to 390 K. The dark count

frequency was measured over 60-sec time intervals and at various temperatures from 79 K to room temperature. Results are graphed in Figs. 8(a) and 8(b) for the diodes tested. As the temperature was increased, the reverse breakdown voltage also increased as expected (Ref. 10) (see Figs. 8[a] and 8[b]).

Aside from the increased breakdown voltage at higher temperatures, the number of counts at a given voltage increment above breakdown remains fairly constant from 79 K to 180 K for the diodes tested. Stated differently, the performance of the diode does not degrade significantly over this temperature range. Since multistage, thermoelectric coolers operated in evacuated environments are capable of operation down to approximately 140 K, they could be useful in cooling the APDs in space applications. At temperatures greater than 180 K, the number of dark counts generated greatly increased making the APD unusable as an efficient communications detector in this mode of operation.

Next, we characterized dark counts of each diode as a function of reverse bias voltage (above the breakdown voltage of the cooled APD). The goal was to determine the relative performance of the APDs from different manufacturers. We saw in the previous section that as the reverse bias is increased, the probability of breakdown is increased, resulting in higher dark counts. However, since the amplitude of the output pulse from the cooled APD is also a function of this reverse bias, there are some definite trade-offs between the output signal amplitude and increased dark current due to higher bias levels when the APD is used to detect actual signal. Of the two APDs tested, Mitsubishi Model No. PD1002 had the best performance with the least number of counts for the greatest range of voltage above breakdown.

During the recovery time of the circuit after an avalanche has occurred, subsequent avalanches are still possible but with reduced probability since the bias is not fully recharged. Figure 9 illustrates this phenomenon of secondary avalanches prior to full recovery of the reverse bias voltage. At point "A" of Fig. 9, the APD is biased ~0.5 volts above breakdown. Then, at point "B," a carrier initiates an avalanche causing a voltage drop to point "C." For approximately 400 μs after this voltage drop, avalanches continue to occur prior to full recovery of the circuit at point "D." Upon full recovery, another carrier initiates an avalanche at point "E" resulting in a substantial voltage drop. This time, however, the circuit fully recharges after the initial breakdown at point "E." As the circuit is recharged to its full value the probability of breakdown increases accordingly.

Finally, the statistics of the interarrival times between pulses were examined to gain some insight into the noise mechanism statistics and to try to determine if trapping or secondary pulses are a significant component of the noise. The time interval between the pulses was measured with the HP 5320 counter. Measurements were taken at various thresholds and reverse bias voltages. Histograms of the time interval data for the two diodes tested are graphed in Figs. 10(a) and 10(b).

The Chi-square goodness of fit test was used to determine whether the observed dark counts were Poisson distributed (i.e., exponential pulse interarrival times). In spite of the various parameters that we tried to fit the experimental data to, the results indicate that unlike the PMT (Ref. 13), and unlike the results reported on cooled APDs elsewhere (Ref. 6), the dark counts in this case do not seem to be Poisson distributed. The data from the two diodes seemed to have too many short interarrival counts and too long a tail of the distribution curve to be Poisson. This may be due to the secondary emission "detrapping" effects of the APD or may be a result of the long recovery time from the passive quenching circuit. The latter effect would be eliminated using the active quenching circuit. Both effects are currently under investigation.

IV. Conclusion

Photon counting with cooled APDs operating in the geiger counter mode may be an attractive alternative to PMTs. An initial investigation of the theory and operational characteristics of the APDs used in this mode for single photon detection has been completed. Experimental investigation of several commercial APDs has commenced, and initial results for dark count statistics have been presented. Further investigations of "trapping" effects have yet to be performed to determine their impact on detection probabilities and hence the value of using the cooled APD as a detector for optical communications. The next phase of the experimental program will include a performance evaluation of the noise signal detection probability which will be compared to the theory presented herein.

Acknowledgment

The authors wish to thank Joe Katz for many helpful discussions and for his critical review of this paper.

References

1. Webb, P. O. and McIntyre, R. J., "Single Photon Detection with Avalanche Photodiodes," *Bull. Amer. Phys. Soc.*, Ser II, *15*, p. 813 (1970).
2. Haecker, W., Groezinger, O., and Pilkun, M. H., "Infrared Photon Counting by Ge Avalanche Diodes," *Appl. Phys. Lett. 19*, pp. 113-115 (1971).
3. Oldham, W. G., Samuelson, R. R., and Antognetti, P., "Triggering Phenomena in Avalanche Diodes," *IEEE Trans. Electron Dev. ED-19*, pp. 1056-1060.
4. Ekstrom, P. A., "Triggered-Avalanche Detection of Optical Photons," *J. Appl. Phys. 52*, pp. 6974-6979 (1981).
5. Cova, S., Longoni, A., and Ripamonti, G., "Active-Quenching and Gating Circuits for Single-Photon Avalanche Diodes (SPADs)," *IEEE Trans. Nucl. Sci., NS-29*, pp. 99-601 (1982).
6. Ingerson, T. E., Kearny, R. J., and Coutler, R. L., "Photon Counting with Photodiodes," *Appl. Opt., 22*, pp. 2013-2018 (1983).
7. Cova, Sergio, et al., "A Semiconductor Detector for Measuring Ultraweak Fluorescence Decays with 70 ps FWHM Resolution," *IEEE Journal of Quantum Electronics, QE-19*, No. 4, April 1983.
8. McIntyre, Robert, "On the Avalanche Initiation Probability of Avalanche Diodes Above the Breakdown Voltage," *IEEE Transactions on Electron Devices, ED-20*, No. 7, July 1973.
9. Tan, H. H., "Avalanche Photodiode Statistics in Triggered-Avalanche Detection Mode," *TDA Progress Report 42-79*, Jet Propulsion Laboratory, Pasadena, CA, July-September 1984, pp. 69-80.
10. Sze, S. M., *Physics of Semiconductor Devices*, (John Wiley and Sons, Inc., New York, 1981), Chapter 13.
11. Lesh, J. R., "Optical Communications Research to Demonstrate 2.5 bits/detected photon," *IEEE Communications Magazine*, Nov. 1982, pp. 35-37.
12. Katz, J., "Detectors for Optical Communications: A Review," *TDA Progress Report 42-75*, Jet Propulsion Laboratory, Pasadena, CA, July-September 1983, pp. 21-38.
13. Lesh, J. R., et al., "2.5/Detected Photon Demonstration Program: Description, Analysis, and Phase I Results," *TDA Progress Report 42-66*, Jet Propulsion Laboratory, Pasadena, CA, September-October 1981, pp. 115-132.

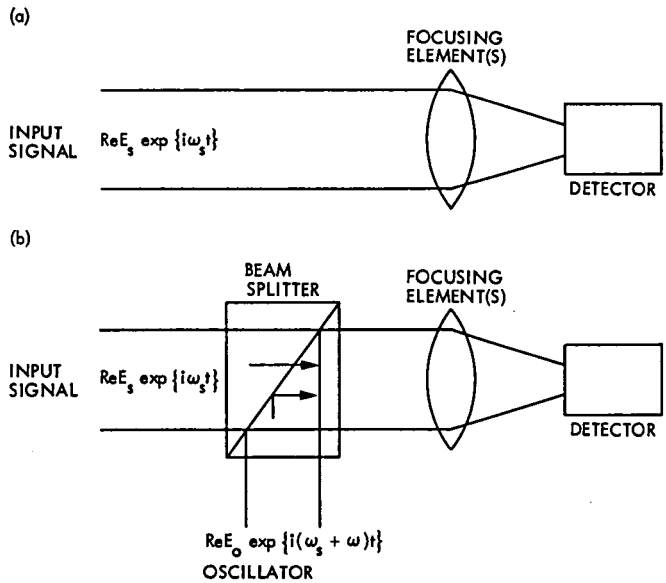

Fig. 1. Schematic representation: (a) direct detection scheme used in optical communication under low background conditions; (b) heterodyne detection scheme used in optical communication under high background conditions

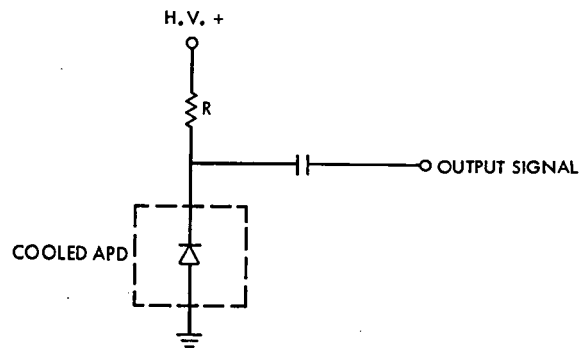

Fig. 2. Schematic of passive-quenching circuit, $R \gtrsim 100\ K\ \Omega$

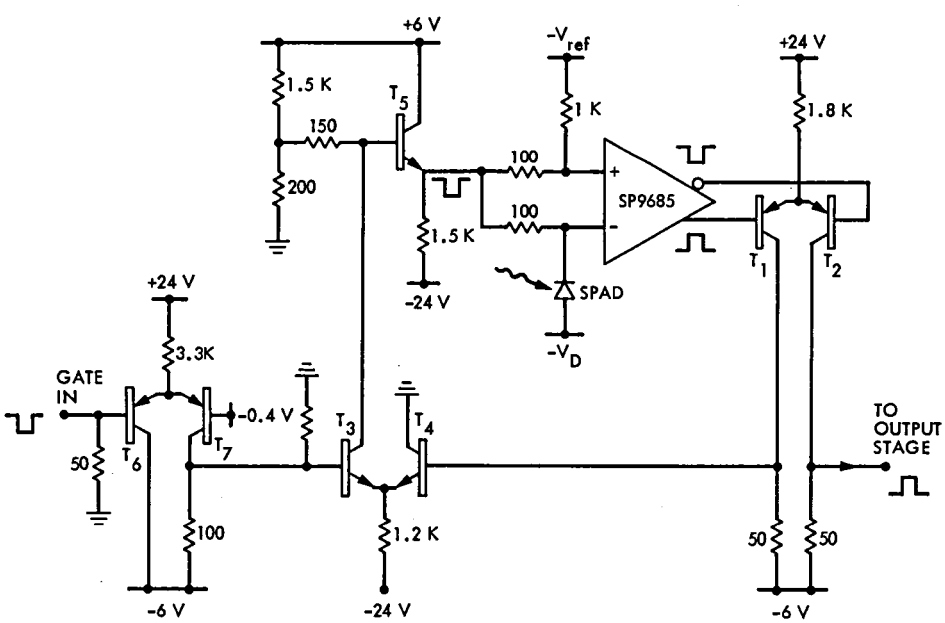

Fig. 3. Diagram of active-quencing circuit (adapted from Ref. 7)

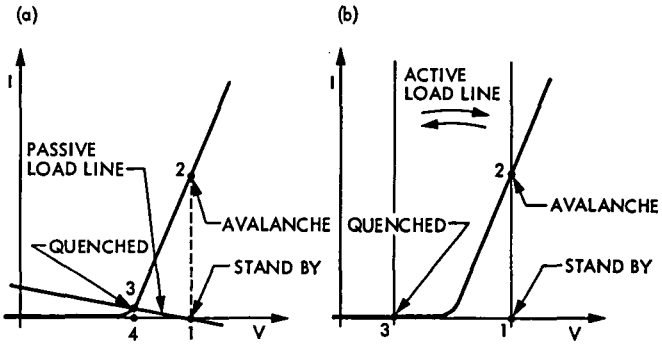

Fig. 4. Cooled APD current-voltage curve during (a) passive quenching and (b) active-quenching. See text for explanation of specific states (adapted from Ref. 4).

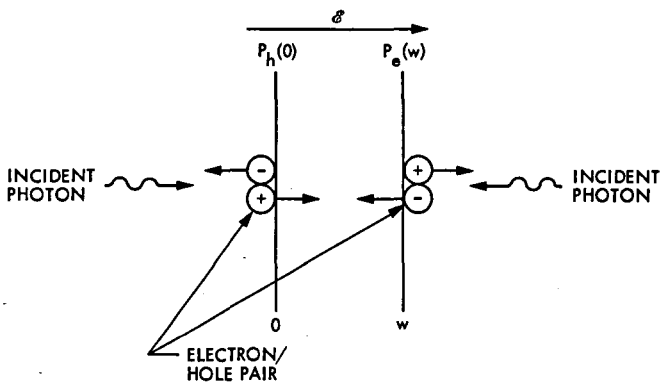

Fig. 5. Schematic representation of photon interaction with an electron/hole pair for an active region of length w. The quantity ξ is the applied electric field.

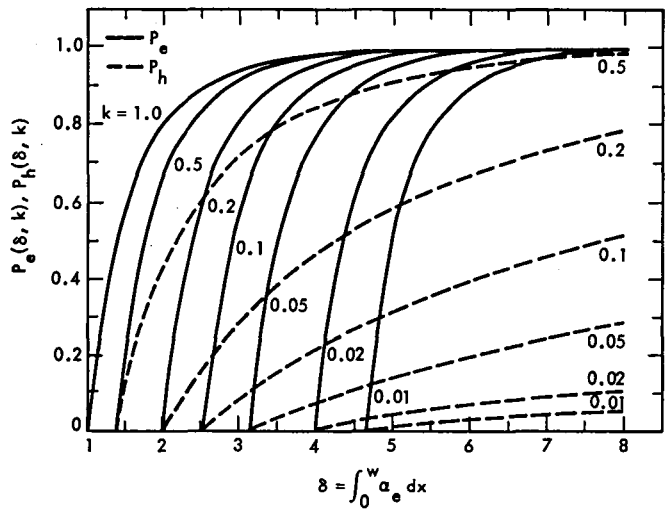

Fig. 6. Avalanche initiation probability by an injected electron (P_e) or hole (P_h) as a function of the electron ionization coefficient (adapted from Ref. 8)

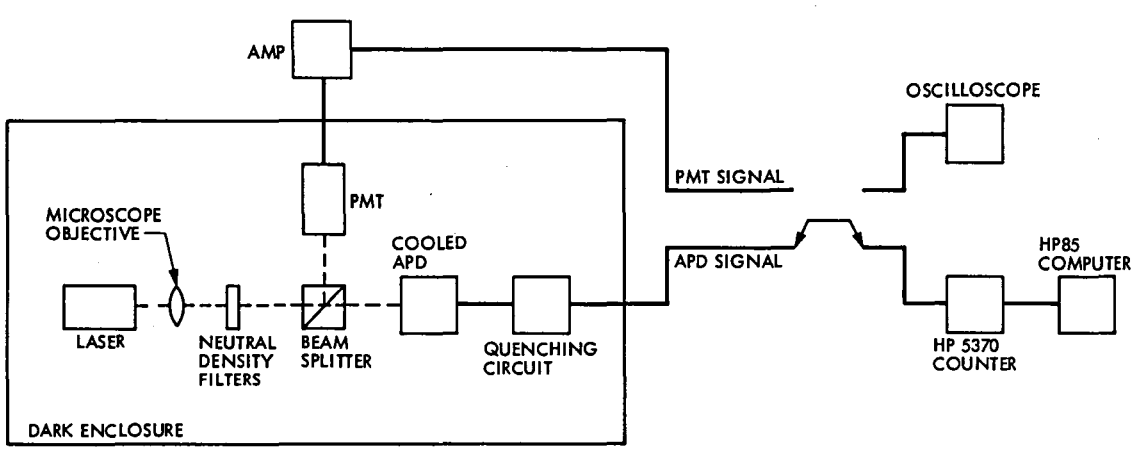

Fig. 7. The cooled APD experimental set-up. A PMT is used to calibrate light intensity from the GaAlAs laser.

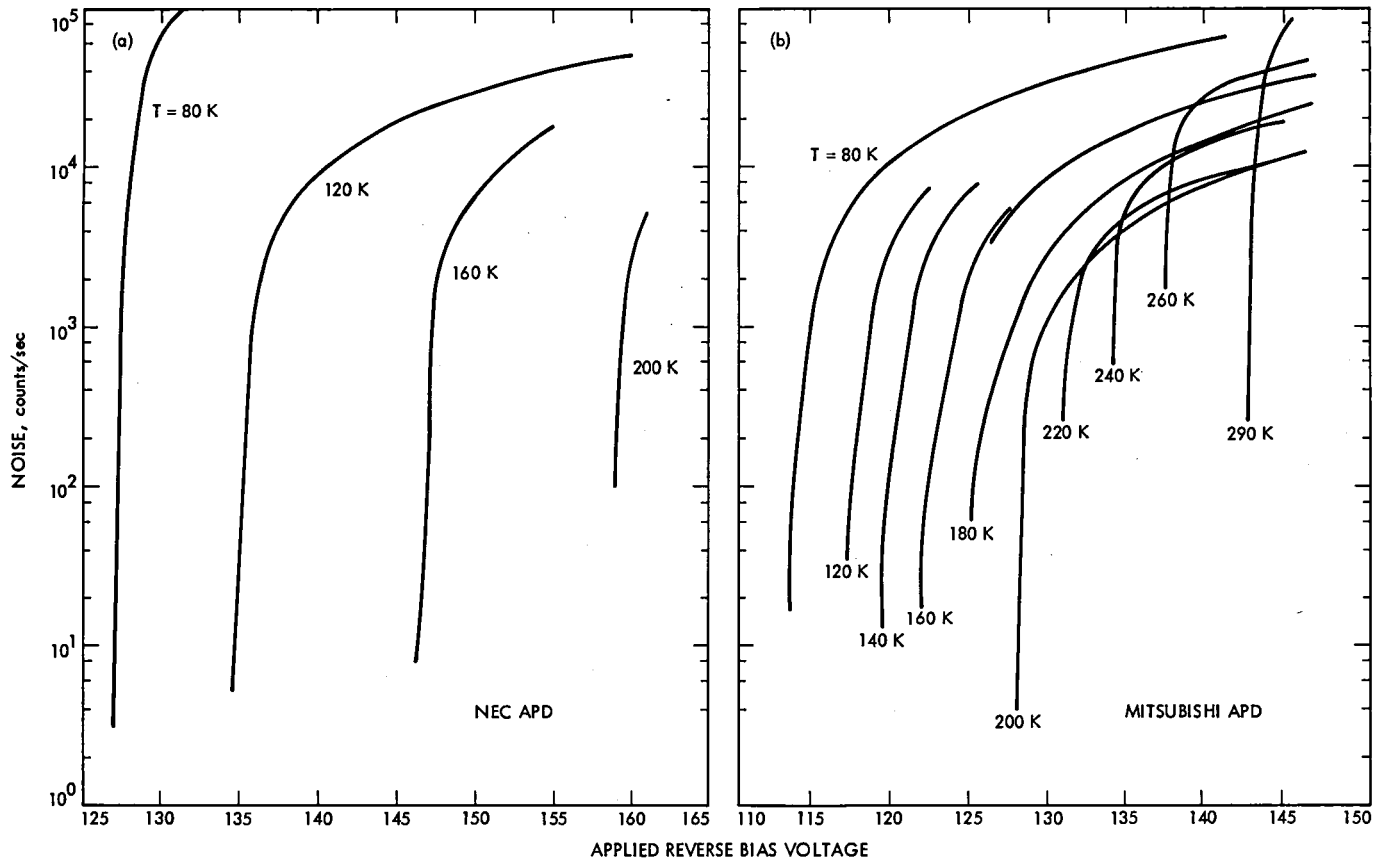

Fig. 8. Dark counts per second of the cooled (a) NEC (Model NDL 1202) APD and (b) Mitsubishi (Model No. PD1002) APD are graphed as a function of temperature and reverse bias voltage

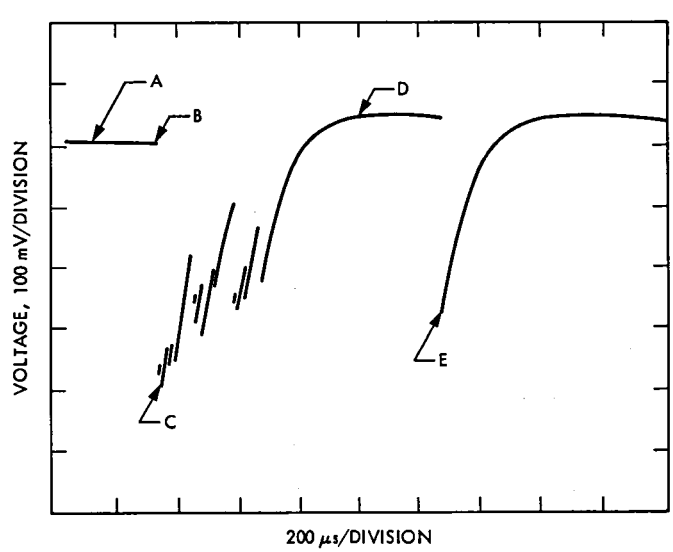

Fig. 9. Oscilloscope trace of output pulses from cooled NEC Model No. NDL1202 APD with passive quenching circuit. APD has been bias ~ 0.5 V above breakdown. Note secondary breakdown of diode before circuit has fully recharged. Temperature = 200 K, applied bias voltage = 160 V.

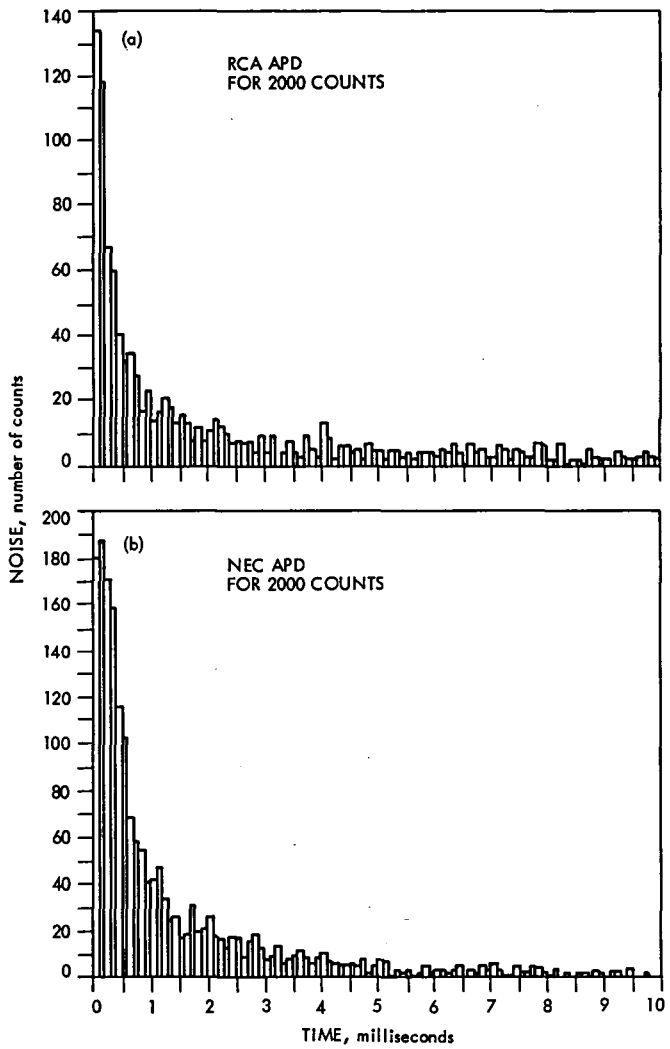

Fig. 10. Histogram of time interval arrival times for: (a) RCA Model No. C30817. Temperature = 80.7 K, applied bias voltage = 117 V; (b) NEC Model No. NDL1202. Temperature = 88.6 K, applied bias voltage = 129.4 V.

Techniques for Computing the DFT Using the Residue Fermat Number Systems and VLSI

T. K. Truong
Communications Systems Research Section

J. J. Chang
Spacecraft Data Systems Section

I. S. Hsu, D. Y. Pei, and I. S. Reed
University of Southern California

In this paper, the integer complex multiplier and adder over the direct sum of two copies of a finite field is specialized to the direct sum of the rings of integers modulo Fermat numbers. Such multiplications and additions can be used in the implementation of a discrete Fourier transform (DFT) of a sequence of complex numbers. The advantage of the present approach is that the number of multiplications needed for the DFT can be reduced substantially over the previous approach. The architectural designs using this approach are regular, simple, expandable and, therefore, naturally suitable for VLSI implementation.

I. Introduction

Recently, the authors (Refs. 1, 2) developed a new method for computing a DFT using the direct sum of two copies of residue number systems. A principal advantage of this algorithm is that a complex integer multiplication can be computed by using similar integer multiplications in two parallel independent residue channels. Using the ideas of Cozzens and Finkelstein (Refs. 1, 2), it is shown in this article that a complex integer DFT can be computed by multiplication, modulo a Fermat number in two parallel independent residue channels. Such a multiplication over the direct sum of two copies of the rings of integers modulo Fermat numbers can be used in the implementation of a systolic array of the DFT as developed by Kung (Ref. 3).

II. Arithmetic Over the Direct Sum of Two Copies of Finite Rings Modulo A Fermat Number

Let $F_n = 2^{2n} + 1$ be a Fermat number and let Z_{F_n} be the ring of residues of integers modulo F_n. Further, let (-1) denote the negative of integer one and let i denote the solution of equation $x^2 = -1$. Finally define the set $Z_{F_n}[i] = \{a + ib \mid a, b \in Z_{F_n}\}$ of F_n^2 elements in such a manner that addition is given by $(a + ib) + (c + id) = (a + b)_{F_n} + i(b + d)_{F_n}$ and multiplication is given by $(a + ib)(c + id) \equiv (ac - bd)_{F_n} + i(bc + ad)_{F_n}$ where $(x)_{F_n}$ denotes the residue of a modulo F_n. The set $Z_{F_n}[i]$ is a commutative ring. (To show that $Z_{F_n}[i]$ is a commutative ring, it is only necessary to show that any arbitrary three elements of $Z_{F_n}[i]$ satisfies the postulates of ring [Ref. 4, p. 1].)

Lemma 1: Let $F_n = 2^{2^n} + 1$ be a Fermat number; where $n \geqslant 1$. The solutions of $x^2 + 1 \equiv 0 \bmod F_n$ are $s = \pm 2^{2^{n-1}}$

Proof: Since $F_n = 2^{2^n} + 1$, then $2^{2^n} \equiv -1 \bmod 2^{2^n} + 1$. Thus,

$$(\pm 2^{2^{n-1}})^2 \equiv -1 \bmod 2^{2^n} + 1$$

Hence, $s = \pm 2^{2^{n-1}}$ are the solutions of $x^2 + 1 \equiv 0 \bmod F_n$.

Next we map an element $a + ib$ in $Z_{F_n}[i]$ into $(a + sb)_{F_n}$. It is easy to show that such a mapping is a homomorphic mapping. It was shown (Ref. 5) that if s is one of solutions of $x^2 + 1 \equiv 0$ modulo F_n, then the set $\{a + sb \mid a, b \in Z_{F_n}\}$ is a field with F_n elements isomorphic to $GF(F_n)$, where F_n is considered as a prime number. If one uses both solutions of $x^2 + 1 \equiv 0 \bmod F_n$, i.e., $\pm s$ for mapping an element into $(\alpha, \overline{\alpha})$, where $\alpha = (a + sb)_{F_n}$ and $\overline{\alpha} = (a - sb)_{F_n}$, then it is shown in the next theorem that such a mapping is an isomorphic mapping and the set $\{\alpha,\overline{\alpha} \mid \alpha,\overline{\alpha} \in Z_{F_n}\}$ is the direct sum of 2 copies of Z_{F_n} of F_n^2 elements.

Hence, by an extension of the ideas given in Ref. 5, the following important theorem, a special case of Lemma 2.3 of Ref. 1, can be proved.

Theorem 1: Let $Z_{F_n}[i] = \{a + ib \mid a,b \in Z_{F_n}\}$ be the ring with respect to addition and multiplication modulo F_n. Then the direct sum of 2 copies of Z_{F_n}, i.e.,

$$S_{F_n} = Z_{F_n} + Z_{F_n} = \{\alpha,\overline{\alpha} \mid \alpha,\overline{\alpha} \in Z_{F_n}\}$$

where $(\alpha,\overline{\alpha}) + (\beta,\overline{\beta}) = (\alpha + \beta, \overline{\alpha} + \overline{\beta})$ and $(\alpha,\overline{\alpha}) \cdot (\beta,\overline{\beta}) = (\alpha\beta,\overline{\alpha\beta})$ is a ring of F_n^2 elements which is isomorphic to the ring $Z_{F_n}[i]$.

Proof: By Lemma 1, integers $s = \pm 2^{2^{n-1}}$ are the solutions of $x^2 + 1 \equiv 0 \bmod F_n$ for $n \geqslant 1$. If $a + ib \in Z_{F_n}[i]$, then let ϕ be the mapping

$$\phi: a + ib \rightarrow ((a + sb)_{F_n}, (a - sb)_{F_n}) = (\alpha,\overline{\alpha}) \tag{1}$$

where

$$\alpha = (a + sb)_{F_n}$$

$$\overline{\alpha} = (a - sb)_{F_n}$$

$$s = \pm 2^{2^{n-1}}$$

To show that ϕ is an isomorphism, one must show that ϕ is both one-to-one and onto and that ϕ preserves addition and multiplication. To show that ϕ is onto, one needs to demonstrate that given an arbitrary element, $(\alpha,\overline{\alpha}) \in S_{F_n}$, there exists an element $a + ib \in Z_{F_n}[i]$ such that $\phi(a + ib) = (\alpha,\overline{\alpha})$ is an element of S_{F_n}. Equation (1) implies that

$$a + 2^{2^{n-1}} b \equiv \alpha \bmod F_n \tag{2a}$$

$$a - 2^{2^{n-1}} b \equiv \overline{\alpha} \bmod F_n \tag{2b}$$

Summing Eqs. (2a) and (2b) yields

$$2a \equiv \alpha + \overline{\alpha} \bmod F_n$$

Since $(2, F_n) = 1$, one can solve for a, i.e.,

$$a \equiv 2^{-1} (\alpha + \overline{\alpha}) \equiv -2^{2^{n-1}} (\alpha + \overline{\alpha}) \bmod F_n$$

Subtracting Eq. (2b) from Eq. (2a) yields

$$2^{2^{n-1}+1} b \equiv \alpha - \overline{\alpha} \bmod F_n$$

Since $(2^{2^{n-1}+1}, F_n) = 1$, one can solve for b, i.e.,

$$b \equiv 2^{-2^{n-1}-1} (\alpha - \overline{\alpha}) \equiv -2^{2^{n-1}-1} (\alpha - \overline{\alpha}) \bmod F_n$$

Hence, the solutions of the system of congruences given in Eqs. (2a) and (2b) are

$$a \equiv -2^{2^{n}-1} (\alpha + \overline{\alpha}) \bmod F_n \tag{3a}$$

$$b \equiv -2^{2^{n-1}-1} (\alpha - \overline{\alpha}) \bmod F_n \tag{3b}$$

Thus by Eqs. (3a) and (3b) it is seen that $(\alpha,\overline{\alpha}) \in Z_{F_n}$ is the image of $a + ib \in Z_{F_n}[i]$ under the mapping ϕ. This proves that ϕ is an onto mapping.

In order to show that ϕ is one-to-one, assume $\phi(a + ib) = \phi(c + id)$. It follows from Eq. (1) that $((a + sb)_{F_n}, (a - sb)_{F_n}, = ((c + sd)_{F_n}, (c - sd)_{F_n})$. This implies that

$$a + sb \equiv c + sd \bmod F_n \tag{4a}$$

$$a - sb \equiv c - sd \bmod F_n \tag{4b}$$

Summing Eqs. (4a) and (4b) yields $2a \equiv 2c \bmod F_n$. But since $(2, F_n) = 1$, $a \equiv c \bmod F_n$. Subtracting Eq. (4a) from Eq. (4b) yields $2sb \equiv 2sd \bmod F_n$. Thus, since $(2s, F_n) = 1$, $b \equiv d \bmod F_n$. Hence $a + ib = c + id$ and ϕ is a one-to-one mapping.

To show that ϕ preserves multiplication and addition, let $a + ib$ and $c + id$ be arbitrary elements in $Z_{F_n}[i]$. Then

$$\begin{aligned} \phi((a + ib) + (c + id)) &= \phi((a + c) + i(b + d)) \\ &= ((a + c) + s(b + d), (a + c) \\ &\quad - s(b + d)) \end{aligned}$$

$$= (a + sb, a - sb) + (c + sd, c - sd)$$

$$= \phi(a + ib) + \phi(c - id)$$

and

$$\begin{aligned}
\phi((a + ib) \cdot (c + id)) &= \phi((ac - bd) + i(bc + ad)) \\
&= ((ac - bd) + s(bc + ad), (ac - bd) \\
&\quad - s(bc + ad)) \\
&= ((a + sb) \cdot (c + sd), (a - sb) \\
&\quad \cdot (c - sd)) \\
&= (a + sb, a - sb) \cdot (c + sd, c - sd) \\
&= \phi(a + ib)\,\phi(c + id)
\end{aligned}$$

Hence, $Z_{F_n}[i]$ is isomorphic to the ring S_{F_n} and the theorem is proved.

Remark 1: An inverse mapping ϕ^{-1} which maps $(\alpha, \overline{\alpha}) \in S_{F_n}$ into $Z_{F_n}[i]$ is defined by

$$\phi^{-1}: (\alpha, \overline{\alpha}) \rightarrow a + ib \tag{5}$$

where a and b can be computed by Eq. (3).

It was shown (Ref. 6) that the multiplication by e powers of two modulo F_n is accomplished simply by a cyclic shift of e bits. Thus by Eq. (1) and Eq. (3), the arithmetic needed to compute the mapping ϕ and its inverse ϕ^{-1} requires only cyclic shifts and additions modulo F_n. As a consequence, both mappings are easily implemented with VLSI technology. Also by Theorem 1, the operations needed to perform integer complex multiplication in $Z_{F_n}[i]$ only require two integer multiplications modulo F_n. Such multiplications modulo F_n can be implemented by using a new VLSI design of a single chip developed in Ref. 7.

To perform multiplication and addition in $Z_{F_n}[i]$ or its equivalent S_{F_n}, one must determine an F_n such that the results of the computations lie in $Z_{F_n}[i]$. The fermat number F_5 is sufficiently large for a good many applications. However, for some applications, larger dynamic range is required to keep the results of a computation within $Z_{F_n}[i]$. This constraint sometimes forces F_n to be too large to be convenient for computations by VLSI technology. To remedy this situation, using the ideas in Ref. 8, complex multiplications are extended in this section to a ring which is the direct sum of $Z_{F_k}[i]$, $Z_{F_{k+1}}[i]$, ..., and $Z_{F_r}[i]$, where for each j, $Z_{F_{k+j}}[i]$ is represented by two copies of $Z_{F_{k+j}}$. To achieve this, the following theorems are needed.

Chinese Remainder Theorem: If $m_1, m_2, \ldots, m_r$ are relatively prime in pairs, then the system of congruences, $x \equiv c_n \bmod m_n$ for $1 \leqslant n \leqslant r$ has a unique solution x given by

$$x \equiv \sum_{n=1}^{r} c_n M_n M_n^{-1} \bmod M \tag{6a}$$

where $M = m_1 m_2 \ldots m_r = m_1 M_1 = m_2 M_2 = \ldots = m_r M_r$ and M_n^{-1} uniquely satisfies (mod m_n) the congruence

$$M_n M_n^{-1} \equiv 1 \bmod M_n \tag{6b}$$

for $1 \leqslant n \leqslant r$. For a detailed proof, see Ref. 9.

Let $M = F_k \cdot F_{k+1} \ldots F_r = (2^{2^k} + 1)(2^{2^{k+1}} + 1) \ldots (2^{2^r} + 1) = F_k M_k = F_{k+1} M_{k+1} = \ldots = F_r M_r$, where $1 \leqslant k \leqslant r$ and $M_n = M/F_n$. Since $F_k, F_{k+1}, \ldots, F_r$ are pairwise relatively prime, by the Chinese remainder theorem, it is shown in Appendix A that the congruences

$$x \equiv c_n \bmod F_n \qquad \text{for } k \leqslant n \leqslant r \tag{7a}$$

have a unique solution x given by

$$x \equiv \sum_{n=k}^{r} c_n M_n M_n^{-1} \equiv \sum_{n=k}^{r} c_n (M/F_n) M_n^{-1} \bmod M \tag{7b}$$

where

$$M_k^{-1} = 2^{-(r-k)} = 2^{(-(r-k)) \bmod 2^{k+1}} \tag{7c}$$

and

$$\begin{aligned}
M_n^{-1} &= -2^{-1}\, 2^{-(r-n)} (2^{2^k} - 1) \\
&= 2^{(2^n - (r-n+1)) \bmod 2^{n+1}} (2^{2^k} - 1) \qquad \text{for } k < n \leqslant r
\end{aligned}$$

Here M_n^{-1} uniquely satisfies the congruence $M_n M_n^{-1} \equiv 1 \bmod F_n$ for $k \leqslant n \leqslant r$.

The number of additions and multiplications modulo F_n needed to compute Eq. (7b) are $r - k$ and $r - k + 1$.

Theorem 2: Let $M = F_k \cdot F_{k+1} \ldots F_r$ be the product of distinct Fermat numbers. Next let $Z_M[i] = \{a + ib \mid a, b \in Z_M\}$ where Z_M is a set of residues, modulo M. Then the direct sum of finite rings

$$S_M[i] = Z_{F_k}[i] + Z_{F_{k+1}}[i] + \cdots + Z_{F_r}[i]$$

where addition and multiplication are defined, respectively, by

$$(\alpha_k, \alpha_{k+1}, \ldots, \alpha_r) + (\beta_k, \beta_{k+1}, \ldots, \beta_r)$$
$$= (\alpha_k + \beta_k, \alpha_{k+1} + \beta_{k+1}, \ldots, \alpha_r + \beta_r)$$

and

$$(\alpha_k, \alpha_{k+1}, \ldots, \alpha_r) \cdot (\beta_k, \beta_{k+1}, \ldots, \beta_r)$$
$$= (\alpha_k \cdot \beta_k, \alpha_{k+1}\, \beta_{k+1}, \ldots, \alpha_r \cdot \beta_r)$$

is a ring of M^2 elements which is isomorphic to the ring $Z_M[i]$.

Proof: If $a + ib \in Z_M[i]$, then let θ be the mapping

$$\theta:(a+ib) \to ((a+ib)_{F_k}, (a+ib)_{F_{k+1}}, \ldots, (a+ib)_{F_r})$$
$$= (a_{F_k} + ib_{F_k}, a_{F_{k+1}} + ib_{F_{k+1}}, \ldots, a_{F_r} + ib_{F_r})$$
$$= (\alpha_k, \alpha_{k+1}, \ldots, \alpha_r) \tag{8}$$

where $\alpha_n = (a+ib)_{F_n} = a_{F_n} + ib_{F_n}$ for $k \leqslant n \leqslant r$.

It is easy to show that θ preserves addition and multiplication. To show that θ is onto and one-to-one, it suffices to show that given an arbitrary element $(\alpha_k, \alpha_{k+1}, \ldots, \alpha_r) \in S_M[i]$, there exists an unique element $a + ib \in Z_{F_M}[i]$ such that $\phi(a+ib) = (\alpha_k, \alpha_{k+1}, \ldots, \alpha_r)$. Equation (8) implies that

$$a \equiv a_{F_n} \bmod F_n \tag{9a}$$

and

$$b = b_{F_n} \bmod F_n \tag{9b}$$

for $k \leqslant n \leqslant r$. By Eq. (7), the unique solution of the systems of congruences in Eqs. (9a) and (9b), are

$$a \equiv a_{F_k}(M/F_k) \cdot 2^{(-(r-k))\bmod 2^{k+1}} + \sum_{n=k+1}^{r} a_{F_n}(M/F_n)$$
$$\times 2^{(2^n-(r-n+1))\bmod 2^{n+1}}(2^{2^k} - 1) \tag{9c}$$

and

$$b = b_{F_k}(M/F_k) \cdot 2^{(-(r-k))\bmod 2^{k+1}} + \sum_{n=k+1}^{r} b_{F_n}(M/F_n)$$
$$\times 2^{(2^n-(r-n+1))\bmod 2^{n+1}}(2^{2^k} - 1)$$

It follows that each element $(a_{F_k} + ib_{F_k}, a_{F_{k+1}} + ib_{F_{k+1}}, \ldots, a_{F_r} + ib_{F_r})$ of S_M is the image of a unique element $a + ib$ of $Z_M[i]$. This proves that θ is one-to-one and onto and hence an isomorphic mapping of $Z_M[i]$ onto $S_M[i]$.

Remark 2: An inverse mapping θ^{-1} which maps $(\alpha_k, \alpha_{k+1}, \ldots, \alpha_r) \in S_M$ into $a + ib \in Z_M[i]$ is defined by

$$\theta^{-1}:(\alpha_k, \alpha_{k+1}, \ldots, \alpha_r) \to a + ib \tag{10}$$

where a and b can be computed by Eqs. (9c).

Theorem 3: Let $M = F_k \cdot F_{k+1} \ldots F_r$, where $(F_i, F_j) = 1$. Next let $Z_M[i] = \{a + ib \mid a, b \in Z_M\}$ be the ring in Theorem 2. Then the direct sum of $Z_{F_k}[i]$, $Z_{F_{k+1}}[i]$, ..., and $Z_{F_r}[i]$, where for each j, $Z_{F_{k+j}}[i]$ is represented by two copies of $Z_{F_{k+j}}$, is

$$S_M = (Z_{F_k} + Z_{F_k}) + (Z_{F_{k+1}} + Z_{F_{k+1}}) + \ldots + (Z_{F_r} + Z_{F_r})$$
$$= \{(\alpha_k, \overline{\alpha}_k), (\alpha_{k+1}, \overline{\alpha}_{k+1}), \ldots,$$
$$(\alpha_r, \overline{\alpha}_r) \mid (\alpha_n, \overline{\alpha}_n) \in (Z_{F_n} + Z_{F_n})\}$$

where addition and multiplication are defined, respectively, by

$$((\alpha_k, \overline{\alpha}_k), (\alpha_{k+1}, \overline{\alpha}_{k+1}), \ldots, (\alpha_r, \overline{\alpha}_r))$$
$$+ ((\beta_k, \overline{\beta}_k), (\beta_{k+1}, \overline{\beta}_k), \ldots, (\beta_r, \overline{\beta}_r))$$
$$= ((\alpha_k + \beta_k, \overline{\alpha}_k + \overline{\beta}_k), (\alpha_{k+1} + \beta_{k+1}, \overline{\alpha}_{k+1} + \overline{\beta}_{k+1}), \ldots,$$
$$(\alpha_r + \beta_r, \overline{\alpha}_r + \overline{\beta}_r))$$

and

$$((\alpha_k, \overline{\alpha}_k), (\alpha_{k+1}, \overline{\alpha}_{k+1}), \ldots, (\alpha_r, \overline{\alpha}_r))$$
$$\times ((\beta_k, \overline{\beta}_k), (\beta_{k+1}, \overline{\beta}_{k+1}), \ldots, (\beta_r, \overline{\beta}_r))$$
$$= ((\alpha_k \cdot \beta_k, \overline{\alpha}_k \cdot \overline{\beta}_k), (\alpha_{k+1} \cdot \beta_{k+1}, \overline{\alpha}_{k+1} \cdot \overline{\beta}_{k+1}), \ldots,$$
$$(\alpha_r \cdot \beta_r, \overline{\alpha}_r \cdot \overline{\beta}_r))$$

is a ring of M^2 element which is isomorphic to the ring $Z_M[i]$.

Proof: Let $\hat{\theta} = \phi \cdot \theta$ be the composition of the mapping ϕ given by Eq. (1) and θ given in Eq. (8). If $a + ib \in Z_M[i]$, then $\hat{\theta}$ is

$$\hat{\theta}: a + ib \rightarrow ((\alpha_k, \overline{\alpha}_k), (\alpha_{k+1}, \overline{\alpha}_{k+1}), \ldots, (\alpha_r, \overline{\alpha}_r)) \quad (11a)$$

where $s_n = \pm 2^{2^{n-1}}$ are the solution of $x^2 + 1 \equiv \bmod F_n$ and $\overline{\alpha}_n = (a + s_n b)_{F_n}$ and $\alpha = (a - s_n b)_{F_n}$, for $k \leqslant n \leqslant r$. Some θ and ϕ are an isomorphic mapping of $Z_M[i]$ onto $S_M[i]$ and an isomorphic mapping of $S_{F_n}[i]$ onto S_{F_n}, respectively, it is evident that $\hat{\theta}$ is an isomorphic mapping of $Z_M[i]$ onto S_M. The arithmetic needed to perform the mapping $\hat{\theta}$ given in Eq. (11a) only requires cyclic shifts and addition modulo F_n.

Remark 3: The inverse mapping of $\hat{\theta}$, i.e., $\hat{\theta}^{-1} = \theta^{-1} \cdot \theta^{-1}$ which maps an element in S_M into an element in $Z_M[i]$ is

$$\hat{\theta}^{-1}: ((\alpha_k, \overline{\alpha}_k), (\alpha_{k+1}, \overline{\alpha}_{k+1}), \ldots, (\alpha_r, \overline{\alpha}_r) \rightarrow a + ib \quad (11b)$$

where Eq. (11b) can be computed by the two inverse mapping ϕ^{-1} and θ^{-1}. In other words, Eq. (5) can be used first to convert an element $((\alpha_k, \overline{\alpha}_k), (\alpha_{k+1}, \overline{\alpha}_{k+1}, \ldots, (\alpha_r, \overline{\alpha}_r))$ in S_M into an element $(a_{F_k} + ib_{F_k}, a_{F_{k+1}} + ib_{F_{k+1}}, \ldots, a_{F_r} + ib_{F_r})$ in $S_M[i]$. Next Eq. (9a) can be used to convert an element $(a_{F_k} + ib_{F_k}, a_{F_{k+1}} + ib_{F_{k+1}}, \ldots, a_{F_r} + ib_{F_r})$ into an element $a + ib \in Z_M[i]$.

In the following, some examples are given to illustrate how the above mappings can be used to efficiently perform complex multiplication.

Example 1: Compute $(3 + i2) \cdot (1 + i4) \bmod 17$, where $3 + i2$ and $1 + i4 \in Z_{17}[i]$ by means of the direct sum of two copies of Z_{17}.

Consider now this operation in the image ring S_{F_2}. The solution of $x^2 + 1 \equiv 0 \bmod F_2$ are $\pm 2^{2^{n-1}} = \pm 2^{2^{2-1}} = \pm 4$. Thus, by the mapping ϕ given in Eq. (1), one obtains

$$\begin{aligned} (3 + i2) &\cong (3 + 4 \times 2, 3 - 4 \times 2) = (11, -5) \\ (1 + i4) &\cong (1 + 4 \times 4, 1 - 4 \times 4) = (0, 2) \end{aligned} \quad (12)$$

Multiplying two images given in Eq. (12) yields

$$(11, -5) \cdot (0, 2) = (0, 7)$$

The corresponding element $a + ib$ of (0, 7) under the inverse mapping ϕ^{-1} given in Eq. (3) is

$$a \equiv -2^3 (0 + 7) \equiv -8 \cdot 7 \bmod 17 = -5$$

$$b \equiv -2 (0 - 7) \bmod 17 = 14$$

The final result is $-5 + i14$ which is verified readily to be the correct answer.

Example 2: Compute $(4 + i5) \cdot (17 + i3) \bmod M = F_1 F_2 = 5 \cdot 17 = 85$, where $(4 + i5)$ and $(17 + i3) \in Z_{85}[i]$ by means of the direct sum of $Z_5[i]$ and $Z_{17}[i]$, where $Z_5[i]$ and $Z_{17}[i]$ are represented by 2 copies of Z_5 and Z_{17}, respectively.

From the mapping Eq. (11), one obtains

$$\begin{aligned} (4 + i5)_{85} &\cong (((4 + 2 \cdot 5)_5, (4 - 2 \cdot 5)_5), \\ &\quad ((4 + 2^2 \cdot 5)_{17}, (4 - 2^2 \cdot 5)_{17})) \\ &= ((4, 4)_5, (7, 1)_{17}) \end{aligned} \quad (13)$$

and

$$\begin{aligned} (17 + i3)_{85} &\cong (((17 + 2 \cdot 3)_5, (17 - 2 \cdot 3)_5), \\ &\quad ((17 + 2^2 \cdot 3)_{17}, (17 - 2^2 \cdot 3)_{17}) \\ &= ((3, 1)_5, (12, -12)_{17}) \end{aligned}$$

where ± 2 and $\pm 2^2$ are the solutions of $x^2 + 1 \equiv 0 \bmod 5$ and the solutions of $x^2 + 1 \equiv 0 \bmod 17$, respectively. Multiplying two images given in Eq. (13) yields

$$\begin{aligned} &((4, 4)_5, (7, 1)_{17}) \cdot ((3, 1)_5, (12, -12)_{17}) \\ &= ((2, -1)_5, (-1, 5)_{17}) \end{aligned}$$

The corresponding elements $a + ib \in Z_5[i]$ and $(c + id) \in Z_{17}[i]$ of $(2, -1)_5$ and $(-1, 5)_{17}$ under the first inverse mapping ϕ^{-1}, given in Eq. (5), are

$$(2, -1)_5 \equiv ((-2)(2 - 1) + i(-1)(2 + 1)) = (-2 - i3)_5$$

and

$$(-1, 5)_{17} = ((-2^3)(-1 + 5) + i(-2)(-1 - 5))_{17} = (2 - i5)_{17}$$

Thus $((2, -1)_5, (-1, 5)_{17}) \cong ((-2 - i3)_5, (2 - i5)_{17})$. Finally, the corresponding element $a + ib \in Z_{85}[i]$ of $((-2 - i3)_5, (2 - i5)_{17})$ under the second inverse mapping θ^{-1} given in Eq. (10) is

$$\begin{aligned} a &\equiv (-2) \cdot 136 + 2 \cdot 120 \\ &\equiv (-272 + 240) \bmod 85 = 53 \end{aligned}$$

and

$$b \equiv (-3) \cdot 136 + (-5) \cdot 120$$

$$\equiv (-408 - 600) \bmod 85 = 12$$

The final result is $a + ib = 53 + i12$ which is verified readily to be the correct answer.

III. Discrete Fourier Transform Over $Z_M[i]$

In this section, a d point Fourier transform over ring $Z_M[i]$ or its equivalent S_M is developed to compute the usual digital Fourier transform of complex numbers. It will not be necessary for the transform length to be a power of two. For the Fourier transform of complex integer numbers in $Z_M[i]$, one needs to scale the powers of the dth root of unity from complex numbers to complex integers in $Z_M[i]$. Then the components of the transforms over the ring $Z_M[i]$ or its equivalent S_M are required to remain in the interval $-(M-1)/2$ to $(M-1)/2$. These results can then be scaled back from the complex integers to the original complex numbers to give a DFT of complex numbers without round-off error. For example, to compute a d point DFT of integer complex numbers $a_n = \alpha_n + i\beta_n$ with $|\alpha_n|, |\beta_n| \leqslant A = 2^{\lambda_1}$, i.e.,

$$A_k = \sum_{n=0}^{d-1} a_n \omega^{n \cdot k}$$

$$= \sum_{n=0}^{d-1} (\alpha_n + i\beta_n) \cdot (x_{n,k} + iy_{n,k}), \qquad 0 \leqslant k \leqslant d-1 \tag{16}$$

where $\omega = \exp(i2\pi/d)$ is a dth root of unity and $\omega^{n \cdot k} = x_{n,k} + iy_{n,k}$.

The components of the truncated complex number $\omega^{n \cdot k}$ are first converted to integers with the dynamic range $B = 2^{\lambda_2}$, i.e., $-B \leqslant \tilde{x}_{n,k}, \tilde{y}_{n,k} \leqslant B$. Here $\tilde{\omega}^{n \cdot k} = \tilde{x}_{n,k} + i\tilde{y}_{n,k}$ denotes the scaled original complex number $\omega^{n \cdot k}$. Next let the DFT of a_n using the scaled truncated sequence $\tilde{\omega}^{n \cdot k}$ be denoted by $\tilde{A}_k$. Thus, $\tilde{A}_k$ is defined by

$$\tilde{A}_k = \sum_{n=0}^{d-1} a_n \tilde{\omega}^{n \cdot k}$$

$$= \sum_{n=0}^{d-1} ((\alpha_n \tilde{x}_{n,k} - \beta_n \tilde{y}_{n,k}) + i(\alpha_n \tilde{y}_{n,k} + \beta_n \tilde{x}_{n,k}))$$

$$= \tilde{\gamma}_k + i\tilde{\delta}_k \tag{17}$$

where

$$a_n = \alpha_n + i\beta_n$$

$$\tilde{\omega}^{n \cdot k} = \tilde{x}_{n,k} + i\tilde{y}_{n,k}$$

$$\tilde{\gamma}_k = \sum_{n=0}^{d-1} \alpha_n \tilde{x}_{n,k} - \beta_n \tilde{y}_{n,k}$$

$$\tilde{\delta}_k = \sum_{b=0}^{d-1} \alpha_n \tilde{y}_{n,k} + \beta_n \tilde{x}_{n,k}$$

To compute Eq. (17), one requires the final DFT in Eq. (17) to lie in the same "dynamic range" as the complex integers a_n and $\tilde{\omega}^{n \cdot k}$. That is,

$$|\tilde{\gamma}_k| = \left| \sum_{n=0}^{d-1} (\alpha_n \tilde{x}_{n,k} - \beta_n \tilde{y}_{n,k}) \right|$$

$$\leqslant \sum_{n=0}^{d-1} (|\alpha_n| \cdot |\tilde{x}_{n,k}| + |\beta_n| \, |\tilde{y}_{n,k}|)$$

$$\leqslant (M-1)/2 \tag{18}$$

and

$$|\tilde{\delta}_k| = \left| \sum_{n=0}^{d-1} (\alpha_n \tilde{y}_{n,k} + \beta_n \tilde{x}_{n,k}) \right|$$

$$\leqslant \sum_{n=0}^{d-1} (|\alpha_n| \, |\tilde{y}_{n,k}| + |\beta_n| \cdot |\tilde{x}_{n,k}|)$$

$$\leqslant (M-1)/2$$

To satisfy Eq. (18) for all complex integer valued sequences a_n and $\tilde{\omega}^{n \cdot k}$ such that $|\alpha_n|, |\beta_n| \leqslant A = 2^{\lambda_1}$ and $|x_{n,k}|, |y_{n,k}| \leqslant B = 2^{\lambda_2}$, it is sufficient to set

$$2dA \cdot B \leqslant (M-1)/2 \tag{19}$$

if $A = B$, then

$$A = \left[\sqrt{\frac{n-1}{4d}} \right] \tag{20}$$

where $[x]$ denotes the greatest integer less than x. The transform $\tilde{A}_k$ in Eq. (17) can be computed by using the direct sum

of $Z_{F_k}[i]$, $Z_{F_{k+1}}[i]$, ..., and $Z_{F_r}[i]$, where $Z_{F_{k+j}}[i]$ is represented by two copies of $Z_{F_{k+j}}$. Finally, the $\tilde{A}_k$'s are scaled back to the scale of original complex numbers by B^{-1} for $1 \leqslant k \leqslant d-1$. By Eq. (17), one observes that the powers of roots of unity always have a truncation error due to approximating the powers of roots of unity. Evidently, the only error made in this computation of $\tilde{A}_k$'s is this truncation error. The error analysis of the DFT caused by $\tilde{\omega}^{n \cdot k}$ is illustrated in the following section.

Example 3: Compute a 4-point DFT of a_n by means of the direct sum of two copies of Z_{F_2}, where $a_0 = a_1 = 1 + i$ and $a_2 = a_3 = 0$.

The 4-point DFT of complex number of a_n

$$A_k = \sum_{n=0}^{4-1} a_n \omega^{n \cdot k} = \gamma_k + i\delta_k \tag{21}$$

where $\omega = i$ is the 4th root of unity and $a_n = \alpha_n + i\beta_n$. Since $d = 4$, $F_2 = 17$, $|\alpha_n|, |\beta_n| \leqslant A = 2^{\lambda_1} = 1$, then by Eq. (19) the dynamic range constraint of the components of $\omega^{n \cdot k}$ is $B = 2^{\lambda_2} = 2^4/(4 \cdot 4 \cdot 1) = 1$. Thus, in this example, $\omega^{n \cdot k} = \omega^{n \cdot k}$. This implies that $|\tilde{x}_{n,k}| = |x_{n,k}| \leqslant B$ and $|\tilde{y}_{n,k}| = |y_{n,y}| \leqslant B$, where $\tilde{\omega}^{n \cdot k} = \tilde{x}_{n,k} + i\tilde{y}_{n,k}$ and $\omega^{n \cdot k} = x_{n,k} + iy_{n,k}$. That is, $\tilde{\omega}^0 = \omega^0 = 1$, $\tilde{\omega} = \omega = i$, $\tilde{\omega}^2 = \omega^2 = -1$ and $\tilde{\omega}^3 = \omega^3 = -i$. Hence, the 4-point DFT of a_n becomes

$$\begin{aligned} \tilde{A}_k &= \sum_{n=0}^{4-1} a_n \tilde{\omega}^{n \cdot k} \bmod 17 \\ &= \tilde{\gamma}_k + i\tilde{\delta}_k \qquad \text{for } 0 \leqslant k \leqslant 3 \end{aligned} \tag{22}$$

The corresponding elements in S_{17} of a_0 and $\tilde{\omega}^{n \cdot j}$ in $Z_{17}[i]$ under the mapping ϕ defined in Eq. (1) is

$$a_0 = 1 + i1 \cong (1 + 2^2 \cdot 1, 1 - 2^2 \cdot 1) = (5, -3)$$

where $\pm 2^2$ is the solution of $x^2 + 1 \equiv 0 \bmod 17$. Similarly, one has $a_1 = 1 + i1 = (5, -3)$, $a_2 = a_3 = 0 \cong (0, 0)$, $\tilde{\omega}^0 = 1 \cong (1, 1)$, $\tilde{\omega}^1 = 1 \cong (4, -4)$, $\tilde{\omega}^2 = -1 \cong (-1, -1)$, and $\tilde{\omega}^3 = -i \cong (-4, 4)$.

Then Eq. (22) over S_{17} becomes

$$\begin{aligned} \tilde{A}_k &= (5, -3)\,\tilde{\omega}^0 + (5, -3)\,\tilde{\omega}^k + (0, 0)\,\tilde{\omega}^{2 \cdot k} + (0, 0)\,\tilde{\omega}^{3 \cdot k} \\ &= (5, -3)\,\tilde{\omega}^0 + (5, -3)\,\tilde{\omega}^k \end{aligned} \tag{23a}$$

For $k = 0, 1, 2, 3$, Eq. (23a) becomes

$$\left.\begin{aligned} \tilde{A}_0 &= (5, -3)\,\tilde{\omega}^0 + (5, -3)\,\tilde{\omega}^0 \\ &= (5, -3)(1, 1) + (5, -3)(1, 1) \\ &= (5, -3) + (5, -3) = (10, 6) \\ \tilde{A}_1 &= (5, -3)\,\tilde{\omega}^0 + (5, -3)\,\tilde{\omega}^1 \\ &= (5, -3)(1, 1) + (5, -3)(4, -4) \\ &= (5, -3) + (3, 12) = (8, 9) \\ \tilde{A}_2 &= (0, 0) \\ \tilde{A}_3 &= (5, -3)\,\omega^0 + (5, -3)\,\omega^3 \\ &= (5, -3) + (-3, 5) = (2, 2) \end{aligned}\right\} \tag{23b}$$

Taking the inverse mapping ϕ^{-1} defined in Eq. (5) yields

$$\begin{aligned} \tilde{A}_0 &= (10, -6) \\ &\cong (-2^{2^2-1}(10 - 6) - i2^{2^{2-1}-1}(10 + 6)) \\ &= ((-8)(4) + i(-2)(16)) \\ &= (-32 - i32) = 2 + i2 \\ A_1 &= (8, 9) \\ &= ((-8)(8 + 9) + i(-2)(8 - 9)) = 2i \end{aligned}$$

Similarly, one has $\tilde{A}_2 = (0, 0) = 0$ and $\tilde{A}_3 = (2, 2) = 2$.

Example 4: Compute a 4-point DFT of a_n by means of the direct sum of $Z_{F_1}[i]$ and $Z_{F_2}[i]$, where $Z_{F_1}[i]$ and $Z_{F_2}[i]$ are represented by two copies Z_{F_1} and Z_{F_2}, respectively. Let the input values be $a_0 = a_1 = 1 + i$ and $a_2 = a_3 = 0$ where $a_n = \alpha_n + i\beta_n \in Z_M[i]$ for $M = F_1 \cdot F_2$.

Since $d = 4$, $M = 85$ and $|\alpha_n|, |\beta_n| \leqslant A = 2^{\lambda_1} = 1$, then by Eq. (19), the dynamic range constraint of the components of $\omega^{n \cdot k}$ is $B = 2^{\lambda_2} = 85/(4 \cdot 4 \cdot 1) \cong 2^2$.

In this example, $|x_{n,k}|$, $|y_{n,k}| \leqslant B = 2^2$, where $\omega^{n \cdot k} = x_{n,k} + iy_{n,k}$. Thus $\tilde{\omega}^{n \cdot k} = \omega^{n \cdot k}$. That is, $\tilde{\omega} = \omega = i$, $\tilde{\omega}^2 = \omega^2 = -1$, $\tilde{\omega}^3 = \omega^3 = -i$ and $\tilde{\omega}^0 = \omega^0 = 1$. Hence, a 4-point transform DFT of a_n due to the scaled truncated sequence $\omega^{n \cdot k}$ is

$$\widetilde{A}_k = \sum_{n=0}^{4-1} a_n \widetilde{\omega}^{n \cdot k} \bmod 85$$

$$= \widetilde{\gamma}_k + i\widetilde{\delta} \quad \text{for } 0 \leqslant k \leqslant 3 \tag{23c}$$

Taking the mapping $\widehat{\theta}$ defined in Eq. (11) yields

$$a_0 = a_1 = (1 + i)$$

$$\cong ((1 + 2 \cdot 1, 1 - 2 \cdot 1)_5, (1 + 2^2 \cdot 1, 1 - 2^2 \cdot 1)_{17})$$

$$\cong ((3, -1)_5, (5, -3)_{17})$$

where 2 and 4 are the solutions of $x^2 + 1 \equiv 0 \bmod 5$ and 17, respectively. Similarly, one has $a_2 = a_3 = 0 \cong ((0, 0)_5, (0, 0)_{17})$, $\widetilde{\omega}^0 = 1 \cong ((1, 1)_5, (1, 1)_{17})$, $\widetilde{\omega}^1 = i \cong ((2, -2)_5, (4, -4)_{-17})$, $\widetilde{\omega}^2 = -1 \cong ((-1, -1)_5, (-1, -1)_{17})$, and $\widetilde{\omega}^3 = -i \cong ((-2, 2)_5, (-4, 4)_{17})$. Thus, Eq. (23c) in S_{85} becomes

$$\begin{aligned}
\widetilde{A}_k &= ((3, -1)_5, (5, -3)_{17})\, \widetilde{\omega}^0 \\
&\quad + ((3, -1)_5, (5, -3)_{17})\, \widetilde{\omega}^k \\
&\quad + ((0, 0)_5, (0, 0)_{17})\, \widetilde{\omega}^{2k} \\
&\quad + ((0, 0)_5, (0, 0)_{17})\, \widetilde{\omega}^{3 \cdot k} \\
&= ((3, -1)_5, (5, -3)_{17})\, \widetilde{\omega}^0 \\
&\quad + ((3, -1)_5, (5, -3)_{17})\, \widetilde{\omega}^k
\end{aligned} \tag{24a}$$

For $k = 0, 1, 2, 3$, Eq. (24a) becomes

$$\begin{aligned}
\widetilde{A}_0 &= ((3, -1)_5, (5, -3)_{17})\, \widetilde{\omega}^0 + ((3, -1)_5, (5, -3)_{17})\, \widetilde{\omega}^0 \\
&= ((3, -1)_5, (5, -3)_{17}) \cdot ((1, 1)_5, (1, 1)_{17}) \\
&\quad + ((3, -1)_5, (5, -3)_{17}) \cdot ((1, 1)_5, (1, 1)_{17}) \\
&= ((1, -2)_5, (10, -6)_{17})
\end{aligned} \tag{24b}$$

$$\begin{aligned}
\widetilde{A}_1 &= ((3, -1)_5, (5, -3)_{17})\, \widetilde{\omega}^0 + (3, -1)_5, (5, -3)_{17})\, \widetilde{\omega}^1 \\
&= ((3, -1)_5, (5, -3)_{17}) \cdot ((1, 1)_5, (1, 1)_{17}) \\
&\quad + ((3, -1)_5, (5, -3)_{17}) \cdot ((2, -2)_5, (4, -4)_{17}) \\
&= ((4, 1)_5, (8, 5)_{17})
\end{aligned}$$

$$\begin{aligned}
\widetilde{A}_2 &= ((0, 0)_5, (0, 0)_{17}) \\
\widetilde{A}_3 &= ((3, -1)_5, (5, -3)_{17})\, \widetilde{\omega}^0 + ((3, -1)_5, (5, -3)_{17})\, \widetilde{\omega}^3 \\
&= ((2, 2)_5, (2, 2)_{17})
\end{aligned}$$

Taking the first inverse mapping ϕ^{-1} defined in Eq. (5) yields

$$\begin{aligned}
\widetilde{A}_0 &= ((1, -2)_5, (10, -6)_{17}) \\
&= (((-2^{2-1})(1 - 2) \\
&\quad + i(-2^{2^{1-1}-1})(1 + 2)), ((-2^{2^2-1})(10 - 6) \\
&\quad + i(-2^{2^{2-1}-1})(10 + 6) \\
&= ((-2)(-1) + i(-1)(3), (-8)(4) + i(-2)(-1)) \\
&= ((2 - i3)_5, (2 + i2)_{17})
\end{aligned}$$

$$\begin{aligned}
\widetilde{A}_1 &= ((4, 1)_5, (8, 5)_{17}) \\
&\cong ((-2)(4 + 1) + i(-1)(4 - 1), (-8)(8 + 5) \\
&\quad + i(-2)(8 - 5)) \\
&\cong ((0 + i2)_5, (-2 - 6i)_{17})
\end{aligned}$$

$$\widetilde{A}_2 = ((0 + i0)_5, (0 + i0)_{17})$$

$$\widetilde{A}_3 = ((2 + i0)_5, (2 + i0)_{17})$$

For $k = 0$, the corresponding element $\widetilde{A}_0 = \widetilde{\gamma}_0 + i\widetilde{\delta}_0$ of $\widetilde{A}_0 = ((1, -2)_5, (10, -6)_{17})$ under the second inverse mapping θ^{-1} given in Eq. (10) is

$$\begin{aligned}
\widetilde{\gamma}_0 &\equiv 2 \times 17 \cdot 2^{(-(2-1)) \bmod 4} + 2 \cdot 3 \\
&\quad \times 2^{(2^2-(2-2+1)) \bmod 2^3} (2^2 - 1) \\
&\equiv 2 \times 17 \times 8 + 2 \cdot 5 \times 8 \cdot 3 = 2 \bmod 85
\end{aligned}$$

and

$$\widetilde{\delta}_0 \equiv (-3)(17) \times 8 + (2) \cdot 5 \cdot 8 \cdot 3 \equiv 2 \bmod 85$$

Thus,

$$\widetilde{A}_0 = ((1, -2)_5, (10, -6)_{17}) \cong 2 + i2$$

Using the same procedure for $\tilde{A}_k$ for $k = 1, 2, 3$, one has finally $\tilde{A}_1 = 2 + i2$ and $\tilde{A}_2 = \tilde{A}_3 = 0$.

IV. Error Analysis of DFT Over S_M

In Eq. (17), let $|a_n| \leqslant \sqrt{2} \cdot A = \sqrt{2} \cdot 2^{\lambda_1}$, where $a_n = \alpha_n + i\beta_n$ such that $|\alpha_n|, |\beta_n| \leqslant A = 2^{\lambda_1}$. In most digital signal processing applications, the input data a_n is an integer complex number, each component of a_n is represented, say, to at most 8 bit accuracy, i.e., $|\alpha_n|, |\beta_n| \leqslant 2^{\lambda_1}$, where $0 \leqslant \lambda_1 \leqslant 8$. Also let

$$\mathrm{Re}\{\omega^{n \cdot k}\} = x_{n,k} = \frac{x_1}{2} + \frac{x_2}{2^2} + \cdots + \frac{x_{\lambda_2}}{2^{\lambda_2}} + \cdots$$

$$\mathrm{Im}\{\omega^{n \cdot k}\} = y_{n,k} = \frac{y_1}{2} + \frac{y_2}{2^2} + \cdots + \frac{y_{\lambda_2}}{2^{\lambda_2}} + \cdots$$

If one truncates both $x_{n,k}$ and $y_{n,k}$ by $2^{-\lambda_2}$ digits, then the truncated sequences for $\tilde{\omega}^{n \cdot k}$ become

$$\mathrm{Re}\{\tilde{\omega}^{n \cdot k}\} = \tilde{x}_{n,k} = \frac{x_1}{2} + \frac{x_2}{2^2} + \frac{x_3}{2^3} + \cdots + \frac{x_{\lambda_2}}{2^{\lambda_2}}$$

$$\mathrm{Im}\{\tilde{\omega}^{n \cdot k}\} = \tilde{y}_{n,k} = \frac{y_1}{2} + \frac{y_2}{2^2} + \frac{y_3}{2^3} + \cdots + \frac{y_{\lambda_2}}{2^{\lambda_2}}$$

The error of A_k in Eq. (16) due to the truncated sequence $\omega^{n \cdot k}$ is

$$|A_k - \tilde{A}_k| = \left| \sum_{n=0}^{d-1} a_n (\omega^{n \cdot k} - \tilde{\omega}^{n \cdot k}) \right|$$

$$\leqq \sum_{n=0}^{d-1} |a_n| \cdot |\omega^{n \cdot k} - \tilde{\omega}^{n \cdot k}| \tag{25}$$

But $\mathrm{Re}\ |\omega^{n \cdot k} - \tilde{\omega}^{n \cdot k}|$, $\mathrm{Im}\ |\omega^{n \cdot k} - \tilde{\omega}^{n \cdot k}| \leqslant B^{-1} = 2^{-\lambda_2}$. Thus, $|\omega^{n \cdot k} - \tilde{\omega}^{n \cdot k}| \leqslant \sqrt{2} \cdot 2^{-\lambda_2}$. Hence since $|a_n| \leqslant \sqrt{2} \cdot 2^{\lambda_1}$ Eq. (25) becomes

$$|A_k - \tilde{A}_k| \leqq d \cdot \sqrt{2} \cdot 2^{\lambda_1} \cdot \sqrt{2} \cdot 2^{\lambda_2}$$

$$= d \cdot 2^{\lambda_1 + 1} \cdot 2^{-\lambda_2}$$

$$= \epsilon \tag{26}$$

where ϵ is the desired error. Since $|\alpha_n|, |\beta_n| \leqslant 2^{\lambda_1}$, then, from Eq. (19), the product of the dynamic range $A = 2^{\lambda_1}$ and $B = 2^{\lambda_2}$ is

$$d 2^{\lambda_1 + 1} \cdot 2^{\lambda_2} \leqslant \frac{(M-1)}{2} \tag{27a}$$

Thus,

$$2^{\lambda_2} \cong \frac{(M-1)}{2^{\lambda_1 + 1} \cdot 2d} \tag{27b}$$

The substitution of Eq. (27b) into Eq. (26) yields

$$\epsilon \cong \frac{(d \cdot 2^{\lambda_1 + 1})^2}{(M-1)/2} \tag{28}$$

Example 5: Let $M = F_5 \cdot F_4 = (2^{2^5+1}) \cdot (2^{2^4} + 1)$ and $d = 2^6$ and $\lambda_1 = 8$. Then $(d \cdot 2^{\lambda_1+1})^2 = (2^6 \cdot 2^9)^2 = 2^{30}$. By Eq. (19), the dynamic range of the components of $\tilde{\omega}^{n \cdot k}$ is

$$B = 2^{\lambda_2} \cong \frac{(2^{32} + 1)(2^{16} + 1)}{2^9 \cdot 2^7} \cong 2^{32}$$

where $\lambda_1 = 31$. By Eq. (28), the desired error of A_k due to the scaled truncated sequence $\omega^{n \cdot k}$ by $2^{\lambda_2} = 2^{32}$ is

$$\epsilon \cong \frac{2^{30}}{((2^{32} + 1)(2^{16} + 1) - 1)/2} \cong \frac{2^{30}}{2^{47}} \cong 2^{-17}$$

V. A VLSI Design for Computing the DFT Over S_M

In this section, a VLSI architecture is developed for computing the d-point DFT over the direct sum of $Z_{F_{k+j}}[i]$ using two copies of the finite ring $Z_{F_{k+j}}$ for all j. This VLSI processor for computing Eq. (17) is composed of d basic cells. Each basic cell performs a sum and product operation over S_M, where $M = F_k \cdot F_{k+1} \ldots F_r$. That is,

$$(a_1, a_2, \ldots, a_r) \leftarrow (a_1, a_2, \ldots, a_r)$$

$$+ (b_1, b_2, \ldots, b_r) \cdot (c_1, c_2, \ldots, c_r)$$

where "←" denotes the operation "is replaced by." The VLSI architecture of the DFT, using the Fermat residue number system with computations in $Z_M[i]$ is illustrated in the following two simple examples.

The calculations of the first example were illustrated in example 3 in Section IV. A VLSI architecture structure for computing a 4-point DFT over $Z_{17}[i]$ for this example is shown in Fig. 1. This figure contains 4 basic cells. The function of each basic cell is

$$(a, \bar{a}) \leftarrow (a, \bar{a}) + (b, \bar{b})(c, \bar{c})$$

$$= ((a + b \cdot c)_{17}, (\bar{a} + \bar{b} \cdot \bar{c})_{17}) \tag{29}$$

Equation (29) is computed by using the direct sum of two copies of Z_{17}. The $\omega^{n \cdot k}$ is first scaled by $B = 2^0$. In this example, $\tilde{\omega}^{n \cdot k} = \omega^{n \cdot k}$. First the integer complex number sequence a_n under the mapping ϕ are converted from $Z_{17}[i]$ into $(a_i, \bar{a}_i) \in S_{17}$ for $1 \leqslant i \leqslant 4$ and are sent to all of the cells simultaneously. Each register in Fig. 1 is composed of two 5-bit subregisters α and $\bar{\alpha}$ of $(\alpha, \bar{\alpha}) \in S_{17}$. $(\alpha, \bar{\alpha})$ is stored in these two 5-bit subregisters.

Assume initially that all registers are set to zero. After the input data are entered completely, the components of A_k in S_{17} given by Eq. (23b) are contained in registers B_k for $0 \leqslant k \leqslant 3$. The values computed in this manner are shifted sequentially out of register R_0. Next these values are converted by the inverse mapping ϕ^{-1} into $\tilde{A}_k = \tilde{a}_k + i\tilde{b}_k$ for $0 \leqslant k \leqslant 3$. Finally, these $\tilde{A}_k$ are scaled back to the scale of the original complex numbers A_k by $B^{-1} = 1$ for $1 \leqslant k \leqslant 4$.

The second example in this section illustrates in example 4 for the application of theorem 3 to the VLSI design of a DFT. A structure for computing the 4-point DFT over $Z_{85}[i]$ is shown in Fig. 2. In this figure, the function of each cell is

$$(a_1, \bar{a}_1)_5, (a_2, \bar{a}_2)_{17}) \leftarrow ((a_1, \bar{a}_1)_5, (a_2, \bar{a}_2)_{17})$$

$$+ ((b_1, \bar{b}_1)_5, (b_2, \bar{b}_2)_{17})$$

$$\times ((c_1, \bar{c}_1)_5, (c_2, \bar{c}_2)_{17})$$

$$= ((a_1 + b_1 c_1, \bar{a}_1 + \bar{b}_1 \cdot \bar{c}_1)_5,$$

$$(a_2 + b_2 \cdot c_2, \bar{a}_2 + \bar{b}_2 \cdot \bar{c}_2)_{17} \tag{30}$$

Equation (30) is computed by using the direct sum of two copies of Z_5 and Z_{17}. The $\omega^{n \cdot k}$ is first scaled by $B = 2^0$. In this example $\tilde{\omega}^{n \cdot k} = \omega^{n \cdot k}$. The complex integer number sequence a_n under the mapping $\hat{\theta} = \phi \cdot \theta$ is converted from $Z_{85}[i]$ to $((a_{1,n}, \bar{a}_{1,n})_5, (a_{2,n}, \bar{a}_{2,n})_{17}) \in S_{85} = S_5 + S_{17}$ and is transferred to all of the cells simultaneously. Each register in Fig. 2 is composed of four subregisters, where the first two are 3-bit subregisters and the last two are 5-bit subregisters. $(a_{1,n}, \bar{a}_{1,n})_5$ and $(a_{2,n}\ \bar{a}_{2,n})_{17}$ are stored in two 3-bit and 5-bit subregisters, respectively. Assume initially that all registers are set to zero. After the input data is entered completely, the results given in Eq. (24b) are stored in register R_k for $0 \leqslant k \leqslant 3$. The above results computed in this manner are shifted sequentially out of register R_0. Using inverse mapping $\hat{\theta}^{-1}$ these values are converted then to $\tilde{A}_k = \tilde{\gamma}_k + i\tilde{\delta}_k$ for $0 \leqslant k \leqslant 3$. Finally, these $\tilde{A}_k$ are scaled back to the scale of the original complex numbers A_k by $B^{-1} = 1$ for $0 \leqslant k \leqslant 3$.

References

1. Cozzens, J. H. and Finkelstein, L. A., "Computing the Discrete Fourier Transform Using Residue Number Systems in a Ring of Algebraic Integers," to be published in *IEEE Information Theory*.

2. Despain, A. M., Peterson, A. M., Rothaus, O. S., and Wold, E. "Fast Fourier Transform Processors Using Complex Residue Arithmetic," to appear in the *Journal of Parallel and Distributed Processing*.

3. Mead, C. and Conway, L., *Introduction to VLSI Systems*, Addison-Wesley Publishing Company, California, 1980, Chapter 8.

4. McCoy, N. H., *Rings and Ideas*, George Banta Company, Inc., Wisconsin, 1948.

5. Reed, I. S. and Truong, T. K., "Convolutions over Residue Classes of Quadratic Integers," *IEEE Trans. on Information Theory*, Vol. IT-22, No. 4, pp. 468-475, July 1976.

6. Leibowitz, L. M., "A Simplified Binary Arithmetic for the Fermat Number Transform," *IEEE Trans. on Acoustics, Speech, and Signal Processing*, Vol. ASSP-24, No. 5, pp. 356-359, October 1976.

7. Chang, J. J., Truong, T. K., Reed, I. S., Hsu, I. S., and Shao, M. H., "VLSI Design of a Single Chip for the Multiplication of Integers Modulo a Fermat Number," *Proceedings ICASS 85*, IEEE International Conference on Acoustics, Speech, and Signal Processing. Vol. 3, March 26-29, 1985, pp. 1388-1391.

8. Reed, I. S. and Truong, T. K. "Complex Integer Convolution over a Direct Sum of Galois Fields," *IEEE Trans. on Information Theory*, Vol. IT-21, No. 1, pp. 657-661, November 1975.

9. Niven, I. and Zuchkerman, H. S., *An Introduction to the Theory of Numbers*, John Wiley and Sons, Inc., New York, 1966.

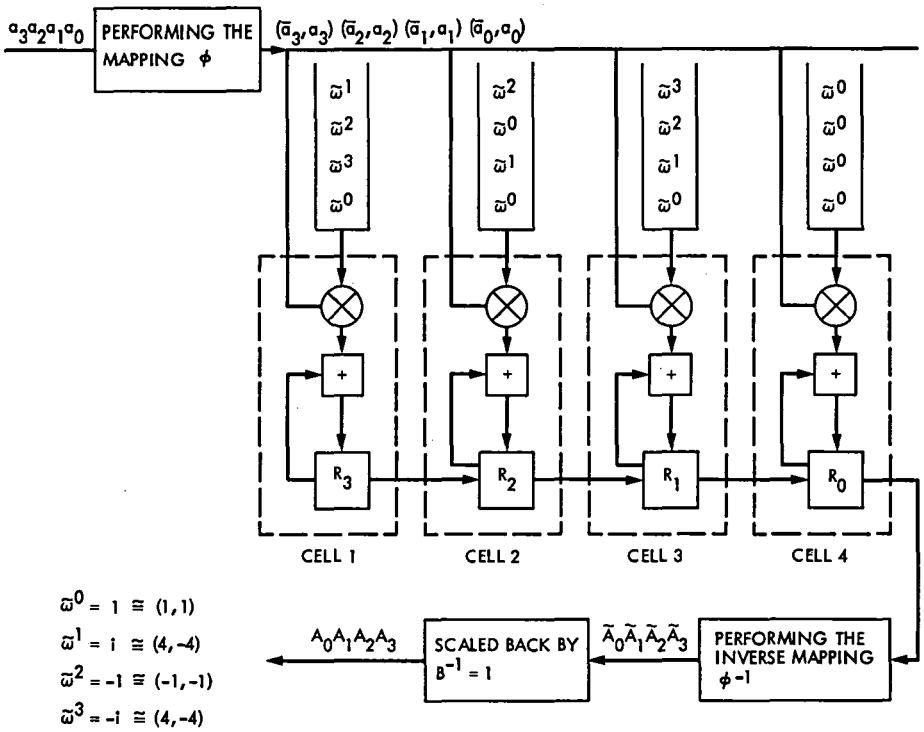

Fig. 1. The systolic array to compute a 4-point DFT over the direct sum of two copies of Z_{17}

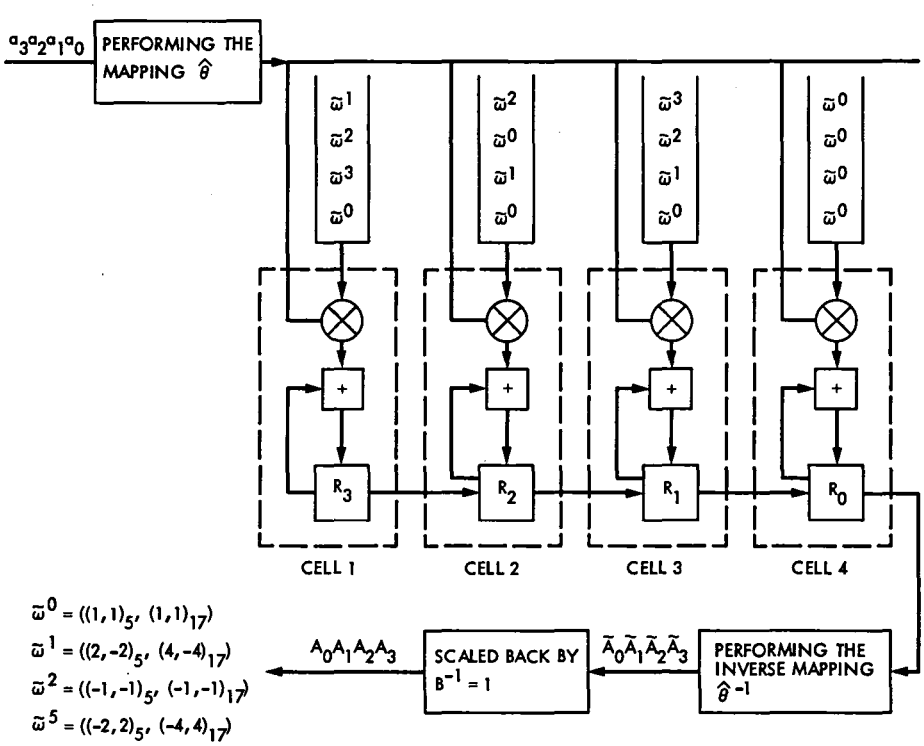

Fig. 2. The systolic array to compute a 4-point DFT over the direct sum of $Z_5[i]$ and $Z_{17}[i]$, where $Z_5[i]$ and $Z_{17}[i]$ are represented by two copies of Z_5 and Z_{17}, respectively

Appendix A

To show that M_n^{-1} in Eq. (7c) satisfies the congruence $M_n \cdot M_n^{-1} \equiv 1 \bmod F_n$ for $k \leqslant n \leqslant r$, consider first the case for $n = k$. Substituting M_k^{-1} in Eq. (7c) into $M_k \cdot M_k^{-1}$ yields

$$\begin{aligned} M_k \cdot M_k^{-1} &\equiv (2^{k+1}+1)(2^{2^{k+2}}+1)\ldots(2^{2^r}+1)\cdot 2^{-(r-k)} \\ &\equiv \underbrace{(2\cdot 2\ldots 2)}_{2^{r-k}}\cdot 2^{-(r-k)} \\ &\equiv 2^{r-k}\cdot 2^{-(r-k)} \equiv 1 \bmod 2^{2^k}+1 \end{aligned}$$

Next consider the case for $n = k + i + 1$, where $k + 1 \leqslant n \leqslant r$. Substituting M_n^{-1} in (7c) into $M_n \cdot M_n^{-1}$ yields the following:

$$\begin{aligned} M_n \cdot M_n^{-1} &\equiv (2^{2^k}+1)(2^{2^{k+1}}+k)\ldots(2^{2^{k+i}}+1)\cdot(2^{2^{k+i+2}}+1)\ldots(2^{2^r}+1)\cdot(-2)^{-1} \\ &\quad \times 2^{-(r-k+i+1))}\cdot(2^{2^k}-1) \\ &\equiv [(2^{2^k}-1)\cdot(2^{2^k}+1)\ldots(2^{2^{k+i}}+1)]\,(2^{2^{k+i+2}}+1)\ldots(2^{2^2}+1)\cdot(-2)^{-1} \\ &\quad \times 2^{-(r-(k+i+1))} \\ &\equiv (2^{k+i+1}-1)\cdot(2^{2^{k+i+2}}+1)\ldots(2^{2^r}+1)(-2)^{-1}\cdot 2^{-(r-(k+i+1))} \\ &\equiv (-2)\underbrace{(2\cdot 2\ldots 2)}_{2^{(r-(k+i+1))}}(-2)^{-1}\cdot 2^{-(r-(k+i+1))} \\ &\equiv (-2)\,2^{(r-k+i+1))}(-2)^{-1}\cdot 2^{-(r-(k+i+1))} \\ &\equiv 1 \bmod 2^{2^{k+i+1}} \quad \text{for } k+1 \leqslant n \leqslant r \end{aligned}$$

where $n = k + i + 1$.

Bit Error Rate of Coherent *M*-ary PSK

P. J. Lee
Communications Systems Research Section

The bit error rate (BER) for the coherent detection of M-ary PSK signals with Gray code bit mapping is considered. A closed-form expression for the exact BER of 8-ary PSK is presented. Tight upper and lower bounds on BER are also obtained for M-ary PSK with larger M.

I. Introduction

The symbol error rate (SER) for the coherent detection of M-ary PSK signals has been studied very extensively. However, except for the binary and quarternary PSK cases, there has not been much effort in finding the bit error rate (BER), which is a more useful performance measure in many cases. After a brief review of the background, we will derive expressions for the BER of M-ary PSK systems with Gray code bit mapping over an additive white Gaussian noise (AWGN) channel.

II. Preliminaries

Let X be the channel input symbol that takes its value from an M-ary alphabet $\{0, 1, \cdots, M-1\}$. In this study, the channel input alphabet size M is restricted to 2^k so that an M-ary symbol can be represented by k bits. When X is m for a given symbol time, the transmitter sends a sinusoidal signal with phase $2ma_k$, where $a_k = \pi/M$. Let E_b be the received signal energy per information bit and N_0 be the one-sided noise power spectral density of the AWGN. When the transmitted symbol is m, then, with ideal coherent detection, the probability density function of the received signal vector $\mathbf{y} = (y_c, y_s)$ is a two-dimensional Gaussian function, given by

$$p_{\mathbf{Y}}(\mathbf{y}) = f\{y_c - d_k \cos(2ma_k)\} \cdot f\{y_s - d_k \sin(2ma_k)\}$$

where $d_k = \sqrt{2kE_b/N_0}$ and $f(t) = \exp(-t^2/2)/\sqrt{2\pi}$. For the 8-ary case, such a symbol-to-signal space mapping is shown in Fig. 1. The optimum decision boundaries, which minimize the decision error probability (i.e., SER) with equiprobable input symbols, are also shown with dashed lines. The decision region for $X = m$ will be denoted by R_m.

When BER is the performance measure, the bit assignment for each M-ary symbol is important. The best bits-to-symbol mapping for M-ary PSK signals is the so-called Gray code mapping, with which the k bits corresponding to adjacent symbols differ in only one position. Such a mapping is shown in Table 1 for $k = 2, 3, 4$, and 5 (or $M = 4, 8, 16$, and 32). With Gray code bit mapping, the BER is independent of the transmitted symbols. Hence, without loss of generality, we will assume that 0 is the transmitted symbol. Notice that the decision regions that are optimum for SER also minimize the BER.

Let A_m be the probability that the received signal vector $\mathbf{y}$ falls into R_m when $X = 0$, i.e., $A_m = \Pr\{\mathbf{Y} \in R_m \mid X = 0\}$. Notice that, for any k, the following relation holds:

$$A_0 > A_1 = A_{M-1} > A_2 = A_{M-2} > \cdots > A_{M/2-1} = A_{M/2+1} > A_{M/2} \tag{1}$$

and these values can be found using one of the following equations:

$$A_m = \int_0^\infty f(z) \cdot \Big\{ Q\big[d_k + z \cdot \tan\big((M/2 - 2m - 1)\, a_k\big)\big] - Q\big[d_k + z \cdot \tan\big((M/2 - 2m + 1) a_k\big)\big] \Big\} \cdot dz,$$

$$m = 1, 2, \cdots, M/2 - 1 \qquad (2)$$

or

$$A_m = \begin{cases} \displaystyle\int_0^\infty f(z - d_k) \cdot \Big\{ Q\big[z \cdot \tan\big((2m - 1)\, a_k\big)\big] - Q\big[z \cdot \tan\big((2m + 1)\, a_k\big)\big] \Big\} \cdot dz, \\ m = 0, 1, \cdots, M/4 - 1 \\ \displaystyle\int_0^\infty f(z + d_k) \cdot \Big\{ Q\big[z \cdot \tan\big((M - 2m - 1)\, a_k\big)\big] - Q\big[z \cdot \tan\big((M - 2m + 1)\, a_k\big)\big] \Big\} \cdot dz, \\ m = M/4 + 1, \cdots, M/2 \end{cases} \qquad (3)$$

where

$$Q(z) \equiv \int_z^\infty f(t)\, dt$$

is the well known Q function, which is tabulated in many references or can easily be computed using simple algorithms.

The SER, P_s, is given by:

$$P_s = \sum_{m=1}^{M-1} A_m \qquad (4)$$

Note that for any k, SER can be represented as the sum of probabilities for two half-planes minus that for the overlapped area $R_{M/2}$:

$$P_s = \sum_{m=1}^{M/2} A_m + \sum_{m=M/2}^{M-1} A_m - A_{M/2} = 2 \cdot Q\big[d_k \sin(a_k)\big] - A_{M/2}$$

For $k = 1$, since $A_{M/2} = A_1$, $P_s = Q\big[d_1 \sin(a_1)\big]$. For $k = 2$, since $R_{M/2}$ is a quadrant, we have $A_{M/2} = Q^2\big[d_2 \sin(a_2)\big]$. For $k \geqslant 3$, the exact $A_{M/2}$ must be evaluated by Eq. (3) or similar expressions available in the literature. Also many bounds have been developed for $A_{M/2}$. See Ref. 1 for an example.

III. Bit Error Rate

Let w_m be the Hamming weight of the bits assigned to symbol m (see Table 1). Since the probability of bit error is w_m/k when $X = 0$ and $y \in R_m$, we have the following expression for average BER, P_b:

$$P_b = \frac{1}{k} \cdot \sum_{m=1}^{M-1} w_m A_m \qquad (5)$$

Since $w_m \geqslant 1$ for all $m \neq 0$, from Eqs. (5) and (4),

$$P_b \geqslant \frac{1}{k} \cdot \sum_{m=1}^{M-1} A_m = \frac{1}{k} \cdot P_s \qquad (6)$$

This "conventional" lower bound appears frequently in the literature (e.g., Ref. 2, p. 231) and is known to be very tight for large E_b/N_0, since, in such a case, most errors occur in adjacent regions. For $k = 1$ $(M = 2)$, $P_b = P_s = Q\big[d_1 \sin(a_1)\big]$. For $k = 2$ $(M = 4)$, since $A_3 = A_1$:

$$P_b = \{A_1 + 2A_2 + A_3\}/2 = A_1 + A_2 = Q\big[d_2 \sin(a_2)\big] \qquad (7)$$

Since $d_2 \sin(a_2) = d_1 \sin(a_1)$, BER for BPSK and QPSK are identical. This fact also has been noticed in the literature (e.g., Ref. 2, p. 234).

However, for larger k, there has been no effort toward finding the exact BER expression or its tight bounds. From Eq. (1), we have the following:

for $k = 3$ $(M = 8)$,

$$P_b = \left\{A_1 + 2A_2 + A_3 + 2A_4 + 3A_5 + 2A_6 + A_7\right\}/3$$

$$= (2/3) \cdot \left\{A_1 + A_2 + A_3 + A_4 + A_5 + A_6\right\}$$

$$= (2/3) \cdot \left\{Q\left[d_3 \sin\left(a_3\right)\right]\right.$$

$$\left. + Q\left[d_3 \sin\left(3a_3\right)\right] \cdot \left(1 - Q\left[d_3 \sin\left(a_3\right)\right]\right)\right\} \tag{8}$$

Hence, we have a closed-form expression for the exact BER of 8-ary PSK only in terms of the Q functions!

For $k = 4$ ($M = 16$),

$$P_b = (2/4) \cdot \left\{\sum_{m=1}^{8} A_m + \sum_{m=2}^{5} A_m + A_5 + 2A_6 + A_7\right\} \tag{9}$$

The probabilities for the half-plane and for the quadrant can be easily found in terms of the Q function. The exact values of the remaining terms can be found by Eq. (2) or Eq. (3). Or, instead, one may use the following upper and lower bounds:

$$\sum_{m=5}^{8} A_m < A_5 + 2A_6 + A_7 < \sum_{m=4}^{7} A_m \tag{10}$$

For $k = 5$ ($M = 32$),

$$P_b = (2/5) \cdot \left\{\sum_{m=1}^{16} A_m + \sum_{m=2}^{9} A_m + \sum_{m=5}^{12} A_m - \sum_{m=7}^{14} A_m\right.$$

$$+ \sum_{m=9}^{16} A_m + 2A_{10} + 2A_{11} + A_{12}$$

$$\left. + 2A_{13} + 2A_{14} - A_{16}\right\} \tag{11}$$

These summations can be found in terms of Q functions, while for the remaining terms one may use the following bounds:

$$\sum_{m=10}^{17} A_m < 2A_{10} + 2A_{11} + A_{12} + 2A_{13} + 2A_{14} - A_{16}$$

$$< \sum_{m=8}^{15} A_m \tag{12}$$

For M-ary PSK with larger M, we can also find very tight upper and lower bounds on BER. These will not be described here, except for the following simple lower bound on BER, which is much tighter than the conventional lower bound of Eq. (6): for $k \geqslant 4$,

$$P_b < (2/k) \cdot \left\{Q\left[d_k \sin\left(a_k\right)\right] + Q\left[d_k \sin\left(3a_k\right)\right]\right\} \tag{13}$$

The exact BER of M-ary PSK is shown in Table 2 for $M = 2$ to 64. Also the accuracy of the bounds on BER is tested in terms of the relative error (difference between the exact BER value and its bound, normalized to the exact value). Those relative errors are tabulated in Table 2, where we see that our bounds are extremely tight for all values of E_b/N_0 of interest.

IV. Conclusions and Discussion

For coherent M-ary PSK over an AWGN channel with Gray code bit mapping we can draw the following conclusions: (1) a general expression for BER is found; (2) a closed-form expression for the exact BER of 8-ary PSK is derived; (3) a lower bound on BER is found which is tighter than the conventional lower bound; (4) in particular, for 16- and 32-ary PSK, much tighter upper and lower bounds on BER are obtained.

The technique developed in this paper can also be used for finding the BER of M-ary PSK signals with either coherent or differentially coherent detection, as long as the noise is circularly symmetric. This was pointed out by Dr. Marvin K. Simon (Ref. 3) after reading the original manuscript of this paper. Using Eqs. (9) and (10) of Ref. 4, he derived the following simple integral expression for the exact BER of 8-ary DPSK over an AWGN channel.

$$P_b = (2/3)\left\{F\left(13a_3\right) - F\left(a_3\right)\right\}$$

where

$$F(\phi) = \frac{-\sin\phi}{4\pi} \int_{-\pi/2}^{\pi/2} \frac{e^{-d_3^2/2 \cdot (1 - \cos\phi \cdot \cos\theta)}}{1 - \cos\phi \cdot \cos\theta}\, d\theta$$

References

1. Chie, C. M., "Bounds and Approximations for Rapid Evaluation of Coherent MPSK Error Probabilities," *IEEE Trans. Commun.*, Vol. COM-33, pp. 271-273, March 1985.

2. Lindsey, W. C., and Simon, M. K., *Telecommunication Systems Engineering*, Prentice-Hall Inc., Englewood Cliffs, New Jersey, 1973.

3. Private communication from M. K. Simon of JPL, January, 1985.

4. Pawula, R. F., Rice, S. O., and Roberts, J. H., "Distribution of the Phase Angle Between Two Vectors Perturbed by Gaussian Noise," *IEEE Trans. Commun.*, Vol. COM-30, pp. 1828-1841, August 1982.

Table 1. Gray bit mapping and Hamming weight *W*

m	bits	W_m	m	bits	W_m
$k = 2$ ($M = 4$)			$k = 5$ ($M = 32$)		
0	0 0	0	0	0 0 0 0 0	0
1	0 1	1	1	0 0 0 0 1	1
2	1 1	2	2	0 0 0 1 1	2
3	1 0	1	3	0 0 0 1 0	1
			4	0 0 1 1 0	2
$k = 3$ ($M = 8$)			5	0 0 1 1 1	3
0	0 0 0	0	6	0 0 1 0 1	2
1	0 0 1	1	7	0 0 1 0 0	1
2	0 1 1	2	8	0 1 1 0 0	2
3	0 1 0	1	9	0 1 1 0 1	3
4	1 1 0	2	10	0 1 1 1 1	4
5	1 1 1	3	11	0 1 1 1 0	3
6	1 0 1	2	12	0 1 0 1 0	2
7	1 0 0	1	13	0 1 0 1 1	3
			14	0 1 0 0 1	2
$k = 4$ ($M = 16$)			15	0 1 0 0 0	1
0	0 0 0 0	0	16	1 1 0 0 0	2
1	0 0 0 1	1	17	1 1 0 0 1	3
2	0 0 1 1	2	18	1 1 0 1 1	4
3	0 0 1 0	1	19	1 1 0 1 0	3
4	0 1 1 0	2	20	1 1 1 1 0	4
5	0 1 1 1	3	21	1 1 1 1 1	5
6	0 1 0 1	2	22	1 1 1 0 1	4
7	0 1 0 0	1	23	1 1 1 0 0	3
8	1 1 0 0	2	24	1 0 1 0 0	2
9	1 1 0 1	3	25	1 0 1 0 1	3
10	1 1 1 1	4	26	1 0 1 1 1	4
11	1 1 1 0	3	27	1 0 1 1 0	3
12	1 0 1 0	2	28	1 0 0 1 0	2
13	1 0 1 1	3	29	1 0 0 1 1	3
14	1 0 0 1	2	30	1 0 0 0 1	2
15	1 0 0 0	1	31	1 0 0 0 0	1

Table 2. Exact BER values of *M*-ary PSK with Gray mapping

E_b/N_0, dB	P_b (M = 2,4)	P_b (M = 8)	P_b (M = 16)	P_b (M = 32)	P_b (M = 64)
−5.0	2.132E-01	2.468E-01	2.867E-01	3.185E-01	3.376E-01
−4.0	1.861E-01	2.217E-01	2.646E-01	3.003E-01	3.242E-01
−3.0	1.584E-01	1.961E-01	2.420E-01	2.817E-01	3.099E-01
−2.0	1.306E-01	1.708E-01	2.191E-01	2.629E-01	2.951E-01
−1.0	1.038E-01	1.461E-01	1.965E-01	2.442E-01	2.800E-01
0.0	7.865E-02	1.227E-01	1.745E-01	2.256E-01	2.649E-01
1.0	5.628E-02	1.008E-01	1.535E-01	2.073E-01	2.497E-01
2.0	3.751E-02	8.061E-02	1.338E-01	1.892E-01	2.345E-01
3.0	2.288E-02	6.225E-02	1.155E-01	1.714E-01	2.194E-01
4.0	1.250E-02	4.589E-02	9.865E-02	1.538E-01	2.043E-01
5.0	5.954E-03	3.186E-02	8.292E-02	1.368E-01	1.895E-01
6.0	2.388E-03	2.048E-02	6.816E-02	1.207E-01	1.747E-01
7.0	7.727E-04	1.195E-02	5.429E-02	1.055E-01	1.599E-01
8.0	1.909E-04	6.181E-03	4.145E-02	9.147E-02	1.452E-01
9.0	3.363E-05	2.748E-03	2.998E-02	7.840E-02	1.307E-01
10.0	3.872E-06	1.011E-03	2.025E-02	6.614E-02	1.165E-01
11.0	2.613E-07	2.937E-04	1.256E-02	5.451E-02	1.030E-01
12.0	9.006E-09	6.338E-05	7.010E-03	4.349E-02	9.027E-02
13.0		9.417E-06	3.427E-03	3.325E-02	7.848E-02
14.0		8.756E-07	1.421E-03	2.406E-02	6.752E-02
15.0		4.516E-08	4.789E-04	1.627E-02	5.724E-02
16.0			1.246E-04	1.010E-02	4.747E-02
17.0			2.342E-05	5.642E-03	3.819E-02
18.0			2.925E-06	2.763E-03	2.950E-02
19.0			2.187E-07	1.147E-03	2.163E-02
20.0			8.573E-09	3.876E-04	1.486E-02
21.0				1.011E-04	9.417E-03
22.0				1.907E-05	5.394E-03
23.0				2.393E-06	2.725E-03
24.0				1.799E-07	1.177E-03
25.0				7.099E-09	4.176E-04
26.0					1.159E-04
27.0					2.361E-05
28.0					3.264E-06

Table 3. Accuracy of the upper and lower bounds on BER

	Relative error of the bound on BER found from:				
E_b/N_0, dB	(6), Lower	(13), Lower	(10), Lower	(10), Upper	: (M = 16)
−3.0	2.82E-01	6.16E-03	1.53E-03	1.40E-02	
0.0	1.67E-01	9.66E-04	2.15E-04	3.11E-03	
3.0	5.72E-02	2.05E-05	4.06E-06	1.05E-04	
6.0	6.30E-03	8.44E-09	1.48E-09	8.17E-08	
9.0	7.90E-05	1.58E-15	2.48E-16	3.90E-14	
E_b/N_0, dB	(6), Lower	(13), Lower	(12), Lower	(12), Upper	: (M = 32)
−3.0	4.13E-01	4.70E-02	1.65E-03	3.25E-03	
0.0	3.29E-01	1.15E-02	1.32E-04	3.83E-04	
3.0	2.28E-01	6.30E-04	8.37E-07	3.84E-06	
6.0	1.11E-01	1.78E-06	3.68E-11	2.89E-10	
9.0	2.47E-02	1.43E-11	8.28E-20	1.25E-18	

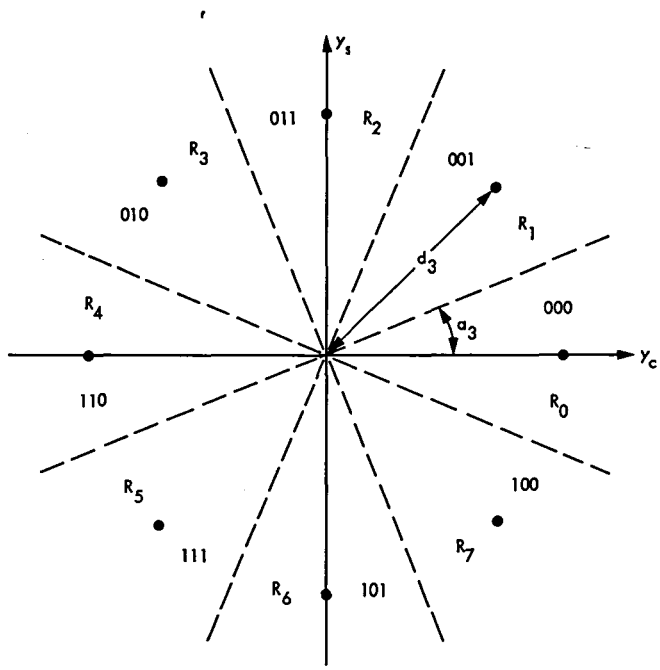

Fig. 1. 8-ary PSK signal space with optimum decision regions

Synchronizing Heavily Encoded Data in Bad Weather

L. Swanson
Communications Systems Research Section

Deep space missions choose a data rate to ensure reliable communication under most conditions. Certain critical data can be more heavily encoded, to be decoded under particularly bad atmospheric conditions. This article shows that, in such a system, finding and synchronizing critical data will not be a problem.

I. Introduction

Deep space missions choose a data rate so that data will be received reliably under most conditions. Under certain atmospheric conditions, however, performance is degraded. Further decreases in the data rate make this less likely, at the cost of less information under most conditions.

In order to increase the probability that certain "critical" data are received reliably, such data can be more heavily encoded. Earlier work (Ref. 1) argued for a very simple system: put critical data into separate frames and, after the usual channel encoding, repeat symbols in those frames. (The number of repetitions would depend on the amount of attenuation.) On the ground, during bad weather, the other data might be useless but the critical data could be decoded.

The analysis in Ref. 1 ignores problems of synchronization: can we find the critical data to decode it? The purpose of this article is to show that, if the symbol synchronizer assembly (SSA) is not losing lock, critical data can be found and synchronized.

II. Analysis

We are assuming a system in which critical data bits are repeated (in whole frames) enough times to make up for possible weather attenuation, and we want to know whether the critical frames can be found and synchronized. We are further assuming that the SSA is not losing lock, and that we will be free to design a frame synchronizer to whatever standards are necessary.

Since the repetitions apply to the frame synchronization marker, we can think of this as a problem of whether the (repeated) marker can be found in a very long frame: the critical frame followed by a lot of noncritical frames. Since the repetition code serves exactly to bring the signal-to-noise ratio (SNR) back after the attenuation, the SNR is not a factor in the answer. The amount of critical data is, however, a factor since it determines the number of non-critical frames between critical frames, and their frame synchronization markers.

Of course, with long enough buffers, one can always find and synchronize data which are different from other data. The question is whether it can be done in a reasonable length of time. The calculations described below show that, under reasonable circumstances, a very simple system declaring synchronization after six critical frames will fail to declare synchronization less often than once in 10^6 and will declare synchronization incorrectly less than one time in 10^8.

We are assuming that all data are (7, 1/2) convolutionally encoded. Consider the following parameters, chosen because they are plausible: Suppose that critical data symbols go into

the SSA at -4.3 dB (symbol SNR). This means that critical data are attenuated 3 dB from the requirement for the bit-error rate 10^{-5} for concatenated coding. (E_b/N_0 is 2.3 dB; subtracting 3.6 dB for concatenated coding overhead and 3 dB for attenuation gives -4.3 dB.) Also suppose that frames are 10,000 bits long and one in every 50 frames is made up of critical data. Assume that each frame begins with a 32-bit synchronization marker, and every symbol corresponding to a critical frame has been repeated once. This would mean that frames of critical data begin with a 104-symbol ($104 = 2 \cdot 2 \cdot (32\text{-}6)$) pattern. (Six bits are needed to flush the encoder. This leaves 26 bits in the marker. Rate 1/2 convolution coding and the repetition make this into a 104-symbol marker.) Finally, assume that 3-bit quantized symbols leave the SSA and go into a long buffer, from which strings of 104 symbols are compared to the pattern which announces the beginning of critical data. What is the likelihood that a simple algorithm could pick out the critical data within 6 critical data frames?

Several simplifying assumptions have been made: that convolutionally encoded random data look like random data, that the sum of 104 independent random variables is Gaussian, and that overlaps between the marker and itself, whether repeated or not, look random. We also assume a very simple algorithm for finding the critical data: at each place, 3-bit quantized symbols leaving the SSA are compared to the marker. They are assigned "disagreement levels" of 0, 1, 2, 3, or 4, depending on whether and how much they disagree with each marker symbol. A threshold and a required number of threshold crossings are set. The 104 disagreements are summed and compared as a possible beginning, until six frames of critical data ($6 \cdot 50$ frames of total data) have been checked. At this time, the place at which the threshold has been reached most often is declared the critical data marker, assuming that threshold has been crossed at that place at least the fixed number of times.

This calculation gave a probability smaller than 10^{-6} of failure to declare synchronization after six critical frames, and smaller than 10^{-8} of incorrect declaration of synchronization. In a system with more critical data, there are fewer non-critical frames between critical frames, and synchronization is faster; less critical data would make synchronization slightly more difficult.

Of course, if this system were really being used, a comparison could be made to a more efficient set of counter increments (Ref. 2), or to a system more complicated than a simple crossing of threshold, and comparisons could be made for different sizes of buffers. The point of this calculation is that finding and synchronizing critical data will not be a problem. Further questions seem more appropriate to a time when such a scheme is being considered.

III. Conclusions

We have shown that, under reasonable circumstances, synchronization will not be a problem in a system which repeats frames of critical data to make up for possible attenuation from atmospheric conditions.

References

1. Swanson, L., and J. H. Yuen, "A Strategy for Successful Deep Space Information Transmission in Bad Weather," *TDA Progress Report 42-78*, Jet Propulsion Laboratory, Pasadena, California, August 15, 1984, pp. 143-151.
2. Swanson, L., *A Comparison of Frame Synchronization Methods*, JPL Publication 82-100, Jet Propulsion Laboratory, Pasadena, California, December 15, 1982.

A Software Simulation Study of a Sequential Decoder Using the Fano Algorithm

F. Pollara
Communications Systems Research Section

A set of subroutines has been developed to simulate the performance of a sequential decoder based on the Fano algorithm. This simulation can be used to verify the coding performance of the ICE communication link. The probability of frame deletion can be measured as a function of the number of computations allowed per frame and of E_b/N_o. Both hard and soft quantized inputs are considered.

I. Introduction

While many deep space missions use short constraint length convolutional codes, which can be decoded by the Viterbi algorithm, some missions use long constraint length codes. These codes are efficiently decoded by sequential methods.

ICE (International Cometary Explorer) is an example of a mission using a long constraint length (K = 24) code. The work described in this article was motivated by the need to verify the coding performance of the ICE communication link. The specific convolutional encoder (K = 24, rate = 1/2) used in this mission is shown in Fig. 1. The frame length can be varied, but is typically set at 1,024 bits, including a fixed tail pattern of 24 bits. The sequential decoder is based on the Fano Algorithm (Ref. 1), which is reviewed in Appendix A.

II. The Simulation

In order to carry out this simulation, a set of C-language subroutines was written, representing the operation of a coded communication link as shown in the block diagram of Fig. 2, where each block corresponds to a subroutine. A program called "universe" controls the execution of each subroutine and defines the topology of their interconnections. The subroutine "generator" produces sequences of binary random data in blocks of 1,000 bits, plus a fixed tail sequence of 24 bits, which is appended at the end of each block. The subroutine "coder" implements a convolutional encoder as shown in Fig. 1. Then Gaussian noise generated by "gauss" is added to the link by the subroutine "add" in order to simulate a given E_b/N_o. The sequential decoding takes place in the subroutine "seq," which also provides quick-look decoded data; this data is useful in replacing

frames that would otherwise be deleted. The heart of the decoder is a shift register which also contains a replica of the encoder. High speed is achieved by using a pointer to the contents of this register to avoid time consuming read/write operations. Finally, the error statistics are displayed by the subroutine "error."

III. Performance Results and Discussion

Two versions of the sequential decoder subroutine "seq" have been developed, for hard and soft quantized (3-bit) inputs. Each performance measure depends on the following parameters: E_b/N_o, frame and tail length, the increment Δ used to update the running threshold in the Fano algorithm, the maximum number of computations C allowed for each frame, and, for soft decoding, the particular metric used. The number of computations is defined as the total number of forward moves per frame. A frame is deleted when it cannot be decoded in C or fewer computations.

Figure 3 shows the performance of the hard-quantized decoder in terms of probability of frame deletion P_{FD} versus E_b/N_o, for some values of C and metric ratio MR, which is the ratio of metric increments assigned to symbol agreements and disagreements (Ref. 2). Figure 4 shows the performance for the soft-quantized decoder.

The performance results obtained by this software simulation can be compared to those of a hardware decoder only if the speed advantage is the same in both cases. Specifically, the number of forward moves is not equivalent to the number of computations per second in the hardware decoder. Furthermore, the presence of a buffer for frames in the hardware version tends to improve the performance at higher E_b/N_o, as shown in Fig. 4, where $\overline{C}$ is the maximum number of computations allowed to decode the 3 frames in the buffer.

Figure 5 shows P_{FD} vs the maximum number of computations per frame C, for hard and soft-quantized inputs, respectively.

Acknowledgment

The author wishes to thank George Pitt for the generation of numerical results.

References

1. Blahut, R. E., *Theory and Practice of Error Control Codes*, Addison-Wesley, 1983.
2. Clark, G. C. and Cain, J. B., *Error-Correcting Coding for Digital Communications*, Plenum, 1982.

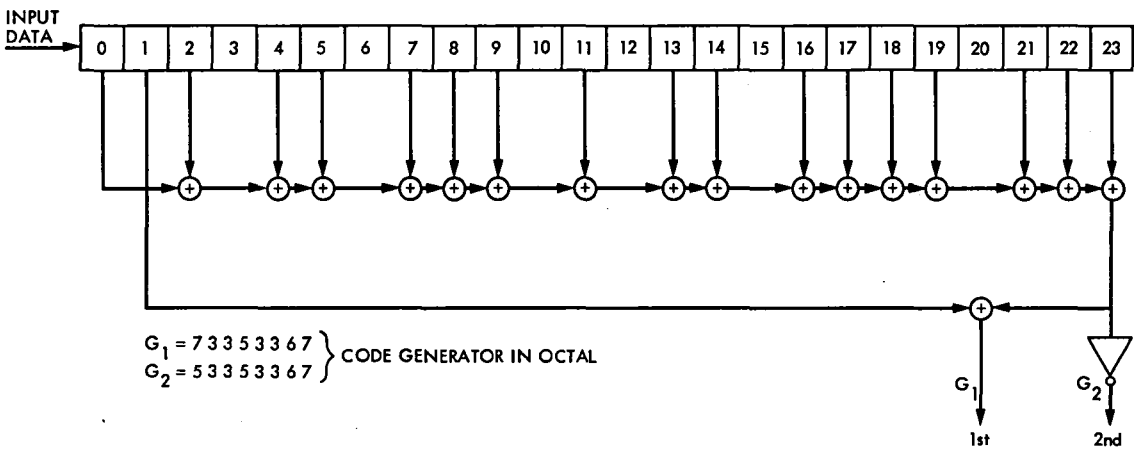

Fig. 1. ICE convolutional encoder (K = 24)

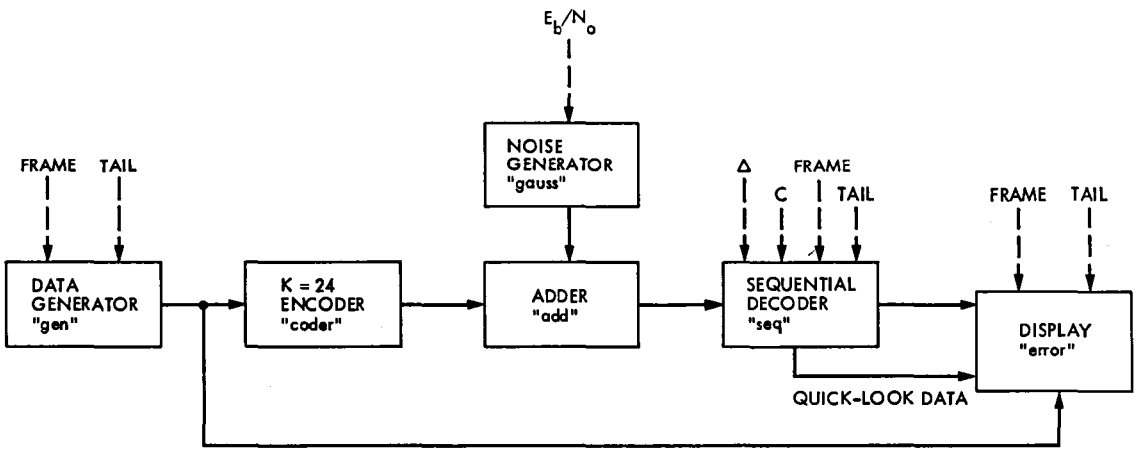

Fig. 2. Sequential decoder simulation block diagram

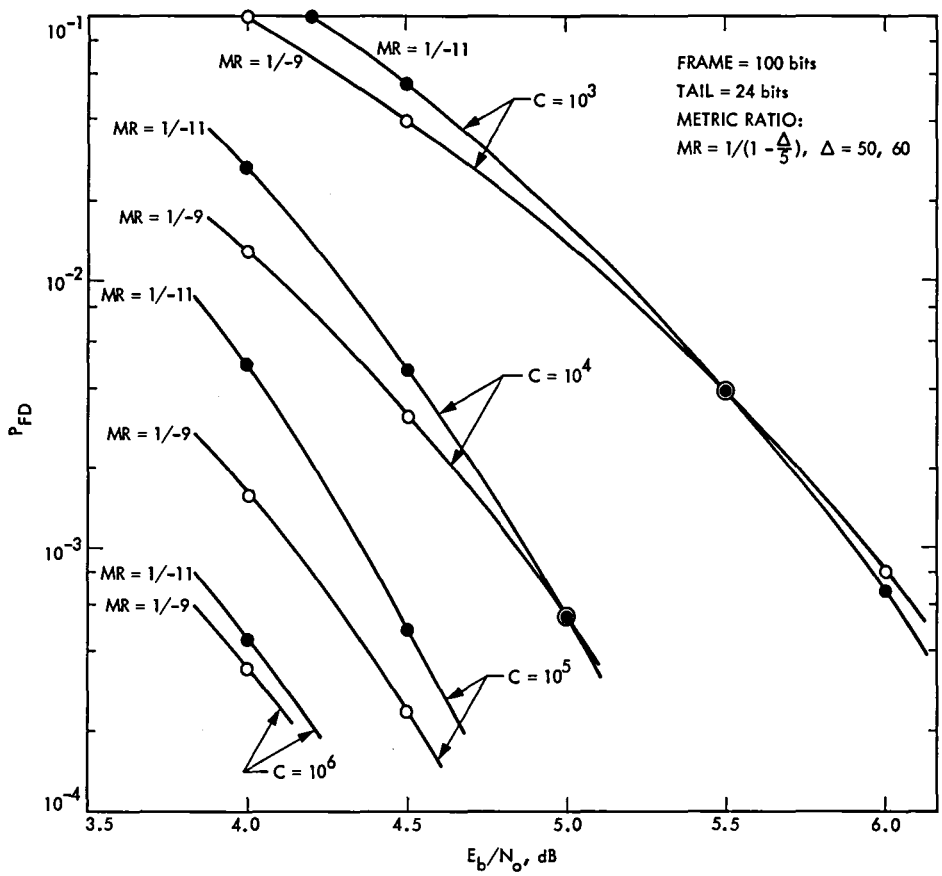

Fig. 3. P_{FD} vs E_b/N_o for hard-quantized decoder

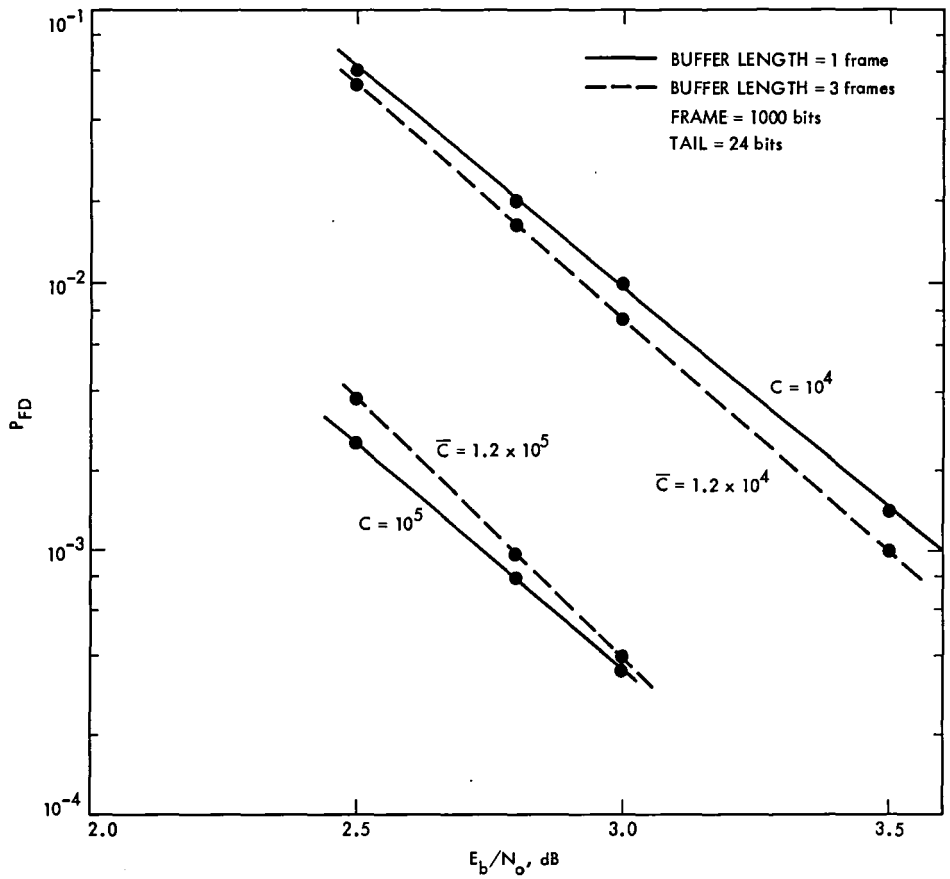

Fig. 4. P_{FD} vs E_b/N_o for soft-quantized decoder (Δ = 256)

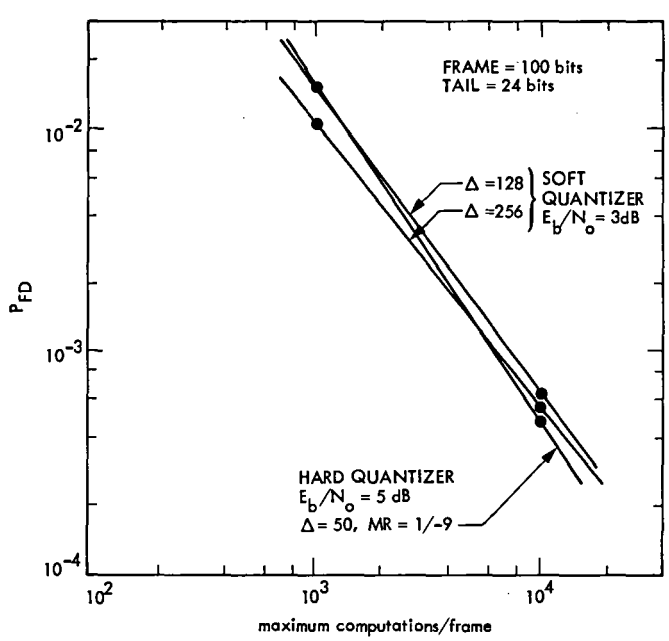

Fig. 5. P_{FD} vs maximum computations per frame

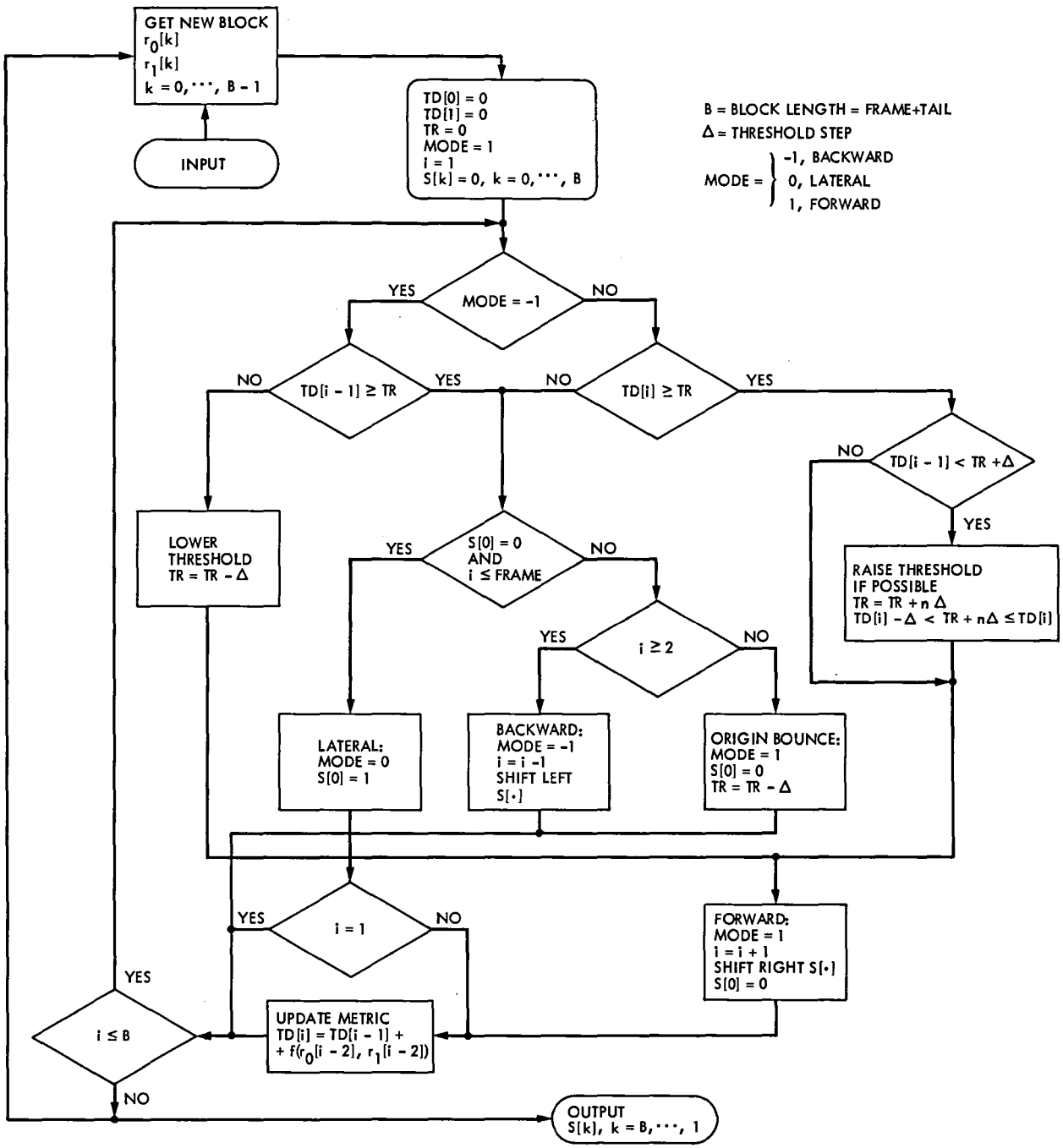

Fig. 6. Sequential decoder flow diagram (hard quantizer)

Appendix A

A brief summary of the Fano algorithm in the form used in this simulation is given for completeness.

Consider the decoding of a frame consisting of FRAME information bits plus TAIL bits in the tail. The task of the decoder is to find the path on a binary tree of length FRAME+TAIL which is the closest approximation to the transmitted frame, according to a given measure criterion (metric). At each node on the tree, the decoder looks forward and attempts a move along the branch corresponding to a "0" information bit. If a "1" was transmitted at that level, the decoder will realize that it is on a wrong path and make a lateral move, which is equivalent to changing the previous attempt into a forward move along the "1" branch. This is the typical behavior of the decoder in the absence of noise.

If there are errors in the received sequence, the decoder will perceive that it is following a wrong path, according to the rules for search described below. Then it will back up a few branches and explore alternative paths, until it finds a satisfactory path of length FRAME+TAIL. At this point the first FRAME bits in the path are taken as the decoded frame sequence. They may still contain errors, even though this kind of error (decoded bit errors) is extremely rare.

If, for some frame, the decoder is forced to move erratically back and forth on the tree up to a certain imposed limit on the number of forward moves, that frame will not be decoded (deleted).

Consider the flow diagram in Fig. 6. The "tilted distance" TD[•] is a function of the distance between the received symbol and the current path through the tree. At high E_b/N_o, TD[•] is an increasing function, and the decoder moves forward (or laterally) on the tree. The decoder decides that TD[•] is increasing or decreasing by comparing it with a "running threshold" TR which is kept as large as possible, but smaller than TD[•], and changes in steps of size Δ. If TD[•] starts to decrease, the decoder will back up and then explore other paths, or even come back to the same node, but with more confidence to get past it (i.e., with a lower TR). Therefore, the decoder will never reach the same node twice with the same threshold, thus preventing infinite loops.

Symbol Stream Combining in a Convolutionally Coded System

R. J. McEliece[1], F. Pollara, and L. Swanson
Communications Systems Research Section

Symbol stream combining has been proposed as a method for arraying signals received at different antennas. If convolutional coding and Viterbi decoding are used, it is shown that a Viterbi decoder based on the proposed weighted sum of symbol streams yields maximum likelihood decisions.

I. Introduction

The use of symbol stream combining has been proposed for decoding data from deep space missions when the received signal is very weak. Under this scheme, a signal is received at two or more antennas, and each antenna's output is processed separately through carrier and subcarrier demodulation and symbol synchronization. Then the two digital copies (of the same signal plus different noise) are combined before decoding.

In Ref. 1, this system was studied and found to be superior to baseband combining. The analysis of Ref. 1 determines the optimal weights for adding the outputs of the two symbol synchronizer assemblies (SSAs) before sending the signals to the Viterbi decoder.

The fact that symbol stream combining is superior to baseband combining follows from timing uncertainties (Ref. 1). But why symbol stream combining? Could a maximum-likelihood decision be made on the pair of symbol streams to yield better performance than using the Viterbi (maximum-likelihood) decoder on a weighted sum of the symbol streams? This article shows that symbol stream combining followed by

[1] Also Electrical Engineering Department, California Institute of Technology.

Viterbi decoding is in fact maximum-likelihood decoding for a pair of symbol streams.

II. Symbol Stream Combining

The digital coding system for a deep space mission can be modeled as shown in Fig. 1 where the output of the convolutional encoder is a stream of bipolar symbols $x_k \epsilon \{-V, V\}$, and the output of the SSA is a stream of real numbers x_k,

$$\hat{x}_k = Ax_k + n_k$$

where $n_1, n_2, \ldots$ are the values of independent, Gaussian, mean zero, variance $N_0/2$ random variables, and A is a positive constant. The Viterbi decoder then makes a maximum-likelihood decision about the symbols $x_1, x_2, \ldots$, and therefore about the data bits, producing the decoded data bits.

Under symbol stream combining, two different symbol synchronizers produce two different output streams:

$$\hat{x}_k = A\,x_k + n_k \tag{1}$$

and

$$\hat{y}_k = \bar{A}\,x_k + \bar{n}_k \tag{2}$$

where $n_1, n_2, \ldots$ and $\bar{n}_1, \bar{n}_2, \ldots$ are samples of two independent stochastic processes, each independent, mean zero, identically distributed, and Gaussian, with variances $N_0/2$ and $\bar{N}_0/2$ respectively, and where A and $\bar{A}$ are positive constants.

As described in Ref. 1, the symbol stream combiner will fit into the system between the two SSAs and one Viterbi decoder, combining the streams $\hat{x}_1, \hat{x}_2, \ldots$ and $\hat{y}_1, \hat{y}_2, \ldots$ to yield one stream

$$z_k = \alpha\,\hat{x}_k + \beta\,\hat{y}_k \tag{3}$$

which is sent to the Viterbi decoder, where α and β are "weighting constants" chosen by the symbol stream combiner to maximize the signal-to-noise ratio $(\alpha A + \beta\bar{A})^2\, x_k^2/(\alpha^2 N_0 + \beta^2\bar{N}_0)$ of the combined stream. The ratio of α to β which maximizes signal-to-noise ratio of the combined stream depends on the signal power and noise power of the two streams,

$$\frac{\alpha}{\beta} = \frac{A/N_0}{\bar{A}/\bar{N}_0}$$

Ways to measure the signal-to-noise ratios of the streams, and to determine the weighting constants, are discussed in Refs. 1, 2, and 3.

In this article, we consider whether better use can be made of the two symbol streams than combining them linearly as in Eq. (3). We find that in fact a Viterbi decoder acting on the stream (Eq. [3]) will perform identically to a maximum-likelihood decoder acting on the two streams (Eqs. [1] and [2]) (assuming perfect knowledge of signal and noise power in both cases). We are ignoring quantization, which of course causes some degradation; we assume that the SSAs produce enough quantization levels that this is not a problem.

III. Maximum Likelihood Decoding

After the two symbol synchronizer assemblies, the information available for maximum-likelihood decoding is

$$\hat{x}_k = A\,x_k + n_k$$

and

$$\hat{y}_k = \bar{A}\,x_k + \bar{n}_k$$

In fact, assuming that x_k was sent, this pair $(\hat{x}_k, \hat{y}_k)$ appears with probability density

$$\frac{1}{2\pi\sqrt{N_0\,\bar{N}_0}} \exp\left[-(\hat{x}_k - A\,x_k)^2/2N_0\right]$$

$$\times \exp\left[-(\hat{y}_k - \bar{A}\,x_k)^2/2\bar{N}_0\right]$$

Given that the stream $\{x_1, x_2, \ldots\}$ was sent, the pair of streams $\{\hat{x}_1, \hat{x}_2, \ldots\}$ and $\{\hat{y}_1, \hat{y}_2, \ldots\}$ will be received with probability density

$$K \exp\left\{-\sum_k \left[(\hat{x}_k - A\,x_k)^2/2N_0 + (\hat{y}_k - \bar{A}\,x_k)^2/2\bar{N}_0\right]\right\} \tag{4}$$

where K is a constant.

Thus, a maximum-likelihood decoder acting on the pair of streams $\{\hat{x}_1, \hat{x}_2, \ldots\}$ and $\{\hat{y}_1, \hat{y}_2, \ldots\}$ will find the stream $\{x_1, x_2, \ldots\}$ which maximizes the probability density in Eq. (4) or, equivalently, which maximizes

$$\sum_k \left(\frac{A}{N_0}\,\hat{x}_k x_k + \frac{\bar{A}}{\bar{N}_0}\,\hat{y}_k x_k\right)$$

Now, if instead, we have a maximum likelihood decoder acting on the stream

$$z_k = \frac{A}{N_0}\hat{x}_k + \frac{\bar{A}}{\bar{N}_0}\hat{y}_k$$

it will maximize

$$K \exp\left\{\frac{-\sum_k \left(z_k - \left(\frac{A^2}{N_0} + \frac{\bar{A}^2}{N_0}\right) x_k\right)^2}{2\left(\frac{A^2}{N_0} + \frac{\bar{A}^2}{N_0}\right)}\right\}$$

which is equivalent to maximizing

$$\sum_k z_k x_k = \sum_k \left(\frac{A}{N_0}\hat{x}_k + \frac{\bar{A}}{\bar{N}_0}\hat{y}_k\right) x_k$$

Thus the two schemes, maximum-likelihood decoding on the pair of streams and Viterbi decoding on the combined stream, will produce identical results.

IV. Determining Signal and Noise Power

In the Deep Space Network, signal and noise power are estimated by the symbol synchronizer assembly, so this information would be available to a symbol stream combiner. If another estimate were desirable, a feed-back system could involve estimates based either on the Viterbi decoder metrics or on channel symbol errors.

References

1. Divsalar, D., "Symbol Stream Combining Versus Baseband Combining for Telemetry Arraying," *TDA Progress Report 42-74* (August 1983), pp. 13-28, Jet Propulsion Laboratory, Pasadena, California.
2. Vo, Q. D., "Signal-to-Noise Ratio and Combiner Weight Estimation for Symbol Stream Combining," *TDA Progress Report 42-76* (February 1984), pp. 86-98, Jet Propulsion Laboratory, Pasadena, California.
3. Lesh, J. R., "Accuracy of the Signal to Noise Ratio Estimator," *JPL TR 32-1526*, vol. X, August 15, 1972, pp. 217-235, Jet Propulsion Laboratory, Pasadena, California.

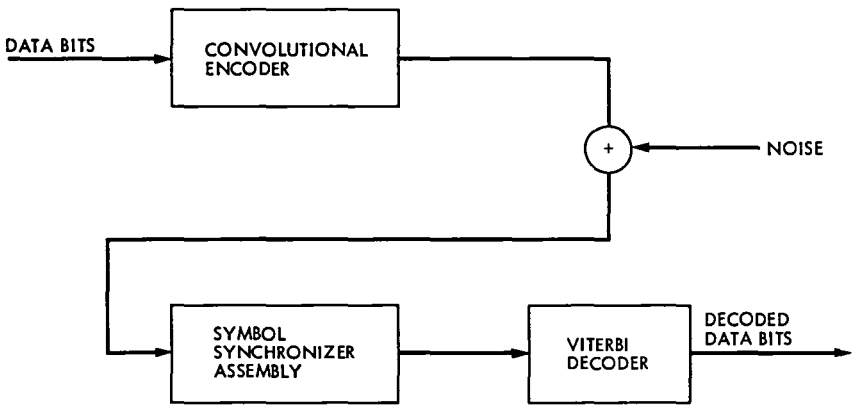

Fig. 1. Digital coding system for a deep space mission

An Integrated UNIX-Based CAD System for the Design and Testing of Custom VLSI Chips

L. J. Deutsch
Communications Systems Research Section

This article describes a computer-aided design (CAD) system that is being used at the Jet Propulsion Laboratory for the design of custom and semicustom very large scale integrated (VLSI) chips. The system consists of a Digital Equipment Corporation VAX computer with the UNIX operating system and a collection of software tools for the layout, simulation, and verification of microcircuits. Most of these tools were written by the academic community and are, therefore, available to JPL at little or no cost. Some small pieces of software have been written in-house in order to make all the tools interact with each other with a minimal amount of effort on the part of the designer.

I. Introduction

The design of VLSI chips would be impractical without the use of CAD tools. This is because the typical VLSI chip that is designed at JPL currently comprises at least 5,000 transistors and in some cases this number is as large as 50,000. In addition to this, each of the six to ten mask layers that correspond to steps in the fabrication process must be defined for these chips. In order to facilitate the design of VLSI chips on a computer, a standard file format for the description of these mask layers was developed at the California Institute of Technology. This description is called the "Caltech intermediate form" (CIF) (Ref. 1). Many chip fabricators will now accept a computer file in CIF format and implement the design on a silicon wafer. In fact, CIF has recently become an industrial standard as well as a university standard for chip description.

The primary purpose of a VLSI CAD system is to allow a designer to specify a chip in some convenient fashion and to produce a file in CIF format that may be sent to a fabrication service. The process of defining the CIF file is called "layout." In addition to layout, there are secondary functions that a good CAD system should perform. One of these is design verification. This consists of an automated check, performed on the chip description, against a set of rules that are fabrication-dependent. These rules might include both "design rules" and "electrical rules." Design rules refer to geometrical constraints on the masks themselves and arise from tolerances and material limitations in the fabrication process. Electrical rules refer to the interconnection of transistors. One example of an electrical rule would be a limitation on device fan-out.

A good CAD system should also contain simulators that allow the designer to "run" a chip in software and hence verify that it performs the desired function. Simulators can take many different forms from low-level programs that model only the digital switching of a transistor, to high-level programs that use very complex models of the transistors. Since the execution time of a simulator depends on its level, several different levels of simulation should be present on the CAD system.

Tools should also be present that allow the same tests that are performed on the chip design with the simulators to be

used on the finished chip itself. This involves a hardware interface from the CAD system computer to a chip testing device.

In addition to the above tools, a complete system will include programs for creating commonly-used subcircuits with a minimum amount of effort. Such subcircuits might include input and output pad drivers, programmable logic arrays, read-only memory (ROM), and simple logic gates.

Much CAD tool development has already been done by universities in support of their own VLSI designer training efforts. This software development is sponsored in part by the Defense Advanced Research Program Agency (DARPA). DARPA also supports the MOSIS (Ref. 2) chip fabrication service that is run by the Information Sciences Institute of the University of Southern California. Because of JPL's standing as a research facility and its involvement with certain DARPA contracts, the university tools and MOSIS fabrication are available to users here at no cost. The CAD tools are written to run on Digital Equipment Corporation VAX computers with the UNIX (Ref. 3) operating system.

A CAD system has been assembled using these university tools as part of the DSN Advanced Systems Program. A VAX 11/750 computer was purchased along with an inexpensive binary license for UNIX (A binary UNIX contains no source code and hence no ability to modify system software). Software was obtained from many sources including Caltech, MIT, the University of California at Berkeley (UC Berkeley), Carnegie-Melon University, and the University of Washington. Some additional pieces of software were written in-house so that the various tools can communicate with each other. This CAD system is used to support both the design of custom and semicustom chips and for the evaluation of new CAD tools as they become available. Some of the chips that have been designed on this system include a multicode convolutional encoder (Ref. 4), a Reed-Solomon encoder (Ref. 5), a syndrome generator for a Reed-Solomon decoder (Ref. 6), a Fermat number multiplier (Ref. 7), and a Massey-Omura multiplier (Ref. 8).

In the following sections, the various software tools in the system will be examined in more detail. They will be grouped according to their function. An overall block diagram of the software CAD system is shown in Fig. 1. Several file formats are used to represent data on the system. One is the CIF format mentioned above. In UNIX, the format of the file is indicated in its name as a string of characters at the end of the name preceded by a period. Hence the computer file "file.cif" would be in CIF format. Other formats used on the system include ".ca" or "caesar format" for a layout graphics file and ".sim" for a file containing wirelist data. These conventions will be used in the remainder of this article.

II. Layout

The primary layout tool on the CAD system is a program called "caesar" (Ref. 9). It was written at the University of California at Berkeley. Caesar requires the use of two computer terminals. One terminal may be one of a variety of high resolution (at least 512 X 512 pixels) color terminals. An Advanced Electronics Design AED-512 terminal is used on this CAD system. The second terminal is a regular CRT-type such as the DEC VT100. In addition to the terminals, caesar may optionally employ a digitizing tablet to help speed up data entry. All commands are entered either from the tablet or the text terminal. The graphics terminal is used only to display the portion of the chip design that is being edited.

Caesar is basically a powerful graphics editor. It allows the user to place, move, modify, copy, and delete colored rectangles on the graphics screen. These colored rectangles form a pictorial representation of the various mask layers in the designer's chip. Caesar allows the editing of arbitrarily large designs by including the ability to zoom in and out of the design and to pan across it. The user can save any part of the design being edited in a file on the computer disk. This file is in .ca format. These .ca files can be called back to the graphics screen to create large hierarchical designs. In addition, the designer may place textual labels on the masks so that they may be referred to in verification and simulation software. Figure 2 is a photograph of the caesar graphics display. It exhibits the hierarchical nature of the caesar program.

The digitizing tablet greatly increases the speed at which designs may be accomplished with caesar. There are four buttons on the tablets "cursor" (a device similar to the "mouse" on many personal computer systems). Two of these are used to position the lower left and upper right corners of a white box on the graphics screen. A third is used to fill in that box with a color. The fourth is used to locate subcells in the chip design and to descend into the hierarchy for editing purposes.

Caesar has been used by various universities to design successful chips with as many as 100,000 transistors. There is no theoretical limit to the size of a chip that may be designed. Caesar is also "technology independent." This means that it may be used to design chips for fabrication in any VLSI process (e.g., NMOS, CMOS, and GaAs). Caesar accomplishes this by reading data files for each of these technologies. New data files may be easily created by the designer as new fabrication processes become available. This means that caesar will never be obsolete. In fact, two additional technologies have been added to caesar here at JPL. These are the Sandia National Laboratory's CMOS process and a GaAs process that is compatible with the Rockwell fabrication line.

Caesar produces a .cif file as output. This file may be sent directly to fabrication, or subsequent software testing may be performed on it. In addition, an in-house program called "ca2cif" has been written to convert .ca files to .cif format without having to run caesar. This means that the user need not have access to a high-resolution graphics terminal to perform this function.

Caesar has one important limitation as a layout tool. Because caesar creates all designs out of rectangular elements that are aligned with the axes of the graphics display, chips may not contain any curved or slanted geometry. Such chips are said to be of "Manhattan geometry." Chips that are designed with curves and bends in them are considered to have "Boston geometry."

Any .cif file that represents a Manhattan design may be edited with caesar. This is accomplished by running the program "cif2ca." Cif2ca produces a .ca file that corresponds to the original .cif file.

There are many programs available for creating hardcopy plots of chip designs from a .cif file. Such plots are invaluable in checking long line interconnections on large chips. Two programs have been evaluated on this CAD system. One of these, "mcp" form UC Berkeley, is used to create color plots on a Trilog color printer/plotter. This device is a slow dot matrix printer that uses a four-color ribbon. It takes about 20 minutes to produce one page of a low-resolution plot with mcp. Also, since the "m" in mcp stands for Manhattan, mcp can plot only Manhattan designs. The second program is called "cifp" and comes from Caltech. This program drives a Hewlett Packard eight-color pen plotter on the JPL CAD system (it can also drive other devices). Cifp is capable of plotting Boston geometry chips.

III. Design Rule Checking

Two programs that perform design rule checking have been evaluated on the CAD system. The first is a program from Carnegie Mellon University called "drc." This program works only on NMOS chips and so it has been replaced by the second program, "lyra" (Ref. 10), from UC Berkeley.

Lyra checks a file in .ca format against a set of rules that describe the limitations of a particular fabrication process. These rules describe, for example, the minimum sizes of transistors and interconnections, the minimum distances allowed between various structures, and the allowed dimensions of via cuts between interconnection layers. Notice that these are all rules that pertain only to the geometric properties of the design. They have nothing to do with the functional behavior of the circuit that is represented by this geometry.

Lyra rules for new technologies may be written by the user. Hence lyra is technology independent. A set of rules for the Sandia CMOS process have been written here at JPL. The program itself is an expert system that checks the .ca file against the set of rules. Any errors are recorded in a new .ca file that includes the old one as a subcell. When this new file is examined using caesar, the design errors appear as black rectangles that are labeled with the appropriate error message. Alternatively, lyra may be run directly from caesar. In this mode, the tablet cursor is used to position caesar's white box around the area to be checked. A command is then typed from the text terminal and, after a short delay, the errors are displayed on the graphics screen. Figure 3 shows a photograph of a caesar graphics screen that has been checked with lyra.

Lyra, like caesar, runs on chips with Manhattan geometry only. This allows lyra to execute very quickly – as much as an order of magnitude faster than more general design rule checkers. Because of this constraint, lyra needs only to check the rules at the corners of the colored rectangles.

IV. Extraction

In order to perform either electrical rule checking or simulation on a chip design, a functional description of the chip must be derived from the .cif file. This is done by a program called an "extractor." On this CAD system, the extractor program is called "mextra" and it comes from UC Berkeley. The "m" in mextra stands for Manhattan so mextra operates under the same constraint as caesar and lyra. Mextra is not technology independent, though. It can only extract NMOS and CMOS chips. The ability to switch easily between NMOS and CMOS extraction was added here at JPL. The output of mextra is a file in .sim format. Each line of this file describes a device (e.g., transistor or capacitor) and how it is interconnected with other devices in the design. Mextra labels all the electrically different nodes of the design. This is done arbitrarily except for those that have been previously labeled with caesar. These retain their previous labels.

Since many of the tools that use .sim files as input report errors by node number, there is a program called "mexnodes" from the University of Washington that allows the designer to see all the node numbers using caesar.

V. Electrical Rule Checking

The software for electrical rule checking on the CAD system is called "erc" and it comes from the Boeing Corporation. It works only on NMOS chip designs. The rules that it checks are not easily modified. This is not as serious a problem as one might expect since electrical rules do not vary

much between different NMOS fabrication processes. Also, CMOS circuits are far more robust with respect to electrical rules than NMOS circuits. It would be preferable, however, to have an electrical rule checker with the same kind of flexibility as the lyra design rule checker.

The erc program needs both a .cif file and a .sim file for the design that is to be checked. In addition, the user can supply a third file that locates the inputs and outputs to the design. The presence of this last file can prevent many erroneous errors. There are many options that may be used when running erc. It is possible to have erc search for only selected rule violations in this way. Erc produces two outputs. The first is a text file that explains each error that it has found. The second is a .cif file that contains the original .cif input file with added labels that indicate the errors. This latter file may be examined by running cif2ca and looking at the result with caesar.

The erc program has been helpful in detecting errors on ratioed NMOS logic. These errors, if not detected by erc, could have been found only by running a very-high-level simulation program or by testing the finished chip.

VI. Simulation

There are many simulation programs on the CAD system. This reflects the fact that careful simulation of chip designs in software can lead to chips that work on the first fabrication iteration. The time that is invested in a thorough software simulation is more than made up for in reductions in chip testing and redesign time.

There are five simulation programs that are currently used by chip designers on the CAD system. In addition, several others have been evaluated. These programs vary in the detail with which they perform their function.

The lowest level simulator on the system is called "esim." Esim is an "event-driven" simulator that was written at MIT (Ref. 11). The version that is installed here can simulate only NMOS circuits although a new version exists (modified at UC Berkeley) that can perform CMOS simulations as well. Esim takes a .sim file for the design as input. In addition, esim implements a comprehensive editing language for the definition of test vectors and the display of output sequences. Esim models transistors as switches that are either open or closed. Signals in esim may have one of three values at any time: 0, 1, or X. An X corresponds to an unknown logical state. Esim ignores resistors and models capacitors as if they have an infinite charge decay time. For this reason, esim runs at a very high speed. A chip with 3,000 transistors can be tested with thousands of bits of test vectors in less than one minute using esim on a moderately loaded VAX computer. Because of its limitations, however, esim is only good for checking the logic design of the chip.

A newer simulator by the same author as esim is "rsim" (Ref. 12). Rsim is really a set of software tools that implement a complete simulation system. The first of these is a program called "netlist." Netlist allows the user to define a circuit by specifying interconnections between predefined logic primitives. Netlist could be used, for example, by a logic designer for software simulation of circuits that consist of off-the-shelf, small-scale integrated (SSI) circuits. Netlist is fully interactive and technology independent. Its output is a file in a format called .1 that is used by the rest of the rsim system. A .1 file for a chip design can be extracted from a .sim file by running an rsim program called "presim." Once a .1 file exists, one of two types of simulation may be run. The first is a program called "net." Net performs a simulation similar to esim. The advantage to net is that the user may run a simulation using a description generated by the netlist program without actually having performed a layout of the circuit. In this way, algorithms may be verified even before layout begins. The second simulator in the rsim package is called "rnl." Rnl has a more sophisticated model of devices than does esim. In particular, rnl has models for resistors and capacitors and it differentiates between sizes and types of transistors. It produces a much more precise simulation than rsim but it takes about five to ten times as long to run. In addition, rnl uses the "lisp" programming language (an artificial intelligence language) as a user interface. This makes it rather difficult to use for a first-time designer. Rnl can simulate both NMOS and CMOS devices.

Because of the need to use lisp to communicate with rnl, a user-friendly front-end program called "rsim" was written here at JPL. Rsim takes a file in .rsim format that describes the test vectors that are to be run through the rnl simulator. Rsim translates this file into the lisp instructions that are needed to run rnl. Rsim then runs rnl and produces an output similar to that produced by esim. In addition, a second program called "makesim" was written that allows the designer to use a subset of the esim editor to create .rsim files. These new programs have allowed even first-time users to take advantage of the power of rnl.

The program "spice" (Ref. 13) has been around for a long time. It was written at UC Berkeley and it has had numerous updates and revisions. Version 2G6 of spice is on the CAD system. Spice is the highest level simulator that is on the system. Spice takes an input file that is written in a fortran-like language as input. This file contains both the circuit description and a description of input waveshapes. Spice performs an analog-level simulation that models the entire circuit as a set of linear equations. It is very accurate and

very time consuming. A spice simulation run for a circuit with 200 transistors for 32 clock periods (and a 1-MHz clock frequency) takes about an hour to complete on the VAX 11/750 computer with a floating point arithmetic accelerator board. In addition, spice will very often fail to complete at all if there are more than 500 transistors in the circuit. Spice is, therefore, most applicable to the simulation of small subcircuits within a chip. A spice-compatible input file (.spc format) may be created from a .sim file by running the program "sim2spice" from UC Berkeley. Spice is technology independent since new device models may be added fairly easily (as long as the new device is similar to one in a catalog of standard device types). New device definitions usually consist of calls to existing device models with a set of specialized parameters.

The timing analyzer program "crystal" is a good compromise between the high detail of simulation that spice provides and the high speed of esim. Crystal has models for most VLSI devices, but it does not keep track of signal values within the circuit. Instead, crystal determines the speed at which a signal wavefront propagates within the circuit. Crystal is a very powerful program. It can be used to find critical paths (those paths that have the longest delays) in a circuit. These paths may be displayed with caesar (see Fig. 4.). In addition, spice input files that describe these critical paths can be generated automatically by crystal. In this way, spice can be used to simulate only the most time-critical parts of a design. This drastically reduces simulation time.

In addition to these simulation programs, a program called "slang" from UC Berkeley was also evaluated. The people at Berkeley have simulated chips with more than 100,000 transistors using slang. However, slang is very hard to learn to use. The user interface is cumbersome and the documentation is inadequate. In addition, rsim seems to perform all of the same functions as slang and is easier to use. For these reasons, slang is not used by most of the designers.

VII. High-Level Design Aids

The software described up to this point is all that is needed to design and verify custom VLSI chips. However, the design process can be made much easier with the addition of certain tools called "high-level design aids." These tools generate and assemble common circuit elements from high-level commands that are issued by the designer. They free the designer from the tedium of actually performing a detailed layout of these basic cells and hence speed up the layout process.

One common circuit element is the "programmable logic array" (PLA) (Ref. 1). A PLA consists of a set of AND gates followed by a set of OR gates and it may be used to implement any combinatorial logic operation. If some of the outputs of the PLA are fed back to its inputs through a set of delay elements, then the result is a "finite state machine" (FSM). Any digital system may be implemented as an FSM. For the remainder of this report, the term PLA will be used to represent both PLAs and FSMs. Despite the apparent power of the PLAs, they are not used for all possible functions because they are inherently large and slow compared to fully custom logic. However, they are extremely useful in parts of a large chip design that are not time critical. There are many programs that have been evaluated on the CAD system for the design of PLA structures. In fact, there is a comprehensive set of tools that address all aspects of their definition and design. All of the PLA tools are from UC Berkeley.

There are several ways that the designer can specify the functionality of a PLA. There is a .pla file format on the system for defining PLAs with text lines that describe the inputs, outputs, and AND-OR connections, as well as labels and clocking considerations. The designer may elect to design a PLA by simply writing such a file with a text editor. In addition, the designer can define the PLA in terms of an equivalent set of Boolean equations. This is done by running the program "eqntott." Eqntott translates the equations into a .pla file. The designer may also describe the PLA with a state diagram. This is done by running "peg" (Ref. 14). Peg also creates a .pla file. The .pla file can be optimized to some extent by running the program "presto." Presto eliminates redundant logical elements and rearranges intermediate products in an attempt to minimize the number of gates in the PLA.

Once a .pla file exists, then a PLA layout may be generated. The program "mkfsm" converts a .pla file into a .cif file that contains a layout of the PLA. Mkfsm, however, will produce only an NMOS layout and, in fact, this layout is incompatible with current MOSIS processes. Mkfsm was modified here at JPL to resolve the process incompatibilities and it has been used in several successful chip projects. It has been replaced recently with a new program called "tpla." Tpla is a PLA layout generator that is written with the "tpack" cell assembly package that will be described below. It is technology independent and new technologies may be easily added by the user. Tpla produces a .ca file as output. Tpla has some additional features that make it a very good PLA generator. Tpla minimizes the capacitance within the PLA (and hence maximizes the speed of the PLA) by reducing the number of interconnections that are made with high-capacitance materials. It also calculates the power consumption of the PLA and generates power distribution lines that are the appropriate size to deliver this power. The outputs of the PLA may be optionally placed on the same or opposite side as the inputs. Figure 5 shows a layout of a PLA that was designed

in less than 5 minutes using eqntott and tpla. It implements a 4-bit binary counter with reset.

The subroutine package tpack that was mentioned above is a set of programs that may be called from a user-written C program. They are used to place, stretch, and interconnect predefined cells that are placed in a template file. This is a very powerful tool for a designer who is also a good C programmer. Once basic cells have been designed, they may be assembled into larger functional blocks (or even into complete chips) under software control. Programs that are written using tpack are actually silicon compilers (Ref. 15). One example is the tpla program.

Another high-level tool is the UC Berkeley program called "quilt." Quilt is used to assemble arrays of rectangular circuit elements. Quilt has been used in almost every chip design that has been performed on the CAD system. Many high-level design aides have been written that are basically sophisticated calls to the quilt program. One of these is the UC Berkeley program "vlsifont" which allows the designer to place macroscopic identifying text on a chip using any of the more than one hundred fonts in the UNIX font catalog. Another program that uses quilt is called "pads." Pads was written here at JPL and it allows the designer to define a ring of input and output pads to place around a chip. Pads is technology independent and templates have been written for three magnifications of NMOS and two of CMOS.

The program "rom," which was written here at JPL, allows the designer to define a read-only memory block by creating a text file (in .rom format) that describes the desired contents of the memory. Rom processes the .rom file and runs tpla to generate the layout. Rom is, therefore, technology independent.

One last high-level design aid that was written here at JPL is called "title." Title, which was written a year before vlsifont, is also used to generate text on a chip. It is still used because it is at least ten times faster than vlsifont. It has only one font and it can be used only for NMOS and CMOS chips.

VIII. Standard Cell Libraries

Once a subcircuit, or cell, has been designed, fabricated, and tested successfully, there is no need to redesign it each time it is needed in subsequent chip projects. For this reason, libraries have been set up on the CAD system, so that all designers can access .ca files for these cells. There are separate libraries for NMOS, MOSIS CMOS, and SANDIA CMOS on the system at this time. Each library is write protected so that only the system manager can add to or edit the cells. Each designer, however, has read access to the libraries. In fact, when caesar is run, a pointer to the appropriate technology library for the current design is generated. This is done through the use of a caesar configuration file in each designer's directory.

The use of predesigned cells can reduce the time needed to complete a complex chip design by orders of magnitude.

Figure 6 shows two standard cells from the SANDIA CMOS library. The cells in this library (as well as the MOSIS CMOS library) each have the same height, the same power distribution bus locations, and inputs and outputs that are accessible from both the top and bottom of the cell. These cells are designed to be assembled into rows with intercell routing performed in the channels between the rows. This type of design is often referred to as "standard cell" design and it is an example of semicustom chip layout.

IX. Testing

Hardware and software are currently under development here at JPL to allow the designer to stimulate a chip with the same test vectors that were used for the software simulation described in Section V. These will be described in a subsequent issue of the *TDA Progress Report*. Currently, testing must be performed with standard test equipment such as signal generators, oscilloscopes, and logic analyzers. The new test station consists of a microprobe station for generating and acquiring signals directly on the fabricated wafer and a digital interface for connecting the chip to the CAD system computer. A photograph of the test station appears in Fig. 7. The microprobe equipment is complete and the hardware interface is currently being installed. The software that will drive the tester is being written at this time. When completed, the test station should greatly enhance a designer's ability to qualify chips quickly and easily.

X. Conclusion

The UNIX-based VLSI CAD station described in this report is a complete, integrated system for the design and verification of custom and semicustom VLSI chips. It has been used in the design of several successful chip projects in both NMOS and CMOS. In fact, most of the chips that are designed on the system work with the first fabrication. The University CAD tools have proven to be robust and adaptable to the needs of many JPL projects. A minimal amount of in-house software was needed to integrate these tools. Also, the establishment of standard cell libraries has reduced the design time needed for new chips substantially.

Since most of the tools are technology independent, the CAD system will be useful far into the future. Some improvements will be required, however. A technology independent extractor will be needed. Also, software for automatic routing of interconnect signals would further reduce design time. Both these problems are currently being addressed at UC Berkeley. In fact, a new version of caesar called "magic" includes place and route functions; it will be released this year.

References

1. Mead, C. and Conway, L., *Introduction to VLSI Systems*, Addison-Wesley Publishing Company, Menlo Park, California, 1980 pp. 115-127.
2. The MOSIS Project, *The MOSIS System (What It is and How to Use It)*, Publication ISI/TM-84-128 Information Sciences Institute, Marina del Rey, California, 1984.
3. Bourne, S. R., *The UNIX System*, Addision-Wesley Publishing Company, Menlo Park, California, 1983.
4. Deutsch, L. J., "A VLSI Implementation of a Multicode Convolutional Encoder," *TDA Progress Report 42-72*, Jet Propulsion Laboratory, Pasadena, California, February 15, 1983, pp. 61-69.
5. Truong, T. K., Deutsch, L. J., Reed, I. S., Hsu, I. S., Wang, K., Yeh, C. S., "The VLSI Design of a Reed-Solomon Encoder Using Berlekamp's Bit Serial Algorithm," *Proceedings of the Third Caltech Conference on VLSI*, California Institute of Technology, Pasadena, California, 1983, pp. 303-330.
6. Shao, H. M., Truong, T. K., Deutsch, L. J., Yuen, J. H., and Reed, I. S., "A Systolic Design of a Pipeline Reed-Solomon Decoder," *TDA Progress Report 42-76*, Jet Propulsion Laboratory, Pasadena, California, February 15, 1984, pp. 99-113.
7. Chang, J. J., Truong, T. K., Reed, I. S., and Hsu, I. S., "VLSI Architectures for the Multiplication of Integers Modulo a Fermat Number," *TDA Progress Report 42-79*, Jet Propulsion Laboratory, Pasadena, California, November 15, 1984, pp. 136-141.
8. Wang, C. C., Truong, T. K., Shao, H. M., Deutsch, L. J., Omura, J. K., and Reed, I. S., "VLSI Architectures for Computing Multiplications and Inverses in $GF(2^m)$," *TDA Progress Report 42-75*, Jet Propulsion Laboratory, Pasadena, California, November 15, 1983, pp. 52-64.
9. Ousterhout, J., *Editing VLSI Circuits with Caesar*, Computer Science Division, University of California, Berkeley, California, 1983.
10. Arnold, M. H., *Specifying Design Rules for Lyra*, Computer Science Division, University of California, Berkeley, California, 1983.
11. Baker, C. and Terman, C., "Tools for Verifying Integrated Circuit Designs," *Lambda*, Fourth Quarter, 1980.
12. Terman, C. J., "RSIM – A Logic-Level Timing Simulator," *Proceedings of the IEEE International Conference on Computer Design: VLSI in Computers*, IEEE Computer Society Press, Silver Spring, Maryland, 1983.

13. Negal, L. W. and Pederson, D. O., "SPICE – Simulation Program with Integrated Circuit Emphasis," Memorandum No. ERL-M382, Electronics Research Laboratory, University of California, Berkeley, California, April, 1973.

14. Hamachi, G., *Designing Finite State Machines with PEG*, Computer Science Division, University of California, Berkeley, California, 1983.

15. Losleben, P., "Computer Aided Design for VLSI," in Barbe, D. F. (editor), *Very Large Scale Integration: VLSI*, Springer-Verlag, New York, 1980, p. 108.

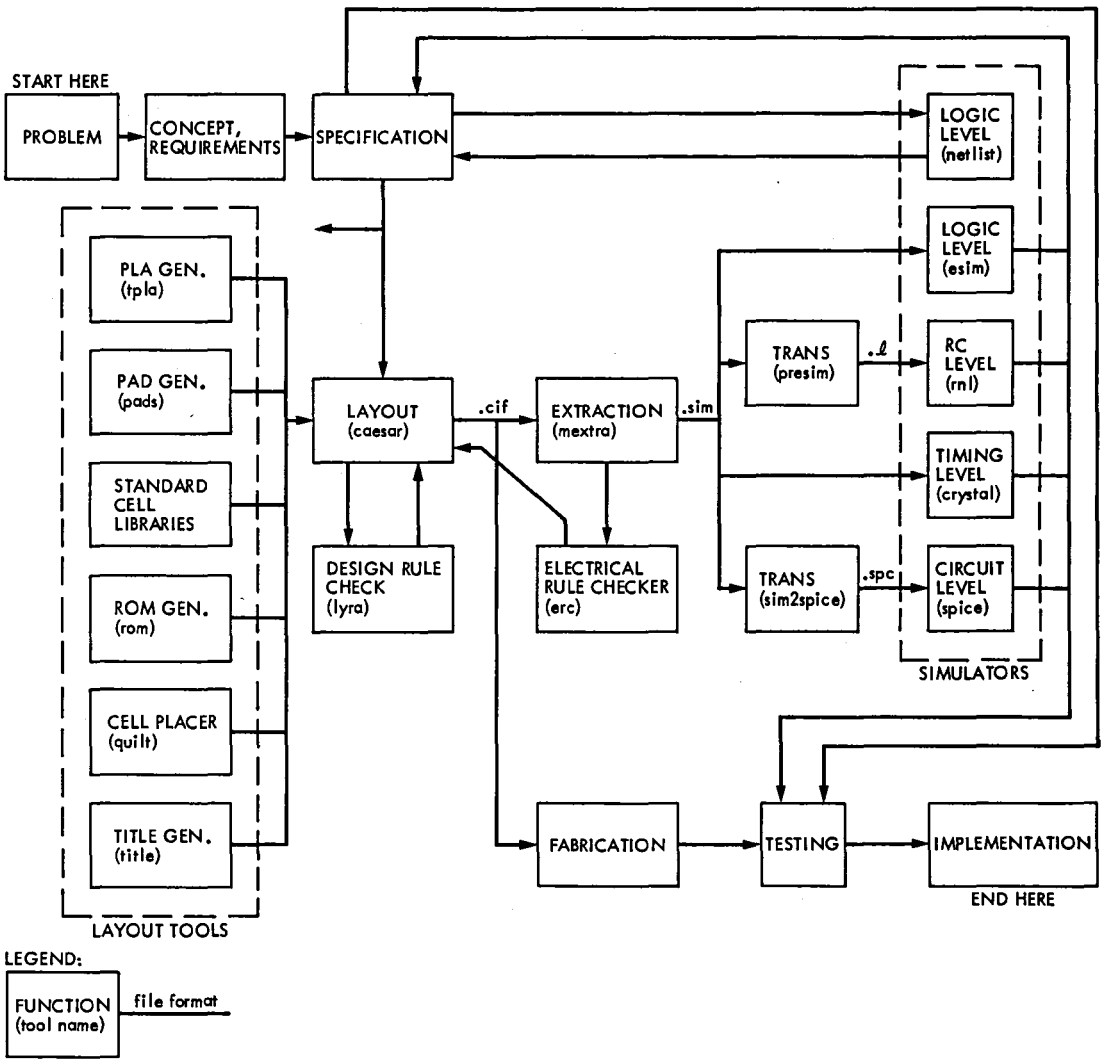

Fig. 1. Integrated UNIX-based VLSI CAD system

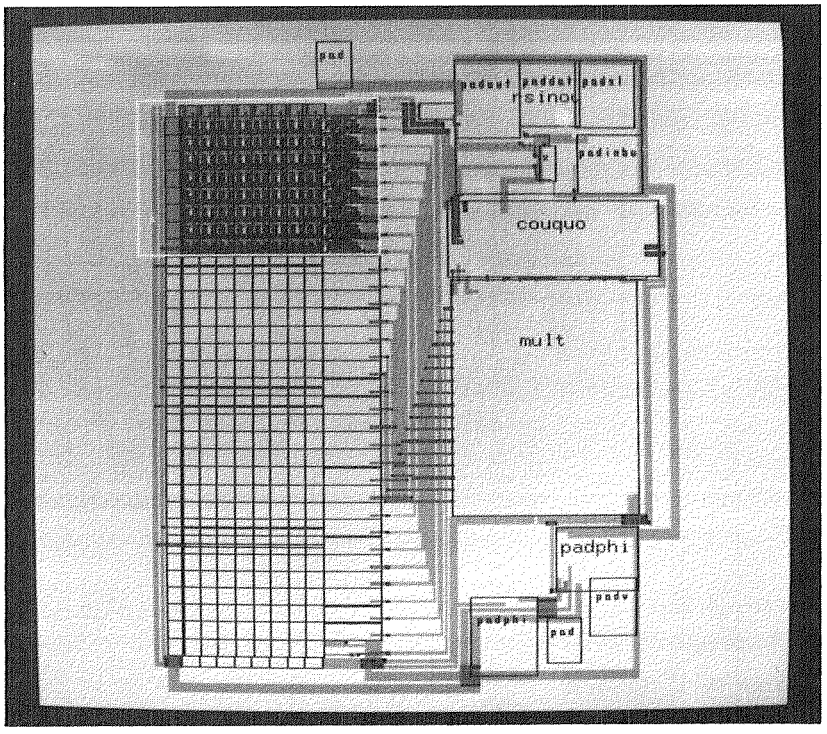

Fig. 2. The caesar graphics display

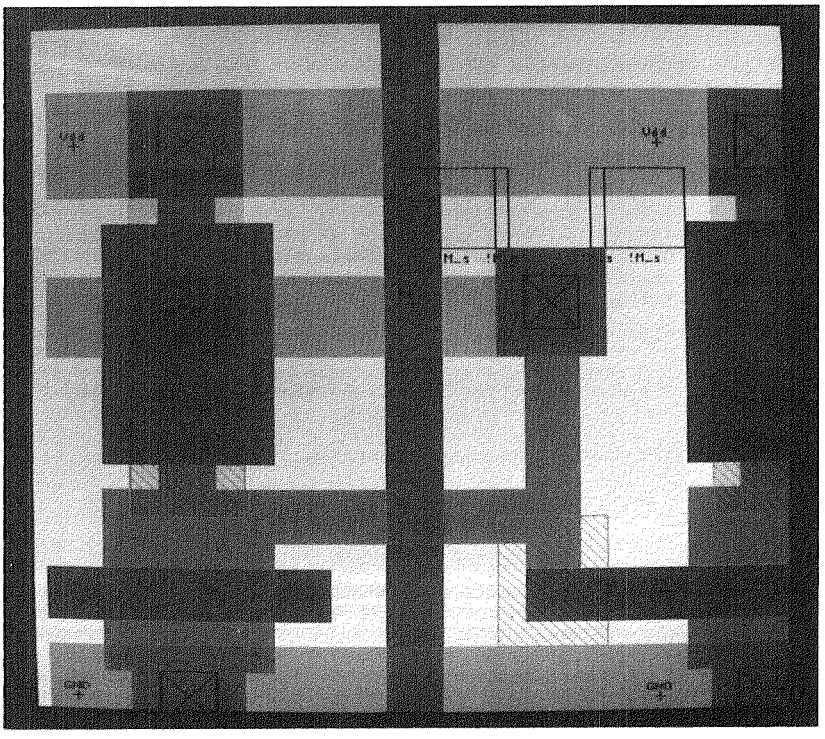

Fig. 3. Design errors located by lyra are displayed interactively with caesar. The black rectangles indicate the magnitude of the violations.

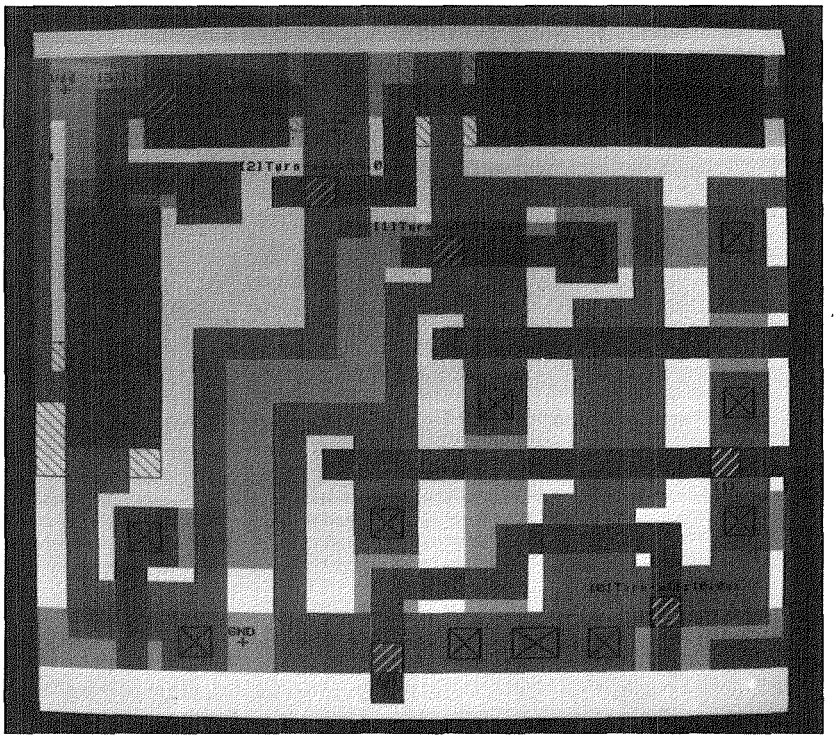

Fig. 4. A caesar display of the output of the crystal timing analyzer

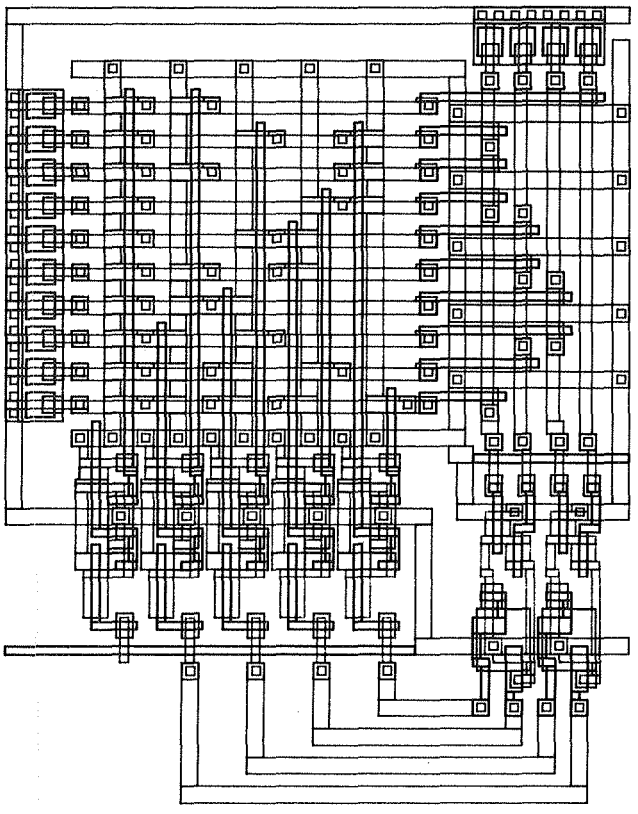

Fig. 5. A 4-bit binary counter with reset implemented as a PLA. The design, accomplished by defining the PLA with Boolean equations, was completed in 5 minutes using eqntott and tpla.

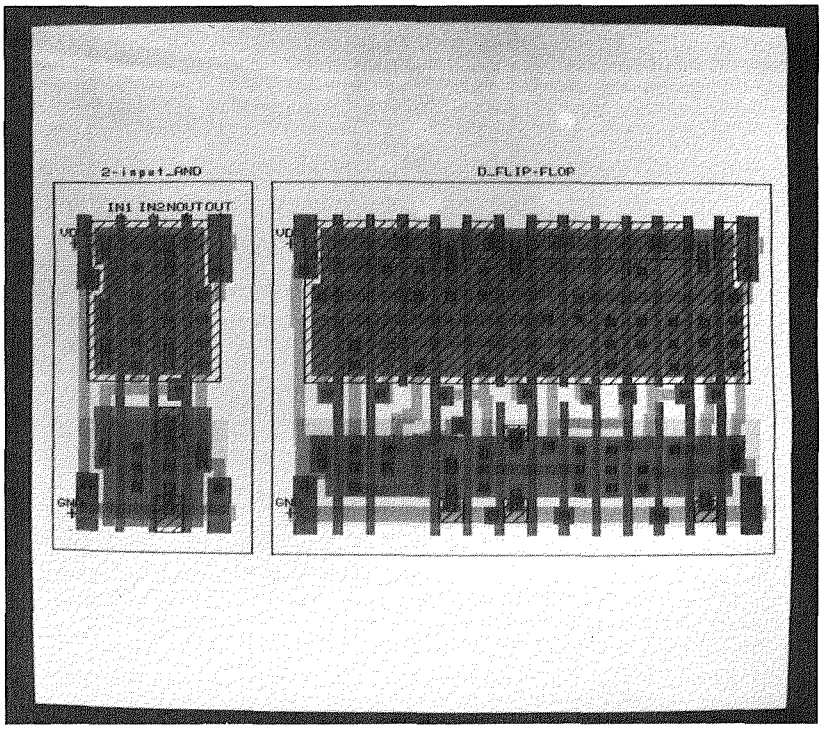

Fig. 6. Two examples of CMOS standard cells

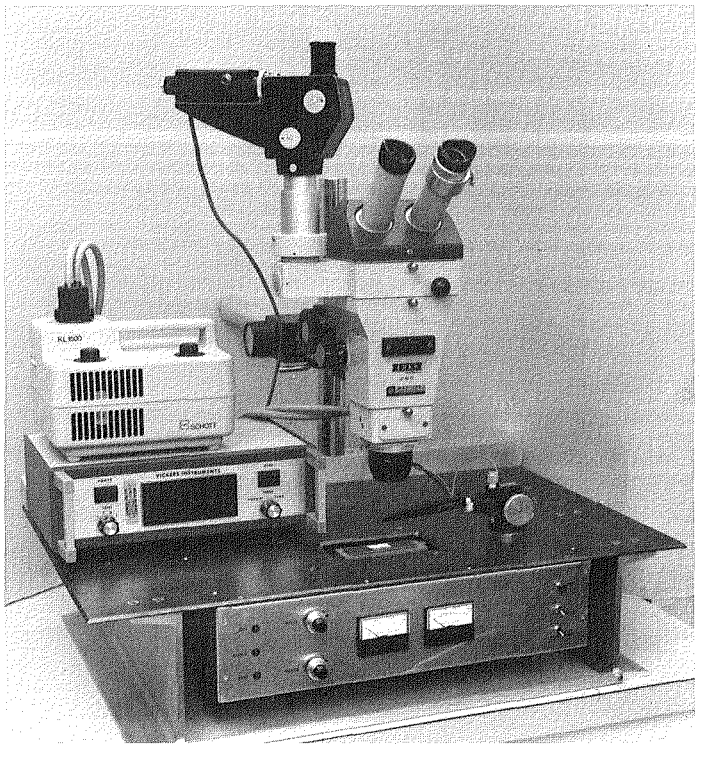

Fig. 7. The testing station for the integrated UNIX-based CAD system

High-Speed Digital Baseband Mixer

F. P. Chan, M. P. Quirk, and R. F. Jurgens
Communications Systems Research Section

This paper explores the feasibility of designing a digital, complex, baseband mixer with a 50 MHz sampling rate. The baseband filter must provide passbands with linear phase response to minimize intersymbol interference. The article includes studies of the effects of signal quantization, filter coefficient quantization, dynamic range, filter response characteristics, and the performance of the mixer when used for cross-correlation and autocorrelation pulse detection techniques. This filter has been designed for use in the High-Speed Data-Acquisition System (HSDAS), an advanced experimental system in the Deep Space Network.

I. Introduction

A High-Speed Data-Acquisition System (HSDAS) is being constructed at Deep Space Station 14 (Ref. 1). Its primary purpose is to sample the 15 MHz bandwidth intermediate-frequency (IF) signal from the Deep Space Network (DSN) radar receivers and perform all necessary data reduction (filtering, phase correcting, and correlating; see Fig. 1) using digital processors. A particular front-end module in the HSDAS is the digital baseband mixer. Its purpose, similar to that of its analog counterpart, is to down-convert the IF signal to a complex baseband signal. The real and imaginary components of the baseband signal are obtained by first mixing the IF signal with cosine and sine carrier signals and then filtering out the high-order frequency components.

The digital mixer design must satisfy the requirements of the HSDAS specification. Firstly, it must have appropriate phase and magnitude response so that it induces minimum intersymbol interference in radar signal correlation at later stages. Secondly, it must eliminate out-of-band signal components. Finally, the mixer must have sufficient dynamic range that weak signals buried among strong radar echoes can be detected.

This article presents the design and simulation results for a digital mixer which complies with the constraints listed above. Section II, Digital versus Analog, discusses the advantages and the disadvantages of the two implementations. Section III, Digital Design, outlines the basic structure of the mixer system. Section IV, FIR filter design, discusses the implementation of the post-multiplier, finite impulse response (FIR) filter. Section V, Simulation, presents the simulation results for the digital mixer design. Finally, Section VI suggests future research.

II. Digital Versus Analog

Traditionally, frequency down-conversion has been performed by analog mixers. Recent advances in digital signal processing (DSP) techniques and digital hardware technology have made a high-speed digital mixer feasible. A digital approach has a number of inherent advantages. Firstly, the

characteristics of a digital device, such as the frequency response of a digital filter, are known exactly. Secondly, the functional characteristics are not affected by component drift, component aging, and ambient temperature change. Thirdly, a digital device can be replicated precisely. Fourthly, a digital circuit can be debugged exactly by slowing down the system clock so that equipment, such as a state analyzer, can be used to monitor or alter logic values in any data path. Furthermore, a digital system is potentially programmable. This feature is an important advantage over an analog device since the latter must be redesigned for any change in system configuration. Finally, a digital hardware implementation can be simulated accurately. An adequate simulation can predict virtually any system performance or design flaw.

In addition to the inherent advantages listed above, a digital mixer design offers implementation alternatives that are lacking in an analog design. Figure 2(a) shows a typical analog design of one channel of a baseband mixer. The first module is a multiplier, usually implemented with diode-switching techniques. A carrier signal in the form of a square wave drives the switching. The output signal contains not only the fundamental baseband signal but also the odd harmonics across the high-frequency spectrum. A low-pass filter with substantial stopband attenuation must be used to filter out the high-frequency harmonics. Figure 2(b) shows a digital design of the same mixer. The incoming signal is arithmetically multiplied with a carrier signal generated from a sine table. The mixed signal contains a baseband component and a component at twice the carrier frequency. Since the component at twice the carrier frequency is the only component to be filtered, the required stopband attenuation is less than that of the analog version. Moreover, system noise caused by the high-frequency odd harmonics found in the diode-switching implementation are nearly eliminated in the digital design.

An important design consideration is the restriction on the filter characteristics imposed by binary coded signals such as those used for telemetry and ranging systems (for example, delay-Doppler radar). In the delay-Doppler technique (Ref. 2), useful information is extracted by cross-correlating the incoming signal with the previously transmitted binary code. Intersymbol interference in correlation, commonly caused by phase distortion in previous filter stages, must be minimized. Therefore, the lowpass filter in the baseband mixer must have a linear phase response, or equivalently, constant group delay, at least over the baseband spectrum. In addition, the magnitude response must preserve as much baseband signal as possible but must cut off sharply near the carrier frequency to remove the high-order frequency component of the mixed signal. This requirement translates to a narrow transition band if the full baseband channel is to be utilized.

In an analog filter design, the requirement for a small transition band conflicts with the requirement for linear phase. For example, Fig. 3 shows the magnitude and phase responses and the group delay of an inverse Chebyshev filter (Ref. 3), designed with the best compromise of the two requirements. Notice that the group delay degrades significantly near the transition band. In a digital design, however, a non-recursive, finite impulse response (FIR) filter (Ref. 4) can be designed such that its phase response is strictly linear without jeopardizing the width of the transition band. Figure 4 shows the magnitude and phase responses and the group delay of an FIR filter with its magnitude response similar to the analog one in Fig. 3. The linear phase property of the FIR filter is one of the most desirable properties of a digital implementation.

The digital approach does have a number of drawbacks. Although the width of the transition band of an FIR filter is not restricted by the phase response, it is limited by the maximum filter length which can be built. It can be shown that the filter length (or number of taps) required is inversely proportional to the normalized transition-band width (Ref. 5). As a result, the digital mixer implemented with an FIR filter that has narrow transition band can be larger and more costly than the analog version. However, the digital design contains modular structures which could be implemented with Very Large Scale Integration (VLSI) technology. Currently the clock rates for VLSI DSP components are about a factor of 5 too slow for our application. Using these components in a parallel and pipe-lined implementation would require about 400 packages. As clock speeds and complexity increase in the next few years, the number of components could drop to about 50 packages at a size and cost comparable to an analog mixer.

A second drawback with the digital design is its limited dynamic range. In the planetary radar system, it is desirable to have the largest dynamic range possible so that weak radar signals can be detected among strong primary radar echoes. In the analog design, the dynamic range, typically 10^{10}, is limited by thermal noise. On the other hand, in the digital design, the dynamic range is limited by quantization. For an N-bit digital system, the dynamic range is approximately 2^N. In general, a larger dynamic range requires more data bits at the expense of more complex and slower hardware. As a result, the optimal data word size in a digital mixer is a compromise between the desired dynamic range and the hardware complexity.

III. Digital Design

A number of parameters must be defined for the digital mixer. These parameters include the sampling resolution (or

amplitude quantization), the sampling rate, and the post-multiplier filter characteristics.

As discussed before, the sampling resolution is determined by the required input dynamic range. A 40 dB sensitivity for the HSDAS represents a good compromise among quantization variance, expected weak signal strength, and hardware complexity. This dynamic range is anticipated to be large enough for the actual radar experiments and for equipment testing. A 40 dB sensitivity translates to a digital system with 8-bit resolution. As a result, the digital mixer should be designed with an 8-bit basic data word size.

The sampling rate is limited by the Nyquist sampling theorem, which states, "If a continuous, bandwidth-limited signal contains no frequency components higher than f_x, then the original signal can be recovered without distortion if it is sampled at a rate of at least $2f_x$ samples per second" (Ref. 6). If the signal contains energy at rate f higher than f_x, f will be folded back and superposed at frequency $2f_x - f$. This phenomenon is known as aliasing and must be avoided.

The Nyquist sampling theorem imposes two design restrictions on the digital mixer. Firstly, the mixer must operate at a sampling rate at least twice the highest frequency component of the incoming IF signal. Since the IF signal contains components up to 15 MHz, the sampling rate in the mixer must be at least 30 MHz. Secondly, the Nyquist theorem requires that signal energy at frequencies higher than f_x, 15 MHz, should be filtered before the A/D converter in order to avoid aliasing. This filtering is guaranteed by the HSDAS analog receiver.

In theory, a sampling rate of 30 MHz is the absolute minimum rate for the mixer. Additional consideration, however, is given to the post-mixer baud integrator (Fig. 1). The baud integrator (Ref. 7) is required to resample the data so that the HSDAS can track the Doppler shift of the signal. In order to keep the resampling error sufficiently small, a 50 MHz sampling rate for the A/D converter, the digital mixer, and the baud integrator has been established as a desirable design goal.

The characteristics of the post-multiplier, lowpass FIR filter can now be defined. As shown in Fig. 2(b), in order to extract the baseband signal from the output of the multiplier, the FIR lowpass filter must have a stopband beginning at 7.5 MHz. Because the stopband frequency is fixed, the sum of the passband and transition-band widths must be constant. The widening of one band results in the narrowing of the other. As explained in Section II, it is desirable to have the widest passband possible to preserve the baseband signal, yet it must also have the widest transition band possible to minimize the FIR filter size. These two are conflicting requirements. A proper compromise can be found by considering the spectral characteristics of the incoming radar signal.

Usually, the incoming signal from the HSDAS receiver is an IF signal phase modulated by a pseudorandom (PR) code of 0.5 μs baud period. The signal power spectrum of the binary PR code, shown in Fig. 5, can be expressed as,

$$P(\omega) = C \frac{\sin^2\left(\frac{\omega t_b}{2}\right)}{\left(\frac{\omega t_b}{2}\right)^2} \tag{1}$$

where ω is the angular frequency, t_b is the period of one baud, and C is a constant. It can be shown that the main lobe, between $-1/t_b$ and $+1/t_b$, contains 90.2% of the overall signal energy. A filter with its passband frequency set at $-1/t_b$ to $+1/t_b$ (2 MHz for a 0.5 μs baud period) should pass sufficient signal energy to be correlated at later stages. A 2 MHz passband width leaves a 5.5 MHz transition bandwidth. It will be shown in Section IV that this FIR filter can be realized with 19 taps, a reasonable size. Here, the choice of the filter characteristics is somewhat arbitrary, and its final acceptance will be based on the mixer simulation to verify if the cross-correlation function between the mixer output and the original binary pseudorandom code is acceptable.

In summary, the overall mixer is chosen to operate at 50 MHz with 8-bit basic data resolution. The FIR, lowpass filter is preliminarily chosen to have a passband from 0 to 2 MHz, a transition band from 2 MHz to 7.5 MHz, and a stopband from 7.5 MHz up. The stopband must also have an attenuation of at least 40 dB.

IV. FIR Filter Design

Having defined the characteristics of the FIR filter, one needs to generate the necessary FIR filter coefficients. A number of methods, such as windowing and iteration techniques, have been published (Ref. 8). In this digital mixer design, a computer-aided method based on the equiripple iteration algorithm is employed to determine the optimal FIR filter coefficients.

The time domain filter response for an FIR filter can be viewed as a discrete time approximation of the convolution integral, summed over finite duration (starting from $n = 0$ for a causal system),

$$y(i) = \sum_{n=0}^{N-1} h(n)\, x(i-n) \tag{2}$$

where $h(n)$ is the FIR filter coefficient, $x(n)$ is the input signal, and $y(n)$ is the output signal. The frequency response of an FIR filter having coefficients $h(n)$ and length N can be described as,

$$H(f) = \sum_{n=0}^{N-1} h(n) \exp\left[-j\, 2\pi\, (nf/f_s)\right] \tag{3}$$

where f_s is the sampling frequency. If the following restriction,

$$h(n) = h(N-n-1) \tag{4}$$

is imposed on the FIR filter coefficients, the filter has linear phase response (Ref. 9). Furthermore, if the filter has odd length, then the group delay, t_g, is an integer multiple of the sampling period depending only on N,

$$t_g = \left(\frac{N-1}{2}\right) t_s \tag{5}$$

where t_s is the sampling period.

Equation (4) suggests that the FIR filter coefficients are symmetrical about the central coefficient (assuming odd filter length). This is an important fact because it implies that the number of hardware multipliers can be halved by first factoring out identical coefficients.

To find the optimal FIR coefficients, one must first define what the "optimal" filter characteristics are. As mentioned before, it is desirable to minimize the filter length, N, and maximize the width of the passband ω_p (Fig. 6). For a fixed stopband edge, maximizing the passband width is equivalent to minimizing the width of the transition band. In addition, δ_p, the maximum ripple deviation from the ideal passband response of unity, and δ_s, the maximum ripple deviation from the ideal stopband response of zero should be minimized. Minimizing the stopband ripple is equivalent to maximizing the stopband attenuation. Not all of these parameters, N, δ_p, δ_s, ω_p, and ω_s, are independent. In particular, a narrower transition-band width or a larger stopband attenuation typically requires a longer filter length. Parks and McClellan (Ref. 10) have written an iterative algorithm to design symmetric (and antisymmetric) equiripple FIR filters.

This iterative algorithm for finding $h(n)$ involves solving a Chebyshev approximation problem which minimizes the maximum approximation error, ϵ. Specifically, one minimizes, over all sets of N coefficients $h(n)$, the maximum of the absolute value of the weighted difference between the desired frequency response, $D(f)$, and the actual filter response, $H(f)$, for the regions of approximation,

$$\epsilon = \min \{\max [W(f)\, |D(f) - H(f)|]\} \tag{6}$$

The weighting function $W(f)$ allows for different relative errors in different bands, and can be used to shape the passband and the stopband.

In the case of the baseband mixer FIR filter, the stopband attenuation has been specified at 40 dB. The following procedure is used to obtain the minimum value of N and the associated filter coefficients, $h(n)$.

(1) Choose an approximate filter length N. The number of coefficients, N, is inversely proportional to the normalized transition-band width,

$$N \approx \frac{C}{f_t/f_s} \tag{7}$$

where f_t is the transition-band width, f_s is the sampling rate, and C is a constant between 1 and 4 and depends on the desired stopband and passband ripples (Ref. 5). A good approximation is to simply choose C equal to 4.

(2) Use the Parks-McClellan algorithm to find the stopband attenuation and the associated filter coefficients.

(3) If the computed stopband attenuation is significantly larger than the desired stopband attenuation, decrease N and return to step 2. If the result is smaller than the desired attenuation, increase N and return to step 2. When the result is just larger than the desired attenuation, the filter has been optimized for minimum N, and the proper filter coefficients, $h(n)$, have been found.

Using the procedure outlined above, a 19-tap FIR filter has been designed to the specifications listed in Section III. Quantized to 8-bit integers, the nineteen FIR filter coefficients are -6, -10, -13, -9, 5, 30, 62, 95, 119, 128, 119, 95, 62, 30, 5, -9, -13, -10, -6. Figure 7 shows the plots of the filter coefficients $h(n)$, the magnitude response (in log scale and in linear scale), and the phase response. Since the filter coefficients $h(n)$ are chosen to be symmetrical, the phase response, as predicted, is linear. From the magnitude response, one observes that the signal rolls off at 2 MHz, reaches -3 dB at about 3.8 MHz, and drops below -40 dB at 7.5 MHz and beyond.

It should be pointed out that the FIR filter hardware constrains only the length of the filter. Within a given filter length, the filter characteristics can be changed simply by reentering a new set of coefficients. Consequently, an FIR filter is programmable. Furthermore, an FIR filter can be, at least in

principle, extended by concatenating additional stages. Thus, a digital FIR filter is a highly flexible filter implementation.

V. Simulation

There are many reasons for a complete simulation of the digital mixer. The principal concern is that, with real radar signal inputs, the mixer must produce a baseband signal that correlates properly with the binary pseuorandom code. One wishes to determine how much the digital mixer will distort the ideal cross-correlation function. In theory, there are two types of errors: intersymbol interference and quantization error. In an analog design, the intersymbol interference will be the main source of distortion because an analog mixer always has a non-linear phase response. In a digital design, on the other hand, the quantization error is likely to be the dominant source of distortion. Through a complete simulation of the digital mixer, one can quantitatively measure the overall quantization error.

A second concern is whether the minimum length filter will provide sufficient stopband attenuation if the FIR filter is operating with fully quantized arithmetic. Furthermore, it must be verified that the 2 MHz passband width is large enough to generate the proper correlation signal. Again, these characteristics can be checked only with a simulation of the hardware. Finally, one would like to determine the minimum signal-to-noise ratio (SNR) of the radar signal in which the pseudorandom code can be detected both by autocorrelation and by cross-correlation methods.

The scope of the baseband mixer simulation is shown in Fig. 8. There are two types of hardware simulated: the active components, such as FIR filters, and the observational components, such as power spectrum display. Figure 8 shows all the active components in rectangular blocks or large circles and all the observational components in small circles.

The active components can be divided into three groups: the source-signal generator, the baseband mixer, and the cross-correlator. The source-signal generator includes a binary pseudorandom code generator, a square-wave generator, an IF radar signal generator, and an analog-to-digital converter. The source-signal generator is responsible for simulating a radar IF signal, phase modulated with either a binary pseudorandom code or a square wave. Complex white noise is added to the IF signal to simulate various SNRs. The source signal can be characterized as,

$$\begin{aligned} \bar{S}(t) &= \bar{N}(t) + \bar{\Gamma} \exp \{j\,[\omega_c t + \phi(t)]\} \\ \bar{\Gamma} &= \gamma + j0 \end{aligned} \tag{8}$$

where $N(t)$ is the complex white noise, γ is the SNR, ω_c is the angular carrier frequency, and $\phi(t)$ is the phase function (either a square wave or a binary pseudorandom code). The real component of $\bar{S}(t)$ is first quantized through an analog-to-digital converter and then sent to the input of the mixer.

The baseband mixer has two channels, one for the real signal and one for the imaginary signal. The mixer consists of three parts: the arithmetic multipliers, the FIR filters, and the optional down-samplers. The incoming IF signal is first arithmetically multiplied with a cosine carrier signal in the real channel and with a sine carrier signal in the imaginary channel. The resulting signals are then filtered through two identical lowpass FIR filters. The output signals from the filters are the baseband complex signal. If one desires, the sampling rate can be reduced by down-sampling the baseband signal. (This option is not used in the present mixer design.)

If the pseudorandom code is used to phase modulate the IF signal, the output channels from the baseband mixer can be fed into two cross-correlators, in which the mixer outputs are correlated with the original binary pseudorandom code.

There are five types of observational components: the time-domain display, the frequency-domain display, the power spectrum display, the autocorrelation display, and the cross-correlation display. The time-domain display shows the two signals in the real and imaginary channels in the time domain. The frequency-domain display shows the magnitude (in dB) of the Fast Fourier Transform (FFT) of the real channel and the FFT of the imaginary channel. The power spectrum display is the magnitude square of the FFT of the complex output signal. The autocorrelation function is then derived by computing the inverse FFT of the power spectrum. Finally, the cross-correlation function is computed by directly correlating two time domain signals. These observational components provide the means with which one can closely examine the characteristics of the signals throughout the system.

The exact simulation of a particular mixer design is determined by a number of user-defined options and parameters. Some of these options and parameters control the characteristics of the source signal, while others control the quantization on the signal paths. The user provides the FIR filter coefficients and the pseudorandom code externally. In addition, the simulation provides an optional signal averaging facility with which the radar signal can be integrated while the random noise is averaged out. Table 1 is a list of parameters chosen for the current mixer design.

Figure 9 shows the results from a typical simulation with an SNR of 10 dB and with no signal averaging. Figure 9(a) shows

the frequency-domain plot of the quantized source signal. The spectrum of the pseudorandom signal is centered about the carrier frequencies at +7.5 MHz and -7.5 MHz. Figures 9(b) and 9(c) show the frequency-domain signals of the real and imaginary channels following multiplication by the cosine and sine carriers. By coincidence, the IF signal phase is lined up with the carrier signal phase such that the output signal energy concentrates solely in the imaginary channel. Generally this would not be true. The IF signals are shifted down to the baseband while the twice-carrier frequency components are also created. Figure 10 shows the FIR filter output signals. The twice-carrier frequency components have been suppressed, leaving only the baseband signals.

Figure 11(a) shows the power spectrum of the complex filter output. The magnitude ratio of the signal peak within the baseband to the noise beyond the baseband is at least 40 dB, as required in the mixer specification. The small lump of signal energy at 15 MHz is the remnant of the original carrier signal.

Figure 11(b) shows the autocorrelation of the radar signal from the mixer. As stated before, the autocorrelation is found by computing an inverse FFT of 2048 frequency samples from the power spectrum (Fig. 10). In this particular plot, the signal has been averaged 16 times. The principal triangular match signal is well defined at time zero. Two smaller triangular match signals exist at time +9.46 μs and -9.46 μs. They are caused by the fact that the 63 baud-long pseudorandom code has a period significantly shorter than the FFT time frame. Since the pseudorandom code period (1575 time samples) is 473 samples short of one FFT time frame (2^{11} or 2048 time samples), the pseudorandom code matches itself again at sample +473 (+9.46 μs) and -473 (-9.46 μs). As a result, the two small signal peaks are artifacts of the way the autocorrelation is computed. They would not occur in an actual implementation.

Figure 12 shows the cross-correlation between the mixer output and the binary pseudorandom code. This plot is generated with no signal averaging. Since the correlation is done in the time domain with exactly one pseudorandom code length, it has no multiple match signals as found in Fig. 11. The match signal is found only in the imaginary channel, a fact consistent with the result from Fig. 9. The match signal is negative because the mixer demodulates the IF signal into an inverse of the original binary pseudorandom code. Furthermore, the peak of the correlation function is found at the 9th time sample because the FIR filter introduced a group delay of 9 sample periods (Eq. [5]) relative to the original binary pseudorandom code.

The cross-correlation function shows a triangular match signal that has no significant distortion from an ideal triangular shape. This result verifies that a 2 MHz filter passband width is sufficient to generate a clean correlation function. Furthermore, the match signal has a peak magnitude defined well above that of the out-of-match correlation noise. No significant intersymbol interference is found. This observation is further supported by the correlation function shown in Fig. 13 where the correlation signal has been avareged 16 times. The out-of-match correlation signal level is held almost perfectly constant. In conclusion, the intersymbol interference, commonly found in an analog system, is almost nonexistent in this digital system.

The relative quantization noise of the overall mixer is evaluated by comparing the cross-correlation function generated by an 8-bit system with that generated by a 30-bit system. The root-mean-square quantization noise level, relative to match signal peak, is found to be -41 dB. Since the quantization noise is below -40 dB, the dynamic range requirement is satisfied.

The effects of a small SNR have also been investigated. In the autocorrelation mode, the pseudorandom code is detectable down to an SNR of 4.7 dB. Below that level, the lowpass characteristics of the FIR filter dominate the autocorrelation signal. In the cross-correlation mode, the pseudorandom code is detectable down to an arbitrarily small SNR provided that enough signal averaging is done to integrate the radar signal and to remove the random noise. It has been verified that the cross-correlation can clearly detect a radar signal down to an SNR ratio of -20 dB by averaging the cross-correlation signal 1600 times.

In summary, the simulation of the digital baseband mixer has verified that the present design meets all specifications. In particular, the current FIR filter generates acceptable cross-correlation functions. There is no significant intersymbol interference detected. The quantization noise is -41 dB relative to the maximum correlation signal. Finally, it is verified that cross-correlation can detect a radar signal with small SNR.

VI. Conclusion

The simulation has shown that an all-digital baseband mixer can satisfy all requirements specified by the High-Speed Data-Acquisition System. The digital mixer has a number of desirable properties, such as stability, programmability, and linear phase response. Furthermore, it has been demonstrated that

a digital mixer generates negligible intersymbol interference in cross-correlation. These very desirable features can not be realized by an analog design. The remaining question is whether the digital mixer can be built with available hardware technology.

With regard to the implementation of the digital mixer, two difficulties exist: It must operate at high speed, and it must be within practical limits in complexity. The digital mixer for the HSDAS must operate at 50 MHz. All digital operations within the mixer, such as multiplying and adding, will be pipelined for synchronous operations. Some parallel processing at lower pipeline clock rates may be necessary. At the present time, the only digital technology that can operate reliably at this speed is the emitter-coupled logic (ECL). One problem associated with ECL is its low logic complexity per chip. To fully implement the logic functions of a digital mixer, a large number of ECL components will be required. To appreciate the complexity problem, one may consider the FIR filter alone. One 19-tap FIR filter as designed in Section IV requires nine 8-X-8-bit multipliers, nineteen 8- to 20-bit adders, and over thirty-eight 8- to 20-bit buffers. In addition, the complex mixer has two filters; thus, the part count doubles. Of course, this has not yet included the carrier signal multipliers and the control logic.

At the present time, this baseband mixer implementation using ECL is considered marginally practical to build. Certainly, the FIR filter length cannot be extended much beyond the present design of 19 taps. However, because of the regular structure of an FIR filter, part of the filter can be implemented with VLSI. The present constraint in this approach is the slow speed (about 20 MHz) of the silicon VLSI technology. In the future, when gallium-arsenide VLSI technology becomes available, 50 MHz FIR filter modules can be built. These VLSI modules can reduce the component count of the baseband mixer considerably.

The Ground Based Radar Astronomy Group anticipates that four identical digital mixers will be built for the HSDAS by 1986. The first step is to construct a prototype so the mixer can be evaluted and adjusted (via programming) in the actual operating environment at DSS 14, Goldstone, California. The simulation results give reasonable assurance that the prototype will operate close to the HSDAS specifications. Programmability of the mixer provides further flexibility since the digital mixer can be fine-tuned to the system requirements. In conclusion, an all-digital high-speed baseband mixer for the HSDAS should be built to take advantage of the digital system performance.

References

1. Deutsch, L. J., Jurgens, R. F., and Brokl, S. S., "The Goldstone R/D High Speed Data Acquisition System," *TDA Progress Report 42-77*, 1984, Jet Propulsion Laboratory, Pasadena, Calif., pp. 87-96.

2. Jurgens, R. F., Goldstein, R. M., Rumsey, H. R., and Green, R. R, "Images of Venus by Three-Station Radar Interferometry – 1977 Results," *Journal of Geophysical Research*, Vol. 85, No. A13, Dec. 30, 1980, pp. 8282-8283.

3. Rabiner, L. R. and Gold, B., *Theory and Application of Digital Signal Processing*, Prentice-Hall, 1975, pp. 230-236.

4. Oppenheim, A. V., and Schafer, R. W., *Digital Signal Processing*, Prentice-Hall, 1975, pp. 155-156.

5. Mintzer, F., and Liu, B., "Practical Design Rules for Optimum FIR Bandpass Digital Filters," *IEEE Trans., Acoust., Speech, Signal Processing*, Vol. ASSP-27, Apr. 1979, pp. 204-206.

6. Zuch, Eugene L., "Principles of Data Acquisition and Conversion," *Data Acquisition and Conversion Handbook*, Datel Intersil, 1982, p. 7.

7. Farazian, K. H., and Jurgens, R. F., "Programmable Digital Baud Integrators for the Radar High-Speed Data Acquisition System," *TDA Progress Report 42-79*, 1984, Jet Propulsion Laboratory, Pasadena, Calif., pp. 142-151.

8. Oppenheim, A. V., and Schafer, R. W., *Digital Signal Processing*, Prentice-Hall, 1975, pp. 239-268.

9. Rabiner, L. R., and Gold, B. *Theory and Application of Digital Signal Processing*, Prentice-Hall, 1975, pp. 77-81.

10. McClellan, J. H., Parks, T. W., and Rabiner, L. R., "FIR Linear Phase Filter Design Program," *Programs for Digital Signal Processing*, IEEE Press, 1979.

Table 1. Parameters of current mixer design

Parameters	Value
Source Signal Parameters:	
(1) Carrier Frequency:	7.50 MHz
(2) Baud Period:	0.50 μs
(3) Binary Phase 0:	$-\pi/2$
(4) Binary Phase 1:	$+\pi/2$
(5) Sampling Frequency:	50.00 MHz
(6) Number of Samples per FFT:	2048
(7) Pseudorandom Code Length:	63 bits
Data Length on Signal Path:	
(1) Source Signal to Multiplier:	8 bits
(2) Carrier Signal to Multiplier:	8 bits
(3) Multiplier to FIR Filter:	8 bits
(4) FIR Filter to Correlator:	8 bits
FIR Filter Configuration:	
(1) Filter Length:	19 taps
(2) Coefficient Bit Length:	8 bits
(3) Product Bit Length:	16 bits
(4) Coefficients:	-6, -10, -13, -9, 5, 30, 62, 95, 119, 128, 119, 95, 62, 30, 5, -9, -13, -10, -6
(5) Filter gain:	0.40 dB
Down Sampling:	none

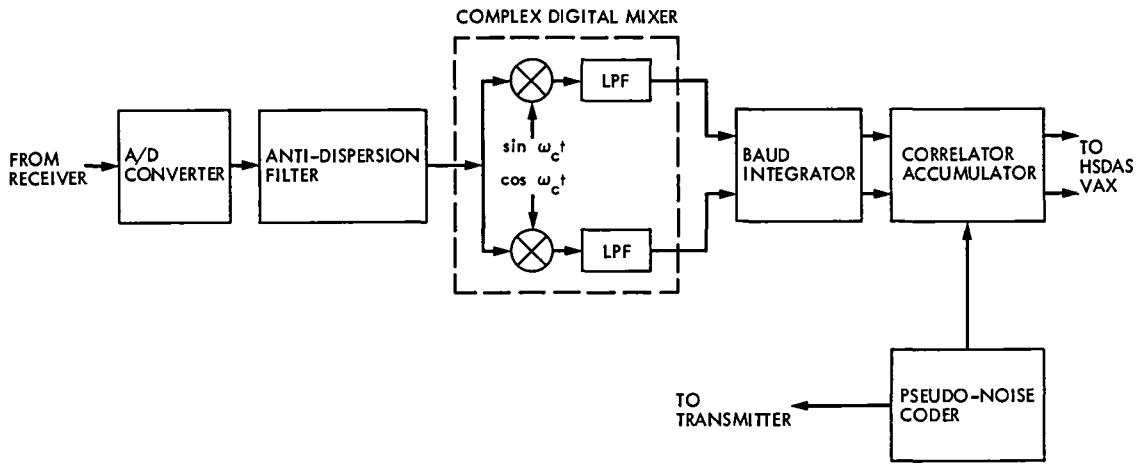

Fig. 1. Simplified block diagram of the HSDAS front end hardware

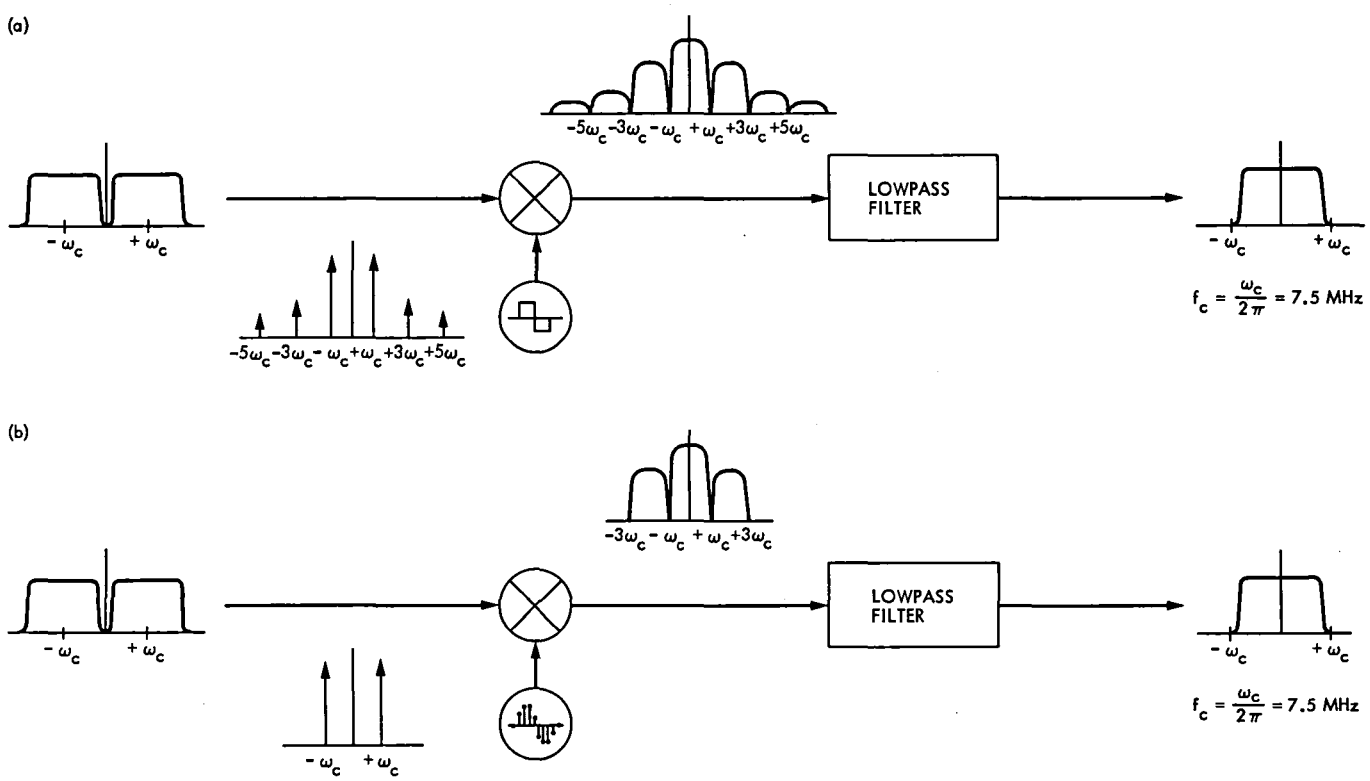

Fig. 2. Signal spectra: (a) analog baseband mixer and signal spectrum; (b) digital baseband mixer and signal spectrum

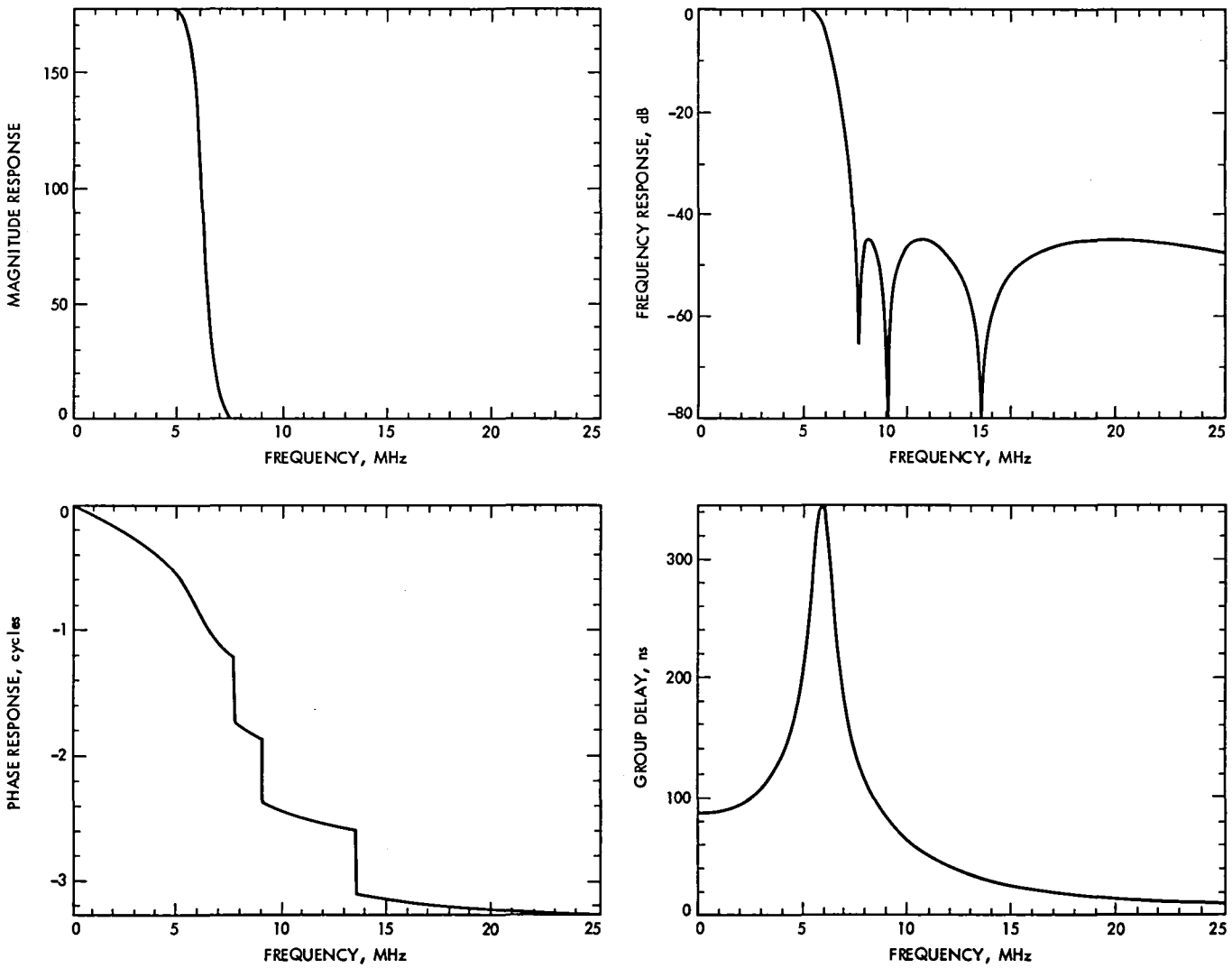

Fig. 3. Analog filter: 8th-order inverse Chebyshev

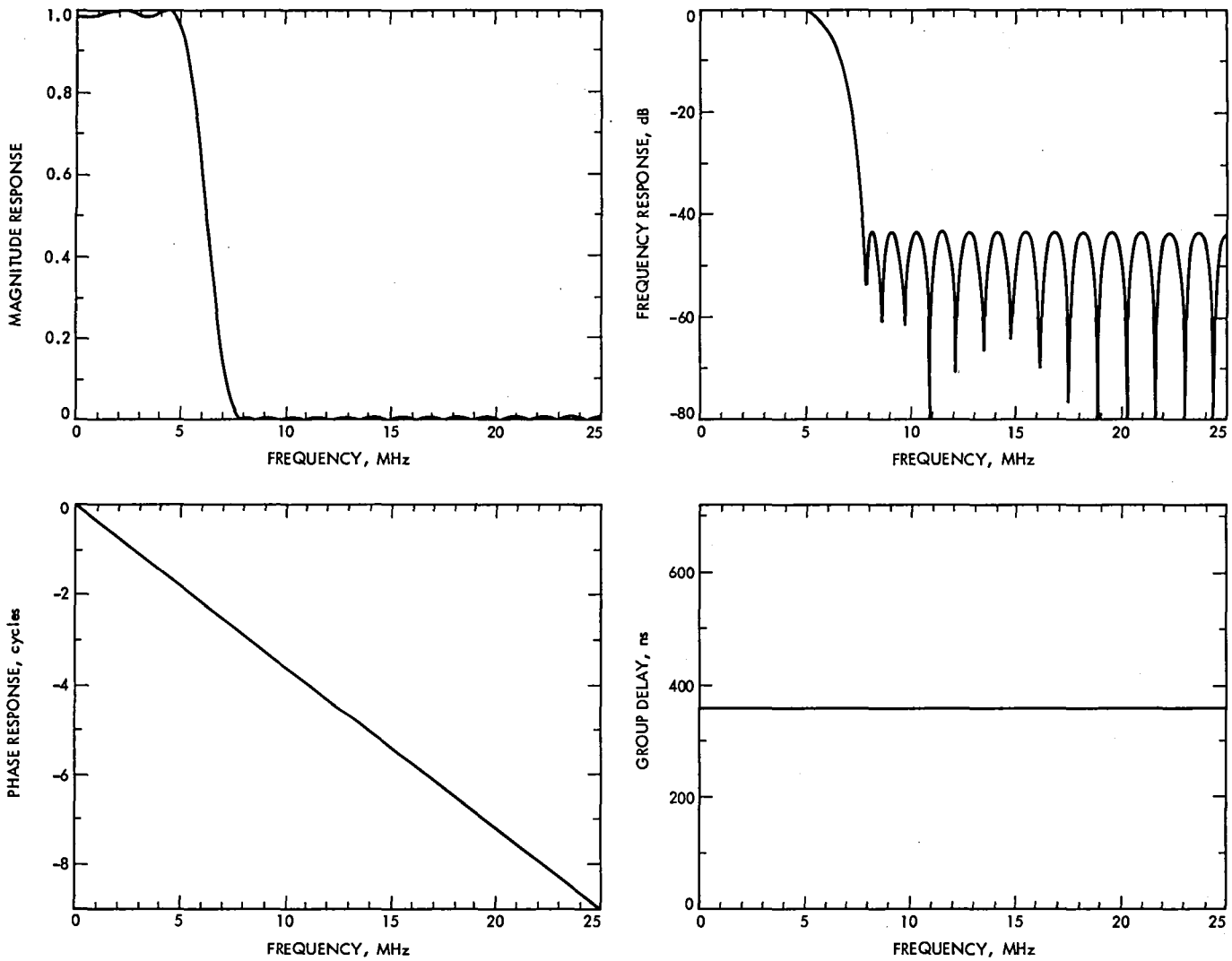

Fig. 4. Digital filter: 37-tap FIR filter

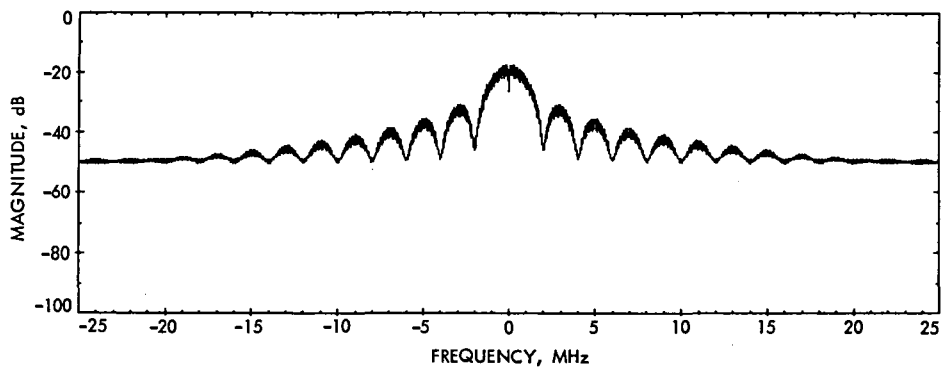

Fig. 5. Power spectrum of a binary pseudorandom code with 0.5 μs baud period

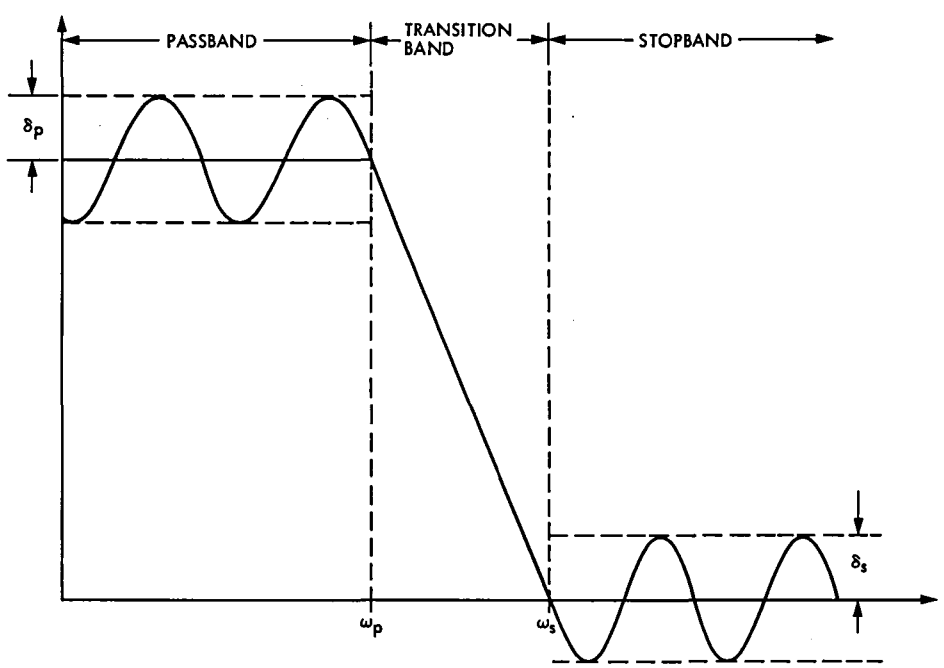

Fig. 6. Parameters of a lowpass FIR filter

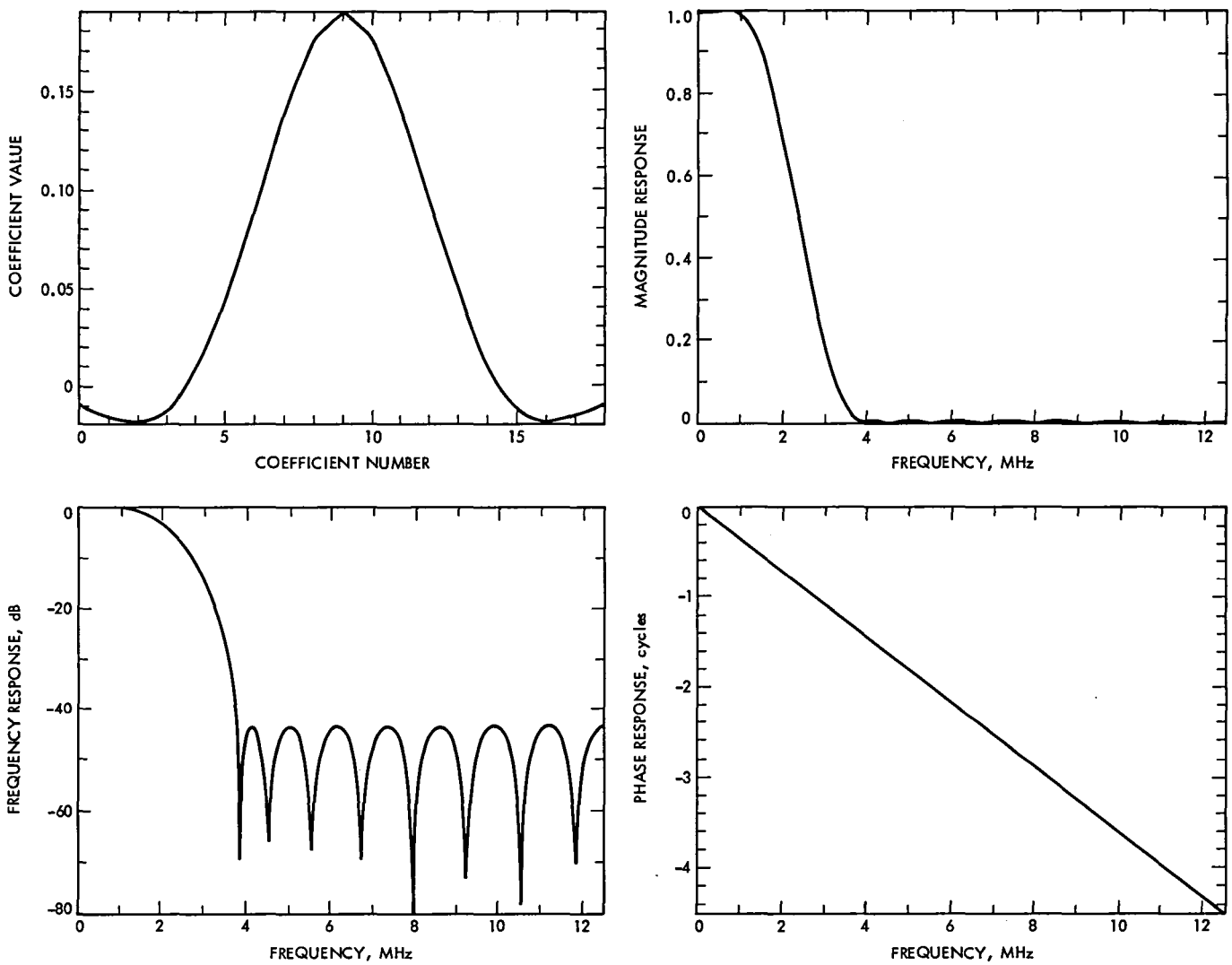

Fig. 7. The 19-tap FIR filter for the digital mixer

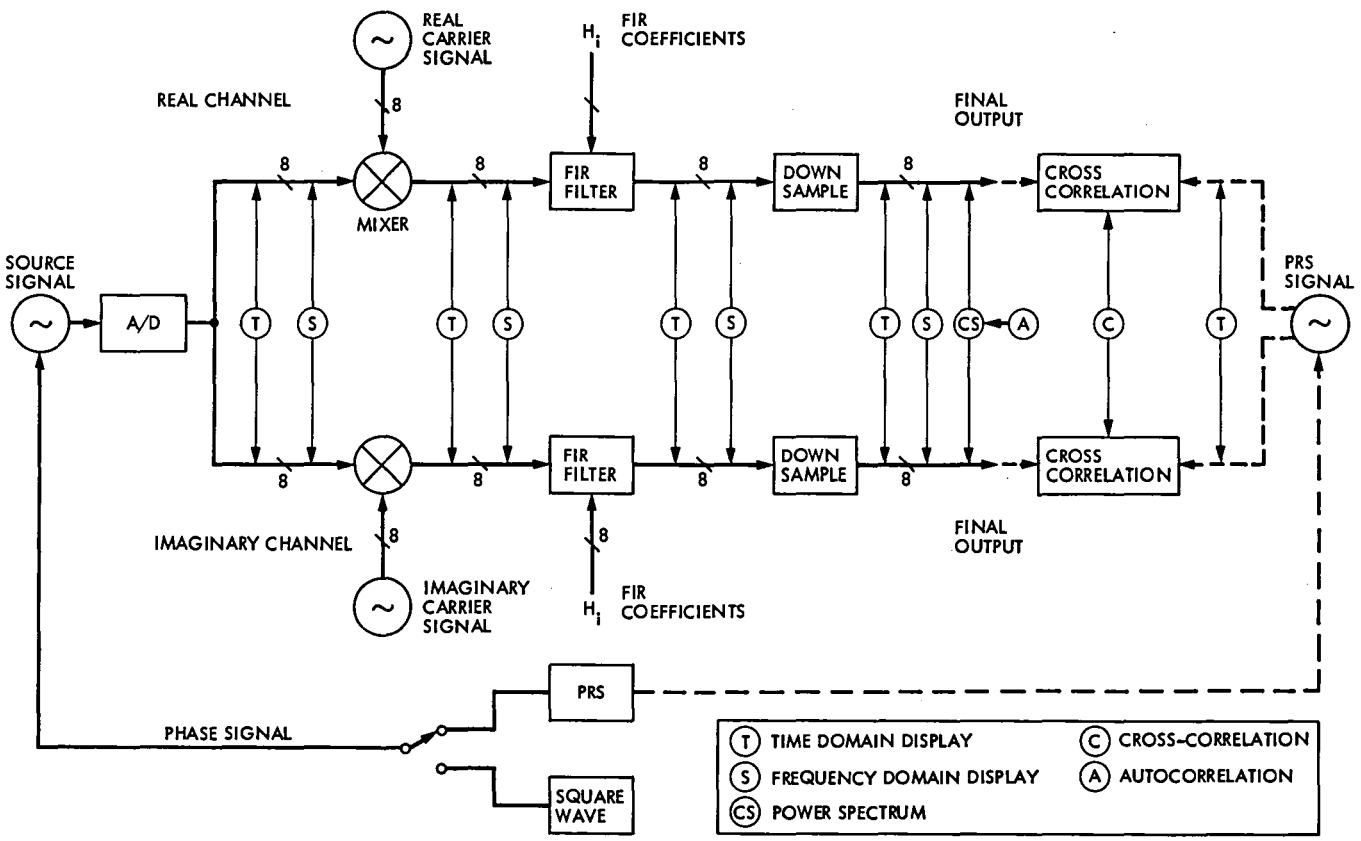

Fig. 8. Baseband mixer simulation block diagram

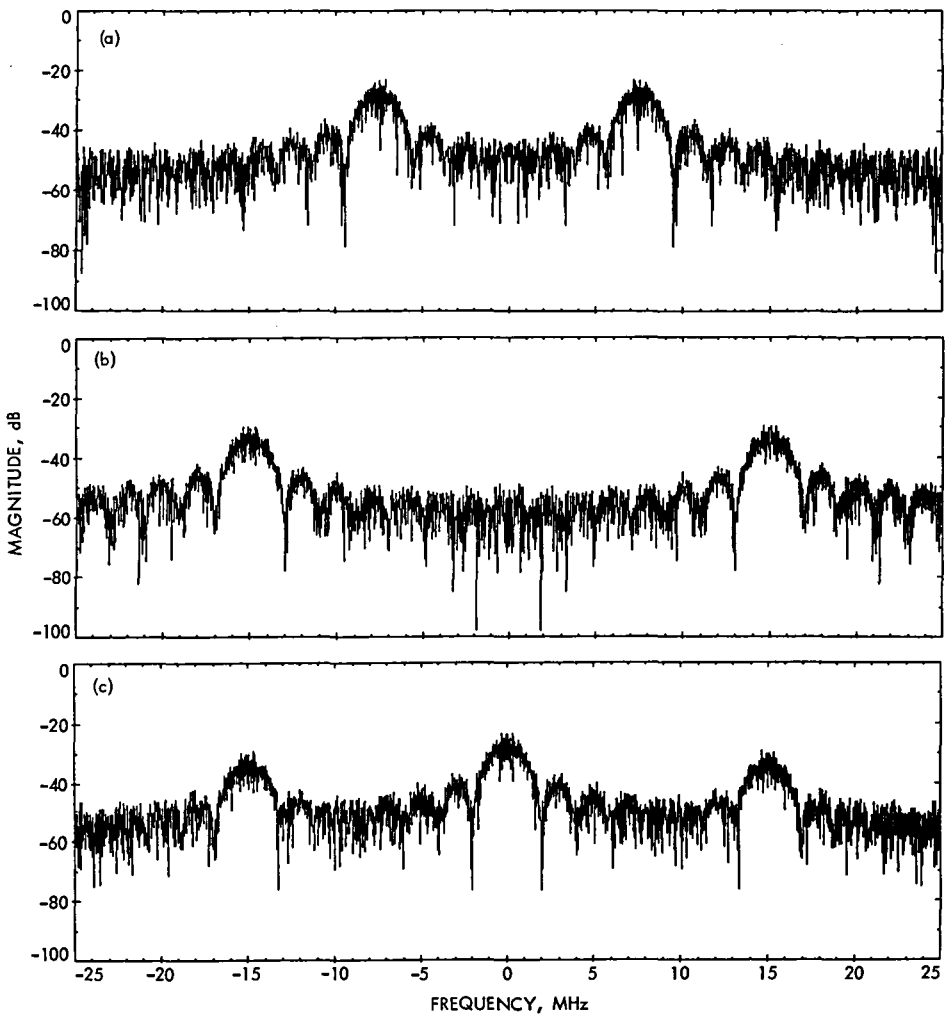

Fig. 9. Simulation results—source and mixer output spectra: (a) source signal frequency spectrum; (b) real channel, multiplier output spectrum; (c) imaginary channel, multiplier output spectrum

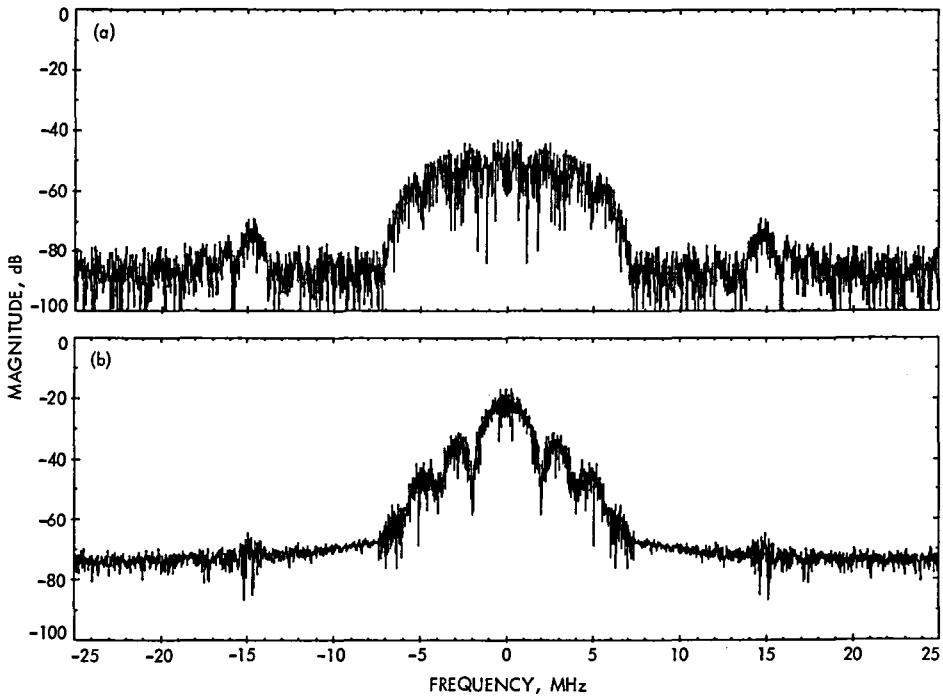

Fig. 10. Filter output spectra: (a) real channel; (b) imaginary channel

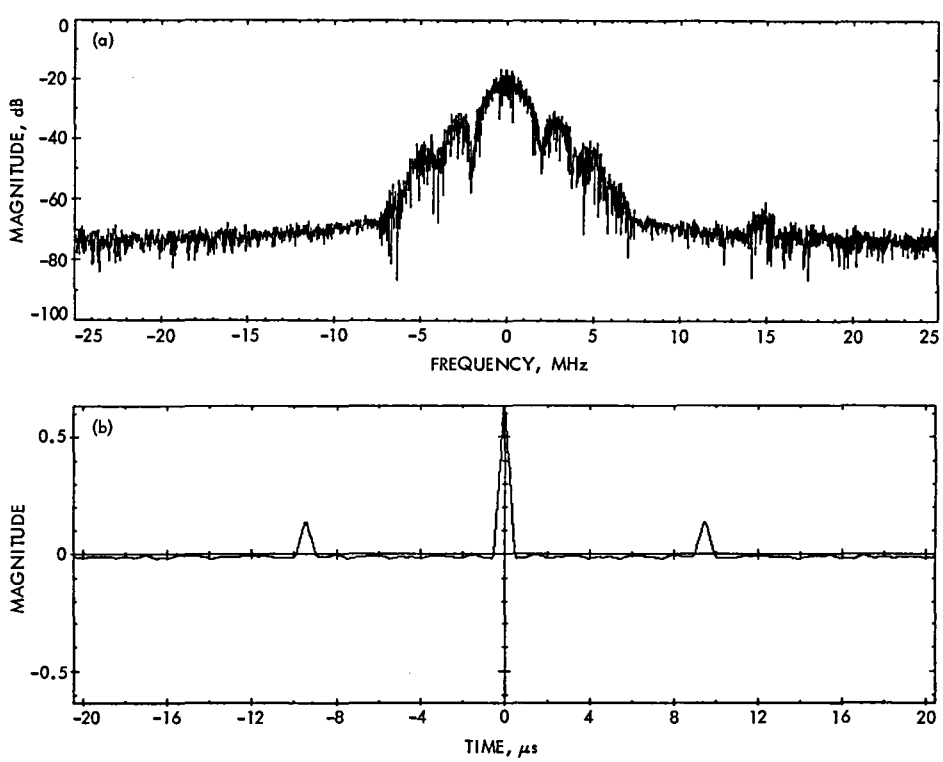

Fig. 11. Mixer output power spectrum and autocorrelation function: (a) power spectrum; (b) autocorrelation

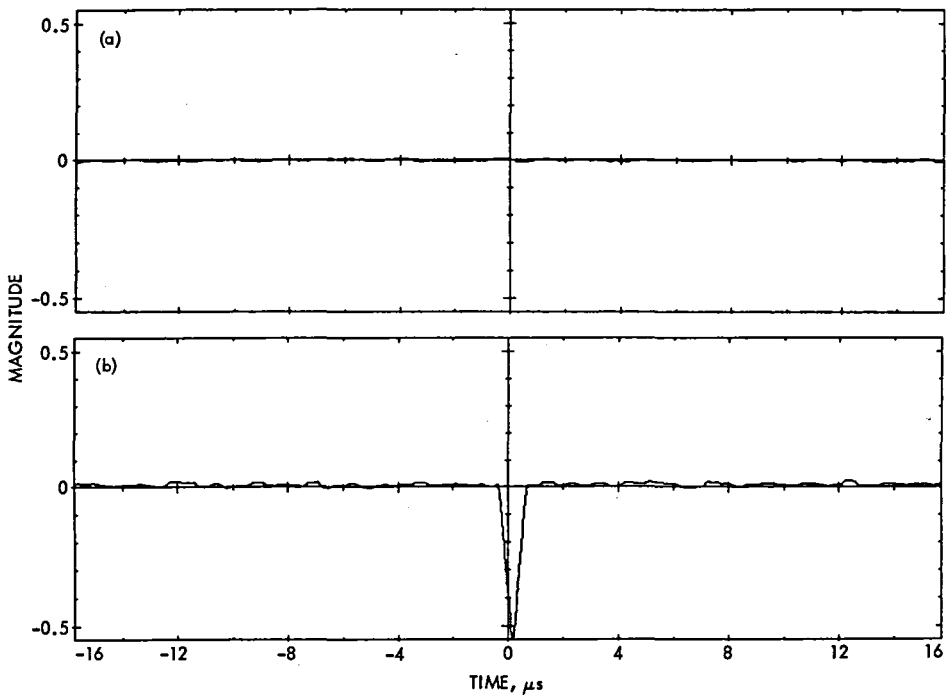

Fig. 12. Cross correlation functions, no signal averaging: (a) real channel, cross correlation; (b) imaginary channel, cross correlation

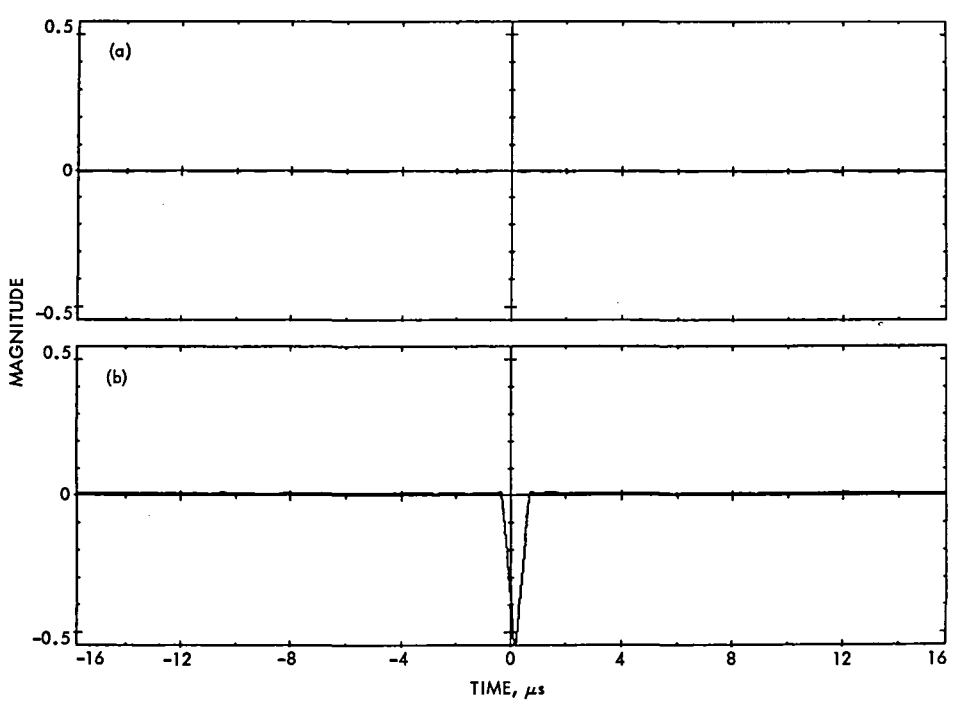

Fig. 13. Cross correlation functions, averaged 16 times: (a) real channel, cross correlation; (b) imaginary channel, cross correlation

Digital Filters for Digital Phase-Locked Loops

M. Simon and A. Mileant
Telecommunications Systems Section

An s/z hybrid model for a general phase-locked loop is proposed in this article. The impact of the loop filter on the stability, gain margin, noise-equivalent bandwidth, steady-state error and time response is investigated. A specific digital filter is selected which maximizes the overall gain margin of the loop. This filter can have any desired number of integrators. Three integrators are sufficient in order to track a phase jerk with zero steady-state error at loop update instants. This filter has one zero near z = 1.0 for each integrator. The total number of poles of the filter is equal to the number of integrators plus two.

I. Introduction

In this article, the impact of a general digital filter on the gain margin, noise-bandwidth, steady-state error and transient response of a digital phase-locked loop is investigated. For the proposed s/z-domain model of a digital phase-locked loop, a wide variety of digital filters was investigated by analysis and by simulation.

A specific type of filter is suggested which has the property of having one zero for each filter integrator. The total number of poles of this filter equals the number of integrators (poles at $z = 1$) plus two. All loop poles are forced to remain on or near the real axis for the maximum possible range of loop gain. The loop remains stable with any number of integrators. The noise bandwidth increases slightly with the number of integrators. Gain margin and transient response are almost insensitive to the number of integrators.

The proposed type of filter allows tracking very high Doppler rates with zero steady-state error (at loop update instants).

II. Loop Components

The basic components of our digital loop (see Fig. 1) are: (a) an integrate-and-dump circuit, which also serves as an analog-to-digital converter, (b) a digitally controlled oscillator (DCO), which also serves as a digital-to-analog converter, and (c) a loop filter. These components are modeled in the hybrid s/z domain as follows:

(a) Integrate-and-dump (According to Ref. 1):

$$I(s, z) = \frac{\epsilon(z)}{\phi(s)} = G_Q \frac{1}{s} \frac{z-1}{z} \tag{1}$$

(b) DCO[1]:

$$D(s, z) = \frac{\hat{\theta}(s)}{\hat{\theta}_d(z)} = \frac{1 - \exp(-sT)}{s^2} = \frac{1 - z^{-1}}{s^2} \quad (2)$$

(c) Loop Filter:

$$F(z) = \frac{\hat{\theta}(z)}{\epsilon(z)} = K_f \frac{(1 - z_1 z^{-1})(1 - z_2 z^{-1}) \ldots (1 - z_m z^{-1})}{(1 - p_1 z^{-1})(1 - p_2 z^{-1}) \ldots (1 - p_n z^{-1})} \quad (3)$$

where

G_Q represents the combined gain of the phase detectors, and other loop components and is proportional to the power of the input signal.

T is the loop update time

$\{z_i\}$ are the zeros of the loop filter

$\{p_i\}$ are the poles of the loop filter

In the actual implementation of the loop filter, there is a time delay between the instants the error signal ϵ_i is read and the estimated phase rate $\hat{\theta}_i$ is computed. This time delay is modeled as

$$T_d(s) = \frac{\hat{\theta}_d(z)}{\hat{\theta}(z)} = \exp(-sgT) \quad (4)$$

where $0 < g < 1.0$ is the normalized time delay

$$g = \frac{T_c}{T} \quad (5)$$

The term T_c is the computation time, and $\hat{\theta}_d(z)$ is $\hat{\theta}(z)$ delayed by T_c seconds.

Referring to Fig. 1, we see that

$$X(s) = \frac{\phi(s)}{s} = \frac{\theta(s)}{s} - \hat{\theta}(z)[1 - \exp(-sT)] \frac{\exp(-sgT)}{s^3} \quad (6)$$

[1]The DCO can be modeled as a Digital-to-Analog converter for which the transfer function is

$$\frac{\hat{\theta}(s)}{\hat{\theta}_d(z)} = \frac{1 - \exp(-sT)}{s}$$

Multiplying this by $1/s$ converts $\hat{\theta}(s)$ to $\hat{\theta}(s)$.

Taking the z transform of Eq. (6), we obtain[2]

$$X(z) = \left(\frac{\phi(s)}{s}\right)^* = \left(\frac{\theta(s)}{s}\right)^* - \frac{T^2}{2} \frac{[(1-g)^2 z^2 + (1 + 2g - 2g^2) z + g^2)]}{z(z-1)^2} \hat{\theta}(z) \quad (7)$$

where the asterisk denotes the z transform of the expression inside the parentheses. Equation (7) has the block diagram representation of Fig. 2. Using the above equation, together with Eqs. (1) and (3), the open-loop transfer function is

$$G(z) \triangleq \left(\frac{\hat{\theta}(s)}{s}\right)^* \frac{1}{\left(\frac{\phi(s)}{s}\right)^*} = \frac{\hat{\theta}_1(z)}{X(z)}$$

$$= G \frac{(z^2 + C_1 z + C_2)}{z^2(z-1)} F(z) \quad (8)$$

where

$$G = \frac{G_Q T^2}{2} (1-g)^2 \quad (9)$$

is the effective loop gain

$$C_1 = (1 + 2g - 2g^2)/(1-g)^2 \quad (10)$$

$$C_2 = g^2/(1-g)^2 \quad (11)$$

Using Eq. (8), the closed-loop transfer function will be

$$H(z) \triangleq \frac{\hat{\theta}_1(z)}{(\theta(s)/s)^*} = \frac{G(z)}{1 + G(z)} \quad (12)$$

III. Selection of the Loop Filter

In general, a digital filter can be expressed by the following difference equation:

$$\hat{\theta}_i = \sum_{j=1}^{n} \alpha_j \hat{\theta}_{i-j} + \sum_{j=0}^{m} \beta_j \epsilon_{i-j} \quad (13)$$

[2]In general, given a function $L(s)$, we always have

$$[\exp(-sgT) L(s)]^* \triangleq L(z, m), \quad m = 1 - g$$

where $L(z, m)$ is the modified z transform of $L(s)$. This technique is used to obtain Eq. (7) from Eq. (6).

The direct form I realization of this filter is shown in Fig. 3. Figure 4 depicts the same filter in the direct form II realization. The transfer function corresponding to Eq. (13) is

$$F(z) = \frac{\hat{\theta}(z)}{\epsilon(z)} = \frac{\beta_0 + \beta_1 z^{-1} + \beta_2 z^{-2} + \ldots \beta_m z^{-m}}{1 - \alpha_1 z^{-1} - \alpha_2 z^{-2} \ldots \alpha_n z^{-n}} \quad (14)$$

which can be factored into the pole-zero representation of Eq. (3).

With $\beta_0 = 1$ and $m < n$, Eq. (14) can be rewritten as follows:

$$F(z) = \frac{\left(z^m + \beta_1 z^{m-1} + \ldots \beta_m\right) z^{n-m}}{z^n - \alpha_1 z^{n-1} - \ldots - \alpha_n} \quad (15)$$

$$= \frac{(z - z_1)(z - z_2) \ldots (z - z_m) z^{n-m}}{(z - p_1)(z - p_2) \ldots (z - p_n)} \quad (16)$$

This filter will always have n poles and n zeros, such that $n - m$ of the zeros will be at $z = 0$.

The filter controls the following four main parameters of the phase-locked loop:

(1) Gain margin

(2) Noise-equivalent bandwidth

(3) Steady-state error

(4) Transient response

The selection of proper values for z_i and p_i is dictated by the necessity of optimizing the above loop parameters. In what follows, we will address each optimization criterion individually.

A. Stability and Gain Margin

Inserting Eq. (16) in Eq. (8) and using Eq. (12), the closed loop transfer function with an nth order filter is

$$H(z) = \frac{G(z - z_a)(z - z_b)(z - z_1)(z - z_2) \ldots (z - z_m) z^{n-m}}{z^2(z - 1)(z - p_1)(z - p_2) \ldots (z - p_n)} \ldots$$

$$\frac{}{+ G(z - z_a)(z - z_b)(z - z_1)(z - z_2) \ldots (z - z_m) z^{n-m}} \quad (17)$$

Here z_a and z_b are the roots of $(z^2 + C_1 z + C_2)$ in Eq. (8). These two zeros result from nonzero computation time. For example, assuming that $g = 0.5$ (a computation time of half an update time), then $z_a = -0.1716$ and $z_b = -5.8283$.

For the effective loop gain G changing from $G = 0$ to $G = \infty$, the poles of $H(z)$ will move starting at the location of the open-loop poles, p_i, of $G(z)$ and ending at the location of the open-loop zeros, z_i, of $G(z)$. The loop will be stable when *all* the poles of $H(z)$ are inside the unit circle in the complex z-plane. Thus, in order to increase the gain margin, given that other constraints are met, we want to place all z_i's and p_i's such that the range of G that maintains a stable loop is maximum.

In order to track high Doppler rates with zero or minimum steady-state error, the loop should have 2 or more integrators, i.e., open-loop poles at $z = 1.0$. For stability, we want these poles to move inside the unit circle with increasing G. The closer the zeros are to the point $z = 1.0$, the faster the poles at $z = 1.0$ will move inside the unit circle. Since here all gains and loop parameters are controlled digitally, there is no danger of instabilities due to drifts of gain values as is the case with analog loops. However, it should be checked that any quantization and truncation errors will not produce undesirable fluctuations in the locations of z_i and p_i.

Performing a root-locus analysis and simulation revealed that the range of allowable G values increases when the poles are forced to stay longer on the real axis. A rule of control theory states that the root locus on the real axis always lies in a section of this axis to the *left* of an *odd* number of poles and zeros. Figure 5 illustrates some root locus diagrams with the number of integrators, N, in $F(z)$ being a parameter.

Using this simple rule, the minimum number of zeros near $z = 1.0$ was determined. For each pole of $F(z)$ at $z = 1.0$, one zero is required. These $m = N$ zeros will force the poles at $z = 1.0$ to move inside the unit circle as shown in Fig. 5. Note from Eq. (8) that the system transfer function contributes one pole at $z = 1.0$. Thus, the total number of poles at $z = 1.0$ (integrators) is $N + 1$.

By trial and error, it was found that, with any number of integrators, the gain margin increases when the open loop transfer function, $G(z)$ has a minimum number of poles. Since the transfer function contributes two poles at $z = 0$ (see Eq. [8]), which try to move quite fast out of the unit circle when the loop gain is increased, it is desirable to cancel these two poles with two zeros at the origin. From Eq. (16), this implies that $n - m = 2$. Since, from the above, the number m of zeros not at the origin was selected equal to the number N of integrators, then the *total* number of poles of $F(z)$ is given by

$$n = m + 2 = N + 2 \quad (18a)$$

and $F(z)$ will be of the form

$$F(z) = \frac{(z-z_1)(z-z_2)\ldots(z-z_N)\,z^2}{(z-p_1)(z-p_2)(z-1)^N} \tag{18b}$$

Finally, using Eq. (18b) in Eq. (8) results in an open loop transfer function of the desired form, namely

$$G(z) = G\,\frac{(z-z_a)(z-z_b)(z-z_1)(z-z_2)\ldots(z-z_N)}{(z-p_1)(z-p_2)(z-1)^{N+1}} \tag{18c}$$

The order of $G(z)$ will be $N + 3$, and the degree of its numerator will be one less than that of the denominator.

The lower bound on the allowable gain G is determined by the proximity of z_i to the point $z = 1.0$. The upper bound on G is controlled by the location of the poles p_1 and p_2 since as G increases these poles move outside the unit circle. By trial and error, it was found that the poles originating at p_1 and p_2 will stay longer inside the unit circle when p_1 and p_2 are placed on the real axis between $z = -1.0$ and $z = z_a$. The maximum upper bound on G is achieved when p_1 is very close to $z = -1.0$ and p_2 is very close to $z = z_a$. The root locus of these two poles is shown in Fig. 5.

Figure 6 illustrates the impact of the location of z_1 on the loop gain margin for the case when $N = 1$.

B. Noise-Equivalent Bandwidth

The closed loop transfer function $H(z)$ of Eq. (17) can be rewritten as

$$H(z) = \frac{B(z)}{A(z)} = \frac{b_0 z^{n+1} + b_1 z^n + \ldots + b_{n+1}}{a_0 z^{n+1} + a_1 z^n + \ldots + a_{n+1}} \tag{19}$$

(Our loop has $b_0 = 0, a_0 = 1$.)

The one-sided noise-equivalent bandwidth is defined as

$$B_L = \frac{1}{2TH^2(1)}\,\frac{1}{2\pi j}\oint H(z)\,H(z^{-1})\,\frac{dz}{z} \tag{20}$$

$$= \frac{1}{2TH^2(1)}\,I_n \tag{21}$$

Let

$$\Omega = \begin{bmatrix} a_0 & a_1 & a_2 & \cdots & a_{n+1} \\ a_1 & a_0 + a_2 & a_1 + a_3 & \cdots & a_n \\ a_2 & & & & \\ \cdot & & & & \\ \cdot & & & & \\ \cdot & & & & \\ a_{n+1} & 0 & 0 & \cdots & a_0 \end{bmatrix} \tag{22}$$

and Ω_1 be the matrix formed from Ω by replacing the first column of Eq. (22) with

$$\begin{bmatrix} \sum_{i=0}^{n+1} b_i^2 \\ 2\sum_{i=0}^{n+1} b_i b_{i+1} \\ 2\sum_{i=0}^{n+1} b_i b_{i+2} \\ \cdot \\ \cdot \\ \cdot \\ 2\,b_0 b_{n+1} \end{bmatrix} \tag{23}$$

According to Ref. 2, the integral I_n is equivalent to the ratio of two determinants as follows:

$$I_n = \frac{|\Omega_1|}{a_0\,|\Omega|} \tag{24}$$

Using Eqs. (22), (23) and (24) in Eq. (21), the bandwidth vs G was calculated for the filters and gain values given in Table 1, and plotted in Figs. 7-11. For loops which are similar in their pole-zero location, increasing the number of integrators in $F(z)$ increases B_L. Adding more poles and/or zeros near $z = 0$ has an insignificant impact on the bandwidth. The impact of the location of z_1 on the bandwidth when $N = 1$ is shown in Fig. 6. B_L was computed for $G = G_{min} + 4$ dB.

C. Steady-State Error

The input to our z-domain loop (see Fig. 2) can be expressed as

$$\left(\frac{\theta(s)}{s}\right)^* = \frac{\theta_1 T z}{(z-1)^2} + \frac{\theta_2 T^2 z(z+1)}{2(z-1)^3} + \frac{\theta_3 T^3 z(z^2+4z+1)}{3(z-1)^4} + \frac{\theta_4 T^4 z(z^3+11z^2+11z+1)}{4(z-1)^5} + \ldots \quad (25)$$

where θ_1, θ_2, θ_3, θ_4 represent phase step, ramp, acceleration and jerk, respectively. Higher orders terms are assumed to be negligible.

The transfer function $H_\epsilon(z)$ is defined as

$$H_\epsilon(z) = \frac{\epsilon(z)}{\left(\frac{\theta(s)}{s}\right)^*} = \frac{G_Q(z-1)}{z(1+G(z))} \quad (26)$$

where $G(z)$ is given by Eq. (8) which results in the steady state error

$$\epsilon_{ss} = \lim_{z\to 1} \left(\frac{z-1}{z}\right) H_\epsilon(z) \left(\frac{\theta(s)}{s}\right)^* \quad (27)$$

Let $F(z)$ be of the form in Eq. (18b). Then, inserting Eqs. (25) and (26) in Eq. (27) and simplifying, we obtain

$$\epsilon_{ss} = \lim_{z\to 1} \left[\frac{\theta_1 T z}{(z-1)^2} + \frac{\theta_2 T^2 z(z+1)}{2(z-1)^3} + \frac{\theta_3 T^3 z(z^2+4z+1)}{3(z-1)^4} + \frac{\theta_4 T^4 z(z^3+11z^2+11z+1)}{4(z-1)^5}\right] \times \frac{G_Q(z-p_1)(z-p_2)(z-1)^{N+3}}{z^2[(z-1)^{N+1}(z-p_1)(z-p_2) \ldots + G(z-z_a)(z-z_b)(z-z_1)\ldots(z-z_N)]} \quad (28)$$

With $N = 1$, θ_3 (phase acceleration) will be tracked with finite steady-state error, but θ_4 (phase jerk) will generate infinite steady-state error. With $N = 2$, θ_4 will be tracked with finite steady-state error. With $N \geqslant 3$ the steady-state error due to phase jerk will be zero. Table 2 lists values of steady-state error for different values of N. Note that the proximity of z_i to the point $z = 1.0$ increases the value of the steady-state error.

Steady-state *phase error*, ϕ_{ss}, can be readily obtained from ϵ_{ss}, using the relation

$$\phi_{ss} = \frac{\epsilon_{ss}}{G_Q T} \quad (29)$$

which is equivalent to

$$\phi_{ss} = \frac{\epsilon_{ss} T(1-g)^2}{2G} \quad (30)$$

by using Eq. (9).

D. Transient Response

In general, for a digital loop with a large number of poles and zeros, it is not easy to calculate the transient response. If, for some specific gain value, the loop has only two dominant poles, then the natural frequency, damping ratio and settling time can be assessed from the second-order loop equations. Otherwise, an inverse z-transform operation has to be performed on the product of the loop transfer function and the step input. There are three methods available for this inverse z-transformation: integration, partial fraction expansion and long division. In our analysis, we have chosen the last of the three.

By performing synthetic (long) division on the ratio of two polynomials in

$$\epsilon(z) = \frac{G_Q(z-1)}{z(1+G(z))} \times \frac{\theta_1 T z}{(z-1)^2} = \epsilon_1 z^{-1} + \epsilon_2 z^{-2} + \epsilon_3 z^{-3} + \ldots \quad (31)$$

the time response of the loop with a step input is obtained at time t_1, t_2, t_3, etc. The settling time T_s is determined when the magnitudes of ϵ_i become less than, say, 5% of the initial value for all t_i, t_{i+1}, etc. Plots of T_s vs G for a loop with filters specified in Table 1 are shown in Figs. 7-11. As can be seen from these figures, the settling time increases very sharply when the two poles on the left portion of the real axis migrate close to the unit circle (see Fig. 5). The impact of the location of z_1 on T_s for $N = 1$ is shown in Fig. 6.

IV. Conclusion

In this article, a model for a general digital-phase locked loop is proposed. The impact of a digital filter on the stability, gain margin, noise-equivalent bandwidth and time response is investigated. A specific type of digital filter is proposed which, for any desired number of integrators, has a minimum number of zeros. The strategy adopted in this analysis in optimizing

the loop performance with the digital filter consists of two steps. First, the lower and upper bounds of the allowable loop gain are obtained by placing the filter's zeros close to the point $z = 1.0$ and the two filter's poles close to $z = -1.0$ and $z = z_a$. Then, the desired bandwidth and settling time are obtained by selecting the corresponding value for the loop gain.

Table 2 lists steady-state error values vs the number of integrators of the loop filter. Making the number of integrators equal to 3, the loop can track phase jerk with zero steady-state error (at loop update instants). Figures 7 through 11 show the variation of the noise bandwidth and settling time with changing gain for different loop types.

References

1. Winkelstein, R. A., "Analysis of the Signal Combiner for Multiple Antenna Arraying," *Deep Space Network Progress Report 42-26*, January and February 1975, pp. 102–118, Jet Propulsion Laboratory, Pasadena, California.
2. Jury, E. I., *Theory and Applications of the Z-Transform Method*, R. E. Krieger, Florida, 1982.

Table 1. Proposed placement of poles and zeros for loop filters

Location of Poles and Zeros[1] of $F(z)$	Number of Integrators of $F(z)$				
	0	1	2	3	4
z_1		0.960	0.960	0.960	0.970
z_2			0.960	0.930	0.960
z_3				0.930	0.940
z_4					0.940
p_1	−0.173	−0.173	−0.173	−0.173	−0.173
p_2	−0.999	−0.999	−0.999	−0.999	−0.999
p_3		1.000	1.000	1.000	1.000
p_4			1.000	1.000	1.000
p_5				1.000	1.000
p_6					1.000
Approximate range of G	0.001 0.30	0.001 0.30	0.01 0.30	0.04 0.30	0.04 0.30

[1] $F(z)$ contains also $n - m$ zeroes at $z = 0$. In our analysis $n - m = 2$.

Table 2. Steady-state error signal vs loop type

Loop Type	Steady State Error, ϵ_{ss}		
	Phase Ramp	Phase Acceleration	Phase Jerk
1	$\theta_2(1-p_1)(1-p_2)$	∞	∞
2	0	$\dfrac{2\,\theta_3 T(1-p_1)(1-p_2)}{(1-z_1)}$	∞
3	0	0	$\dfrac{6\,\theta_4 T^2(1-p_1)(1-p_2)}{(1-z_1)(1-z_2)}$
4	0	0	0

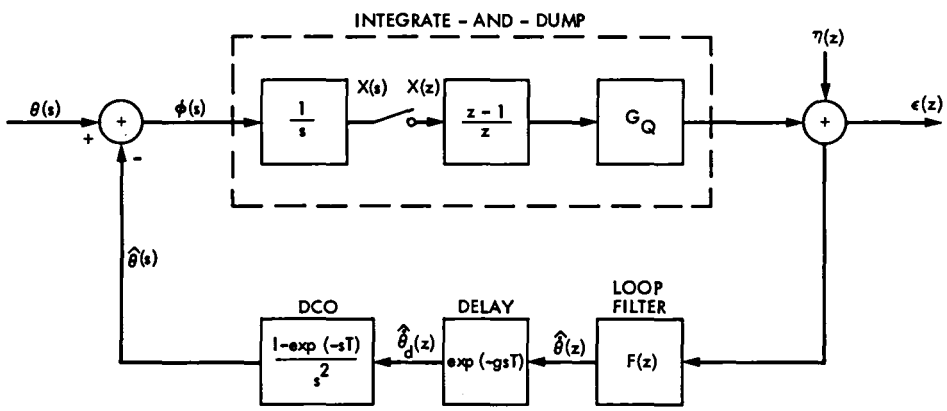

Fig. 1. Closed loop hybrid s/z diagram

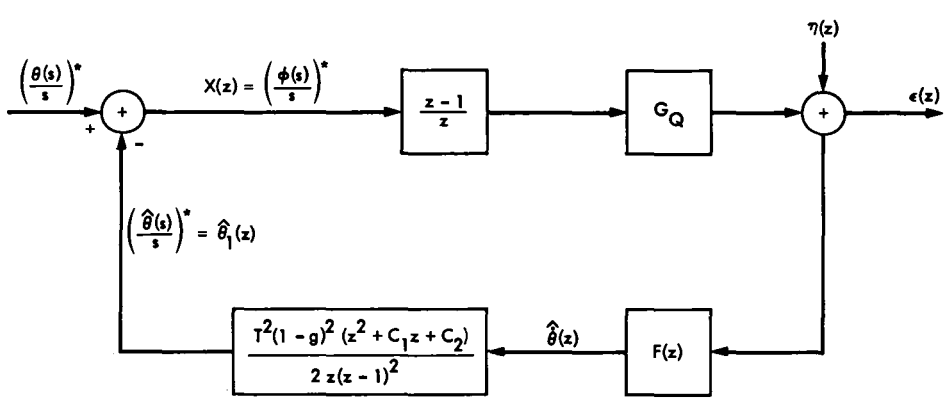

Fig. 2. Equivalent closed loop z-domain diagram

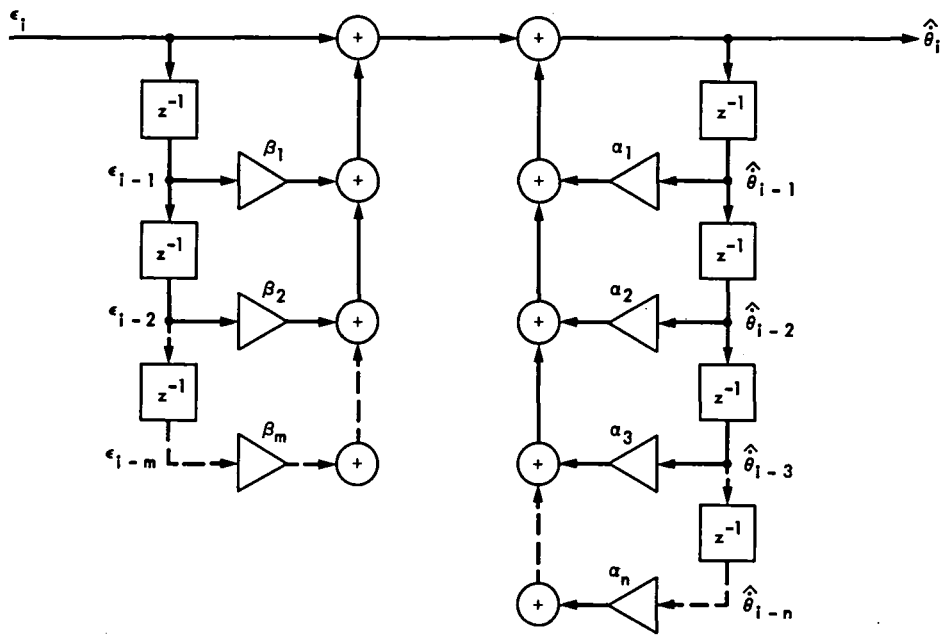

Fig. 3. Direct form I realization of $F(z)$

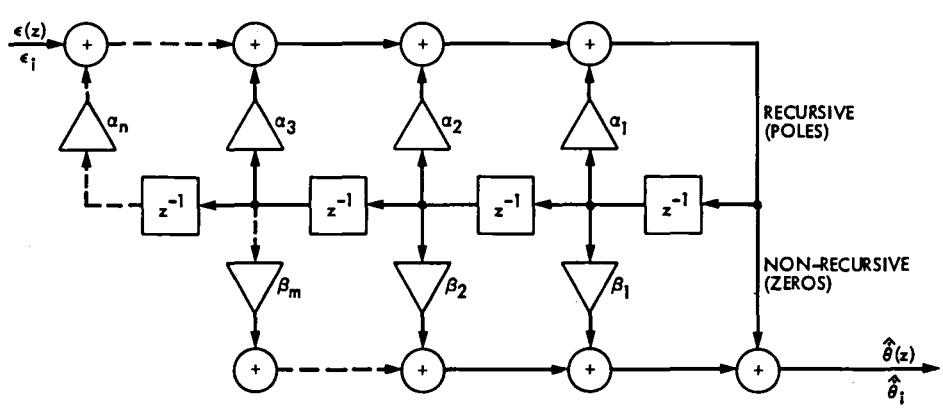

Fig. 4. Direct form II realization of $F(z)$

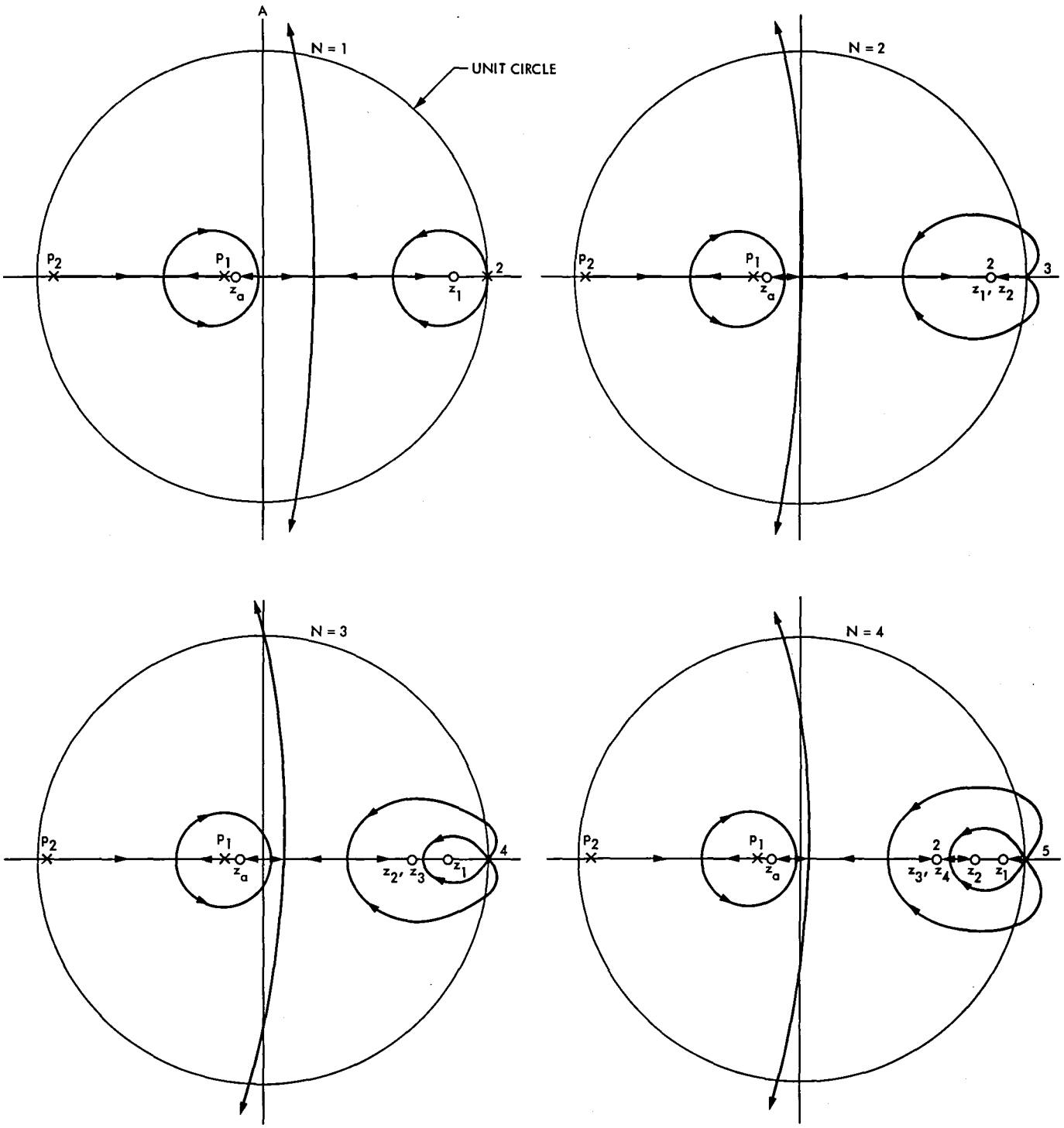

Fig. 5. Root-locus in the complex *z*-plane. *N* = number of integrators of *F*(z).

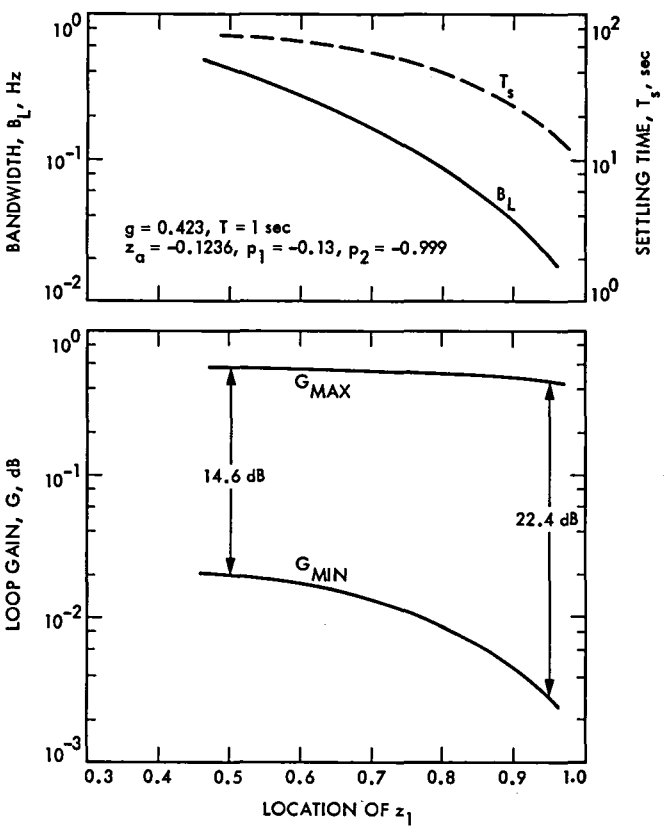

Fig. 6. G_{max}, G_{min}, B_L and T_S vs location of z_1, for $F(z)$ with 1 integrator

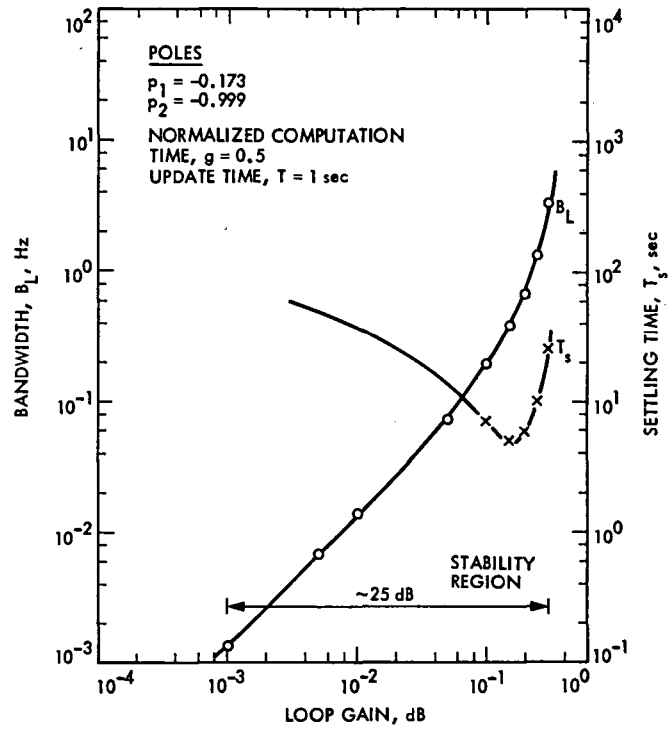

Fig. 7. Bandwidth and settling time vs loop gain. Number of integrators: 0.

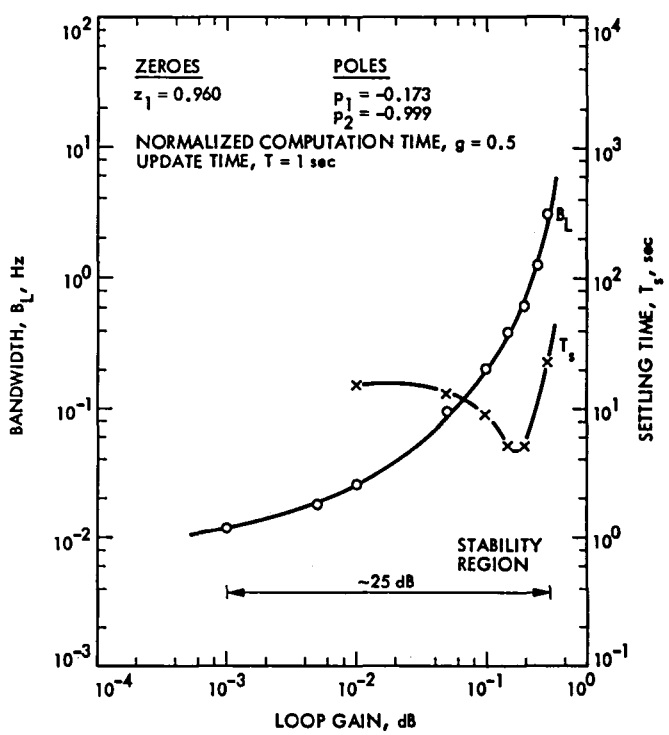

Fig. 8. Bandwidth and settling time vs loop gain. Number of integrators: 1.

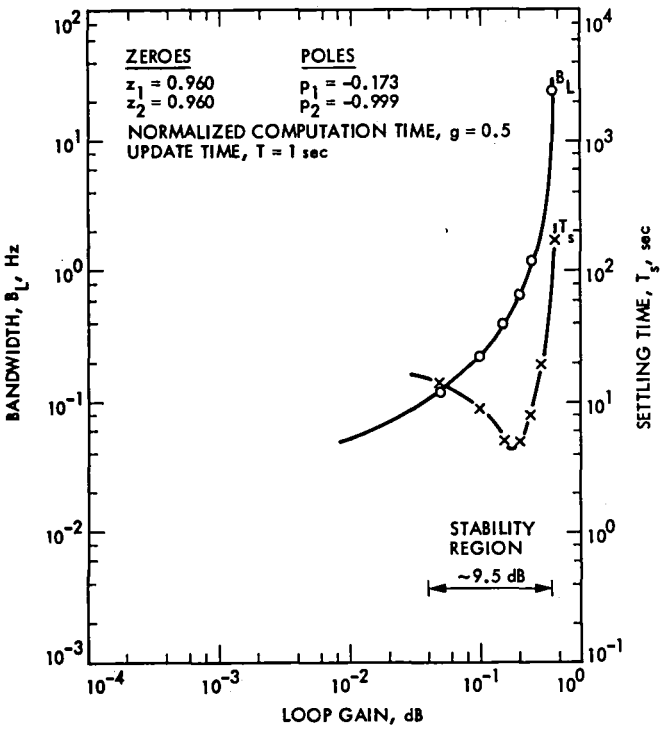

Fig. 9. Bandwidth and settling time vs loop gain. Number of integrators: 2.

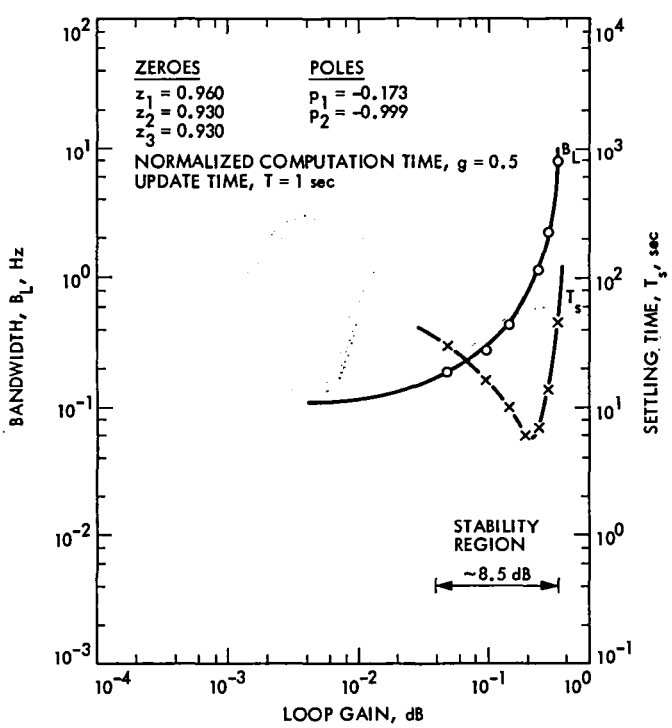

Fig. 10. Bandwidth and settling time vs loop gain. Number of integrators: 3.

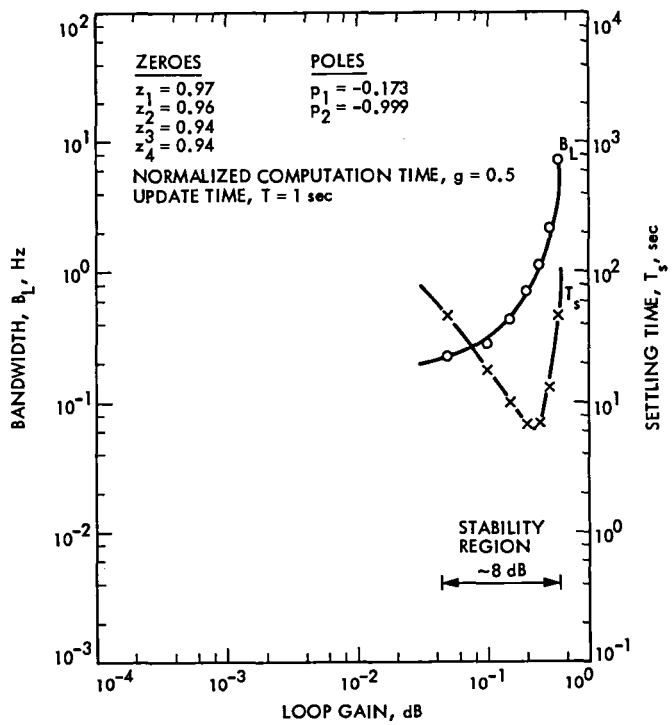

Fig. 11. Bandwidth and settling time vs loop gain. Number of integrators: 4.

Errata

M.K. Simon and A. Mileant (Telecommunications Systems Section) have submitted the following errata to their article "Performance of the DSA's Subcarrier Demodulation Digital Loop" that appeared in the *Telecommunications and Data Acquisition Progress Report 42-80,* October-December 1984, February 15, 1985:

Page No.	Eq. No.	Is	Should Be
185	63	$\dfrac{\ddot{\theta}_p T_L^3 z(z^2 - 4z + 1)}{6(z-1)^4}$	$\dfrac{\ddot{\theta}_p T_L^3 z(z^2 - 4z + 1)}{3(z-1)^4}$
186	67	$\dfrac{\ddot{\theta}_p T_L (1 - C - D)}{(A + B)}$	$\dfrac{2\ddot{\theta}_p T_L (1 - C - D)}{(A + B)}$

These corrections do not affect any other equations or figures in the article.

Maintenance of Time and Frequency in the DSN Using the Global Positioning System

P. A. Clements and A. Kirk
Communications Systems Research Section

S. E. Borutzki
DSN Control Center Operations Section

The Deep Space Network must maintain time and frequency within specified limits in order to accurately track the spacecraft engaged in deep space exploration. The DSN has three tracking complexes, located approximately equidistantly around the earth. Various methods are used to coordinate the clocks among the three complexes. These methods include Loran-C, TV Line 10, Very Long Baseline Interferometry (VLBI), and the Global Positioning System (GPS). The GPS is becoming increasingly important because of the accuracy, precision, and rapid availability of the data; GPS receivers have been installed at each of the DSN complexes and are used to obtain daily time offsets between the master clock at each site and UTC (USNO/NBS). Calculations are made to obtain frequency offsets and Allan variances. These data are analyzed and used to monitor the performance of the hydrogen masers that provide the reference frequencies for the DSN Frequency and Timing System (DFT). This article contains: (1) a brief history of the GPS timing receivers in the DSN, (2) a description of the data and information flow, (3) data on the performance of the DSN master clocks and GPS measurement system, and (4) a description of hydrogen maser frequency steering using these data.

I. Introduction

The Deep Space Network is a network of three complexes of antennas used to track spacecraft. These complexes are located approximately equidistantly around the earth at Goldstone, California; Canberra, Australia; and Madrid, Spain. Each of the complexes contains a frequency and timing system which provides the required frequencies and timing pulses throughout the complex. These three subsystems are a part of a network-wide DSN Frequency and Timing System (DFT).

The process of tracking spacecraft engaged in deep space exploration requires a highly accurate and stable timing system. Navigation parameters such as spacecraft range and relative velocity are obtained by measuring a radio signal's round-trip light time and the doppler frequency shift of the received

signal. Since the long spacecraft distances involved result in long round-trip light times, one complex may need to hand over tracking to the next complex before these measurements are completed. In addition, Very Long Baseline Interferometry (VLBI) and the ongoing study of radio signal perturbations due to various causes (planetary occultations, solar wind electron density fluctuations, gravitational waves, etc.) necessitate further requirements for a highly synchronized and syntonized DFT.

Presently, DFT requirements are to maintain time to within ±20 microseconds with a knowledge of ±10 microseconds, and to maintain frequency to within $\pm 1 \times 10^{-12}$ $\Delta f/f$ with a knowledge of $\pm 3 \times 10^{-13}$ $\Delta f/f$. In addition, time synchronization must be maintained between the DSN and Universal Coordinated Time (UTC) to ±20 microseconds, with a knowledge of ±5 microseconds (see Fig. 1). The anticipated need of the DSN for 1986-1990 is for time synchronization of 10 nanoseconds between the stations (Ref. 1). While this may not be realizable, it seems possible to have knowledge of the time offset to within 10 nanoseconds. In general, the DFT should be able to provide a value of time and frequency offset for any given past date. (Date is defined here as a specific point on a time scale; e.g., 1 January 1972, 0 h, 0 m, 10 s UTC is a date on the UTC time scale.) Therefore, the DFT must continually estimate the time and frequency offsets as well as keep past estimates and data archived.

II. Frequency and Timing Control System Description

Historically, the DFT has consisted of three fairly independent systems, each located at one of the three complexes. Various traditional methods (clock trips, VLBI, and Loran-C) were used in an attempt to keep these three systems synchronized and syntonized with respect to each other. In 1983, using the Global Positioning System (GPS) timing receivers, a tighter control system was designed (see Fig. 2). The system consists of GPS measurements, an analysis of the output of daily offsets, and, if needed, a frequency adjustment and/or clock reset. Using the GPS receivers, the DFT is capable of identifying changes in frequency on the order of 1×10^{-13} $\Delta f/f$ in a matter of a few days.

The GPS receivers are queried weekly and a TWX message is issued with the calculations of time and frequency offset. The time offset of the Goldstone complex with respect to UTC realized at the National Bureau of Standards (UTC (NBS)) is obtained from NBS so that a calculation of the other complexes with respect to UTC (NBS) can be made. The information is distributed about a week later. These data, as well as VLBI, Loran-C, and other measurements, are used to determine what action should be taken to keep the master clocks within their specified operating parameters.

III. GPS Installation and Coordination

In 1982, JPL installed two GPS timing receivers in the DSN. The receivers were located in Goldstone, California, and Madrid, Spain. The results of this installation were reported in Ref. 2. Mutual view observations were made and the time offsets were compared to those offsets derived from VLBI measurements. (In the mutual view technique, two or more receivers take time offset data from a spacecraft at the same time; ideally, the elevation of the spacecraft above the horizon is the same when viewed from all of the receivers involved.)

In 1983, a receiver was installed at the Deep Space Station near Canberra, Australia. The plan was to use the Madrid receiver in Australia and provide only a single leg again, but the Madrid receiver proved so useful it was decided to lease a receiver from NBS so the two JPL-owned receivers could be deployed overseas. By early 1983, JPL had an operating worldwide network of GPS receivers. The primary 1983 effort was to evaluate the California–Australia line. The results of this effort were reported in Ref. 3. Because of the great distances involved, both mutual view and flyover techniques were used, and comparisons were made using both VLBI and clock trips.

The GPS timing receivers at the complexes receive a timing pulse from the station's master clock, which is referenced to station time by the receiver. Each of these receivers has a modem attached which may be queried remotely; at JPL a Hewlett-Packard desk calculator (HP 9845) interfaces to a modem. (In the continental United States the regular phone system is used to query the receivers; the intercontinental queries are made using the voice communication system operated by NASA.) This calculator is used to store the receiver data on tape and to generate the weekly report of time offsets between the station clocks and between Goldstone and UTC (NBS).

JPL uses the NBS time coordination service (Ref. 4) to relate the station time at Goldstone, California, to UTC (NBS). These data are obtained in two forms: NBS provides a monthly report, and daily offsets are available by telephone from a computer at NBS. The NBS service provides the raw measurement data, a daily filtered estimate, a monthly filtered estimate, Allan variance plots, and other useful data about the performance of the JPL clock. This service eliminates the technical need for regular clock trips between JPL and NBS. The regular clock trips are still maintained, but they may be

eliminated as operational confidence is gained in the performance of the GPS timing receivers.

In order to ensure that a time and frequency offset can be estimated for any past date, all of the data taken from the receivers are archived. Presently, the data accumulation rate amounts to about 2 megabytes per year. It is estimated that a maximum rate would be 6 to 8 megabytes per year. This small amount of data is easily handled by a personal computer, while several years of data can be stored on a hard disk and backed up using either flexible diskettes or magnetic tape.

All of the data presented in this paper were taken using the common view technique. For the data taken between Goldstone, California, and NBS (located at Boulder, Colorado), the elevation angles of the spacecraft were above 60 degrees. The Goldstone, California, to Madrid, Spain, angle was usually 40 to 45 degrees elevation – still quite high above the horizon. On the other hand, the mutual view between Goldstone, California, and Canberra, Australia, was approximately 18 degrees above the horizon, which presents a substantial problem with respect to variations in group delay due to the earth's atmosphere. While these problems could be largely overcome by using a flyover or long-arc technique (Ref. 3), because of computational difficulties, this method was not used as a normal procedure in 1984.

As Fig. 3 demonstrates, the application of a Kalman smoother filter substantially improves the standard deviation for shorter sampling times on the short baseline (less than 1000 km) between Boulder, Colorado, and Goldstone, California. The longer baselines between California and Spain and between California and Australia promise to show the same sort of improvement with the application of appropriate Kalman smoothers.

Figure 4 shows a comparison of the Allan variance of the data between California and Australia and between California and Spain. At 8 days both of the standard deviations are near in value to that of the shorter Boulder–Goldstone baseline. Presumably, the greater amount of noise associated with the California to Australia measurement is caused by the low observation angles. An analysis shows a substantial amount of white phase noise, which implies that a Kalman smoother should help considerably.

IV. Analysis

The synchronization and syntonization of the DSN master clocks are accomplished by analyzing the time offset data obtained from all available sources. These sources include the GPS, VLBI (interstation), Loran-C (Goldstone and Madrid), TV line 10 (Canberra), and the local backup clocks at each station. (Time offset rates are also obtained from the GPS and VLBI measurements, but are not discussed in this article.) These unfiltered time offset data and the data provided by the NBS Time and Frequency Bulletin, the USNO Series 4 Bulletin, and Australia's Department of Resources and Energy Division of National Mapping (NATMAP) Bulletin E are entered into a computer database at JPL. Any events, whether occurring at the station, NBS or USNO, are noted in the data files.

Estimates of frequency offsets for the clocks with respect to each other and to UTC (NBS/USNO) are made on a regular basis. These offsets are calculated by a least-squares linear fit on segments of the raw time offset data. The average time offset rate over the length of the fit segment is taken to be the relative frequency offset between the clock oscillators. The standard deviation of linear fit residuals is also calculated to determine the confidence of the calculation. Second-order effects (frequency drift) are estimated by the changes in the average time offset rate over a period of time; this is more difficult to determine because it requires relatively long periods of unperturbed clock operation. Because there have been both explainable and unexplainable perturbations in the hydrogen maser operating frequency at all of the stations, accurate determination of frequency drift has not yet been possible.

The results of the measurements and calculations are studied to determine how the master clocks are performing with respect to the specification requirements. All known events are taken into account for this appraisal. For any unexplained time steps or frequency shifts, the station personnel are asked to provide any additional information which may help to uncover the reason for the behavior. Based on all of this information, time and/or frequency adjustments are proposed.

The decision to change the output frequency of a hydrogen maser is made by JPL personnel in charge of the standards. The method and the procedures to offset the frequency by the desired amount are determined using the history of that particular maser. The station activity schedule is consulted to find a time when there will be minimal impact on operations, then a TWX containing information on the proposed adjustment is issued to the station and to interested JPL personnel. This TWX includes a brief summary of the performance which prompted the action, the instructions for accomplishing the frequency adjustment, and the station clock reset instructions (if any). After the work has been completed, the station confirms the operation by TWX. The clock performance is watched closely after the procedure to determine hydrogen maser adjustment parameters and verify accuracy.

The results of the maintenance of time and frequency in the DSN using the GPS may be seen in the time offset data

shown in Figs. 5 through 8. The particular timespan chosen (December 11, 1983, through June 28, 1984) is representative of what has been accomplished with this system. All events and the results of the linear fits on the time offset data are presented in Tables 1 through 3. (UTC (NBS) was chosen as a reference so that the events at each station may be seen more clearly.) As is evident from the data, the hydrogen maser frequency standard clock at each complex has been maintained to within the synchronization and syntonization requirements with respect to both an external time scale and to the other clocks in the DFT.

One goal in the implementation of the GPS was to allow more stringent frequency controls on each hydrogen maser. The results of four planned frequency adjustments may be seen in Table 4. As is discussed under clock correction methods, only a synthesizer adjustment will vary the operating frequency by a precisely known amount. Therefore, the results seen in the table were considered successful.

Of particular interest to JPL hydrogen maser standards personnel is the sensitivity of the standards to environmental changes in the field. The parameters most likely to vary and cause a disturbance are room temperature and the local magnetic field. Although the Deep Space Stations provide a controlled environment, there are occasional disturbances which are either unforeseeable or unavoidable. The events occurring at Goldstone on the 75th day of 1984 (84075) and at Madrid (84080) are examples of this. There was an unplanned temperature increase in the maser room at Goldstone, accompanied by extensive equipment movement in the adjoining room, which may have affected the magnetic environment. At Madrid, a modification kit was installed in the maser and a cesium clock was removed from a neighboring rack. There was also some activity in the room in Canberra which may have affected maser behavior, although the effects are not as definite. As more data are collected and correlated to the changes in the operating environment, effects can be predicted and appropriate steps can be taken to prevent disturbances. Planned upgrades to the frequency standards rooms and more strictly limited access to these areas will improve these situations.

The maser failure in Madrid (84054) is fortunately a relatively rare occurrence. In this case, the problem was found to be a marginally low hydrogen pressure setting. After the pressure was increased, the maser returned to normal operation with no frequency change. Currently, the DSN has only one hydrogen maser at each site; backup is provided by a cesium standard. An additional hydrogen maser is planned for each location, and this will minimize the impact to data quality in the event of a prolonged maser failure.

The behavior of the hydrogen maser in Canberra is least understood. During this timespan there were no known events which would have produced frequency changes except for the frequency adjustments at NBS. This particular maser had undergone work at the Smithsonian Institution Astrophysical Observatory (SAO) and was returned to the station on 83320. From the GPS data, it appears to have decreased in frequency until approximately 84120. (In the past, the usual aging rate seen in an SAO maser was +3 to +5 $\times$ 10^{-15}/day.) Even with a frequency aging rate of only +1 $\times$ 10^{-15}/day, the frequency offset should have reached zero in about 60 days. But the time offset data and the associated linear fits show that it took approximately 150 days for this to happen, which would correspond to an aging rate of only +0.4 $\times$ 10^{-15}/day. When the NBS adjustments are taken into account (they were made in the negative direction for the most part), they show an even lower aging rate for the Canberra maser. Table 5 shows the relative frequency offsets when the NBS changes are removed. The results of this calculation show that the maser is not exhibiting the usual aging seen in this type of maser, at least not during this time period. It is possible that aging effects are appearing after 84122, but it is difficult to determine without comparison to another external standard.

The relative frequency offsets obtained by the calculations described above are complicated by several factors. First, it is essential that all time steps must be properly noted so that a fit is not made over any discontinuities. Second, the fit timespans must be chosen carefully so that misleading information is not obtained because of frequency shifts. Both the low and high frequency noise on the data will cause different frequency offset results, depending on the period chosen for the fit (see footnote b, Table 2). This is especially important when determining the effects of any environmental changes on the operating frequency. There are situations where no cause can be found to explain a change in the maser frequency (such as the case in Madrid after the frequency adjustment on 84146) but the data cannot be included as part of the previous fit segment. Future GPS time synchronization data should make it possible to see the more subtle changes in the behavior of a hydrogen maser. This information will allow more detailed analysis, leading to the development of a more accurate time and frequency system to meet more demanding future requirements.

V. Frequency Adjustment Methods

An important parameter when using the hydrogen maser to drive the complex clock is its long-term stability (over several months). Due to cavity aging, most hydrogen masers have a small amount of long-term drift; drift due to a change in wall shift may add to or cancel part of the cavity drift. In

addition, there are perturbations to the output frequency that are caused by changes in the ambient temperature, magnetic field, barometric pressure, humidity, etc. Constant monitoring and precise control of the maser's environment are essential to meet the DFT specifications.

Once a maser is installed in its environment, the magnetic field bias and receiver offset synthesizer are set to previously determined calibration values. The maser cavity is then carefully tuned by the spin exchange method and the frequency offset from UTC (NBS) is measured. The cavity frequency is then offset by a specified amount in the opposite direction of the drift (Fig. 9). This not only maximizes the frequency correction interval but also maintains the best average cavity frequency. Constant monitoring will then determine if non-scheduled frequency corrections are required.

The output frequency of a hydrogen maser may be changed by (1) cavity frequency adjustment, (2) receiver synthesizer offset adjustment, and (3) magnetic field bias adjustment. The range and resolution of the magnetic field adjustment are adequate to steer the output frequency. This adjustment is generally not used for this purpose because of its difficulty. Rather, an optimum magnetic field bias is initially determined and maintained for calibration. This adjustment offsets the hydrogen line frequency.

The receiver offset synthesizer adjustment is easily performed and does not disturb continuous operation of the maser if done in small increments (no phase steps are introduced). Resolution and range vary among maser types. The synthesizer is used to initially calibrate the maser's output frequency. Depending on the various systematic frequency offsets such as wall shift, each maser will have a unique synthesizer calibration setting. This adjustment offsets the receiver output from the hydrogen line frequency.

The cavity frequency adjustment is easily performed in the field and continuous operation of the hydrogen maser is not affected. Resolution is 2×10^{-16} to 2×10^{-14}, depending on the maser type. Range is 1×10^{-10} to 5×10^{-10}. Frequency change is instantaneous with varactor types or has a 5- to 24-hour time constant with thermal types. The cavity adjustment has a pulling effect on the line frequency (pulling factor Q-cavity/Q-line).

As previously mentioned, the cavity is initially tuned by the spin exchange method and the hydrogen maser is calibrated. Subsequent changes in hydrogen maser output frequency have been found to be due primarily to cavity aging and environmentally induced cavity shifts. Thus, it makes sense to correct a maser's frequency by readjusting the cavity only.

During 1984, the method described above was used to steer the hydrogen maser with reference to UTC (NBS) using the GPS. Spin exchange tuning was performed about once a year in order to determine total cavity shift and long-term behavior of the hydrogen line with respect to UTC.

VI. Problems Associated with the Present Control System and Proposed Solutions

A major problem is caused by noise factors and associated inaccuracies in the data. The GPS timing measurements have noise associated with them for several reasons. First, there is well-known noise that is intrinsic to the GPS (such as ephemeris errors, ionospheric errors, etc.). In addition, there is noise caused by the operation of the receivers; i.e., poor estimates of time offset are caused by an inexact mutual view, differences in elevation angles for the spacecraft at different receivers, and missing readings or readings averaged incorrectly. If a system of receivers is to be used to exploit the intrinsic accuracy and precision of the GPS, more accurate coordination among the receivers is required and more sophisticated analysis of the data is needed.

Over the course of the past year, about 20% of the days have had no GPS estimate of clock offset between the complexes provided by the GPS. The most common cause of missing data was power outages at the complexes. The receivers normally store less than a week's data in the failsafe memory, so if they are queried only once a week and there is a power failure, some of the data will probably be lost. The Goldstone receiver was relocated to a temporary location while major reconfigurations were being made at the Complex. This situation has now been changed and the receiver is presently in its permanent location, powered by an uninterruptible power system, as are the master clock and the frequency standards. It has become obvious that control must be improved over temperature and magnetic variations in the frequency standards environment. Security must be improved to limit personnel access to the area, and movement of equipment near the frequency standards.

VII. Conclusions

Using the GPS timing receivers has proven to be a cost-effective and reliable method to coordinate time and frequency to meet the requirements of the DSN. The performance of the master clocks was monitored on an almost daily basis. Frequency shifts and time jumps that were unexpected and in some cases unexplained were observed in the clocks. The hydrogen masers responded to frequency adjustments within

the expected limits of knowledge of their performance behavior. Control of the time and frequency offset of the clocks was established to within the limits of the performance requirements of the DSN. It appears that with improved techniques the hydrogen maser master clocks can be controlled to much closer tolerances.

Acknowledgment

The authors wish to thank the personnel at the DSN stations for their assistance in the implementation effort, specifically Sr. D. Munoz, Madrid, Spain; Mr. J. Myers, Goldstone, California; and Mr. J. Wells, Canberra, Australia. Also, thanks to Mr. D. Allan, Mr. D. Davis, and Dr. M. Weiss of NBS for their technical assistance.

References

1. Kuhnle, P. F., and Sydnor, R. L., "Present and Future Frequency and Timing Capabilities of the Deep Space Network," *Journal De Physique*, Colloque C8, Supplement No. 12, December 1981, p. 42.

2. Clements, P. A., "Global Positioning System Receivers in the DSN," *Proceedings of the Fourteenth Annual Precise Time and Time Interval (PTTI) Applications and Planning Meeting*, NASA Conference Publ. 2265, 1982, p. 517.

3. Luck, J. McK., Woodger, J. R., Wells, J. E., Churchill, P., and Clements, P. A., "First Results of GPS Time Transfer to Australia," *Proceedings of the Fifteenth Annual Precise Time and Time Interval (PTTI) Applications and Planning Meeting*, NASA Conference Publ. 7962, December 6-8, 1983, p. 87.

4. Stein, S. R., Kamas, G., and Allan, D. W., "New Time and Frequency Services at the National Bureau of Standards," *Proceedings of the Fifteenth Annual Precise Time and Time Interval (PTTI) Applications and Planning Meeting,* NASA Conference Publ. 7962, December 6-8, 1983, p. 17.

Table 1. Goldstone versus UTC (NBS) relative frequency offsets

Event	Timespan (YYDDD)	$\Delta f/f$ ($\times 10^{-13}$)	Sigma	Comments
	83345-84008	2.36	0.04	Start
1	84009-84011	6.41	0.30	Backup cesium standard online during maser frequency adjustment (spin exchange tune); time step due to switchover
2	84012-84030	0.13	0.05	Maser prime and clock reset
3	84030-84060	0.20	0.02	NBS frequency adjustment of $+0.88 \times 10^{-14}$
4	84061-84072	0.02	0.02	NBS frequency adjustment of -1.41×10^{-14}
5	84075-84091	2.58	0.12	Temperature change in maser room and equipment movement in adjoining room
6	84092-84113	2.81	0.07	NBS frequency adjustment of -2.31×10^{-14}
7	84115-84121	3.39	0.08	Maser maintenance in response to frequency change on DOY 75 (magnetic field bias adjustment); time step due to switchover
8	84122-84123	–	–	NBS frequency adjustment of -2.31×10^{-14}
9	84124-84152	5.65	0.04	GPS clock resynched to station clock (at this site only, the GPS uses a different frequency counter than the station)
10	84153-84163	6.68	0.10	NBS frequency adjustment of -2.31×10^{-14}
11	84167-84173	-1.33	0.06	Maser frequency adjustment (cavity) and clock reset

Table 2. Canberra versus UTC (NBS) relative frequency offsets

Event	Timespan (YYDDD)	$\Delta f/f$ ($\times 10^{-13}$)	Sigma	Comments
	83346-84015	-0.61	0.03	Start
1	84033-84060	-1.34	0.05	NBS frequency adjustment of $+0.88 \times 10^{-14}$
2	84061-84091[a]	-1.51	0.09	NBS frequency adjustment of -1.41×10^{-14}
3	84092-84121	-1.69	0.06	NBS frequency adjustment of -2.31×10^{-14}
4	84122-84152[b]	-1.22	0.05	NBS frequency adjustment of -2.31×10^{-14}
5	84153-84172[a]	0.19	0.07	NBS frequency adjustment of -2.31×10^{-14}

[a]Maintenance work was done on the backup cesium clock located in the same vicinity on days 83-86 and 157. The effect on the maser is unknown.

[b]The following is an example of how the results depend on the timespan chosen for the fit:

84122-84129	-0.86	0.17
84136-84141	-2.25	0.32
84146-84152	-0.49	0.44

Table 3. Madrid versus UTC (NBS) relative frequency offsets

Event	Timespan (YYDDD)	$\Delta f/f$ ($\times 10^{-13}$)	Sigma	Comments
	83345-83360	7.19	0.04	Start
1	83364-84030	-0.15	0.04	Maser frequency adjustment (cavity) and clock reset
2	84033-84053	-0.08	0.10	NBS frequency adjustment of $+0.88 \times 10^{-14}$
3	84055-84060	–	–	Maser source failure; maser restarted and clock reset
4	84061-84072	-0.15	0.04	NBS frequency adjustment of -1.41×10^{-14}
5	84080-84091	1.34	0.10	Maser modification kit installed; cesium standard removed from nearby rack
6	84092-84121	2.76	0.14	NBS frequency adjustment of -2.31×10^{-14}
7	84122-84142	2.83	0.19	NBS frequency adjustment of -2.31×10^{-14}
8	84146-84152	-1.74	0.28	Maser frequency adjustment (cavity)
9	84153-84173	-0.23	0.05	NBS frequency adjustment of -2.31×10^{-14}

Table 4. Results of the hydrogen maser frequency adjustments (change in relative frequency with respect to NBS)

Date (YYDDD)	Complex	Goal ($\times 10^{-13}$)	Result ($\times 10^{-13}$)	Method of adjustment
83362	Madrid	-8.5	-7.3	Cavity frequency
84009	Goldstone	-3.0	-2.2	Magnetic field, receiver synthesizer, and cavity frequency (spin exchange tune)
84144	Madrid	-5.0	-4.6	Cavity frequency
84166	Goldstone	-8.4	-8.0	Cavity frequency

Table 5. Effect of the NBS frequency adjustments on the Canberra hydrogen maser relative frequency offsets

Timespan (YYDDD)	NBS adjustments included $\Delta f/f$ ($\times 10^{-13}$)	NBS adjustments removed $\Delta f/f$ ($\times 10^{-13}$)
83346-84015	-0.61	-0.61
84033-84060	-1.34	-1.25
84061-84091	-1.51	-1.56
84092-84121	-1.69	-1.97
84122-84152	-1.22	-1.73
84153-84172	+0.19	-0.06

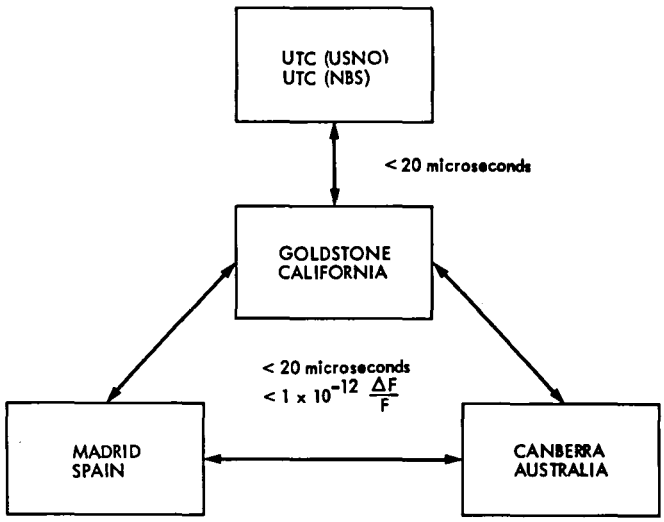

Fig. 1. DFT system functional block diagram

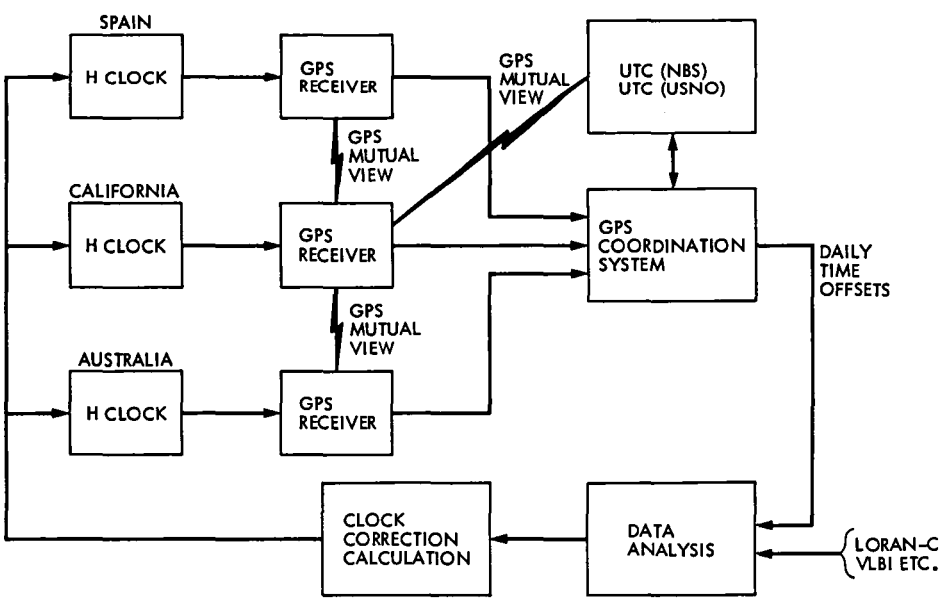

Fig. 2. Frequency and timing control system

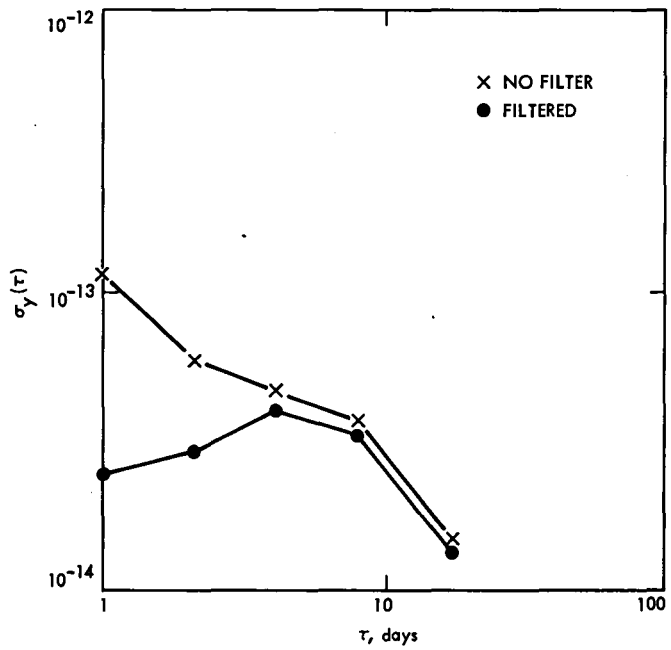

Fig. 3. Allan variances of Goldstone–UTC (NBS) before and after Kalman filter

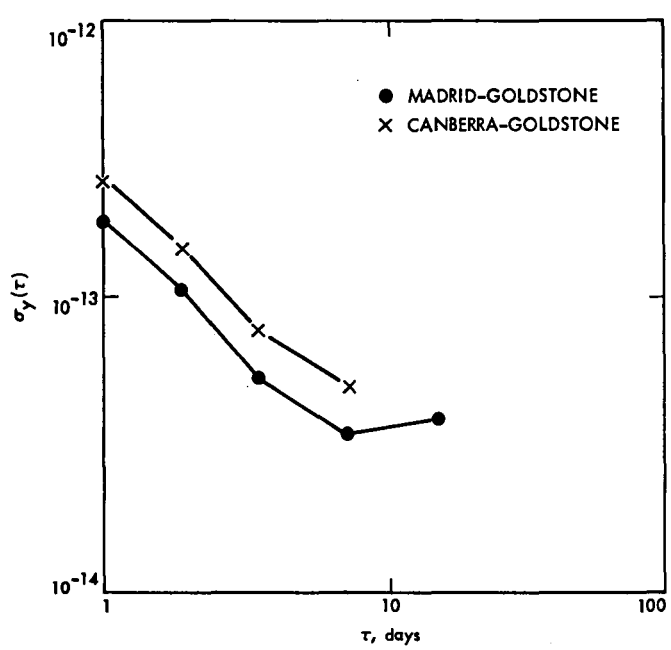

Fig. 4. Allan variances of Spain–California and Australia–California

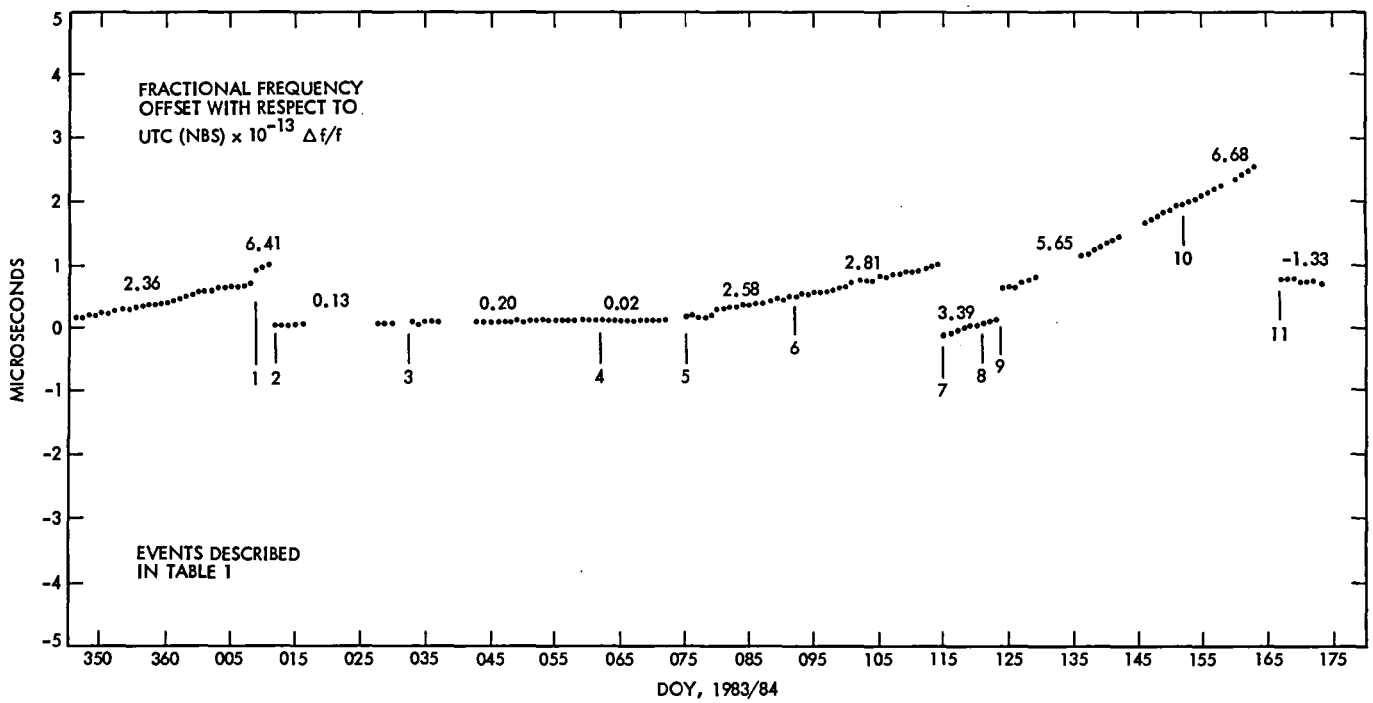

Fig. 5. Time offset, Goldstone versus UTC (NBS)

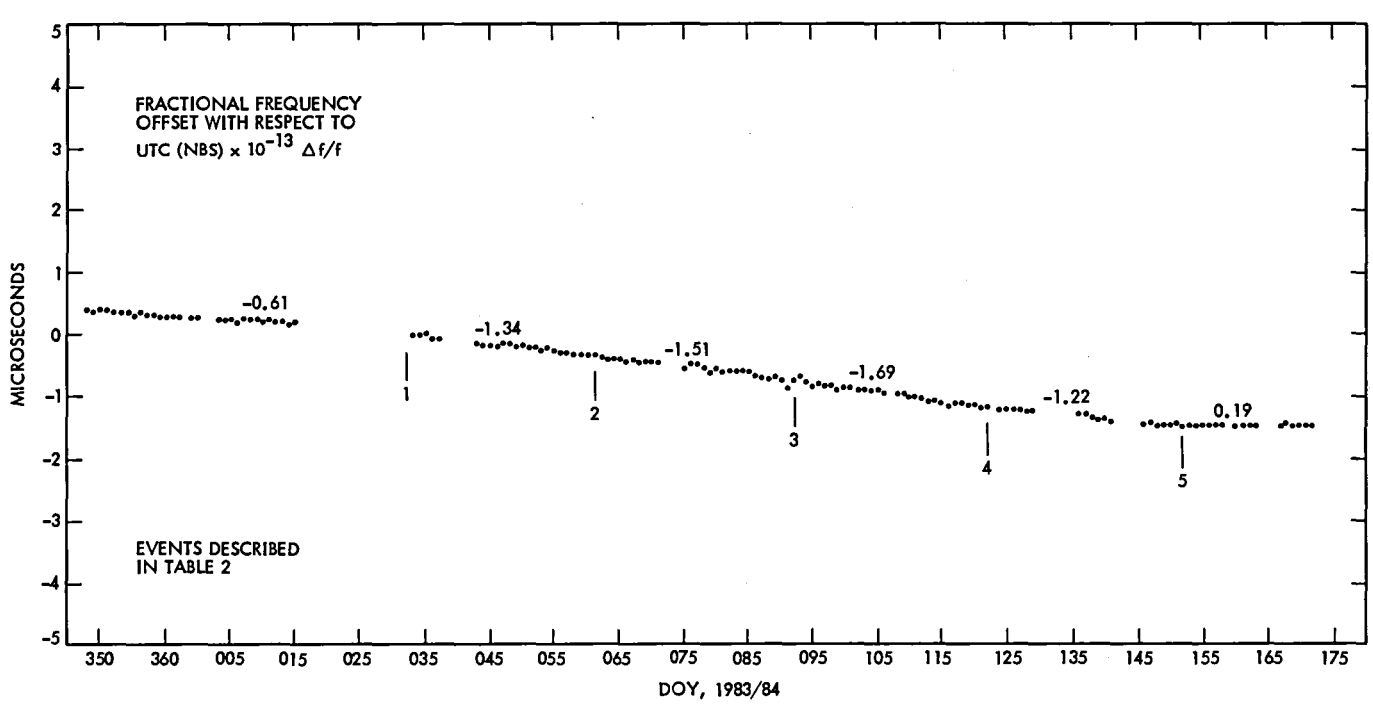

Fig. 6. Time offset, Canberra versus UTC (NBS)

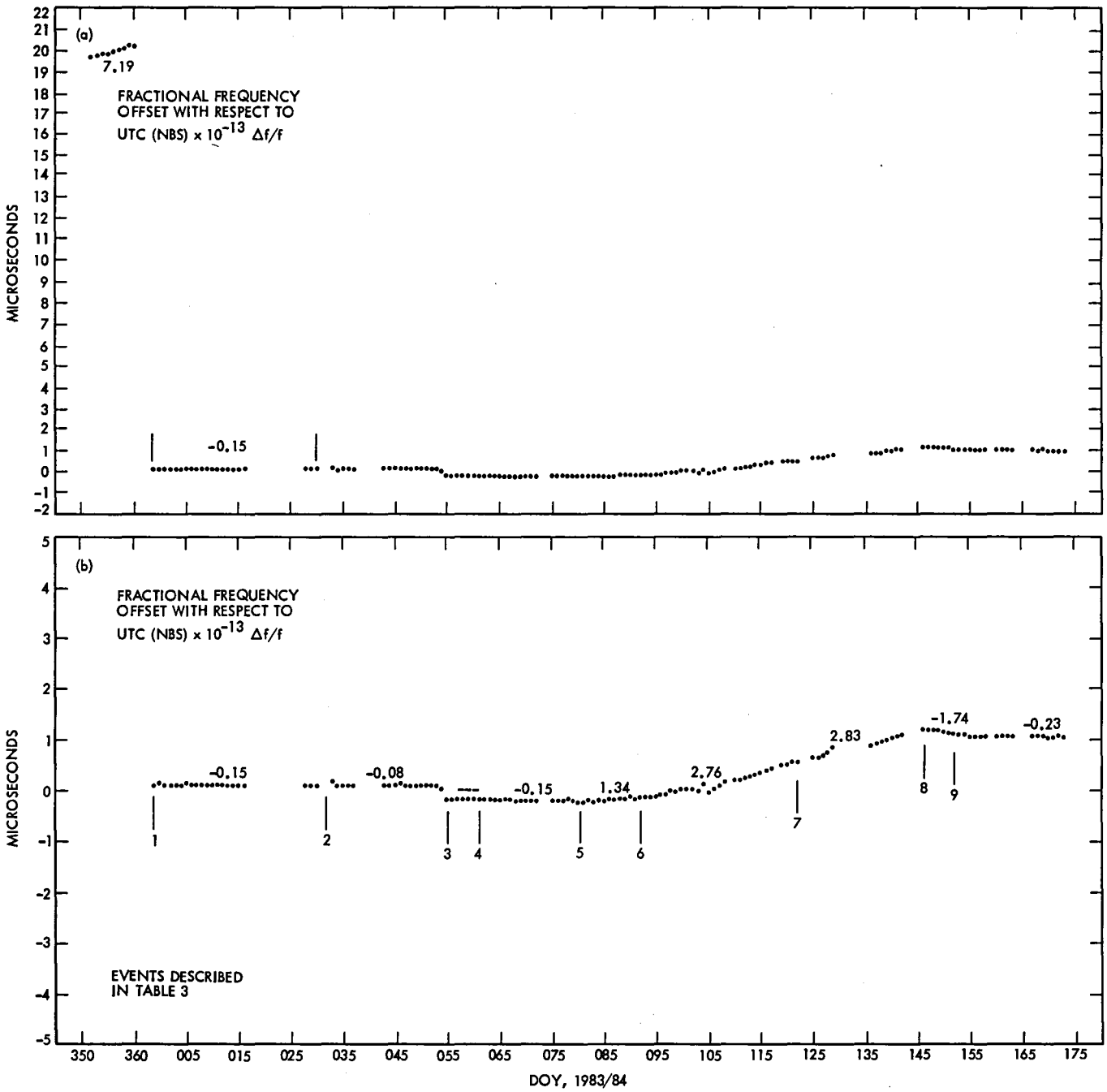

Fig. 7. Time offset, Madrid versus UTC (NBS) showing frequency adjustment and clock reset: (a) using an ordinate scale range of from 22 to −2 microseconds, and (b) using an ordinate scale range of from 5 to −5 microseconds

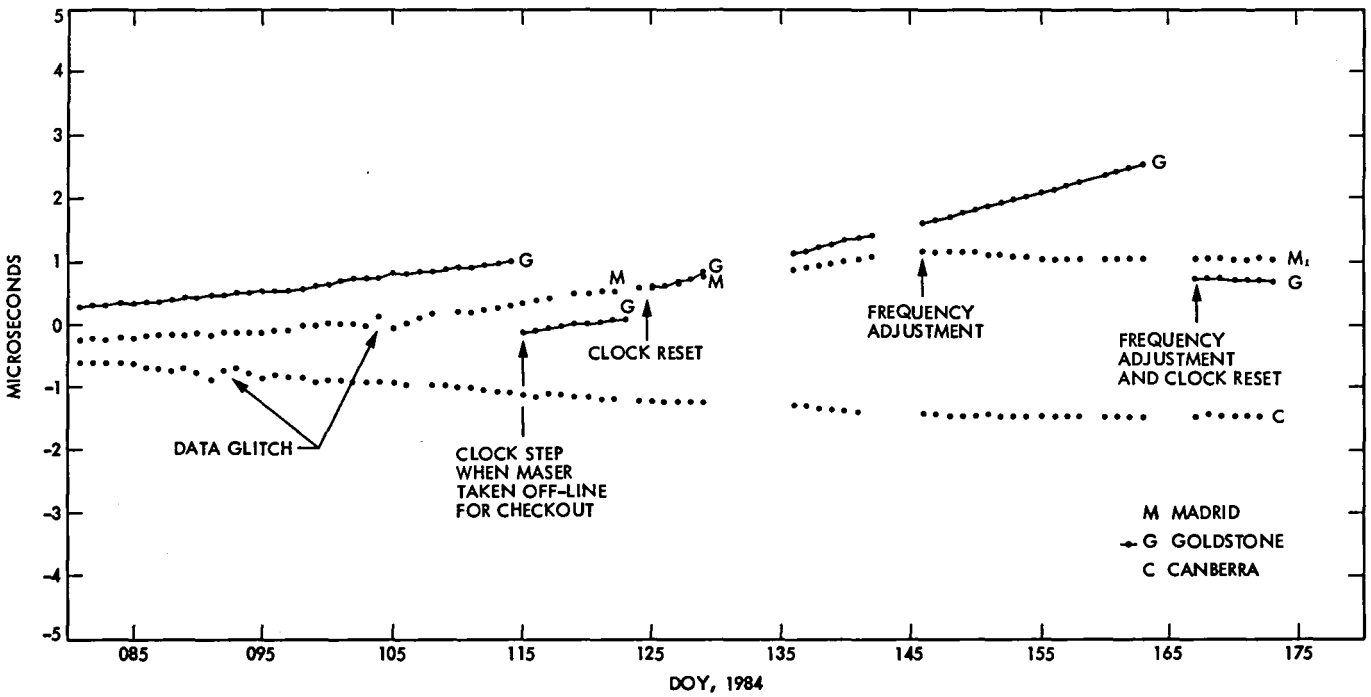

Fig. 8. Time offset, DFT system versus UTC (NBS), showing all three stations

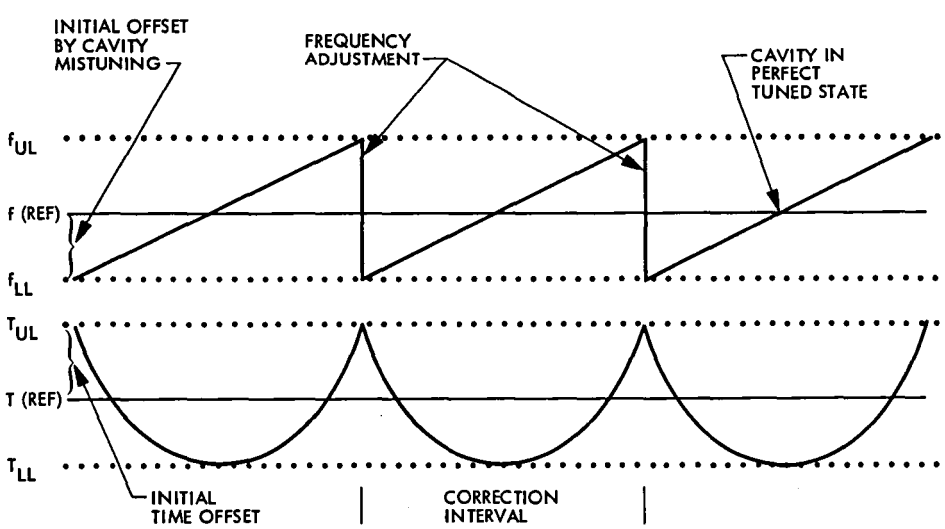

Fig. 9. Frequency correction intervals based on known cavity drift and allowable limits

Network Information Management Subsystem

C. C. Chatburn
DSN Operations and Engineering Support Section

The Deep Space Network is implementing a distributed database management system in which the data are shared among several applications and the host machines are not totally dedicated to a particular application. Since the data and resources are to be shared, the equipment must be operated carefully so that the resources are shared equitably. This article discusses the current status of the project and recommends policies, roles, and guidelines for the organizations involved in the project.

I. Introduction

Development of the Network Information Management Subsystem (NIMS) has now progressed into a phase where the uses of the NIMS and the roles and responsibilities of the organizations which are involved with it need to be considered in detail. A previous article (Ref. 1) described the initial phases of the project. This article discusses the NIMS network and node configurations, current status of the project, and the planned approach to full network operation.

II. NIMS Configurations

A. NIMS Hardware

The NIMS consists of a four-node network of intercommunicating minicomputers. Each node is similar and consists of a TANDEM Non-Stop II (NS-II) computer, disk drives, printers, terminals, and other peripheral devices (Fig. 1). The NS-II design features a unique multiprocessor architecture where each processor module is a totally autonomous computer system with its own memory, power supplies, and I/O capabilities. Processors are interconnected by a high-speed bus independent of the I/O bus. Each major hardware module is dual ported. If a processor or an I/O port fails, operating system backup processes take ownership of the failed component's peripheral devices and access them through the other I/O port, thus assuring nonstop operation.

B. NIMS Software

Each NIMS node is equipped with extensive commercial software to support the administrative data processing needs of various NIMS users. The software is grouped into seven major areas:

(1) General system interface programs including a command interpreter (COMINT), editor (ED), file utility program (FUP), peripheral utility program (PUP), sort/merge, backup/restore, and general-purpose procedures.

(2) The GUARDIAN operating system, consisting of a data base record manager (ENSCRIBE), a spooler, a performance monitor (X-RAY), and data communications software (ENVOY).

(3) Subsystem maintenance programs SYSGEN and INSTALL.

(4) Program development tools, consisting of the TANDEM Application Language (TAL), UPDATE, and DEBUG.

(5) A database management system (ENCOMPASS), consisting of a data definition language (DDL), a transaction processing system (PATHWAY), a transaction monitoring facility (TMF), a relational query/report writer (ENFORM), and a interactive application generator (ENABLE).

(6) The languages COBOL, FORTRAN, and BASIC.

(7) Other utilities, including electronic mail (T/MAIL), and word processing (T/TEXT).

III. Current Status

Hardware and software to support three NIMS nodes have been delivered. One node is installed at the JPL Hill Street facility. A second node is currently used to develop application software (Engineering Change Management Phase II) and is temporarily installed at a vendor facility in Glendora, California. At the conclusion of the software development, this equipment will be relocated overseas. A third node is installed at the Barstow facility of the Goldstone Deep Space Communications Complex (Fig. 2). A fourth node is currently funded for delivery in FY 86.

The nodes are connected together with leased telephone company circuits so that users at each node have access to the total resources of all nodes. Users from overseas complexes have access to the NIMS via high-speed NASCOM communications circuits using standard NIMS terminal equipment. These same lines will also be used for communications between nodes after overseas installations are completed (Fig. 2).

IV. Planned NIMS Implementation Approach

The NIMS concept represents a new approach to DSN information management in several ways. It is not totally dedicated to a single application, and the data handled are intended to be shared and thus are not necessarily the "property" of one application. Provisions are made for various levels of application, depending on the needs of the NIMS users. The "sharing" concept requires that information management support be provided impartially to a wide range of applications. This is a new NIMS function, and its role needs to be carefully considered to minimize conflicts between applications.

The implementation approach being used for the NIMS is divided into the following major areas:

(1) Organizational roles and tasks.

(2) NIMS Standards and policies.

(3) Application development.

(4) Organization roles and tasks.

Four geographically separate, functionally similar, but interdependent organizations are involved in NIMS operations. They are the management organizations at JPL and at each Deep Space Communications Complex (DSCC). Their responsibilities change as a function of the level of application (i.e., network, node, subnode) that they support. The roles and responsibilities of these organizations are more fully discussed in the sections which follow.

A. Organizational Roles

1. **Operations planning.** "Operations planning" addresses how the organization operates in the long term, existing standards or conventions that must be adopted, and any new standard procedures which must be developed and followed. Implicit in this activity is the need for a stable environment and a well defined base from which to evolve. This is established by making the process of change one which requires management approval. At the network application level, this is done via the ECM process. At the node level, it is delegated to local management.

2. **Systems operations.** "Systems operations" deals with short-term daily operations of the NIMS. This includes hardware/software maintenance activities and requested user/applications support.

3. **Systems monitoring.** "Systems monitoring" deals with ascertaining the ability of the total system (hardware, software, and people) to support assigned tasks. The NIMS does not exist as an independent entity; it is a support service that depends on users and user satisfaction for its existence. Performance standards are established and system performance is tested in order to verify that user needs are satisfied.

4. **Configuration management.** The NIMS configuration (both hardware and software) must be consistent across all nodes and controlled in order to support users and applications properly. Standard interfaces, naming conventions, definitions, protocols, and mnemonics, will be adopted for netwide use.

5. **NIMS library.** Each organization must have access to NIMS documentation necessary to support users and their applications. The library acts as the repository for this material and controls its distribution at each node.

B. Organizational Tasks

JPL and Deep Space Communications Complex management organizations must perform a similar set of general tasks

regardless of the level of NIMS application being supported. These can be divided into external (oriented to users) and internal (oriented to the organization).

1. **External.** External tasks are concerned with accepting data from a source, manipulating them, and providing useful information to users. Implicit in this process are the tasks of data entry, database creation, reporting, maintenance, and security. These are discussed below.

a. Data entry. This task includes activities required to accept data into the NIMS by any of the techniques that are available such as conversational, forms-mode, or batch input. If a forms-mode method is used, this activity may be done by some agent of the user, but it remains the responsibility of the NIMS organization to establish and/or develop the techniques. The objective is to minimize the special skills required of users.

b. Database creation. This task includes all activities required to develop the application database using utility software packages (tools) supplied with the NIMS. It includes analyzing existing databases to determine which data are shared, establishing linkages, considering security aspects, and creating or modifying data dictionaries and directories. Also included is full documentation of the database.

c. Reporting. This task includes activities associated with the manner, form, and content of the information presented to users. Depending on circumstances, these may range from formal reports to informal responses.

d. Maintenance. This task includes maintenance of software as well as hardware. It includes all activities that are associated with database upkeep, such as "tuning" for more efficient operation, and audits for completeness and correctness.

e. Security. This task includes activities required to guarantee that the data are not compromised, either by being made available to the wrong user or by being changed inadvertently. Included are the assignment of pass words and access levels and routine examination of those who have access to the various databases resident on the node.

2. **Internal.** Internal tasks verify that the man-machine system is providing the necessary external support that is needed by the various users and is cost-effective overall.

C. Special Organizational Responsibilities

1. **JPL node.** The JPL node organization is responsible for all support required for network applications. This support includes but is not limited to the following areas:

(1) NIMS and networking applications training.

(2) Hardware procurement.

(3) Utility software procurement.

(4) Standards and protocol development.

(5) Applications registration.

(6) NIMS configuration management.

2. **DSCC node.** Each DSCC node organization is responsible for all support required to develop local and subnode applications and for conforming to established NIMS standards and protocols. It also will support the portions of network databases that reside on the local node. It will maintain local hardware and provide local follow-on user training.

V. NIMS Standards and Policies

The following standards and policies have been established for developing applications on the NIMS to insure optimum use of resources and to encourage logical, well-ordered program development:

(1) All NIMS software developed for network-level applications will follow the policies for generating DSN software as established in *Software Implementation Guidelines and Practices*, Document 810-13, August 1, 1977 (JPL internal document). Node and subnode software will follow the intent of the standard insofar as practical.

(2) New NIMS networking applications will be planned and reported according to the technique of "Network of Demonstrable Functions", Ref. 2.

(3) All networking applications will be reviewed in accord with *DSN Engineering Change Review Program*, Document 810-10, June 1, 1979 (JPL internal document).

(4) Specific standards, such as file-naming conventions, peripheral names, user identifications, etc., are discussed in detail in the NIMS Software Operators Manual, SOM-DTN-5536SP, January 3, 1985 (JPL internal document).

(5) JPL and DSN computer security standards currently being developed will be adapted for NIMS. Local node management will be responsible for local node security and for complying with Network standards.

VI. Application Development

A. Levels of Applications

The NIMS is intended to support three levels of information management applications: network, node, and subnode. These are defined and discussed below.

1. **Network level.** Network-level applications involve data that may reside at several nodes and information that may be used by personnel at other nodes. An example of a network level application is the Engineering Change Management System (ECMS).

2. **Node level.** Node-level applications involve data that may come from several sources, but are of interest only to the personnel at a single node. Generally, these data will be input by personnel at the local complex and the information derived from this data will be used by the various levels of local management. Examples of this application are telephone and address lists.

3. **Subnode level.** Subnode-level applications involve private databases that are created, monitored, and controlled by the user/creator and are not shared with other applications.

B. Development Methodology

The development of new applications requires resources and must therefore have management approval before they are implemented. The level of approval will depend upon the application. New network applications require approval through the Engineering Change Management (ECM) process. Node applications require local node management approval. Subnode applications require approval of the appropriate database administrator.

The data to be managed should be available in a form that can be collected and entered into the appropriate database. The data should be clearly identified and defined, and the effect of data errors should be understood. Access to both the data and the resulting information must be established. The requirements for the application must be accurately and clearly specified.

1. **Requirements definition.** A formal requirements document is required for proposed applications that are network-wide in scope. Node and subnode application requirements will be documented in accord with local management policies.

2. **Software development.** Applications software will be developed by a sustaining contractor under the supervision of the DSN Database Administrator (DBA).

Local applications programs can be generated and implemented on local nodes. Control of these activities is the responsibility of local management.

3. **Documentation requirements.** The three application levels have different requirements for supporting documentation. Since network applications are long-lived and affect many aspects of DSN operations, they must be carefully documented. Node and subnode applications have less impact and consequently have less stringent documentation requirements. The detail of proposed documentation for each level of application is shown in Table 1.

4. **Changes or modifications to applications.** Changes or modifications to NIMS-hosted applications require management approval prior to being implemented. Generally, the level of approval follows precedents established by ECMS. Applications that are under ECM control require ECR/ECO activity.

Changes to node and subnode applications require the approval of the appropriate database administrator and management levels. DBA approval is required because NIMS resources, e.g., disc space, can be impacted by the changes.

5. **Testing.** All new applications require testing during the design and installation process. The application level will determine the formality and detail of the tests. The tests will be further defined in the Software Test and Transfer document STT-DTN-5536SP, January 3, 1985 (JPL internal document) for network applications. Testing of node and subnode applications is under the control of local node management.

References

1. Wales, K. J., "The Network Information Management System (NIMS) in the Deep Space Network," *DSN Progress Report 42-73*, Jet Propulsion Laboratory, Pasadena, Calif., pp. 85-88, May 15, 1983.

2. Jacobson, G. N., and Spinak, A., "Top Down Implementation Plan for System Performance Test Software," *DSN Progress Report 42-70*, Jet Propulsion Laboratory, Pasadena, Calif., pp. 190-199, August 15, 1982.

3. Tausworthe, R., *Standard Classifications of Software Documentation*, Technical Memorandum 33-756, Jet Propulsion Laboratory, Pasadena, Calif., January 15, 1976.

Table 1. Application level documentation standards

Applications documentation		Applications level					
		Network		Node		Subnode	
Name[a]	Purpose	Class[b]	Format[b]	Class	Format	Class	Format
SRD	Program requirements schedule and resource for design phase	B	3	C	3	–	–
SDD	Architectural design, interfaces test and design goals	B	3	C	3	–	–
SOM	Operating instructions	B	2	C	2	D	4
STT	Acceptance tests and transfer criteria	B	3	–	–	–	–
SSD	Program design and code listings	C	3	D	3	D	4

Class B: sufficient for skilled programmers with minimum CDE consultation.
Class C: sufficient for skilled programmers with dialog with the CDE.
Class D: suitable for maintenance only by original programmer.
Format 2: external report quality.
Format 3: internal report quality.
Format 4: freehand documents, internal quality.

[a]SRD: software requirements document
SDD: software definition document
SOM: software operators manual
STT: software test and transfer document
SDD: software specification document
[b]Definitions of Class and Format per Ref. 3.

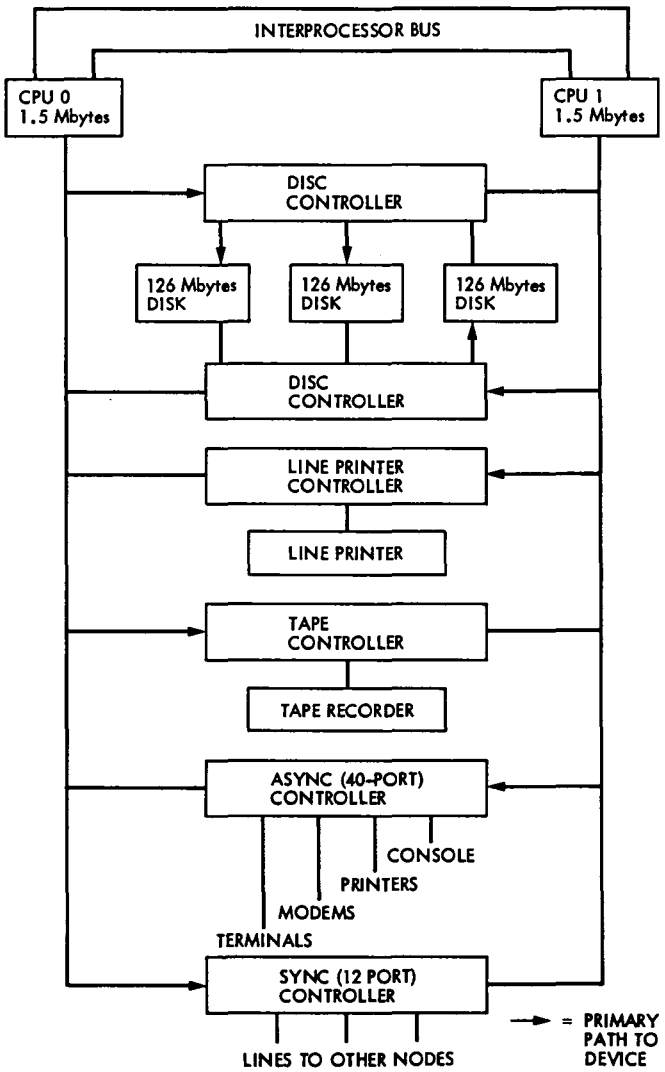

Fig. 1. Typical NIMS node block diagram

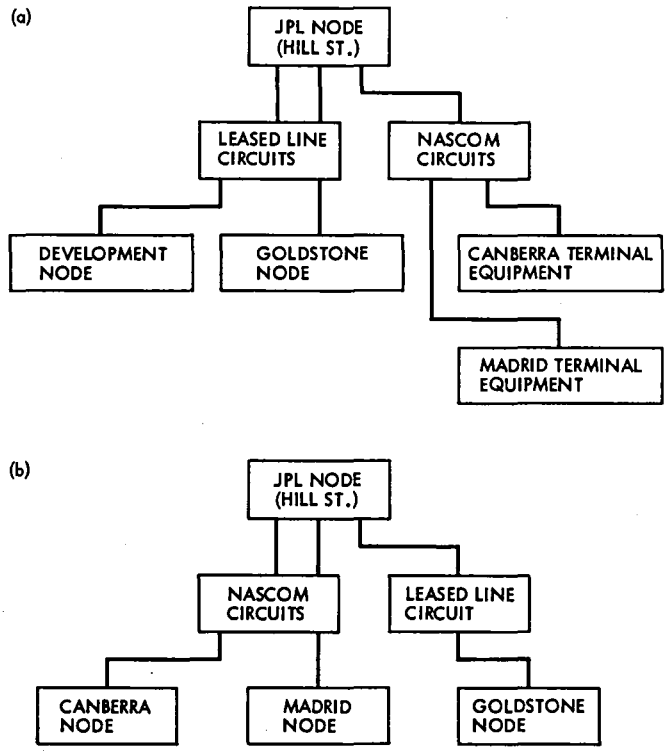

Fig. 2. NIMS network configuration: (a) current; (b) final

A Description of the 64-Meter Antenna Elevation Drive Gears and Their Strange Wear

H. McGinness
Ground Antennas and Facilities Engineering Section

The elevation drive gears are described and their wear is compared to the wear of other antenna drive gears. The comparison is perplexing and satisfying explanations have not yet been made.

I. Introduction

The 64-m antenna elevation axis drive is executed by torquing two bull gears, concentric to the elevation axis, with the output pinions of four gear boxes. These gear boxes have functioned well during the 18 and 11 years, respectively, that the DSS 14, and the DSS 43 and DSS 63 antennas have been in service. A strange wear pattern gradually developed on the bull gears and driving pinions of all three antennas. These patterns were well developed after 8 years and apparently are intensifying in all instances.

II. Description of the Drives and the Gear Wear

The gear boxes are mounted so as to allow the output pinions to self-align to the bull gears. Figures 1 and 2 show how the gear boxes are pivoted with a ball joint at one end such that the tangential load on the output pinion passes through the ball joint. The other end of each gear box is supported by one horizontal and two vertical spring-loaded struts. The gear box contains a reaction roller, mounted opposite the pinion, which rolls on the inside of the bull-gear ring and equilibrates the separation force between the bull gear and pinion. The ball-joint pivot, together with the three spring-loaded struts, allows the pinion to execute small angles of roll, pitch, and yaw which may be required to maintain near-perfect mesh between the pinion and the bull gear, as the bull gear deviates from perfection. A detailed description of this gear-box suspension is given in Ref. 1.

Each gear box has two input shafts which are geared to a common shaft. One input shaft has a constant torque applied in a direction opposite to that of its corresponding shaft on the other gear box, which meshes with the same bull gear. The two opposing, countertorquing shafts eliminate backlash from the gear system. The second input shaft is the driving input and its torque has the proper direction and magnitude to equilibrate the antenna axis torque caused by wind or imbalance. A schematic of this torquing system is shown in Fig. 3. Whenever the wind torque is below a certain value, the countertorques are greater than the driving torques and the two output pinions bear against opposite faces of the bull-gear teeth. This is designated as Case I loading. It is estimated that this Case I loading condition prevails more than 97% of the time.

When the wind torque is above a certain value, the driving torques are greater than the countertorques. This is designated as Case II loading. One driving torque direction is always the same as its countertorque direction, whereas the other driving torque is always opposite to its countertorque direction; hence, for Case II loading, one of the output pinions bears against the bull-gear tooth face opposite to that for the Case I loading. For either Case I or Case II loading one of the output

pinions has its load increased from its countertorque loading whenever the wind blows, and the amount of the increase is proportional to the square of the wind speed and the wind torque coefficient. Therefore, the load range on one of the output pinions is from the countertorque value to approximately four times that value at a wind speed of 22.35 m/sec (50 MPH). Wind records at DSS 14 [Ref.9] show that the wind exceeds 4.47 m/sec (10 MPH) only *44%* of the time; therefore, for *56%* of the time the countertorque loading of a *68877* N (15485 lb) tangential force is barely exceeded. The wind loading may be obtained from Ref. 2.

The strange wear pattern, which is described below, exists on all bull-gear teeth which are exposed to the driving pinions. It is believed that if the wear pattern were caused by the high loads from infrequent high winds, the patterns would exist only on relatively few teeth, namely, those in mesh during the few predominant antenna orientations of high loading. Therefore, the conclusion is that the wear pattern is caused primarily by the constant but much smaller forces from the countertorquing pinions. The sides of the teeth subjected to this constant countertorquing are shown in Fig. 4.

The bull-gear wear pattern is shown in Figs. 5, 6, and 7. It consists of a series of diagonal waves (with peak-to-valley amplitudes judged to be as much as 0.50 mm) terminating at the pitch line of each gear tooth. The direction of the diagonals is sometimes reversed across the pitch line. The phenomenon has been described by several gear consultants as a plastic flow condition. Several references allude to plastic flow, for example, page 506 of Ref. 3 states,

> With the softer and more plastic materials tested, a definite plastic flow of the surface material occurs, even though particles are not sheared out of the surface. Sometimes this plastic flow develops into a series of waves on the surface. With the introduction of sliding between the two surfaces in generally rolling contact, this corrugation effect is increased greatly. . . . Some borderline cases may show up with inadequate lubrication that would not exist under more favorable conditions of lubrication, notably the plastic flow of the surface with the development of hollows and ridges.

Page 520 of Ref. 3 states, "On the softer steels under 200 Brinell hardness number, for example, corrugations or waves are developed on the surface, particularly if sliding action is present, under relatively light loads." Page 16 of Ref. 4 states,

> Plastic flow is the cold working of the tooth surfaces, caused by high contact stresses and the rolling and sliding action of the mesh. It is a surface deformation resulting from the yielding of the surface and subsurface material. It is usually associated with the softer gear materials, although it often occurs in heavily loaded case hardened and through hardened gears.

This same reference discusses the plastic flow phenomena termed "rippling" and "ridging" and associates them with high contact stresses. Photographs of rippling and ridging examples are shown in Ref. 4.

None of the above references quantitatively relate plastic flow to the ratio of contact stress to material yield stress. If a gear designer assiduously evaluates all load and stress conditions and selects a material having yield strengths above any possible stress value, he might expect that plastic flow would be prevented. Since plastic flow sometimes occurs in spite of such considerations, the explanation probably lies in a possible reduction of the material yield strength under the cyclical loading which is, of course, the nature of gear-tooth loading. Since plastic flow does not occur most of the time when gears are designed in accordance with rules which ensure that maximum contact stresses are sufficiently below the "nominal yield strength" of the material, it might be that certain alloys at certain hardnesses require that, in order to prevent plastic flow, the maximum contact stresses must be below the "nominal yield strength" by a much greater amount than is usually required. The "nominal yield strength" as used above means the yield strength as determined by a monotonically increasing load. The phenomenon of material strain softening as described in Refs. 5 and 6 is a weakening effect that is much greater for some materials than for others. The curve of Fig. 11 indicates that for 4142 steel at a Brinell hardness of *380*, the yield strength after cyclical loading is approximately 50% of the monotonic yield strength. This 4142 alloy is approximately the same as the elevation bull-gear material 4140 although the bull-gear hardness range was originally about 245 to 285 Brinell.

The elevation bull-gear and pinion specifications can be obtained, respectively, from the JPL drawings 9436786 and 9435055. Some of the specifications are listed in Table 1.

The bull gears and pinions are exposed to debris which is transported by wind. The use of a sticky lubricant was considered inappropriate because of the debris it would collect. The dry lubricant which has been employed comes from a spray can and is called Molycote G Rapid Spray and is supplied by Dow Corning.

III. Discussions of the Analyses

Appendix 1 contains the derivation of the maximum shear stress in the contact area of a misaligned gear tooth in terms

of the misalignment angle, the tangential load, the pinion pitch diameter, the elastic modulus, and a tooth-shape factor. The maximum shear stresses versus the tooth misalignment are plotted in Fig. 8 for several values of the friction coefficient and for the countertorquing load corresponding to 700 psi. The ordinates of the curves at the left side of the figure pertain to the case of perfect tooth alignment. In order to determine how the calculated maximum shear stresses compare with the shear yield of the gear tooth material, the shear yield value, $\tau_y = 1/\sqrt{3}\,\sigma_y$ from Ref. 7, page 138, will be used. By taking the lower value of 104000 psi tensile yield from Table 1, the lowest value of τ_y becomes 60000 psi or 41370 (10^4) N/m^2. For the case of perfect tooth alignment, the ordinates of the curves at the left edge of Fig. 8 are all well below 60000 psi. The left-edge ordinate values are 14500, 17000, 20000, 22500, and 25500 psi, respectively for the friction coefficients 0.111, 0.20, 0.30, 0.40, and 0.50. It is believed that misalignment angles of more than 0.001 radian seldom occurred. For such a misalignment a friction coefficient of 0.40 would be required to exceed the 60000 psi shear yield. Under wind conditions the shear stresses would of course increase. Equation (A-21) shows that for the case of a misaligned tooth, the maximum shear stress, τ_{max}, varies with the 1/4 power of the tooth load. Hence, for the maximum tooth load at a wind of 22.35 m/sec (50 MPH) the shear stresses would be approximately only $(4)^{0.25} = 1.41$ times as much as indicated by the curves of Fig. 8. But such shear stresses at a misalignment of 0.001 radian would be above the shear yield even at friction coefficients as low as 0.15. These maximum shear stresses at misalignment occur only very close to the end of the gear tooth. Thus, plastic flow has been explained only at the ends of a tooth.

Appendix 2 describes the results of a strain gage test made on two of the bull-gear teeth at DSS 63. From the results of these tests it is concluded that the maximum magnitude of the tooth loading during elevation axis slew is as expected. The vacillating nature of the tooth strain as shown in Fig. 9, however, is not understood. It would appear that, because of the load vacillation, the actual number of loading cycles is approximately twice what was expected.

For the case of no misalignment, Eq. (A-18) shows that the maximum shear stress, τ_{max}, varies with the square root of the load. Therefore, at a wind speed of 22.35 m/sec (50 MPH) the maximum shear stresses would be approximately twice that shown by the ordinates at the left edge of Fig. 8, and these values would be 29000, 34000, 40000, 45000, and 51000 psi, respectively, for the friction coefficients 0.111, 0.20, 0.30, 0.40, and 0.50. None of these is equal to the shear yield, so that plastic flow across the entire width of the gear tooth, as shown in Fig. 5, is not explained.

As stated before, it is believed that the plastic flow damage is caused by the lower but more frequently applied countertorque loading, rather than by the infrequently applied high-wind loading. This opinion is reached by observing that the plastic flow is on all the teeth which come into mesh with the pinions when the elevation axis is slewed through 85°. Figure 4 shows which tooth surfaces show the plastic flow condition. It is estimated that the central teeth undergo 4 slew loadings per day or approximately 1500 per year. After a period of 8 years, 12000 slew loadings would have occurred, and from the strain gage tests which showed a loading vacillation, this could be equivalent to 24000 cyclic loadings during the 8-year period.

It is tempting to try to explain the plastic flow by the phenomenon of strain softening as described in Refs. 5 and 6. Figure 10 is from Ref. 8 and shows that the yield after cyclic loading is approximately half that after monotonic loading. If the shear yield of the bull-gear material were reduced by a factor of two, giving a shear yield of 20685 N/cm^2 (30000 psi), the left-edge ordinates of the curve of Fig. 8 for $\mu = 0.50$ would be getting quite close to the new shear yield. This indeed might be the explanation, but it is difficult to accept because another bull gear on the antenna at DSS 12 has had about the same length of service and is in excellent condition. Its hardness is slightly less than that of the DSS 14 bull gear, and the tooth stress due to countertorquing is somewhat more (Ref. 9) than that of the DSS 14 bull gear. A comparison of these values is set out in Table 2. If strain softening caused the plastic flow at DSS 14, why did not the DSS 12 gear undergo the same softening? At the present time no satisfactory explanation has been offered.

The cylinder of Fig. 11 depicts a roller in contact with a plane surface, represented by the cube. The purpose is to show the direction of the normal Hertz stress, σ_h, and the two at right angles to it, namely, another σ_h and $\sigma_{h/2}$. On the contact surface the frictional force, $\tau_c = \mu\sigma_h$, acts as shown, and this frictional force is the result of gear-tooth sliding. Reference 10 shows that when the friction coefficient exceeds 1/9, the maximum shear is located at the point of contact, but not in the contact plane. The three principal stresses are directed as indicated by σ_{p1}, σ_{p2}, and σ_{p3} and the angles and magnitudes can be calculated by the usual methods of calculating principal directions and stresses, for example, as shown in Ref. 7. Figure 12 shows a multi-view picture of the principal stresses and the maximum shear-stress plane. Notice that when the maximum shear-stress vector is projected onto the contact surface of the gear tooth, it makes a certain angle with the tooth boundary, which appears to be approximately the same as that shown by the ridges of Fig. 5. It seems likely that there might be a relationship between the plastic flow ridges and this

projection of the maximum shear stress. From symmetry, the ridges could have had a mirror-image direction.

IV. Consequences of the Tooth Plastic Flow

It should be emphasized that the plastic flow exists only in the volume of material very near the working surface of the tooth, that is, limited to the region very close to the contact surface. Since both the calculated and measured strains at the tooth root are very small, there is no concern that there will be any catastrophic failure. Since it appears that the corrugated condition of the tooth surfaces is slowly intensifying, there is concern that eventually the pointing accuracy of the antenna will be affected. For example, if the corrugation spacing should be three millimeters and if there were a tendency for a corrugation peak of the pinion to fit into a corrugation valley of the bull gear, the servo drive might not be able to hold the commanded position. The angular pointing error might be approximately three millimeters divided by the radius of the bull gear (3/12650 = 0.000237 radian or 0.013 degree). It is possible that the servo drive could overcome such a situation, nevertheless it is a point of worry.

V. Conclusions and Recommendations

An examination of Table 2 shows that the Hertz stress is higher and the material hardness is lower on the DSS 12 bull gear, which is the one which is in very good condition. The DSS 12 gear-tooth sliding velocity at antenna slew speed is about twice the sliding velocity of the DSS 14 gear at its slew speed. This is because the DSS 12 antenna has a higher angular slew speed. It is conceivable that lubrication is better at the higher sliding velocities.

It is recommended that an attempt be made to determine if the DSS 14 gear teeth have experienced strain softening. Reference 5 states that material softening cannot always be detected by hardness tests. Possibly this can be done by cutting off small material samples and having them examined by metallurgical experts. It is recommended that the consulting services of one or more of the persons experienced in the field of strain softening be obtained. Although the DSS 14 and DSS 12 gear material is nominally the same, it might be that the small actual difference in material composition is significant.

If new gears must be ordered before there is a good understanding of the nature of DSS 14 gear plastic flow, it is recommended that both the bull gears and pinions be made harder. If strain softening is limited to some certain percentage of the original yield strength, then a sufficient increase in the original yield strength could prevent the plastic flow. Gear manufacturers have stated that it is feasible to cut through-hardened gears having a Brinell hardness of 320 to 360. Greater hardnesses near the surface could be obtained by flame or induction hardening. The hardness of pinions should be appreciably more than that of the gears.

Two or more gear consulting engineers have regretted that a better lubricant is not being used, yet they have been unable to recommend a better one for the existing environmental conditions. There are lubrication specialists who concoct special lubricants for special situations. It is also recommended that the services of such a specialist be obtained.

Table 1. Gear Specifications

	Bull Gear	Pinion
Tooth Type	Spur	Spur
Circular Pitch, mm	88.90	88.90
Pitch Diameter, m	25.298	0.4527
Outside Diameter, m	25.341	0.5235
Addendum, mm	21.209	35.382
Whole Depth, mm	61.036	63.665
Root Diameter, m	25.219	0.3962
Backlash with Mate, mm	0.635 to 1.016	0.635 to 1.016
Material	4140 Steel	4140 Steel
Brinell Hardness Range	245 to 285	285 to 325
Tensile Yield (psi)[a]	104000 to 118000	118000 to 140000
JPL Drawing Number	9436786	9435055
Pressure Angle	25°	25°
Contact Ratio 1.44		

[a]Tensile yield stresses, corresponding to Brinell values, are from Reference 11.

Table 2. Comparison of three antenna bull gear tooth stresses, hardnesses, and condition

Antenna	Lubricant	Gear tooth load from countertorque N (lb)	Nominal Hertz stress at full tooth contact N/cm^2 (psi)	Gear material steel	Brinell hardness range	Max. sliding velocity of tooth at max. slew speed cm/sec (inch/sec)	Condition
64-m DSS 14	Molycote	69144 (15545)	33360 (48385)	4140	285 245	1.89 (0.745)	Plastic flow damage
26-m DSS 12	Molycote	19046 (4282)	43000 (62368)	4140	260 220	2.95 (1.161)	Excellent
34-m DSS 15	Molycote	42548 (9568)	41955 (60850)	4340	320 280		New

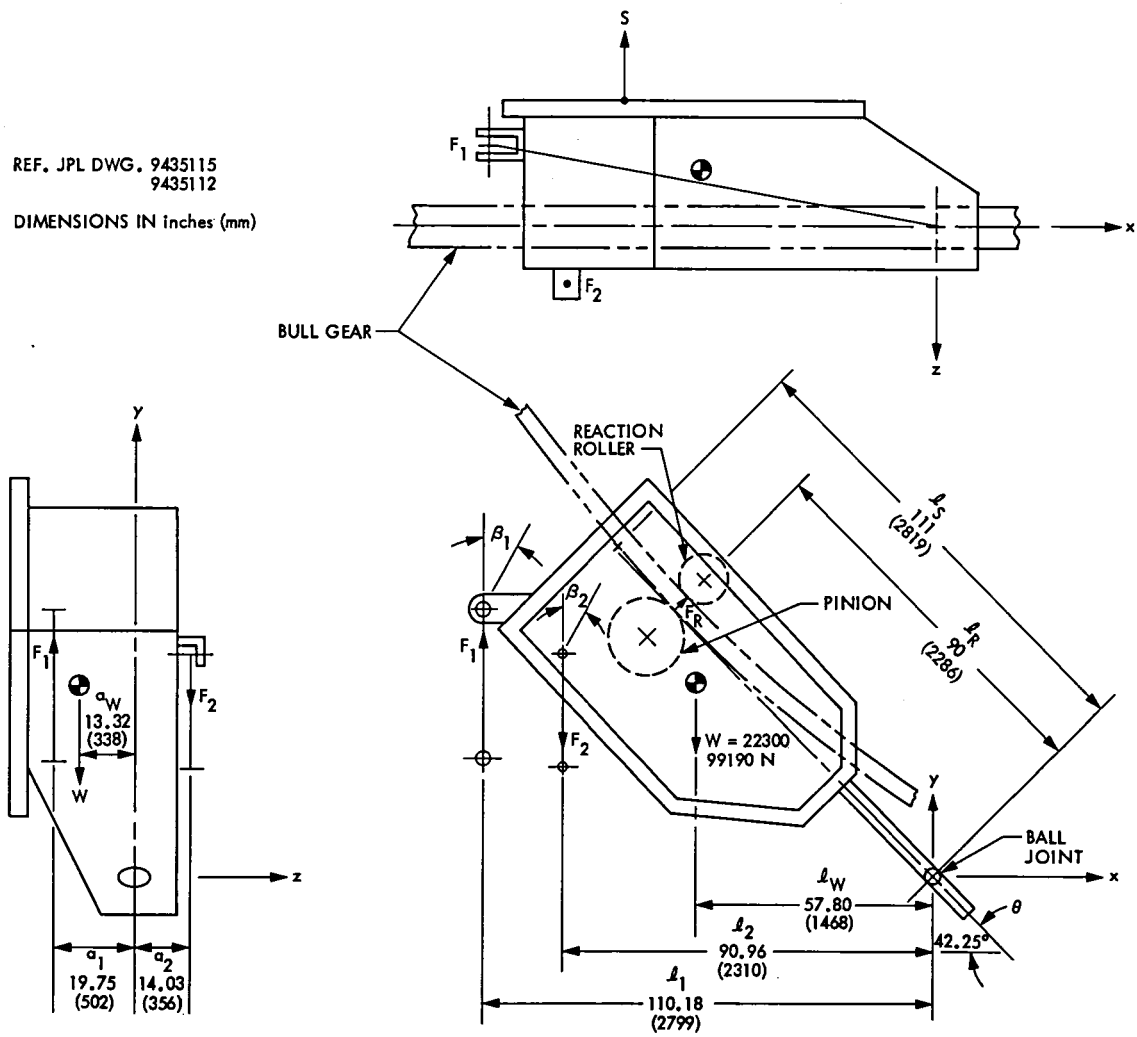

Fig. 1. Upper elevation drive gear box no. 2

REF. JPL DWG. 9435115
9435110

DIMENSIONS IN inches (mm)

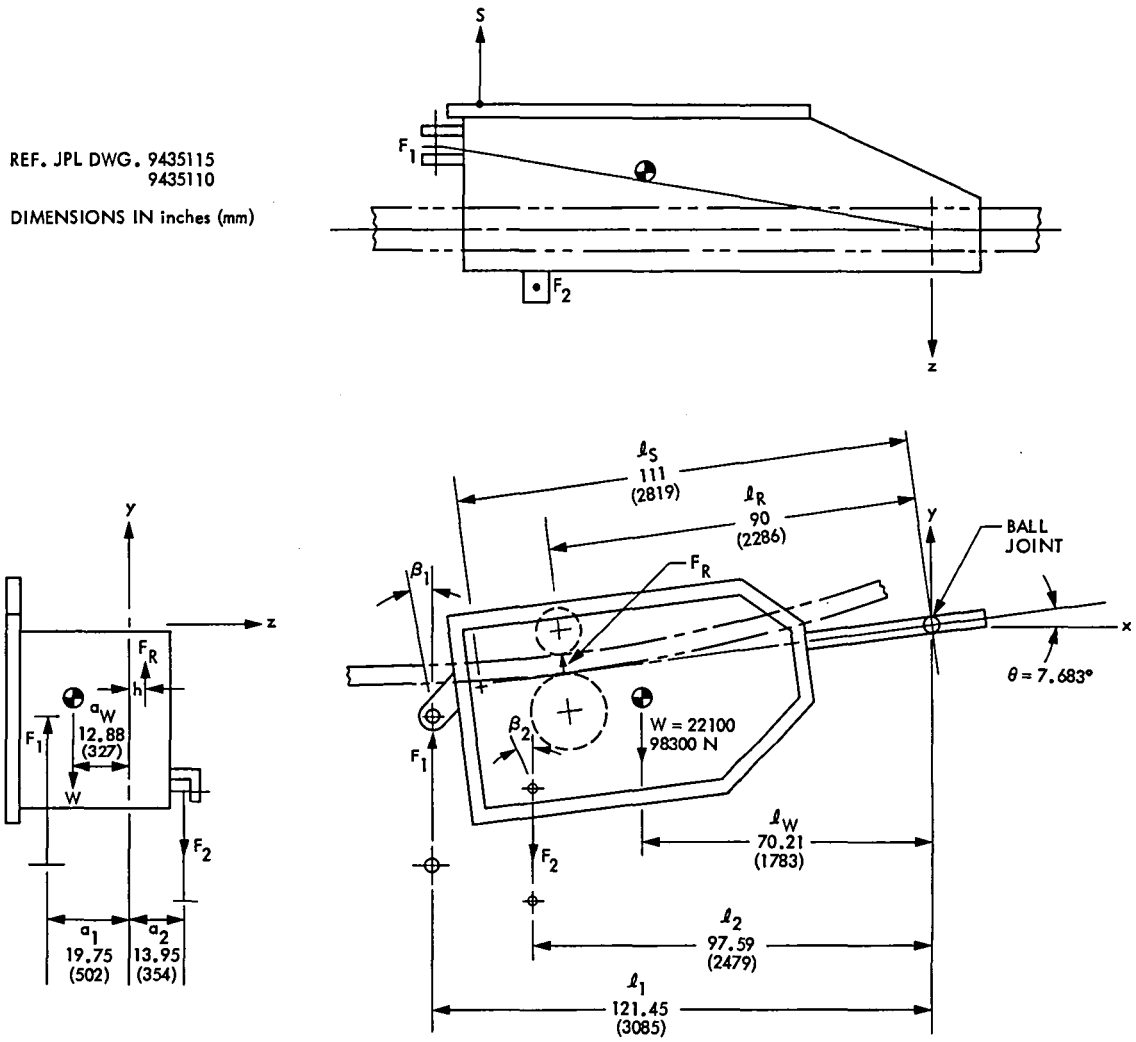

Fig. 2. Lower elevation drive gear box no. 3

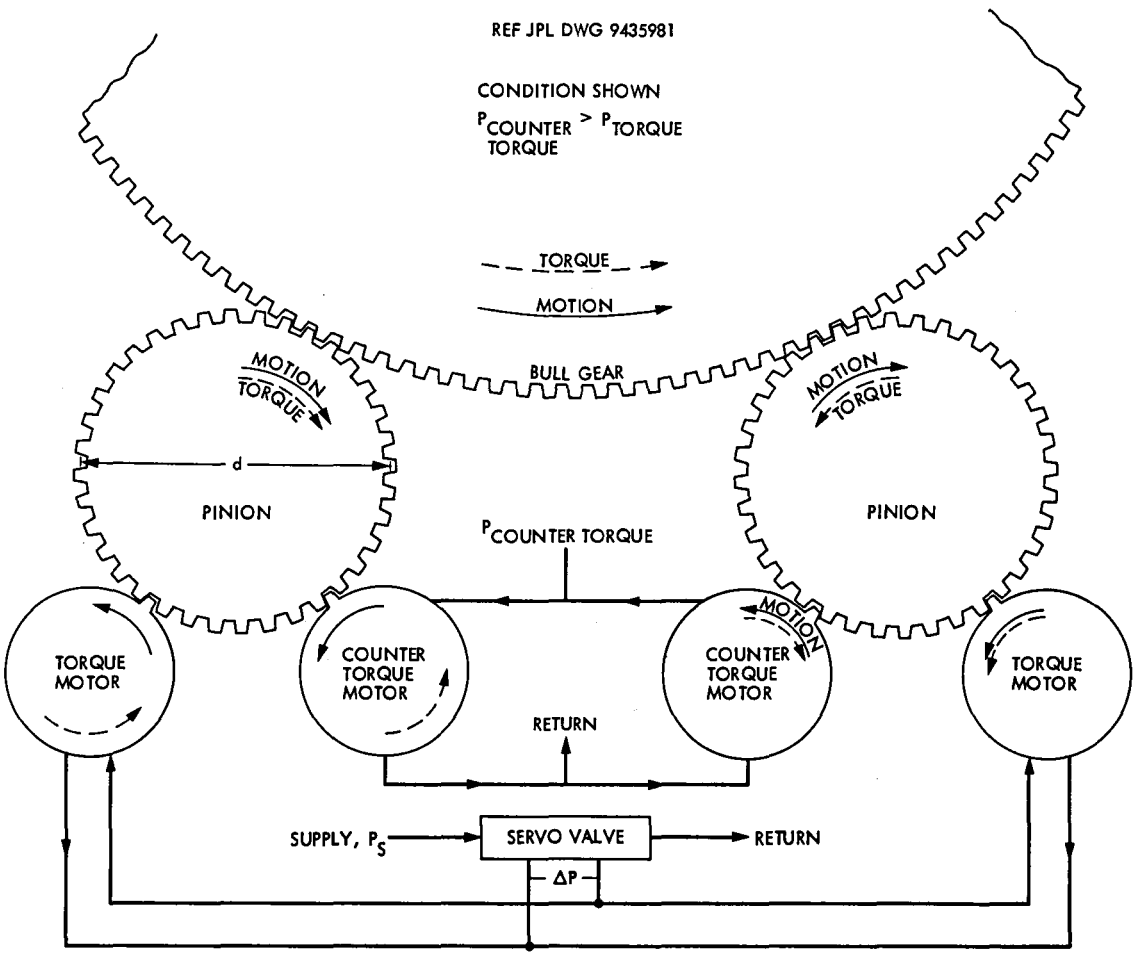

Fig. 3. Schematic of bull gear, pinions, hydraulic motors, and servo valve

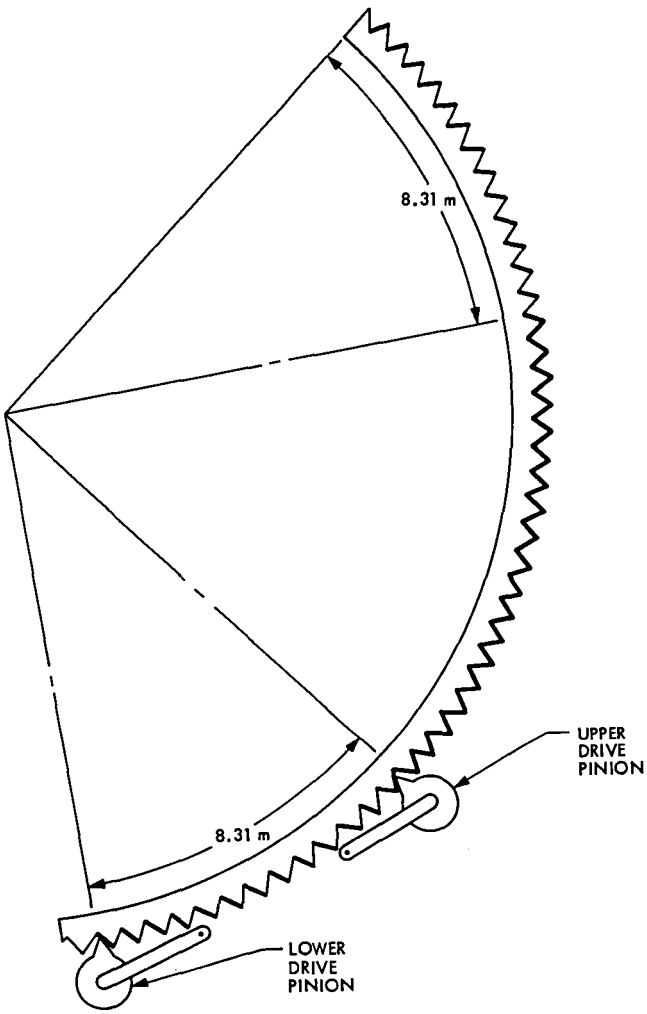

Fig. 4. Schematic of bull gear showing, by heavy lines, the tooth surfaces subjected to countertorque loading

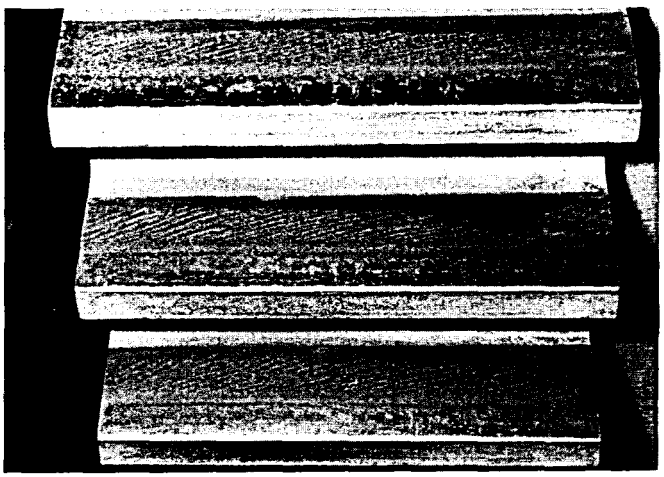

Fig. 5. Plastic flow across entire width of bull gear tooth

Fig. 6. Change in direction of corrugation pattern across pitch line

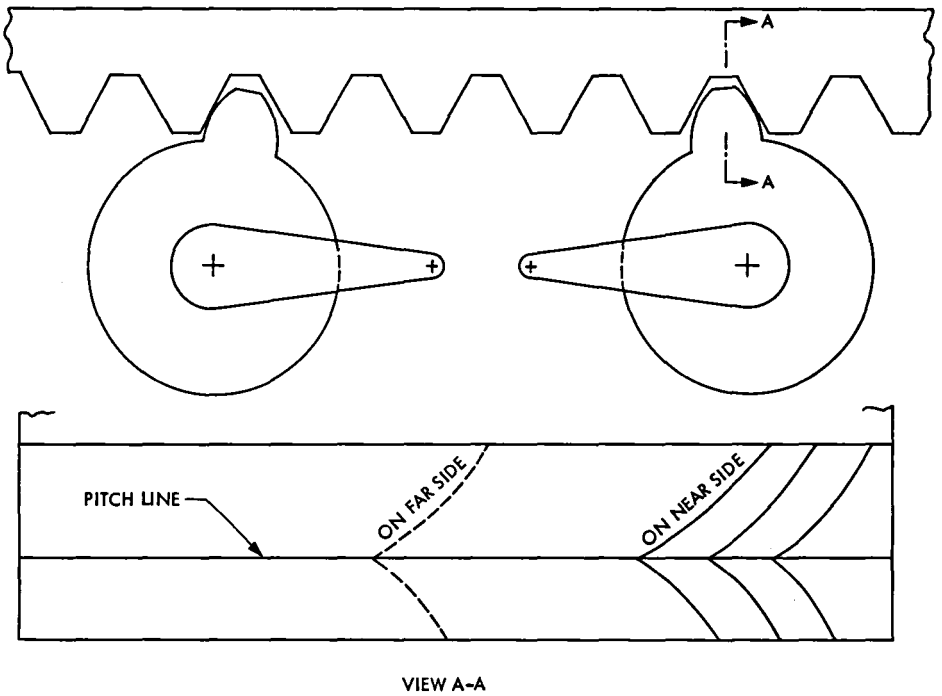

Fig. 7. Schematic of tooth ridge pattern

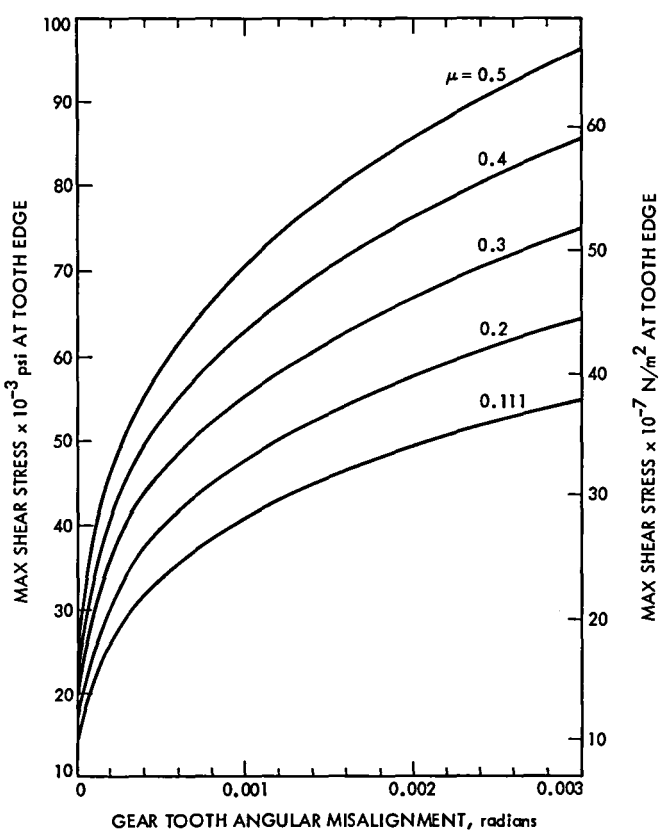

Fig. 8. Maximum shear stress versus tooth misalignment

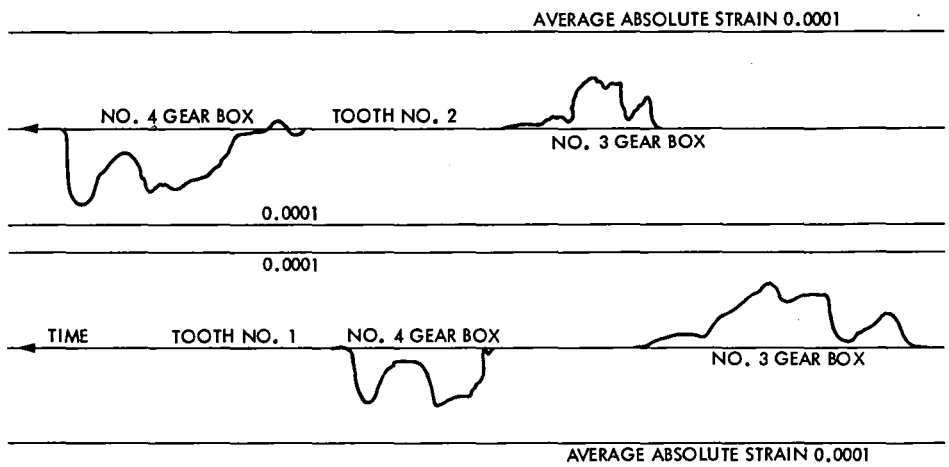

Fig. 9. Average absolute strain of gages on two different teeth of a bull gear, measured at DSS 63, elevation axis speed 0.0042 deg/sec

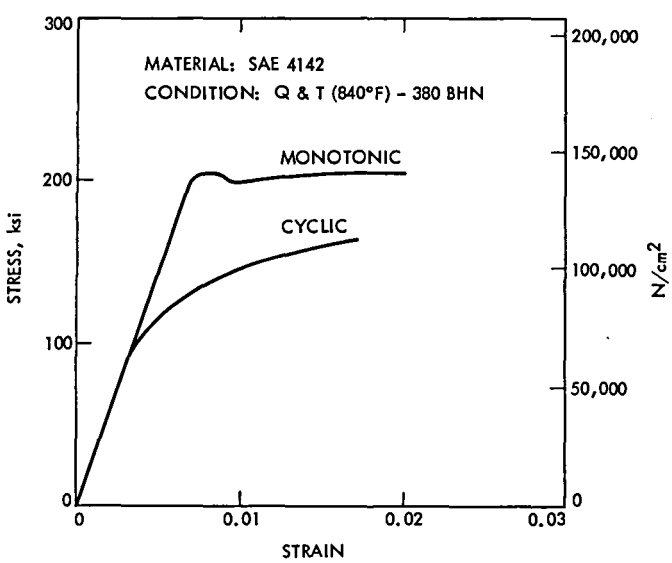

Fig. 10. Stress strain curve for material which has strain softened under cyclic loading

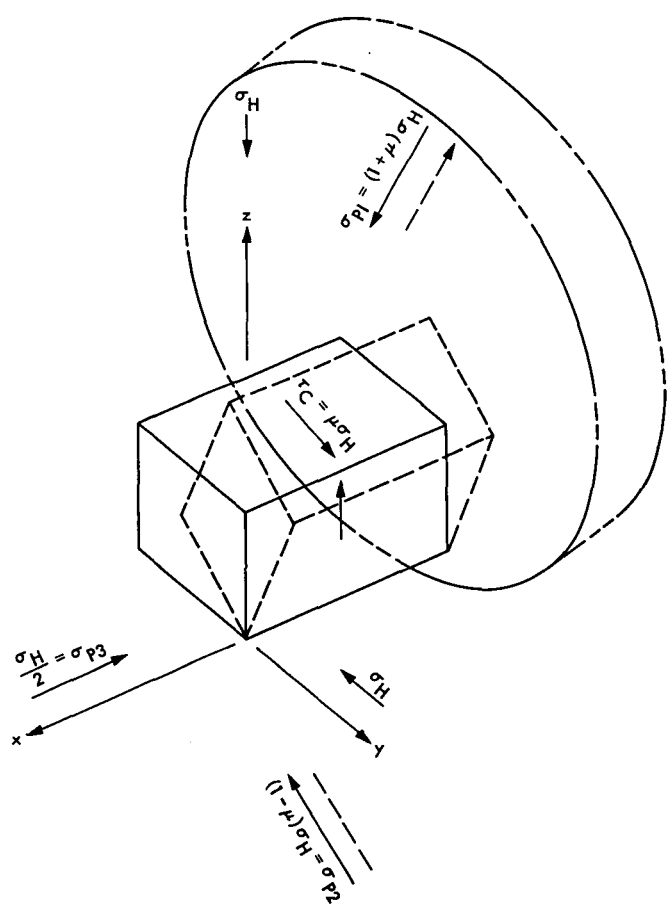

Fig. 11. Orientation of principal stresses σ_{P1}, σ_{P2}, σ_{P3} with respect to x-axis, which is parallel to roller axis

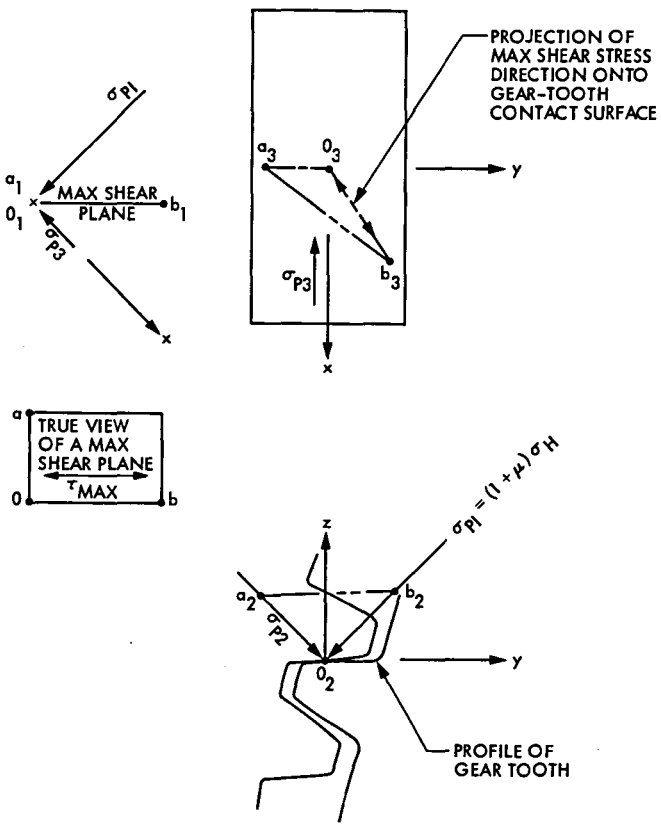

Fig. 12. Multiple view orientation of maximum shear direction

Appendix A

Figure A-1 depicts the contact between the teeth of a misaligned gear set. When contact first occurs at the right-hand edge, the clearance at the left edge is γ. As the force between the teeth increases, the contact becomes a flat surface which bisects the angle θ formed by the dashed lines of the figure. At equilibrium the length of contact is h. Let the origin of x be where contact begins. From Fig. A-1, the following relationships may be obtained:

$$Y = Y_{MAX}\frac{x}{h} = \frac{\delta_2}{2h}x \tag{A-1}$$

$$\delta_1 + \delta_2 = \gamma \tag{A-2}$$

$$\delta_1 = \frac{\ell - h}{h}\delta_2 \tag{A-3}$$

$$\delta_2 = \frac{h}{\ell}\gamma \tag{A-4}$$

$$\theta = \frac{\delta_2}{h} \tag{A-5}$$

Substitute (A-5) into (A-1) and obtain:

$$Y = \frac{\theta}{2}x \tag{A-6}$$

From Ref. 13, the following expression for the deflection, Y_u, of a cylindrical roller of length ℓ, when pressed against a flat plate of infinite extension is:

$$Y_u = 2.54\frac{P^{.9}}{E^{.9}\ell^{.8}} \tag{A-7}$$

where

P is the total force between the plate and the roller

E is the common elastic modulus of the plate and the roller

Y_u is the deflection of the center of the roller

The deflection Y_u is caused by local deformation in the roller and in the plate. If these two components of deflection are assumed to be equal, then the local deflection of either is half that given by (A-7) namely

$$Y_u = 1.27\frac{P^{.9}}{E^{.9}\ell^{.8}} \tag{A-8}$$

Solving for P there is obtained:

$$P = \left(\frac{Y}{1.27}\right)^{10/9} E\,\ell^{8/9} \tag{A-9}$$

If it is assumed that the load per unit length, w, can be approximated by dividing (A-9) by ℓ, then:

$$w = \left(\frac{Y}{1.27}\right)^{10/9}\frac{E}{\ell^{1/9}} \tag{A-10}$$

Substituting (A-6) into (A-10) and letting $\ell = h$, yields:

$$w = \left(\frac{\theta x}{2.54}\right)^{10/9}\frac{E}{h^{1/9}} \tag{A-11}$$

The total tangential force acting on the gear tooth, F, must be equal to the integral of (A-11) between the limits h and zero.

$$F = \int_0^h w\,dx = \left(\frac{\theta}{2.54}\right)^{10/9}\frac{E}{h^{1/9}}\int_0^h x^{10/9}\,dx$$

$$= 0.168\,E\theta^{10/9}\,h^2 \tag{A-12}$$

Solve (A-12) for h and obtain:

$$h = \left[\frac{F}{0.168\,E\theta^{10/9}}\right]^{1/2} \tag{A-13}$$

Substitute (A-13) into (A-11), let $x = h$ and obtain w_{MAX}:

$$w_{MAX} = 0.8656\,E^{1/2}\,F^{1/2}\,\theta^{5/9} \tag{A-14}$$

Equation (A-14) expresses the maximum load per unit length in terms of the elastic modulus, the gear tangential load, and the angular misalignment.

The task now is to express w_{MAX} in terms of the maximum stress and the gear-tooth dimensions.

From Ref. 3 the Hertz stress, σ_H, for the case of normal stresses only at the contact, is:

$$\sigma_{H0} = 0.798\sqrt{\frac{wE\left(1+\frac{1}{\rho}\right)}{d(1-\nu^2)\sin 2\phi}} \qquad \text{(A-15)}$$

where

ρ is the gear-to-pinion diameter ratio

ν is Poisson's ratio

d is the pinion pitch diameter

ϕ is the pressure angle of the involute gear

The maximum shear stress, τ_{0MAX}, for the condition of only normal stresses at the tooth contact, exists beneath the contact surface, and its magnitude is:

$$\tau_{0MAX} = 0.304\,\sigma_{H0} \qquad \text{(A-16)}$$

Reference 10 shows that if frictional forces exist at the contact surface, the location of the maximum shear stress is closer to the surface, and if the friction coefficient is greater than 1/9, the maximum shear stress is at the surface. By using the Ref. 10 equations for the stress components, and letting Poisson's ratio be 1/4, the following expression for the maximum shear stress, τ_{MAX}, can be derived:

$$\tau_{MAX} = [0.575\,\mu + 0.238]\,\sigma_o, \text{ for } \mu > \frac{1}{9} \qquad \text{(A-17)}$$

where μ is the friction coefficient.

Substitute (A-15) into (A-17) and obtain:

$$\tau_{MAX} = (0.459\,\mu + 0.190)\sqrt{\frac{wE\left(1+\frac{1}{\rho}\right)}{d(1-\nu^2)\sin 2\phi}} \qquad \text{(A-18)}$$

Let ν be 1/4, and C be

$$\frac{1+\frac{1}{\rho}}{\sin 2\phi},$$

then (A-18) becomes:

$$\tau_{MAX} = (0.473\,\mu + 0.196)\sqrt{\frac{wEC}{d}},\ \mu > \frac{1}{9} \qquad \text{(A-19)}$$

Solve (A-19) for w and obtain:

$$w = \left(\frac{\tau_{MAX}}{0.473\,\mu + 0.196}\right)^2 \frac{d}{EC} \qquad \text{(A-20)}$$

Equate (A-20) to (A-14), solve for τ_{MAX}, and obtain:

$$\tau_{MAX} = \frac{(0.44\,\mu + 0.182)\,C^{1/2}\,E^{3/4}\,F^{1/4}\,\theta^{5/18}}{d^{1/2}} \qquad \text{(A-21)}$$

Estimates of maximum shear stress can be made using the following equations.

If the friction coefficient μ is less than 1/9 and the gear misalignment is zero use equations (A-15) and (A-16) to obtain:

$$\tau_{MAX} = 0.241\sqrt{\frac{wEC}{d(1-\nu^2)}} \qquad \text{(A-22)}$$

If the friction coefficient is less than 1/9 and there is a gear-tooth angular misalignment θ,

$$0.241\sqrt{\frac{wEC}{d(1-\nu^2)}} < \tau_{MAX} \leqslant 0.232\,\frac{C^{1/2}\,E^{3/4}\,F^{1/4}\,\theta^{5/18}}{d^{1/2}} \qquad \text{(A-23)}$$

If the friction coefficient is greater than 1/9 and the gear misalignment is zero, then:

$$\tau_{MAX} = (0.473\,\mu + 0.196)\sqrt{\frac{wEC}{d}} \qquad \text{(A-24)}$$

If the friction coefficient is greater than 1/9 and there is a gear-tooth angular misalignment θ,

$$(0.473\,\mu + 0.196)\sqrt{\frac{wEC}{d}} < \tau_{MAX}$$

$$\leqslant (0.44\,\mu + 0.182)\,\frac{C^{1/2}\,E^{3/4}\,F^{1/4}\,\theta^{5/18}}{d^{1/2}} \qquad \text{(A-25)}$$

These maximum shear stresses are plotted in Fig. 8 for the following values of the parameters which pertain to the 64-m antenna elevation drive gears.

C = 1.329, E = 29,000,000 psi or 19,994 716 (10^4) N/m^2

F = 15,545 lb or 69,144 N

d = 17.825 inches or 0.453 m

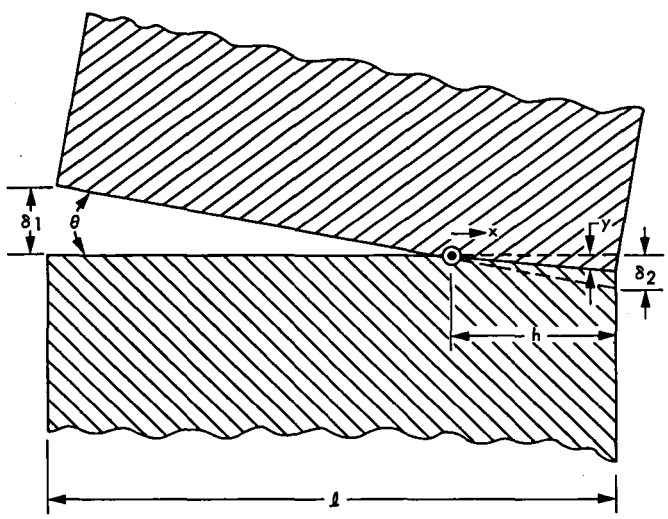

Fig. A-1. Geometry of misaligned gear teeth

Appendix B

Measurement of Bull Gear Tooth Bending Strain

In order to verify that the gear-tooth loading from countertorque is close to the calculated value, two bull-gear teeth were instrumented with foil strain gages so that the average absolute strain value could be measured. The locations of the gages on the ends of one tooth, as well as the bridge circuitry, are shown in Fig. B-1. The tests were conducted in April 1984 at DSS 63 because DSS 14 was undergoing extensive repair at the time. Calculated values should be fairly accurate, but in view of the plastic flow which has developed on the tooth surfaces it was wondered if there might be some dynamic effect which substantially increased the expected strain values. To determine if the tooth loading was speed dependent, the tests were run at various slew speeds and at a typical tracking speed.

I. Installation of the Strain Gages and Recording Equipment

(1) The strain gages were mounted on the edges of a tooth as shown in Fig. B-1. The four gages on one tooth constituted the resistances of the four legs of a Wheatstone bridge; hence, all the gages were active, thereby producing the maximum sensitivity.

(2) Two separate teeth were instrumented with sets of four gages in order to improve the reliability of obtaining good data.

(3) The teeth on which the gages were placed were located sufficiently far from the gear ends so that the gaged teeth meshed with both drive pinions at full slew speed.

(4) The gages were the foil type, having gage factors of approximately 2 and resistances of 350 ohms. The gages used were obtained from Measurements Group, Inc., of Raleigh, N.C., and are model number EA-06-125 AC-350 Option W3. The cement used was M Bond 200. The bridge input voltage was 10 volts DC.

(5) The ancillary equipment used consisted of a bridge balance supply unit, an amplifier, and a signal recorder having at least a 40-Hz response.

A. Conditions of Tests

The tests were conducted under the following conditions:

(1) The wind was less than 4.47 m/second.

(2) The countertorque pressure was 483×10^4 N/m^2 (700 psi).

(3) Both instrumented teeth were recorded while being driven past both drive pinions at an angular speed of 0.0042 degrees per second.

(4) Both instrumented teeth were recorded while being driven past both drive pinions at 0.0042 degrees per second, in the direction opposite to that of step 3.

(5) Both instrumented teeth were recorded while being driven past both pinions at the slew speed of 0.20 degree per second.

(6) Both instrumented teeth were recorded while being driven past both pinions at the slew speed of 0.20 degree per second, in the direction opposite to that of step 5.

(7) Both instrumented teeth were recorded while being driven past both pinions at the slew speed of 0.10 degree per second.

(8) Both instrumented teeth were recorded while being driven past both pinions at the slew speed of 0.10 degree per second, in the direction opposite to that of step 7.

B. Estimation of the Strain at the Gage

The tangential force between a countertorquing pinion and the bull gear, F_T, is given by the following equation (see Fig. 3):

$$F_T = \frac{2pDR\eta}{d} \tag{B-1}$$

where

p is the pressure to the hydraulic countertorquing motor

D is the hydraulic-motor displacement per radian

R is the gear-box ratio

η is the gear-box efficiency

d is the gear-box output pinion pitch diameter

For the 64-m antenna, the tangential force is:

$$F_T = \frac{2\,(700)(0.385)514(0.92)}{17.82} = 14{,}300 \text{ lb } (63{,}600 \text{ N}) \tag{B-2}$$

The bending stress, σ_b, at the tooth root per the Lewis formula [Ref. 3] is:

$$\sigma_b = \frac{F_T}{aLS} = \frac{14{,}300}{3.5(9.75)0.15} = 2430 \text{ psi } (1675 \text{ N/cm}^2) \tag{B-3}$$

where

a is the circular pitch

L is the tooth width

S is the form factor

The estimated stress at the gages, σ_G, is less than σ_b because the gages are closer to the neutral axis, and is:

$$\sigma_G = 2430 \frac{1.35}{1.50} = 2187 \text{ psi } (1508 \text{ N/cm}^2) \tag{B-4}$$

The strain at the gages, ϵ_G, is:

$$\epsilon_G = \frac{\sigma_G}{E} = \frac{2187}{29{,}000{,}000} = 0.0000754 \tag{B-5}$$

The voltage-output-to-voltage-input ratio of the gage circuitry shown in Fig. B-1 is:

$$\frac{V_o}{V_{IN}} = \frac{\Delta r}{r} = f\epsilon \tag{B-6}$$

where f is the defined gage factor.

The calibration strain, ϵ_c, was obtained by shunting across one leg of the bridge with a 811,000-ohm resistor. The calibration strain was:

$$\epsilon_c = \frac{r}{4(r+R)f} = \frac{350}{4(350+811{,}000)2} = 0.0000539 \tag{B-7}$$

By comparing the recorded bridge output voltage signals to the calibration signal, which corresponds to a strain of 0.0000539, the desired strains, ϵ_G, were obtained:

$$\epsilon_G = \epsilon_c \times \frac{\text{Recorded Signal Amplitude}}{\text{Recorded Calibration Amplitude}} \tag{B-8}$$

The maximum strain, ϵ_G, was found to be 0.0000772, which may be compared with the estimated value of 0.0000754 from Eq. (B-5). Therefore, it is clear that none of the elevation axis speeds tested caused any unexpected high gear-tooth forces. Traces from the actual strip chart are shown in Fig. 9. Although the maximum strain values are close to the predicted ones, the vacillating characteristics of the curves is not understood.

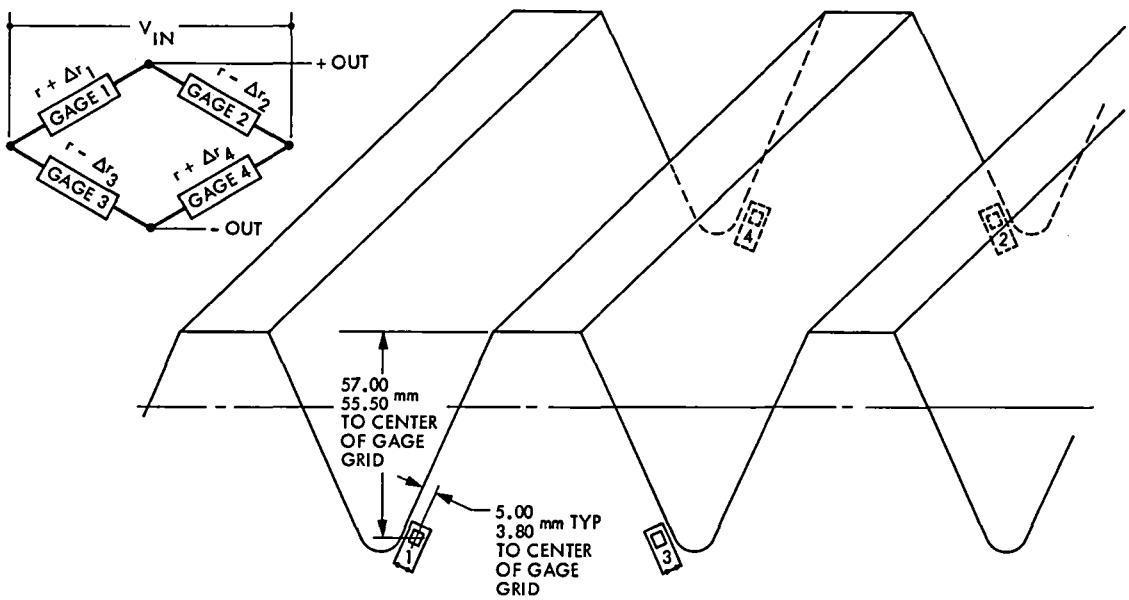

Fig. B-1. Location of strain gages on elevation drive bull gear and strain gage bridge

Appendix C

Estimation of Nominal Hertz Stress in the DSS12 Declination Bull Gear

The antenna at DSS 12, before its conversion to a 34-m antenna with electric drives, was a 26-m antenna with hydraulic drives incorporating countertorquing, which served to eliminate backlash. Thus, its drives were similar to those of the DSS 14 antenna. Reference 9 shows that a differential pressure of 300 psi was used on the two drive motors, so that for a zero wind condition the tangential force on the bull-gear tooth can be calculated by Eq. (B-1), obtaining:

$$F_T = \frac{2(\Delta p)DR\eta}{d} = \frac{2(300)(0.232)(285)0.80}{6.50} = 4882 \text{ lb} \tag{C-1}$$

From Eq. (A-15) the nominal Hertz stress, σ_{H0}, at full tooth contact is:

$$\sigma_{H0_{12}} = 0.798\sqrt{\frac{wE\left(1+\frac{1}{\rho}\right)}{d(1-\nu^2)\sin 2\phi}}$$

$$= 0.798\sqrt{\frac{814(29)10^6\left(1+\frac{1}{73.8}\right)}{6.5\,(1-0.25^2)\sin 40^\circ}} = 62{,}368 \text{ psi} \tag{C-2}$$

where $w = F/\ell = 4882/6 = 814$ lb/inch.

The corresponding stress for the DSS 14 elevation bull gear is:

$$\sigma_{H0_{14}} = 0.798\sqrt{\frac{15545\,(29)\,10^6\left(1+\frac{1}{56}\right)}{9.75(17.825)(1-0.25^2)\sin 50^\circ}}$$

$$= 48385 \text{ psi} \tag{C-3}$$

Acknowledgment

Drs. C. Chian and C. Hsieh of JPL directed our attention to the phenomenon of strain softening under cyclic loading and supplied a great deal of information on the subject.

References

1. McGinness, H., Characteristics of the Elevation Drive Suspension of the 64m Antennas, *TDA Progress Report 42-80*, March, 1985, pp. 146-175, Jet Propulsion Laboratory, Pasadena, California.
2. McGinness, H., *The Effects of Wind Loading on the Bearings and Drives of a 64m and 72m Diameter Antenna*, unpublished, Reorder number 84-2, Jet Propulsion Laboratory, Pasadena, California, May, 1984.
3. Buckingham, E., *Analytical Mechanics of Gears*, McGraw-Hill, First Edition, 1949.
4. *AGMA Standard, Nomenclature of Gear Tooth Failure Modes*, American Gear Manufacturers Association, August, 1980, p. 16.
5. Sandor, I., *Fundamentals of Cyclic Stress and Strain*, University of Wisconsin Press, 1972.
6. Raske and Morrow, *Mechanics of Materials in Low Cycle Fatigue Testing*, Manual on Low Cycle Fatigue Testing, ASTM STP 465, American Society for Testing Materials, 1969.
7. Timoshenko, S., *Theory of Elasticity*, McGraw-Hill, First Edition, 1934.
8. Landgraph, Mitchell, and LaPointe, *Montonic and Cyclic Properties of Engineering Materials*, Ford, 1972.
9. Menninger, F., *26m Antenna HA-dec Counter Torque Modifications*, Technical Report 32-1526, Vol. III, Jet Propulsion Laboratory, Pasadena, California, March, 1971.
10. Smith and Liu, "Stresses Due to Tangential and Normal Loads on an Elastic Solid with Applications to Some Contact Stress Problems," *Journal of Applied Mechanics*, June, 1953.
11. *Properties of Frequently Used Carbon and Alloy Steels*, Booklet 211, Bethlehem Steel Co., 1946, p. 60.
12. Levy, R. and H. McGinness, *Wind Power Prediction Model*, Technical Memorandum 33-802, Jet Propulsion Laboratory, Pasadena, California, 1976.
13. Palmgren, A., *Ball and Roller Bearing Engineering*, SKF Industries, Third Edition, 1959.

Repair of the DSS-14 Pedestal Concrete

D. McClure
64-Meter Rehabilitation and Performance Upgrade Project

The 64-meter antenna at the Goldstone Deep Space Communications Complex was dedicated in 1966, the first of three 64-meter antennas in the Deep Space Network. About three years after the antenna was dedicated, grout under the hydrostatic bearing runner was found to be interacting with the runner, causing rust to form between the runner and the sole plates upon which it rests. The rust formed unevenly and the runner could not be kept flat so in 1969 the grout was removed and replaced with a Portland cement and sand dry-pack grout that was less likely to produce rust. In the years that followed, oil leaking from the runner assembly caused progressive deterioration of the dry-pack grout. In 1982 over one thousand hours of spacecraft tracking time were lost due to this deterioration. In 1982 a plan was developed to rehabilitate the bearing. The plan called for raising the rotating structure free from the concrete pedestal and placing it on three pairs of external support columns. With the weight of the structure transferred to the columns, the pads and runner could be removed and the repair started. The very successful repair described here included the replacement of a significant portion of the antenna pedestal.

I. Background

The pedestal is the structure which supports the rotating part of the antenna. It is a cylindrical reinforced-concrete structure, 80 feet in diameter and about 30 feet high. Figure 1 shows a cross section of the pedestal. Lateral loads from the antenna are supported by the azimuth radial bearing assembly. Vertical loads from the antenna alidade are supported at three locations on hydrostatic bearing pads spaced equidistantly around the perimeter of the pedestal. Each pad rides on a thin film of oil on a steel runner 5 inches thick. The runner rests directly on steel sole plates grouted to the top surface of the pedestal. Figure 2 is a simplified cross-section diagram of this system.

The pedestal was designed such that the deflection of the runner and concrete under the bearing pad load matched that of the pad to allow the proper operation of the hydrostatic bearing. The concrete mix was designed to achieve a Young's Modulus of Elasticity (MOD E) of at least 5 million psi. Careful quality control was observed during the placement of the concrete to insure that the high MOD E requirement was met, and the test cylinders cast at that time (1964) confirmed the design.

By 1980, 16 years after the pedestal was built, surface cracking in an unusual pattern was noticed. Table 1 is a chronological listing of the events that followed. In May 1980 a core

was removed in an effort to determine the depth of one of the vertical cracks in the haunch. The core was sent to a laboratory for a petrographic examination. The examination report suggested alkali aggregate reactivity. At the time the pedestal was built, in 1964, it was known that reactive aggregate was being used. The American Society of Testing Materials (ASTM) specified the use of a low alkali cement (Type II) when this type of aggregate was used based on the results of tests it had conducted. These tests showed no expansion due to reactivity if low alkali cement was used. Unfortunately, these tests were conducted only over a one-year period. It now appears that the use of low alkali cement only postpones the inevitable.

Perhaps the most sobering event came with the measurement of the MOD E for the first cores removed in July 1982. Figure 3 shows the expected behavior of the MOD E with time. Very little data is available since the MOD E is not ordinarily a concrete design characteristic; concrete design engineers usually design for strength, not stiffness. Nevertheless, the measured values of less than 2 million to about 4 million psi were considerably less than the approximately 7 million psi expected. This was the first evidence that a serious problem was at hand. (It should be noted that there was no danger of the pedestal collapsing; the strength was more than adequate.) It was the declining stiffness that was alarming, for that could be contributing to the hydrostatic bearing problem.

A literature search showed that silica alkali reaction in concrete was first recognized in the late 1930s by the California Department of Highways. Although the process was recognized, most work was devoted to understanding the causes and effects. Little was being done to find remedies or corrective action for existing structures.

The primary concerns were establishing what the minimum acceptable MOD E could be, and at what rate the MOD E was deteriorating. In addition to removing and testing core samples, a program of frequent measurements using ultrasonic test equipment was started. The velocity of ultrasonic waves through concrete is proportional to the MOD E, but no information regarding the absolute value can be obtained. However, it is useful for establishing a trend, and, used in concert with the other tests, might give some idea of the useful life of the pedestal. Figure 4 shows the results of these tests. In terms of pulse velocity, the haunch area under the runner was the poorest.

When the pedestal was built, Carlson strain meters were embedded in the concrete. Their purpose was to monitor the curing process of the concrete. Typically concrete shrinks as it cures, fairly rapidly for the first year, then very slowly thereafter. These meters were read regularly for about 24 months, then the readings were discontinued because the meters were indicating little if any shrinkage was continuing to take place. When the readings were resumed in 1981, several of them showed significant expansion since the last readings 16 years earlier, exactly what would be expected if an alkali-aggregate reaction were taking place.

By late 1982 three monitoring programs were under way: 1) removal and test of core samples, 2) ultrasonic testing, and 3) reading of the Carlson strain meters.

In February 1983, measurements of pedestal deflection under load were made. These measurements were compared to similar measurements made in 1968 which confirmed a decrease in the MOD E of the pedestal concrete (Reference 1).

Recognizing that expert help was needed, a contract was let on March 1, 1983, to Construction Technology Laboratories (CTL) in Skokie, Illinois, a division of the Portland Cement Association. CTL is recognized in the construction industry as the leading concrete research organization in the United States, if not the world. It was asked to review the existing data, take its own measurements as required, and address the following:

(1) Confirm that the MOD E was deteriorating.

(2) Determine the rate of deterioration.

(3) Recommend when corrective action should be taken.

(4) Recommend solutions.

The thrust of its activity was to seek a solution that did not require complete replacement of the pedestal, and to do so before the start of the antenna downtime for the hydrostatic bearing repair scheduled for June of that year.

In its first report (Reference 2) CTL stated that the concrete quality had deteriorated within several of the sampled areas of the pedestal, and that it was continuing to deteriorate in the haunch. The average rate of deterioration was estimated to be 5% per year, with the largest estimated rate at particular locations to be approximately 15% per year. CTL went on to state:

> From a review of the data currently available, it cannot be assured with any degree of certainty that concrete in the pedestal will continue to provide the required stiffness for the operation of the hydrostatic bearing. It is possible that the bearing pads may become inoperable in certain regions of the pedestal within the next two years.

Voyager Uranus encounter was 30 months away.

With the hydrostatic bearing downtime scheduled to start June 6, it seemed appropriate to develop a solution before the downtime started. If the solution proved to require significant planning, it could be necessary to delay the start of the downtime. With this in mind, an Engineering Review Panel was established, and the review set for late in the month of May. At that review CTL presented the results of its study effort.

At the review several schemes were presented for repairing the pedestal. Figure 5 illustrates those considered. Plans A and C were basically containment schemes. Plan B was modified to include as much of the haunch as practical (Plan B-1) and was the plan adopted. The review panel unanimously agreed that removal of most of the haunch was the prudent course of action.

II. Description of Repair Action

On June 13, 1983, the antenna was taken out of service and preparations made to start the repair. Prior to this time the steel support columns had been designed, fabricated and shipped to the site. The design criterion of these columns (illustrated in Fig. 6) was that they must support the antenna such that it could withstand all forces included in the basic design. This included wind and seismic forces. Reinforced concrete spread footings for these columns had been constructed several weeks prior to the start of the downtime period.

All components that were to be removed and saved for reinstallation were tagged with plastic identification labels. After the reservoir walls and hydrostatic bearing piping were removed, hydraulic jacks were placed under each of the three corners of the alidade structure. The estimated weight of the alidade was 2.1 million pounds at Pad #3, and 2.0 million at each of the other two pads. Four jacks were placed under each corner weldment: two rated at 400 tons and two rated at 300 tons for a lifting capability of 2.8 million pounds. All jacks and associated equipment had been previously tested and certified by an independent laboratory.

The antenna structure had to be raised enough to allow the removal of the pad assembly. In previous situations the structure was lifted 0.25 inch. In this case, since the structure weight was to be transferred to external supporting columns, the compression of the columns, and the soil under the columns, had to be considered. The column compression was straightforward to calculate and found to be 0.100 inch. The soil characteristics were less well known and the most conservative estimate of compression was 0.60 inch. All factors considered, it was decided to raise the antenna 0.9 inch. Instrumentation was installed to monitor not only the vertical motion as the structure was being raised, but the horizontal as well. This was necessary to insure that undue forces were not transmitted to the radial bearing during this operation.

The structure was raised 0.1 inch at a time at each of the three corners. A 6-inch-diameter steel stool was placed alongside each jack as a safety precaution, and shims were added to fill the gap as the structure was raised. When the antenna had been raised the full amount, the bearing pads were removed, and the steel support columns installed. When Pad #2 was removed, a crack was discovered in the bottom plate of the corner weldment. This crack is similar to one found at DSS-43 several years earlier. The crack appeared to be an old one and was repaired before the pad was reinstalled.

To prevent sudden loading of the soil under the column foundations, the load was transferred from the jacks to the columns over a three-day period. Instrumentation was installed to monitor the settling of the columns. After several days the settlement stopped at about 0.45 inches. The actual weight of the rotating part of the antenna was measured as 6,123,856 pounds based on the hydraulic pressure required to raise it.

With the pedestal free of the antenna structure, the hydrostatic bearing runner segments were removed. Particular care was taken during this removal so that the condition of the old grout could be observed. Of special interest was the epoxy grout which had been installed 9 months earlier as a test case. Epoxy grout was being evaluated as an alternative to the Portland cement grout because of its better oil resistance property. While it appears to be a viable product for grout repair, the complex and demanding handling requirements were too severe for use in this repair task.

The runner segments were removed to a work area to the east of the antenna where they could be reworked. Before the runner was removed, careful measurements were taken of the distance from the top of the runner to the top of the azimuth bull gear. In this way the runner could be replaced at the same elevation.

With the runner segments off the pedestal, work could start on the removal of the concrete. Although the MOD E was below the design requirements, the compressive strength was still quite high and it was recognized that this would make removal difficult. In addition, the concrete contained a large amount of reinforcing steel which further complicated removal. Prior to the antenna downtime a proprietary expansive agent had been tested which could be used to crack the concrete in preparation for removal by jackhammers. One-inch holes were drilled six feet deep on 12-inch centers in a horizontal plane. These holes were then filled with the expansive material and allowed to set for 24 hours. Although some

cracking did take place, the contractor had considerable difficulty in breaking up the concrete with jackhammers. At this point he employed a hydraulically powered machine which imparted forces on the concrete of several thousand pounds at 250 cycles per minute. This caused the whole pedestal to vibrate such that there was concern for its safety. Work on concrete removal was stopped until another approach could be developed.

After a week of tests, a stronger expansive agent was employed, and a new pattern of breakage was established. First, the outer four inches of the pedestal wall were removed, exposing the one-inch reinforcing steel. These steel bars were then cut, and horizontal holes were drilled on 12-inch centers, so that a horizontal cracking plane was established. The stronger expansive agent generated horizontal cracks of 0.5 to 1 inch. Removal by jackhammer was thus made easier. It took about 5 days for a crew of four men to remove a segment forty feet long.

The concrete was not removed all at one time. The pedestal is basically a cylindrical structure with a roof deck. The portion to be removed consisted of the corner between the vertical wall and the roof deck. It was impractical to support the roof deck from below. Furthermore, the radial bearing, which resists lateral loads, is an integral part of the roof deck. Two steps were taken to insure the structural integrity of the pedestal during the removal process. First, six 2.25-inch-diameter steel cables were wrapped around the pedestal just below the area to be removed. These cables were tensioned to 180,000 pounds and provided circular restraint. Second, the concrete was removed three segments at a time as shown in Fig. 7. After each set of three segments had been replaced with new concrete, it was allowed to cure for seven days before removal was started on the adjacent segments. In this way, two-thirds of the connection between the pedestal wall and roof deck was in place at all times. The first three segments removed were those at the pad locations. Thus, when the antenna structure was replaced on the pedestal, it would rest on the oldest concrete. This strategy was adopted to minimize creep since it would be several months before the antenna would be rotated.

Replacing the concrete meant that a new mix design had to be developed. Several sources of non-reactive aggregate were identified in California and three of these were selected for test. Construction Technology Laboratories tested fourteen mix designs which are summarized in Table 2. Aggregate from Lytle Creek in San Bernardino County has the reputation for being of excellent quality and had the added advantage of being close to the job site. It was therefore disappointing when the MOD E values for those samples were lower than the design goal of 5.0 million psi. Investigation revealed that the aggregate, from a river bed, had a relatively soft surface due to long term exposure to the elements. This made it necessary to consider only quarried and crushed aggregate so that the surface would be "fresh." The aggregate ultimately selected came from a quarry near Mountain View, California, some 400 miles from the job site.

Other factors which influence concrete quality are the cement content (sacks/cubic yard), the water/cement ratio (which determines the slump), and the use of a super-plasticizer (which improves workability of a mix with a low water/cement ratio). In general the MOD E is improved with increasing cement factor and decreasing water/cement ratio. There is no test data to indicate the effect on the MOD E with the use of a super-plasticizer although CTL felt there would be no deleterious effect.

Mix 12-7 with super-plasticizer was selected for the replacement concrete. Pumping the concrete into the first section was extremely difficult. It was concluded that the large (1.5 inch) aggregate was getting lodged in the hose, so the mix was changed to use 1-inch aggregate, and the water/cement ratio lowered to 0.42 from 0.45. As it later developed, the difficulty was that the water content was lower than thought due to the way the aggregate absorbed the moisture. Fortunately, low water content raises the MOD E, a desirable feature. Table 3 summarizes the two mixes.

Test cylinders were cast during the placement of the concrete and these cylinders were tested after cure times of 7, 28 and 60 days. The results of these tests show MOD E values well in excess of the 5 million psi specified. The test results are plotted in Fig. 8.

III. Conclusion

Raising the 6-million-pound antenna and placing it in a temporary support structure, removing the hydrostatic bearing, and removing and replacing 450 cubic yards of concrete was a monumental task. The task was completed on schedule, within budget, and without a lost-time accident. The concrete replacement required working with state-of-the-art technology, and the development of new design considerations for high MOD E concrete. As a result, the replacement concrete now provides a stiff ring around the pedestal which will provide excellent support for the hydrostatic bearing at DSS-14 for many years.

Acknowledgment

The author thanks F. McLaughlin, H. Phillips, A. Riewe and I. Wells for their help in preparing this article.

References

1. H. McGinness and G. Anderson, "Evaluation of Antenna Foundation Elastic Modulus," TDA Progress Report 42-73, January-March 1983, Jet Propulsion Laboratory, Pasadena, California, pp. 89-91.
2. "Evaluation of DSS-14 Pedestal–Review of Concrete Quality, Report No. 1 to JPL Contract No. 956494," May 1983, Construction Technology Laboratories, Skokie, Illinois.

Table 1. History of DSS-14 pedestal concrete analysis

Date	Comment
May 1980	Cracks in the pedestal had been observed prior to this time, but in May 1980, a core was removed from the haunch area (135 degrees trough azimuth). This core was taken on a vertical crack in an effort to determine how deep the crack went. The sample was sent to an independent laboratory for a petrographic examination.
August 1980	A report was made to the DSS-14 Life Maintenance Task Force which included results of the petrographic study on the pedestal cores. The petrographic study included the words "strongly suggest" alkali aggregate reactivity. A recommendation was made at that time to reestablish the Carlson meter readings, maintain integrity of the paint (to prevent moisture intrusion), caulk the cracks, and discontinue steam cleaning the pedestal.
Late 1980 to Mid 1982	An extensive literature search was conducted. Also, the contract industry was surveyed to determine what others had experienced in the way of reactive aggregate and, furthermore, what steps might be taken to arrest the reaction. Some of the organizations contacted were: Owl Rock, owner of the Barstow Pit (source of the original aggregate); Bureau of Reclamation; Caltrans; Corps of Engineers; Holmes and Narver (did original pedestal design); Portland Cement Association; and University of California, Berkeley.
October 1981	Dave Stark of Construction Technology Laboratories (CTL) visited both DSS-13 and DSS-14 to inspect cracking and concluded that reactivity was occurring in both antennas.
December 1981	Started recording Carlson strain meter readings once a month. (The start was delayed due to some difficulty in locating the documentation of the first two years' readings, the measurement device, and instructions for using it.)
July 1982	Started a program to periodically remove core samples from various portions of the pedestal. These samples were to be tested for Young's Modulus of Elasticity (MOD E) in an effort to determine if the MOD E was changing.
August 1982	Contracted for the consulting services of Mr. J. Dobrowolski (a private consultant) to perform pulse-velocity tests through the concrete pedestal at several locations. Mr. Dobrowolski was formerly with the Portland Cement Association and is a distinguished engineer in the concrete industry. Pulse-velocity measurements were taken once a month in an effort to develop the rate of the MOD E deterioration. These tests were to complement the direct measurement of the MOD E on core samples removed from the pedestal.
December 1982	JPL cognizant engineer met with CTL engineers to outline a program to determine rate of deterioration and possible solutions to the problem of the pedestal. The feeling at that time was that the issue would have to be addressed either shortly before Neptune encounter (1989) or perhaps after that encounter.
January 25, 1983	Proposal from CTL was received.
March 1, 1983	A contract was let to CTL to: a. Confirm that the MOD E was deteriorating. b. Determine the rate of deterioration. c. Determine when corrective action should be taken. d. Recommend solutions. The thrust of the CTL activity was to find out when corrective action was necessary and if something short of replacing the entire pedestal was feasible. The time schedule was to provide a preliminary report in April, with the final report due in October 1983.
April 8, 1983	In a letter reporting its preliminary findings, CTL stated that the rate of deterioration in the haunch area was such that serious hydrostatic bearing support problems could be expected within the next two years if corrective action was not taken. It further recommended that some form of corrective action be taken during the hydrostatic bearing downtime scheduled to start June 6, 1983.
May 2, 1983	CTL made a presentation to JPL which showed the results of its analysis of test data taken both before and after CTL was placed on contract. Based on this presentation, a meeting was set for the next day to seek solutions.
May 3, 1983	Meeting was held at JPL with JPL engineers, Project staff, CTL, and Mr. Robert Hoggan (a professional structural engineer consultant from H. Robert Hoggan & Associates). The purpose of the meeting was to explore means of replacing the major portion of the haunch concrete as recommended by CTL. Two options were developed but additional test data was needed to support the design of either of them.
May 27, 1983	An engineering review panel met at JPL to review the options for replacing haunch concrete and the advantages, disadvantages, cost, and schedule impact for each. The review panel and audience included structural engineering personnel, engineering managers, and Project staff, with CTL participating in the review. At the conclusion of the review, the unanimous choice of the review board, as well as the engineering personnel in the audience, was a plan to remove essentially all of the haunch material and replace it with new concrete.
June 13, 1983	The antenna was taken out of service, and the repair work started. Over the next twelve months, the rotating structure was raised and supported on temporary columns, the hydrostatic bearing removed, the haunch concrete removed and replaced, the bearing replaced, and the antenna returned to service. The performance of the hydrostatic bearing was equal to, and in some areas exceeded, the original performance.
June 15, 1984	The antenna was placed on-line to support the Mark IVA implementation.

Table 2. Mix designs and test results

Mix number	Coarse aggregate	Fine aggregate	Cement, sacks/yard^3	Water/ cement	SWR[a]	Slump, inches	Density, PCF	Compressive strength and MOD E[b] 1 day	7 days	28 days
10-1	Owl Rock Lytle Creek	Owl Rock Lytle Creek	7.0	0.35	Melment	2.4	152.5	4825 3.21	4170 2.97	
10-3	Kaiser	Owl Rock Lytle Creek	7.0	0.35	Melment	1.5	154.5	3935 3.09	5830 4.82	7330 5.32/5.26
10-4	Watsonville Rock Co.	Kaiser Olympia	7.0	0.35	Melment	0.5	155.6	6400 4.10	6600 4.38	8280/8280 4.93/4.76
10-5	Kaiser	Kaiser Olympia	7.0	0.35	Melment	2.6	153.0	5280 4.56	5740 5.04	7440 5.59/5.68
10-7	Kaiser	Kaiser Olympia	7.0	0.35	Melment	0.4	152.9	6160 5.34	6400 5.67	7910 5.90
12-1	Owl Rock Lytle Creek	Owl Rock Lytle Creek	6.7	0.42	None	3.3	150.5	3445 3.51	4710 3.10	N/A N/A
12-2	Watsonville Rock Co.	Owl Rock Lytle Creek	6.7	0.45	None	1.5	155.3	4340 3.04	N/A N/A	7230 4.2
12-3	Kaiser	Owl Rock Lytle Creek	6.7	0.42+ (0.33?)	None	3.7	151.0	5755 4.80	3900 3.90	5700 4.43
12-3A	Kaiser	Owl Rock Lytle Creek	6.7	0.41	None	1.0	151.9	4810 3.96	N/A N/A	7700 5.38
12-4	Watsonville Rock Co.	Kaiser Olympia		0.45	None	0.6	154.3	4670 3.52	5140 3.85	7100/7100 4.50/4.30
12-5	Kaiser	Kaiser Olympia	6.7	0.42	None	1.3	151.0	4735 4.29	5020 4.44	7320 5.38
12-7	Kaiser	Kaiser Olympia	6.7	0.45	None	0.9	150.9	4370 4.51	4850 4.84	7030 5.31

[a]Super Water Reducer

[b]Top value is compressive strength, psi. Bottom value is MOD E, psi x 10^6.

Table 3. Comparison of design and final mix

Ingredient	Design mix quantity, lb/cubic yard[a]	Final mix quantity, lb/cubic yard[a]
Cement	627	627
Water (net)	284	260
Coarse aggregates:		
1.5 inches to .75 inch	660	2011
1 inch to No. 4	1340	
Fine aggregate	1196	1214
Admixture	None	8.2
Slump	0.9 inch	1.13 inch
(after admixture)	Not applicable	3.87 inch

[a]Weights based on 1% air in concrete.

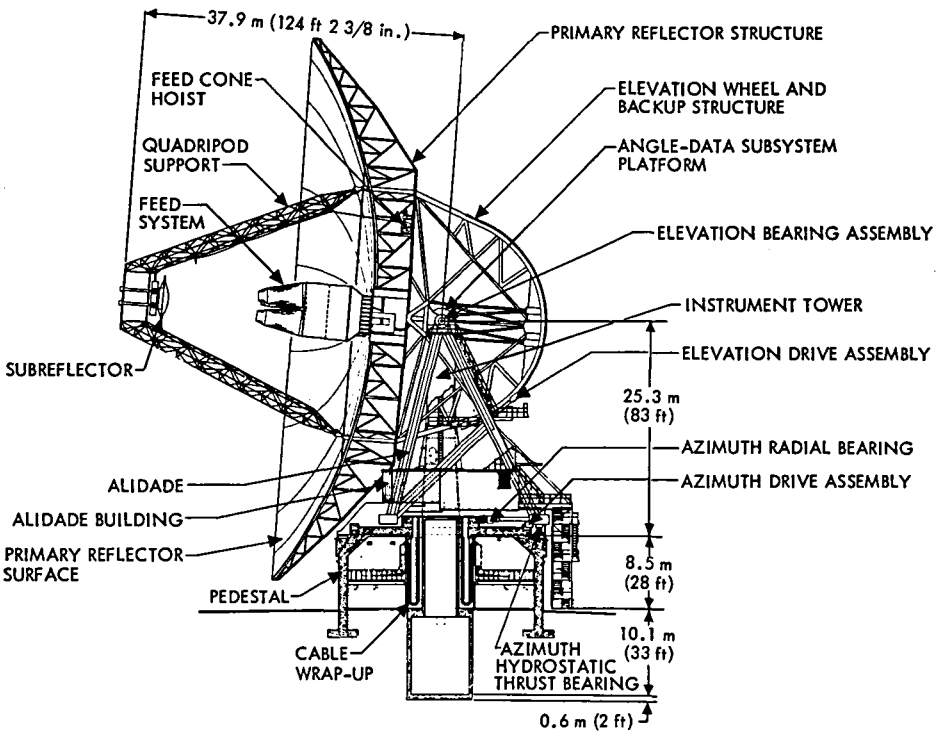

Fig. 1. DSS-14 antenna cross section

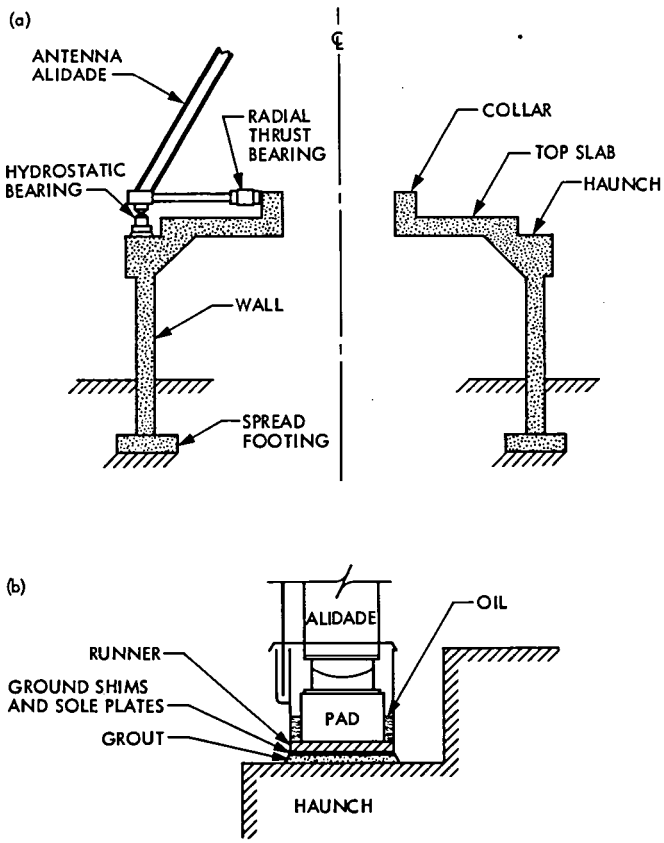

Fig. 2. Simplified cross section of (a) pedestal, and (b) hydrostatic bearing

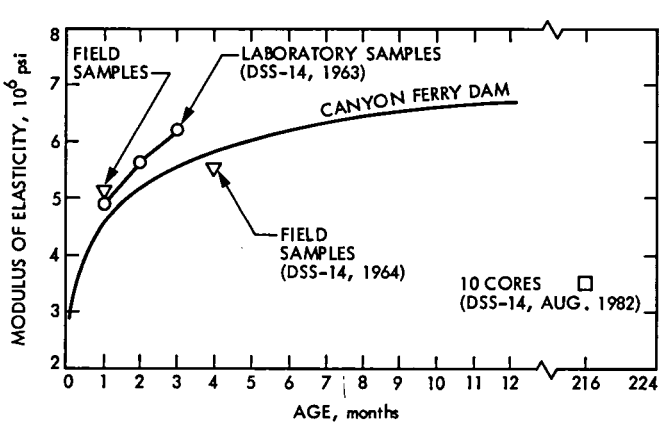

Fig. 3. Modulus of elasticity vs. time

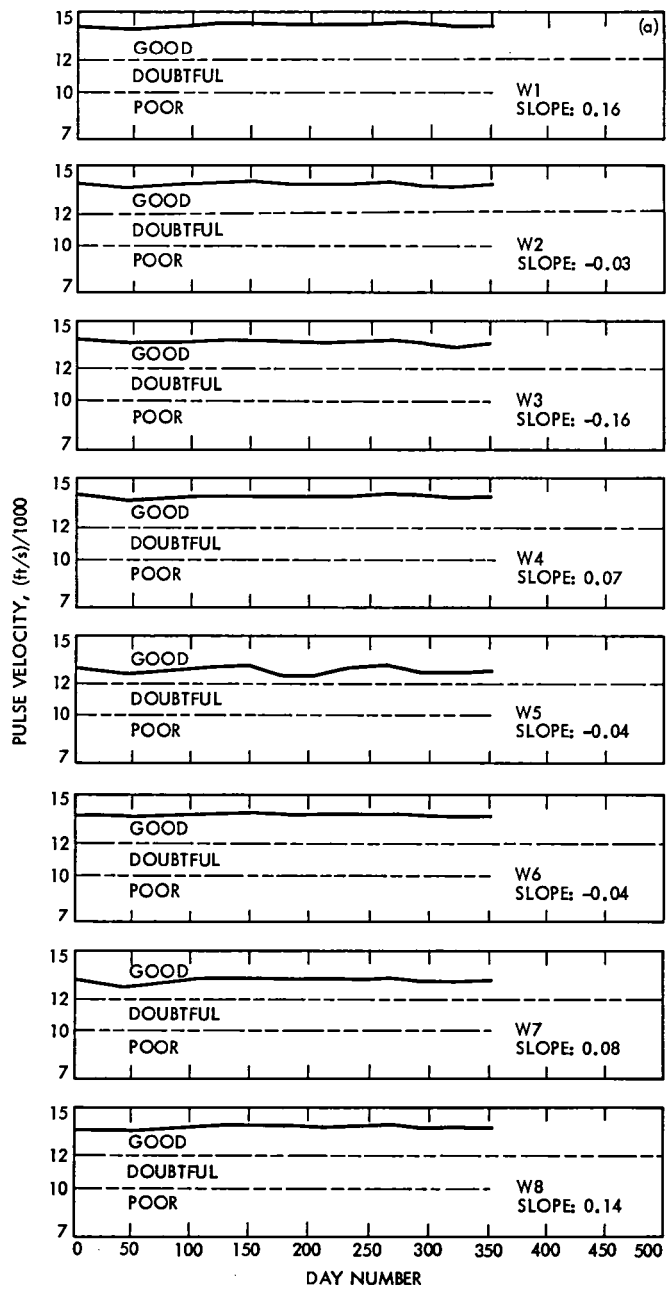

Fig. 4. DSS-14 pulse velocity readings of the (a) pedestal wall, (b) pedestal haunch, and (c) pedestal collar. Day 0 is July 21, 1982, and the slope is in units of (ft/s/year)/1,000.

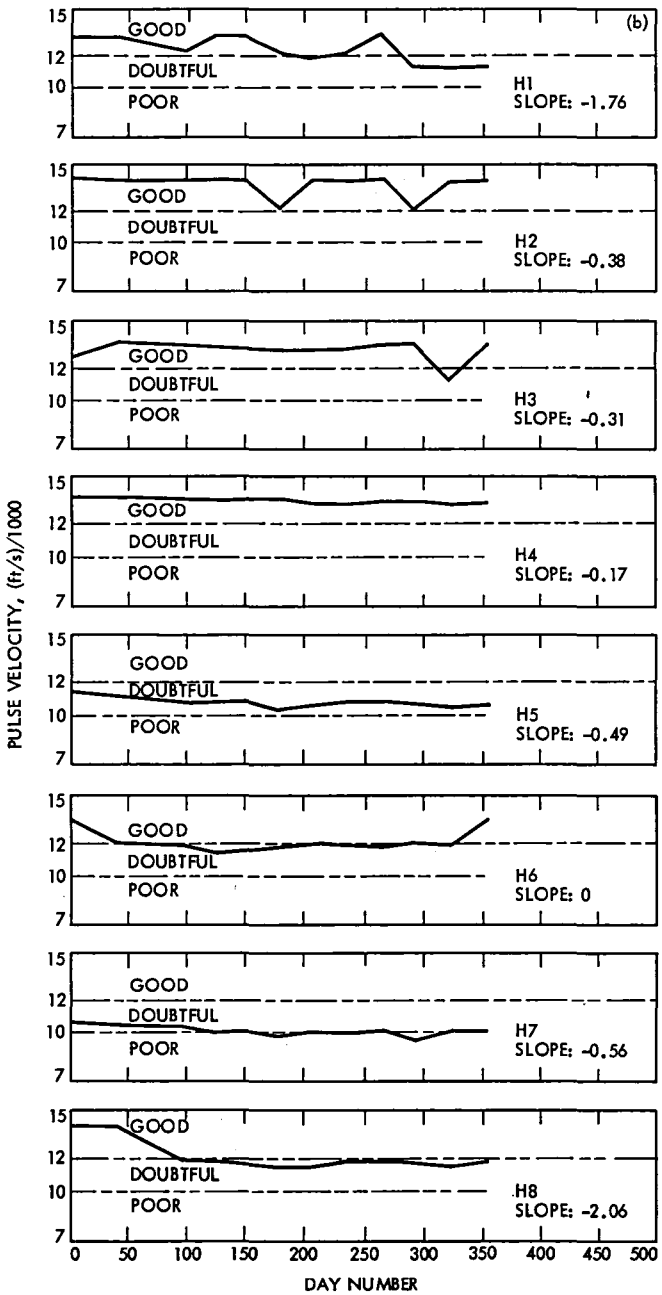

Fig. 4 (contd)

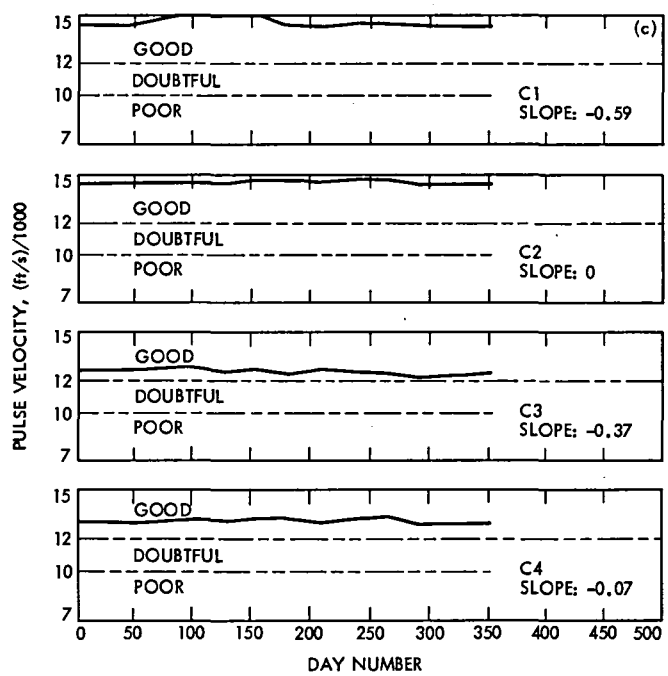

Fig. 4 (contd)

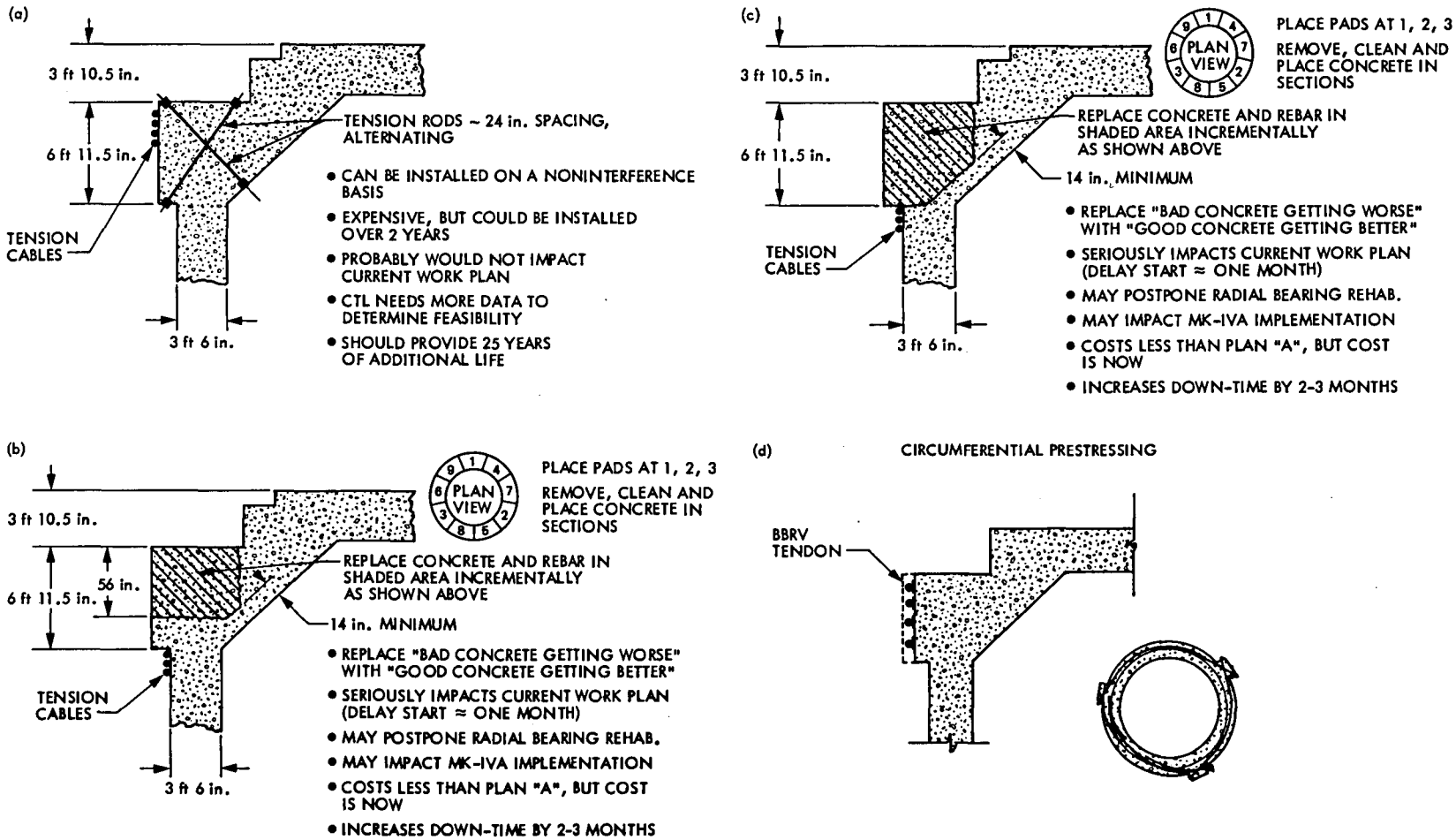

Fig. 5. Repair plan options: (a) Plan "A," (b) Plan "B," (c) Plan "B-1," and (d) Plan "C"

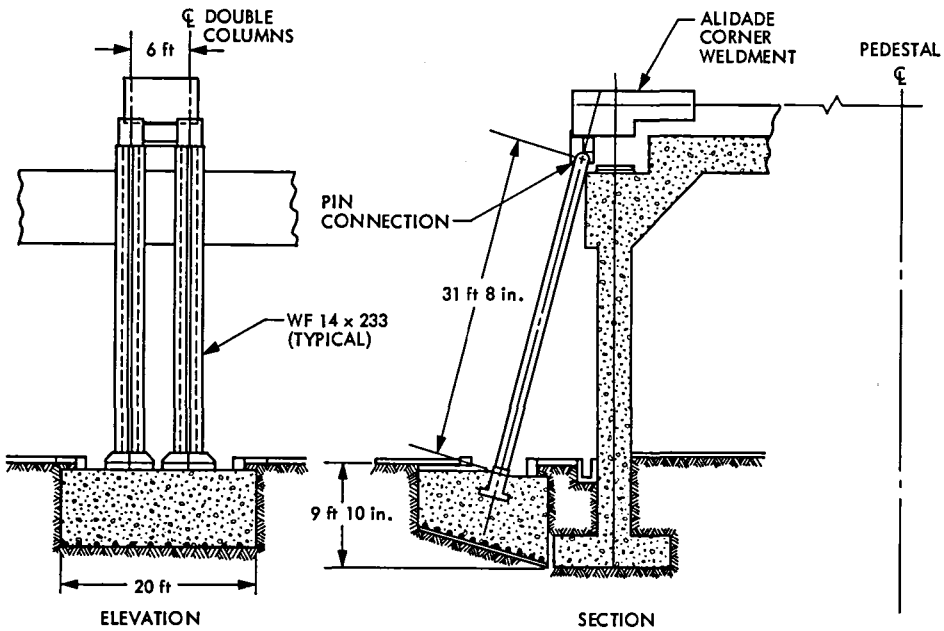

Fig. 6. Support structure and foundation

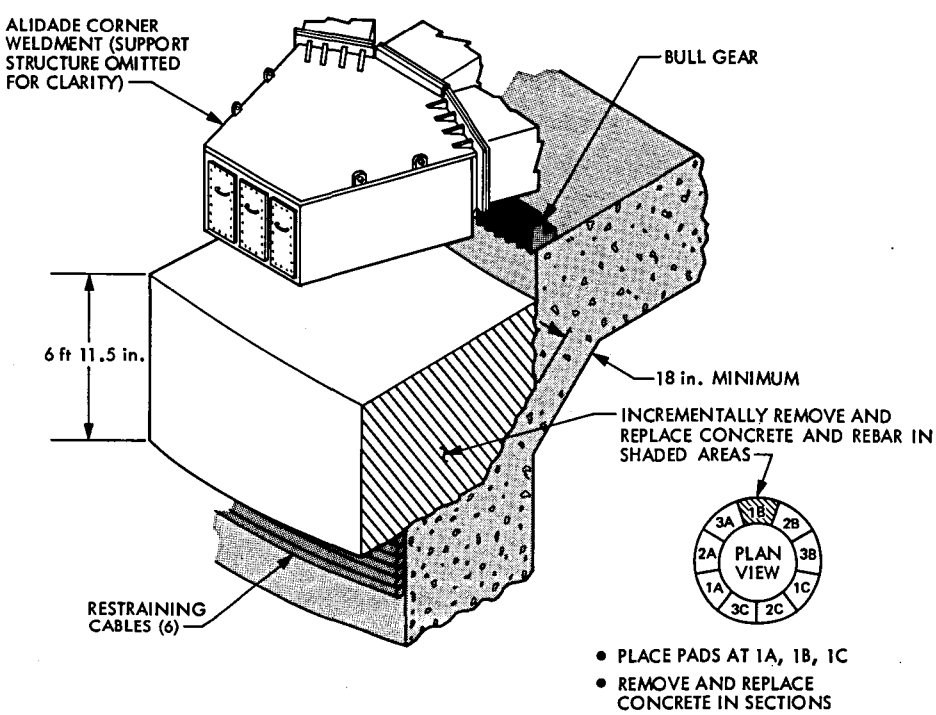

Fig. 7. Pictoral of replacement strategy

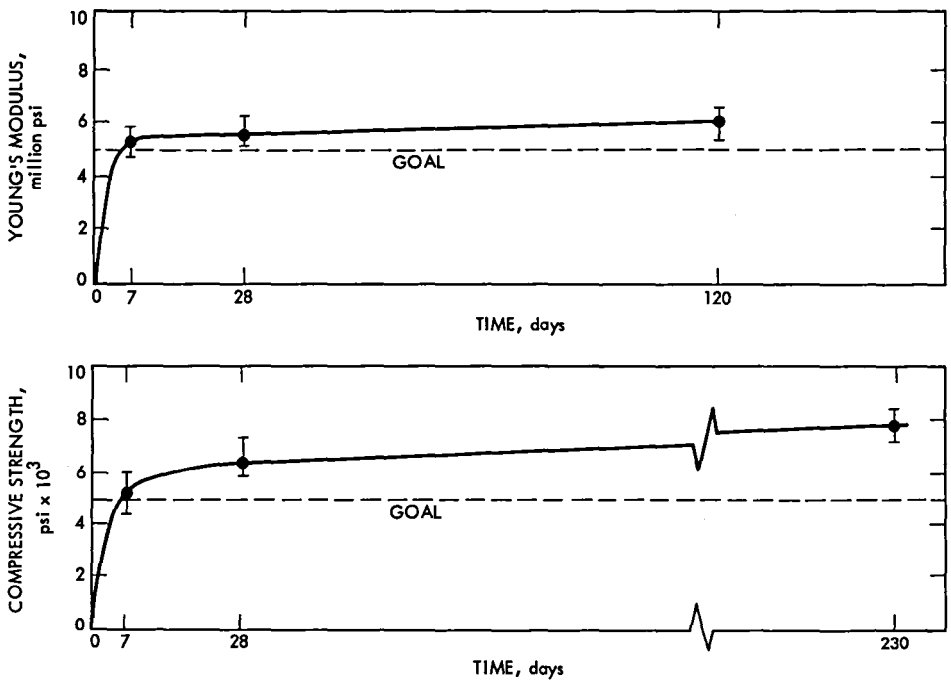

Fig. 8. Replacement concrete test results

Determining Availability Characteristics of DSN Data Systems Using Discrepancy Report Data

A. M. Ruskin
Telecommunications and Data Acquisition Planning Office

C. T. Quach
DSN Data Systems Section

A reasonably economical way has been developed to determine availability characteristics of DSN data systems, subsystems, and assemblies using the DSN Discrepancy Report (DR) database and DSN operating schedule and history databases. Operating Mean Time Between Failures (OMTBF), Operating Mean Time to Restore Service (OMTTRS), and Operating Functional Availability (OFA) can be computed by year, by system, by subsystem, by assembly, and by station.

In this report, the effort required to produce the desired reports is described; specific data on the Telemetry, Command, and Tracking Systems are presented; and major contributors to system outages are identified. Future improvements in preparing and analyzing DR data are also outlined to enhance their use in correcting conditions that lead to outages.

I. Introduction

The purpose of this investigation is to develop an economical way to determine the Operating Mean Time Between Failures (OMTBF), Operating Mean Time To Restore Service (OMTTRS), and Operating Functional Availability (OFA) of DSN data systems, subsystems, and assemblies using an existing Discrepancy Report (DR) database. The DR database contains records of DSN outages that occur during scheduled service. It is an attractive source because it is mandated by JPL policy[1] and is necessarily maintained even when budgets are oversubscribed. The availability characteristics (OMTBF, OMTTRS, and OFA) of DSN data systems and their major elements can be used to determine which aspects of the DSN are causing service downtime. The latter information can of course be used in prioritizing DSN maintenance and redesign activities.

This investigation is based on Discrepancy Reports (DR) for the DSN Telemetry (TLM) System, Command (CMD) System, and Tracking (TRK) System, and their respective subsystems and assemblies for the period January 1981 through September 1984. While DRs were prepared long before 1981, it has been only since that time that they have been stored in a machine-readable form. Data are available by day, by week, and by year and by DSN station.

An outage of a DSN system other than the Telemetry, Command, and Tracking Systems does not necessarily cause a

[1] JPL Standard Practice Instruction 4-11-5, *Problem/Failure Accountability*, September 17, 1984, 4 pages (internal document), and Document 841-1, *DSN Standard Operations Plan*, Section 9, May 24, 1982, 11 pages (internal document).

DR to be written if it does not cause an outage in one of these three key data systems. Also, DRs are not necessarily written even for outages in a key system if the data are recovered by auxilliary means, e.g., via playback of a tape recorder.

Discrepancy Reports are written only when a station is scheduled to provide certain types of service, namely spacecraft tracking, project-related support, project preparation, and multimission support. DRs are not written during periods of maintenance, implementation, and other non-service periods. Accordingly, the parameters presented below are based only on so-called operating hours and are therefore labeled Operating Mean Time Between Failures (OMTBF), Operating Mean Time to Restore Service (OMTTRS), or Operating Functional Availability (OFA).

As described in Section II.A, the calculation of availability characteristics requires knowledge of the hours of operation scheduled for each system. Unfortunately, the operating data now available lack detail about when some functions were actually used or were scheduled for use. This latter phenomenon severely limits analyses of both Command System and Tracking System parameters. It does not significantly affect the Telemetry System, which is almost always "on" whenever a station is scheduled to provide service. As a consequence, availability characteristics can be readily calculated for the Telemetry System, but similar calculations for the Command and Tracking Systems cannot be performed using the historical data.[2]

Also, when parallel assemblies exist, i.e., a prime with backups, the DR database does not distinguish among the alternative assemblies. Nor does the DR database necessarily include information on whether a backup assembly was available when a prime assembly failed or whether service was restored by using a backup or by recovery of the prime unit.

II. Approach

A. General Description

A Discrepancy Report (DR) is prepared whenever the DSN fails to serve a customer as planned. Each DR identifies the system, subsystem, assembly, and station that caused the failure, the time that the outage occurred and its duration, and a description of the failure. These reports are entered into a computer database called the DR database. The DR database can thus be sorted to provide summaries of outages for various data systems, for their respective subsystems and assemblies, and for individual stations, all for various periods of time.

Separately, the DSN records the history of its operations by station. These records show the number of operating hours by week, but they do not show which functions are performed while operating. However, it is commonly believed that a station's Telemetry System is "on" nearly 100% of the time that the station operates. The Command and Tracking Systems are generally operated only fractions of the time that a station is "on," but the fractions cannot be determined without manually searching a multitude of project logs and then inferring how long the equipment was "on."

The Operating Mean Time Between Failure (OMTBF) for a particular system, subsystem, assembly, or station can be calculated by dividing the number of operating hours in a given period by the corresponding number of outages.[3] Likewise, the Operating Mean Time to Restore Service (OMTTRS) for a system, subsystem, assembly, or station can be calculated by dividing the total duration of outage in a given period by the corresponding number of outages.

Operating Functional Availability (OFA) is the fraction of the time that a system, subsystem, assembly, or other element functions according to plan. It can be calculated by dividing the average "on" time (or "up" time) by the sum of the average "on" time and the average "down" time. The average "on" time is OMTBF and the average "down" time is OMTTRS, so OFA is given by the following formula:

$$OFA = (OMTBF)/(OMTBF + OMTTRS)$$

In the following sections are descriptions of the data sources and their use and of the processes used to reduce the data.

B. Data Sources

The Discrepancy Report (DR) database is a computerized database compiled from information gathered on the form shown in Fig. 1. This form was designed originally to describe individual outages and not particularly to facilitate statistical studies. Accordingly, much information is in narrative form, with little or no control of vocabulary or level of detail. Only

[2]Project logs contain operating history data that are needed to calculate availability characteristics for the Command and Tracking Systems. However, these logs are generally scattered manual records that cannot be readily searched for relevant data. Moreover, some inference is required to determine how long the Command or Tracking Systems were actually "on" for the events noted in these logs.

[3]More precisely, an OMTBF can be calculated by dividing the number of outages into scheduled operating time less outage time. However, when outage times are small compared with scheduled operating times, as is the case here, then the differences in the two calculational approaches are insignificant.

synopses of narratives are recorded in the DR database unless, of course, they are so brief that they can be recorded in their entirety.

The DR database is a hierarchically organized computer-based file. The Telemetry, Command, and Tracking Systems' data are thus in separate, unrelated records. Data on subsystems that are part of more than one system, e.g., the Antenna Mechanical Subsystem, are repeatedly filed under each system of which they are part.

Station operating hours (SOH) and end user hours (EUH) are summarized weekly in hard-copy DSN Station Utilization Summary Reports. An example of a Station Utilization Summary Report is given in Fig. 2. The raw data for the utilization reports for the current year are readily available, but tapes for prior years are now kept only in archive files. Station Utilization Summary Reports are organized by station, by project, and by support category. "Support category" includes spacecraft tracking (category 1A1), project-related support (category 1A2), project preparation (category 1A3), multimission support (1A4), preventive maintenance (category 2A1), corrective maintenance (category 2A2), and so forth. Finer levels of detail of these categories have not been recorded.

Several qualifying comments about the data are warranted. First, the fact that DRs are written only when a DSN customer is being supported eliminates all categories other than 1Ax from further consideration in this study. Also, DRs are not written during system integration tests, which are part of category 1A3, and tests of automatic gain controls, which are part of category 1A4. However, each of these activities amounts to less than one percent of its respective category, which is itself only a few percent of the total time for category 1Ax. Thus, the inclusion of system integration tests and tests of automatic gain controls hardly affects the overall results reported below.

DRs are not necessarily written for outages that occur during pre-pass and post-pass calibrations. If an outage affects DSN service to a customer or would have done so if it were not for heroic efforts, then a DR is written. Otherwise, a DR might not be written. The extent of the impact of this uneven practice on the data is not clear, but the direction of the impact is clear: It causes calculated OMTBSs and OFAs to be somewhat more attractive than they really are.

Second, DR data are subject to being "corrected" as detailed DR investigations continue. Also, minor adjustments are sometimes made to SOH data after initial SOH summaries are prepared. Accordingly, this investigation has used the latest data available, which may produce small differences from any results obtained using earlier data. Our tests of such instances indicate that these differences are insignificant in the context of this study.

Third, a class of DRs exists, known as master DRs, which are not considered in this study. A "master DR" is a DR file used to collect information from individual DRs all of which seem to be related to a common situation. Since a master DR duplicates information already contained in "regular" DRs, it is inappropriate to include them in this investigation.

Fourth, instances of misspelling of DSN subsystems and assemblies have been discovered in the DR database when listing outages by subsystem or assembly. In most cases, misspelled elements can be properly identified, and indeed this study consolidates apparently different categories when it is appropriate to do so. In a few cases, however, a misspelled element remains a mystery, and the outage escapes being correctly listed as part of a given class. In addition, some DRs show no subsystem or assembly for the outage; these too escape listings by these parameters.

And finally, data are reported weekly but longer periods such as a month, a quarter, or a year are often more convenient in analyzing trends. Because none of these is composed of even multiples of a week, the following convention is used by the DSN. A year is generally divided into four quarters of thirteen weeks, and each quarter is then divided into three periods of four, four, and five weeks, respectively. Of course, no year is exactly fifty-two weeks, and every few years a fifty-three week year, i.e., a leap year, is required. When this occurs, the extra week is added to the first period of the fourth quarter. This leap quarter then has three periods of five, four, and five weeks, respectively. The year 1981 was a fifty-three week year, and 1982, 1983, and 1984 were fifty-two week years.

C. Data Processing

Three approaches to data processing were considered. The first is to perform all calculations in the JPL IBM 3083 computer, on which the DR database is installed. In this approach, operating history data would be added to the IBM 3083 computer and the DR database would be queried directly for the information needed for each calculation. This approach was rejected in favor of another because it is difficult to access the DR database on demand.

The second approach is to derive files of DRs from the DR database which would be kept in the Univac 1100/81 system and used there together with operating history data, which it already contains. This approach would obviate the need to access the original DR database on demand, but it still involves depending upon third parties and their facilities to do interactive processing.

Both of the approaches described above were rejected in favor of a third approach. This latter approach uses a personal computer to maintain both DR files extracted from the DR database and operating history data. The same personal computer is then used to process the data. This approach simplifies both administrative and operational considerations and allows ready access to the data for analyses.

The actual calculations for processing the data are as described in Section II.A. The only additional information required to produce the desired reports is the set of parameters by which some DRs are selected and others are not, e.g., station, system, subsystem, assembly, period of interest, and so forth. These factors are readily used to sort the database in order to prepare specific analyses.

III. Findings

The findings of this investigation are of two types: (1) findings concerning methods, and (2) findings concerning outage and availability characteristics (OMTBF, OMTTRS, and OFA) of DSN data systems. Both are discussed in this section.

A. Methodological Findings

Four methodological findings have been made. First, files can be extracted from the existing Discrepancy Report (DR) database with about 10 minutes of an analyst's time. They are normally received in hardcopy form within 24 hours of the extraction. Data from existing DSN Station Utilization Summary Reports can be entered in about 30 minutes for a one-week reporting period covering up to nine stations. (Note, however, that these reports lack detail about the use of the Command and Tracking Systems. If the latter were included, the time required to enter utilization data could double.)

Second, once all the data files of interest are obtained, a report that lists each outage, its duration, and the station, system, subsystem, and assembly involved can presently be prepared with about two to three hours of an analyst's time, which includes manual data entry from the hard copies into a computer file. Outages can also be listed by station, by system, by subsystem, or by assembly as well as by period.

Third, once outages have been selected, as in the previous paragraph, availability characteristics such as OMTBF, OMTTRS, and OFA can be calculated within one to two hours of elapsed time, with an operator at hand.

Fourth, plots of the data described in the two preceding paragraphs can be readily made in about 15 minutes of elapsed time per plot, with an operator at hand.

B. Data System Findings

Data system findings are presented in two parts. The first part concerns information on data system outages *per se.* The second part concerns Operating Mean Time Between Failures (OMTBF), Operating Mean Time to Restore Service (OMTTRS), and Operating Functional Availability (OFA) information.

1. **Data system outages.** Table 1 shows the number of outages, outage time, and "on" time for the Telemetry System and the number of outages and outage time for the Command and Tracking Systems for 1981, 1982, 1983, and the first nine periods of 1984. "On" time is not available for the latter two systems (see Section II.A).

Both the number of Telemetry System outages and outage time decreased over the period studied. The main reason for these decreases is that the total "on" time also decreased during this period as the number of active stations decreased.[4]

Tables 2, 3, and 4 break down the data in Table 1 by subsystem for the Telemetry, Command, and Tracking Systems, respectively. Breakdowns of the data in Table 1 by facility as well as by subsystem were also prepared and are available from the authors upon request.

2. **Data system availability characteristics.** Table 5 presents OMTBF, OMTTRS, and OFA data for the DSN Telemetry System by subsystem for the period 1981 through period 9 of 1984. Similar calculations cannot be made for the Command and Tracking Systems because of a lack of "on" time information for these systems (see Section II.A). Likewise, similar calculations cannot be made for individual assemblies within the Telemetry System.

The data presented in Tables 1 through 5 lead to the following conclusions:

(1) The Telemetry System had its lowest Operating Functional Availability (OFA) in 1984, whether radio frequency interference (RFI) is included or excluded in the calculation; it was 98.5% when RFI is included and 98.8% when RFI is excluded. The Telemetry System OFA was highest in 1981, when it was 99.1% whether RFI is included or excluded in the calculation (to three-place precision). (Table 5)

(2) The three subsystems within the Telemetry System that accumulated the greatest outage times were the

[4]The number of stations operating from 1981 through September 30, 1984, is as follows: nine stations in 1981, six stations in 1982 and the first half of 1983, and five stations in the last half of 1983 through September 30, 1984.

Antenna (ANT), Microwave (UWV), and Receiver (RCV) Subsystems. Together they accounted for just over 51% of all outage time of the Telemetry System. (Table 2)

(3) The three subsystems within the Telemetry System that were most prone to failure were the Antenna (ANT), Receiver (RCV), and Telemetry (DTM) Subsystems. Together they accounted for just over 40% of all failures of the Telemetry System. (Table 2)

(4) The three subsystems within the Telemetry System that had the longest average restoration times were the Frequency and Timing (FTS), Microwave (UWV), and Transmitter (TXR) Subsystems. Taken as a whole, their average restoration time was 1.67 hours. (Table 2)

(5) The three subsystems within the Command System that accumulated the greatest outage times were the Antenna (ANT), Command (DCD), and Transmitter (TXR) Subsystems. Together they accounted for over 59% of all outage time of the Command System. (Table 3)

(6) The three subsystems within the Command System that were most prone to failure were the Antenna (ANT), Command (DCD), and Transmitter (TXR) Subsystems. Together they accounted for just over 49% of all failures of the Command System. (Table 3)

(7) The four subsystems within the Command System that had the longest average restoration times were the Antenna (ANT), Frequency and Timing (FTS), Microwave (UWV), and Transmitter (TXR) Subsystems. Taken as a whole, their average restoration time was 1.93 hours. (Table 3)

(8) The three subsystems within the Tracking System that accumulated the greatest outage times were the Antenna (ANT), Facilities (FAC), and Tracking (DTK) Subsystems. Together they accounted for just over 51% of all outage time of the Tracking System. (Table 4)

(9) The three subsystems within the Tracking System that were most prone to failure were the Antenna (ANT), Tracking (DTK), and Receiver (RCV) Subsystems. Together they accounted for just over 49% of all failures of the Tracking System. (Table 4)

(10) The three subsystems within the Tracking System that had the longest average restoration times were the Facilities (FAC), Microwave (UWV), and Tracking (DTK) Subsystems. Taken as a whole, their average restoration time was 2.43 hours. (Table 4)

IV. Conclusions and Observations

The DSN Discrepancy Report database and DSN Station Utilization Summary Reports can indeed be used to calculate Operating Mean Time Between Failures (OMTBF), Operating Mean Time to Restore Service (OMTTRS), and Operating Functional Availability (OFA) for the DSN Telemetry System and for various combinations of Telemetry subsystems and DSN stations or facilities. Similar calculations could be made for the Command and Tracking Systems if the Station Utilization Summary Reports also contained "on" time information for these systems.

The amount of time involved on the part of an analyst to extract relevant data and to perform the desired calculations is not insignificant. Much time is now spent in manually re-entering data that were already in machine form in the databases. Moreover, analysts require special training in order to extract files of interest.

Outage and availability information on specific assemblies cannot be determined from existing information. However, if the Network Support Subsystem gathers "on" time information by assembly, which ought to be possible once the Mark IVA Monitor and Control System is fully implemented, then assembly-level outage and availability data can be obtained.

Presently, Discrepancy Reports are prepared only for DSN systems that specifically deliver data to DSN customers. Other DSN systems are not included in Discrepancy Reports unless they affect these so-called data systems. Again, however, the Mark IVA Network Support Subsystem can be designed to provide outage and availability information on these network elements, too.

The Discrepancy Report (DR) database could yield greater insight into system and subsystem failures if information now available only in narrative form could be readily searched and sorted. If specific categories of failure were coded, DRs could be sorted accordingly. Also, a menu-driven selection of system and subsystem designators (or a spelling checker) would minimize the number of misspelled entries, which precludes proper classification of some DRs.

Additionally, it is noted that the threshold for initiating a DR depends partly on the precision of the predicts for the application. This of course makes sense, since an application with loose tolerances can accommodate sloppier performance than one with tight tolerances. Yet the DSN's performance *per se* might be the same in two different cases, one with fairly precise predicts and the other with relatively imprecise predicts. When the predicts are fairly precise, a DR would be

initiated; when they are imprecise, no DR would be initiated. Thus, the number and duration of outages that are registered in a given period are partly a function of customer predicts, i.e., of the customers themselves, and are not purely measures of DSN performance. It might be worthwhile in the future to stratify DR data by customer or tolerance before analyzing them in order to identify any tolerance-dependent effects.

Finally, it is noted that a significant number of outages are not recognized in real time but are initiated in post-pass analysis by a network operations analyst (NOA). This procedure suffices for discrepancies that can be recognized by NOAs, but it is not comprehensive. In particular, discrepancies that involve two-station operations, e.g., very long baseline interferometry (VLBI), are not necessarily apparent to NOAs but appear only when data from both stations are correlated together by the "project team." It appears that such discrepancies are often not entered into the DR database. To this extent, the DR database understates the number and duration of outages and overstates OMTBFs and OFAs.

V. Future Improvements

Improvements to enhance the use of Discrepancy Reports in determining Deep Space Network (DSN) availability characteristics are being considered in three areas: (1) preparing Discrepancy Reports (DR) and Station Utilization Summary Reports, (2) analyzing outages and availability characteristics of DSN systems, subsystems, and assemblies, and (3) correcting conditions that lead to outages.

(1) Preparing Discrepancy Reports and Station Utilization Summary Reports

(a) Use of a CRT forms-mode input for Discrepancy Reports (DR): A comprehensive input form of this type can provide a controlled and appropriately detailed vocabulary for characterizing outages and their causes, thus facilitating later analyses. Moreover, it can facilitate revising input forms as configurations change in the DSN and as new insight is gained into failure modes and causes. It might also reduce the amount of time needed to log and enter DR inputs.

(b) Automatic compilation of reports of station use, now termed Station Utilization Summary Reports, either from information in the Monitor and Control System or from information entered by station operators using a CRT forms-mode input: This approach can facilitate identifying not only the use of each station (or link, in Mark IV parlance) but also the equipment engaged for each user (see [1] [c] below).

(c) Logging of equipment usage (and perhaps also software usage) from information available in the Monitor and Control System or Network Support Subsystem: This information can be used to compute Operating Mean Time Between Failures (OMTBF), Operating Mean Time to Restore Service (OMTTRS), and Operating Functional Availability (OFA) providing the log also shows the function being performed (see [1] [b] above).

If outages are also recorded when a link is used for maintenance and other non-support activities, then "true" Mean Time Between Failures (MBTF), Mean Time to Restore Service (MTTRS), and Functional Availability (FA) can be determined.

(d) Storage of DR data, equipment usage data, and software usage data in a common machine: This improvement will facilitate outage and availability analyses (see [2] below). (Alternatively, if, for good reasons, the data are maintained in different machines, the data can be organized in ways that facilitate file transfer, combination, and manipulation for the requisite analyses in a single machine.)

(2) Preparing Outage Reports and Availability Analyses

(a) Routine preparation of outage reports and availability analyses, perhaps monthly, for the previous three-, six-, and twelve-month periods.

(b) Use of outage reports to rank culprit systems and subsystems according to frequency and duration of outage and by unavailability for service. Assemblies can also be ranked by unavailability for service if equipment usage is appropriately logged (see [1] [c] above).

(3) Correcting Conditions That Lead to Outages

Routine distribution of outage reports and availability analyses (see [2] [b]) to DSN system engineers to use in assessing system, subsystem, and assembly performance and taking appropriate corrective action.

Acknowledgments

The authors thank Robertson Stevens for encouraging this study, R.E. Armour and J.C. Sutton for providing access to the Discrepancy Report database, and G.C. Smith, Kuohwa Tan, and Paula Cooke for providing operating schedule and history data.

Table 1. Telemetry, Command, and Tracking System outages, by year

System	1981			1982			1983			1984[a]		
	No. of Outages	Outage, Minutes	"On" Time, Hours	No. of Outages	Outage, Minutes	"On" Time, Hours	No. of Outages	Outage, Minutes	"On" Time, Hours	No. of Outages	Outage, Minutes	"On" Time, Hours
Telemetry	516	25,198	47,932	482	23,038	31,882	528	24,365	29,190	409	17,459	22,790
Command	355	23,224	–	216	16,815	–	136	11,155	–	197	15,608	–
Tracking	463	39,426	–	364	23,911	–	289	23,291	–	280	29,102	–

[a]Up to and including September 30, 1984

Table 2. Telemetry System outages by subsystem and by year

Year	1981		1982		1983		1984[a]	
S/S	No.	Min.	No.	Min.	No.	Min.	No.	Min.
AES	0	0	0	0	0	0	0	0
ANT	108	5892	120	5340	77	5094	47	2970
APS	32	657	23	605	15	258	31	910
DCD	0	0	2	95	1	1	0	0
DMC	4	112	4	353	3	110	3	84
DRG	0	0	0	0	1	3	0	0
DRS	1	8	0	0	2	131	1	10
DTK	4	80	6	173	7	164	4	68
DTM	68	2876	53	2892	47	636	65	3718
DTS	0	0	0	0	0	0	1	360
EXT[b]	2	70	0	0	0	0	0	0
FAC	32	1210	22	1112	18	875	16	589
FTS	4	168	8	661	4	406	5	449
GHS	32	964	6	67	7	45	11	409
GPS	1	1	0	0	0	0	0	0
GVC	1	23	4	212	2	23	0	0
GWB	5	50	2	8	1	17	2	70
NCD	0	0	0	0	0	0	1	15
NCE	5	73	5	46	0	0	0	0
NDS	3	44	3	47	1	43	0	0
NMC	2	22	1	22	0	0	0	0
NSS	0	0	0	0	1	21	0	0
NTK	1	2	0	0	1	45	1	5
NTM	4	42	0	0	1	158	2	17
OSA[b]	0	0	1	23	0	0	0	0
OSG[b]	0	0	2	33	1	2	9	78
PDX	7	139	8	157	6	807	5	73
RCV	80	4561	61	3533	68	3431	50	2950
RFI	16	434	55	2282	196	6706	114	3515
TXR	15	1422	9	290	12	667	20	1220
UWV	40	4817	25	3658	36	4246	12	1021
UNK[c]	49	1531	63	1435	20	476	49	1716
Total	516	25198	483	23044	528	24365	449	20247
Hours		419.966		384.066		406.083		337.45

[a]Up to and including period 9 (September 30, 1984)
[b]Not a standard DSN abbreviation
[c]UNK: Unknown

Table 3. Command System outages by subsystem and by year

Year	1981		1982		1983		1984[a]	
S/S	No.	Min.	No.	Min.	No.	Min.	No.	Min.
AES			0	0	0	0	2	213
ANT	63	5381	55	6034	32	2611	17	1607
APS	11	343	6	173	2	69	9	628
DCD	63	1496	20	869	23	907	44	4041
DMC	1	590	0	0	0	0	2	235
DRG	0	0	0	0	0	0	0	0
DRS	0	0	0	0	0	0	0	0
DTK	10	405	0	0	3	47	2	67
DTM	0	0	0	0	0	0	0	0
DTS	0	0	0	0	0	0	0	0
EXT[b]	0	0	0	0	0	0	0	0
FAC	27	1361	10	901	13	899	10	698
FTS	5	395	11	999	2	210	6	614
GHS	24	570	25	376	2	17	10	403
GPS	0	0	0	0	0	0	0	0
GVC	0	0	3	20	0	0	0	0
GWB	0	0	2	8	7	130	0	0
NCD	4	209	13	226	3	58	3	309
NCE	5	72	5	47	0	0	0	0
NDS	3	4	5	80	1	3	0	0
NMC	2	32	1	9	2	22	0	0
NSS	0	0	0	0	0	0	1	5
NTK	1	2	0	0	0	0	1	4
NTM	0	0	1	50	1	158	0	0
OSA[b]	0	0	0	0	0	0	0	0
OSG[b]	0	0	0	0	1	10	3	35
PDX	2	32	5	86	3	126	3	55
RCV	39	2434	3	1070	8	327	20	1272
RFI	1	40	0	0	0	0	0	0
TXR	43	5578	27	3834	18	3072	40	4505
UWV	17	2346	4	955	9	1933	2	73
UNK[c]	34	1894	20	1078	6	556	24	1057
Total	355	23224	216	16815	136	11155	197	15608
Hours		387		280		186		260

[a]Up to and including period 9 (September 30, 1984)
[b]Not a standard DSN abbreviation
[c]UNK: Unknown

Table 4. Tracking System outages by subsystem and by year

Year	1981		1982		1983		1984[a]	
S/S	No.	Min.	No.	Min.	No.	Min.	No.	Min.
AES	0	0	0	0	0	0	0	0
ANT	95	5399	108	5049	66	3725	40	2996
APS	24	1159	20	426	15	263	29	894
DCD	0	0	1	94	1	1	0	0
DMC	3	643	2	80	2	54	2	30
DRG	2	2792	0	0	1	12	2	947
DRS	4	92	1	23	1	180	0	0
DTK	88	8170	43	5716	32	5199	32	4303
DTM	2	39	0	0	1	1	0	0
DTS	0	0	0	0	0	0	0	0
EXT[b]	0	0	0	0	0	0	0	0
FAC	30	1822	20	2101	20	2711	29	13125
FTS	2	114	7	648	4	398	5	499
GHS	31	621	9	154	7	43	9	243
GPS	1	2	0	0	0	0	0	0
GVC	1	20	2	19	0	0	0	0
GWB	0	0	2	8	0	0	0	0
NCD	0	0	0	0	0	0	1	15
NCE	5	67	4	40	0	0	0	0
NDS	3	44	2	41	0	0	0	0
NMC	3	144	0	0	0	0	0	0
NSS	0	0	0	0	1	56	1	5
NTK	3	58	4	43	4	155	2	16
NTM	1	31	0	0	1	158	0	0
OSA[b]	0	0	1	23	0	0	0	0
OSG[b]	0	0	1	20	2	62	9	68
PDX	9	364	10	268	5	395	3	44
RCV	59	3949	39	3128	46	3553	44	2422
RFI	4	196	11	291	20	297	4	178
TXR	18	1493	10	1045	15	919	19	1226
UWV	29	3836	17	3070	25	3906	12	1051
UNK[c]	46	8371	50	1624	20	1203	37	1040
Total	463	39426	364	23911	289	23291	280	29102
Hours		657		399		388		485

[a]Up to and including period 9 (September 30, 1984)
[b]Not a standard DSN abbreviation
[c]UNK: Unknown

Table 5. Telemetry System OMTBF, OMTTRS, and OFA by subsystem and by year

Year	1981			1982			1983			1984[a]		
S/S	OMTBF	OMTTRS	OFA	OMTBF	OMTTRS	OFA	OMTBF	OMTTRS	OFA	OMTBF	OMTTRS	OFA
AES												
ANT	444	0.91	99.7	266	0.74	99.7	379	1.1	99.7	485	1.05	99.7
APS	1498	0.34	99.9	1386	0.44	99.9	1946	0.29	99.9	735	0.49	99.9
DCD				15941	0.79	99.9	29190	0.02	99.9			
DMC	11983	0.47	99.9	7971	1.47	99.9	9730	0.61	99.9	7597	0.47	99.9
DRG							29190	0.05	99.9			
DRS	47932	0.13	99.9				14595	1.09	99.9	22790	0.17	99.9
DTK	11983	0.33	99.9	5314	0.48	99.9	4170	0.39	99.9	5698	0.28	99.9
DTM	705	0.7	99.9	602	0.91	99.8	621	0.23	99.9	351	0.95	99.7
DTS										22790	6	99.9
EXT[b]	23966	0.58	99.9									
FAC	1498	0.63	99.9	1449	0.84	99.9	1622	0.81	99.9	1424	0.61	99.9
FTS	11983	0.7	99.9	3985	1.38	99.9	7298	1.69	99.9	4558	1.5	99.9
GHS	1498	0.5	99.9	5314	0.19	99.9	4170	0.11	99.9	2072	0.62	99.9
GPS	47932	0.02	99.9									
GVC	47932	0.38	99.9	7971	0.88	99.9	14595	0.19	99.9			
GWB	9586	0.17	99.9	15941	0.07	99.9	29190	0.28	99.9	11395	0.58	99.9
NCD										22790	0.25	99.9
NCE	9586	0.24	99.9	6376	0.15	99.9						
NDS	15977	0.24	99.9	10627	0.26	99.9	29190	0.72	99.9			
NMC	23966	0.18	99.9	31882	0.37	99.9						
NSS							29190	0.35	99.9			
NTK	47932	0.03	99.9				29190	0.75	99.9	22790	0.08	99.9
NTM	11983	0.18	99.9				29190	2.63	99.9	11395	0.14	99.9
OSA[b]				31882	0.38	99.9						
OSG[b]				15941	0.28	99.9	29190	0.03	99.9	2532	0.14	99.9
PDX	6847	0.33	99.9	3985	0.33	99.9	4865	2.24	99.9	4558	0.24	99.9
RCV	599	0.95	99.8	523	0.97	99.8	429	0.84	99.8	456	0.98	99.7
RFI	2996	0.45	99.9	580	0.69	99.8	149	0.57	99.6	200	0.51	99.7
TXR	3195	1.58	99.9	3542	0.54	99.9	2433	0.93	99.9	1140	1.02	99.9
UWV	1198	2.01	99.8	1275	2.44	99.8	811	1.97	99.7	1899	1.42	99.9
UNK[c]	978	0.52	99.9	506	0.38	99.9	1460	0.4	99.9	465	0.58	99.8
System Total	93	0.81	99.1	66	0.8	98.8	55	0.77	98.6	51	0.75	98.5

[a]Up to and including period 9 (September 30, 1984)
[b]Not a standard DSN abbreviation
[c]UNK: Unknown

JPL DSN DISCREPANCY REPORT DR NO. C 2990

INITIATOR

1. PRECEDENCE LEVEL (CHECK ONE) ☐ CLASS 1 ☐ CLASS 2 ☐ CLASS 3
2. CLASS 1 AUTHORIZATION
3. ☐ FACILITY NOTIFIED _____ BY _____ DOY _____
4. LAST NAME FIRST M.I.
JPL EXT.
MAIL STATION
5. DATE WRITTEN
6. MASTER DR NO.

PROBLEM IDENTIFICATION

7. USER/PROJECT
8. PASS NO./TEST
9. TIME OF FAILURE/INCIDENT DOY _____ UTC _____
10. FACILITIES AFFECTED

11. DATA TYPE AFFECTED (FILL IN AS APPROPRIATE) (START UTC/END UTC)

IMPACT ON SYSTEMS →	TLM	TRK	CMD	MON	GCF	OTHER _____
DATA OUTAGE	/	/	/	/	/	/
DEGRADED DATA	/	/	/	/	/	/
RECOVERABLE DATA	/	/	/	/	/	/

SUSPECTED CAUSE OF PROBLEM (CHECK ALL APPLICABLE BOXES)

12. CATEGORY ☐ H/W ☐ S/W ☐ PROC ☐ DOC ☐ RFI ☐ UNKNOWN ☐ OTHER _____

13. FACILITY ☐ NDP ☐ NOCC ☐ GCF ☐ SPC ____ ☐ DSS ____ OTHER _____

14. SYSTEM ☐ FTS ☐ VLBI ☐ TRK ☐ TEST SUPPORT ☐ TLM ☐ MON & CONT ☐ CMD ☐ RADIO SCIENCE
15. SUBSYSTEMS
16. ASSEMBLY
17. CIRCUIT OUTAGE (COMM ONLY) FROM _____ TO _____ TOTAL OUTAGE _____

18. DESCRIPTION OF PROBLEM/FAILURE/INCIDENT (DESCRIBE IN AS MUCH DETAIL AS POSSIBLE)

19. RELATED DOCUMENTS AND REPORTS
FR _____ WLC _____
ISA _____ OTHER _____

☐ ADDITIONAL DATA ATTACHED

CLOSE OUT

20. REAL TIME RESTORE AND CLOSEOUT ACTION
☐ WARM LOAD ☐ COLD LOAD ☐ SYSTEM SWAP ☐ POWER RESTORE ☐ EQUIPMENT SWAP ☐ CIRCUIT SWAP ☐ OTHER _____

SEF (Y/N) ☐

21. SUBSYSTEM STATUS ☐ COMMITTED H/W OR S/W ☐ R&D H/W OR S/W
22. PROBLEM FAULT ☐ FACILITY DEPENDENT ☐ FACILITY INDEPENDENT ☐ UNAVOIDABLE ☐ OTHER _____

CONTROL

23. ASSIGNED TO ☐ OC&S ☐ PAG ☐ OTHER _____ DATE
24. APPROVAL DATE
REASSIGNED TO ☐ OC&S ☐ PAG ☐ OTHER _____ DATE
25. CLASS 1 APPROVAL DATE

COPY DISTRIBUTION: JPL 0156 R9/84
WHITE – ORIGINAL, GREEN – RETURN, CANARY – CORRECTIVE AGENCY, PINK – DR CONTROL, GOLDENROD – ORIGINATOR RETAINS

Fig. 1. DSN Discrepancy Report form

AUG 30,84 DSN STATION UTILIZATION SUMMARY REPORT FOR WEEK 33 - 33 PAGE 1

	12		14		42		43		61		63		TOTAL	
	SOH	EUH	SOH	EUH	SOH	EUH	SOH	EUH	SOH	EUH	SOH	EUH	SOH	EUH
1A1														
PN-10	2.5	1.5	0.0	0.0	0.0	0.0	34.5	29.7	5.1	3.6	18.3	15.3	60.5	50.3
PN-11	33.0	27.5	0.0	0.0	35.6	30.0	5.6	4.9	26.6	22.9	0.0	0.0	101.0	85.4
PN-12	25.5	21.0	0.0	0.0	22.3	17.5	0.0	0.0	40.3	35.0	3.7	3.0	91.9	76.6
HEL-01	18.5	14.0	0.0	0.0	0.0	0.0	0.0	0.0	8.5	6.3	0.0	0.0	27.1	20.4
ICE	0.0	0.0	0.0	0.0	0.0	0.0	25.2	20.7	0.0	0.0	47.2	40.2	72.5	61.0
ACCE	0.0	0.0	0.0	0.0	0.0	0.0	21.0	11.1	24.1	19.6	0.0	0.0	45.1	30.8
AIRM	53.7	41.2	0.0	0.0	33.1	25.1	0.0	0.0	0.0	0.0	25.7	19.7	112.6	86.1
AUKS	0.0	0.0	0.0	0.0	0.0	0.0	0.0	0.0	0.0	0.0	14.4	12.1	14.4	12.1
VGR-01	0.0	0.0	0.0	0.0	4.7	4.0	18.9	16.9	4.0	3.3	7.1	6.4	34.9	30.6
VGR-02	8.4	7.4	0.0	0.0	12.2	11.5	20.8	17.8	2.5	2.0	32.0	23.3	76.0	62.0
1A4	9.0	5.5	0.0	0.0	0.0	0.0	4.5	3.0	0.0	0.0	0.0	0.0	13.5	8.5
TOTAL 1A	150.8	118.3	0.0	0.0	108.1	88.3	130.6	104.3	111.5	93.0	148.7	120.2	649.9	524.2
APCT*	87.5	100.0	0.0	0.0	67.6	100.0	81.7	100.0	70.3	100.0	88.5	100.0		

NOTE:

APCT:TOTAL 1A/GD.TOTAL PER STATION
1A1:SPACECRAFT TRACKING
1A2:PROJECT RELATED SUPPORT
1A3:DSN PROJECT PREPARATION
1A4:MULTIMISSION SUPPORT

SOH:STATION OPERATING HOURS
1B1:RADIO SCIENCE-OSSA
1B2:RADIO SCIENCE-RAES
1B3:RADIO SCIENCE-OSTDS
1B4:RADIO SCIENCE-OA

EUH:END USER HOURS
1C1:ADVANCED SYSTEM-OSTDS
1C2:ADVANCED SYSTEM-OSTDS SPE.
1D1:SPECIAL

Fig. 2. Sample DSN station utilization summary report

End of Document